XANES, EXAFS and Kβ Spectroscopic Studies of the Oxygen-Evolving Complex in Photosystem II

by

John Henry Robblee

B.S. (Haverford College) 1995

A dissertation submitted in partial satisfaction of the

requirements for the degree of

Doctor of Philosophy

in

Chemistry

in the

GRADUATE DIVISION

of the

UNIVERSITY OF CALIFORNIA, BERKELEY

Committee in charge:

Professor Kenneth Sauer, Chair
Professor Kenneth N. Raymond
Professor Richard Malkin

Fall 2000

XANES, EXAFS and Kβ Spectroscopic Studies of the

Oxygen-Evolving Complex in Photosystem II

by

John Henry Robblee

Abstract

XANES, EXAFS and Kβ Spectroscopic Studies of the
Oxygen-Evolving Complex in Photosystem II

by

John Henry Robblee

Doctor of Philosophy in Chemistry

University of California, Berkeley

Professor Kenneth Sauer, Chair

A key question for the understanding of photosynthetic water oxidation is whether the four oxidizing equivalents necessary to oxidize water to dioxygen are accumulated on the four Mn ions of the oxygen evolving complex (OEC), or whether some ligand-centered oxidations take place before the formation and release of dioxygen during the $S_3 \rightarrow [S_4] \rightarrow S_0$ transition. Progress in instrumentation and flash sample preparation allowed us to apply Mn Kβ X-ray emission spectroscopy (Kβ XES) to this problem for the first time. The Kβ XES results, in combination with Mn X-ray absorption near-edge structure (XANES) and electron paramagnetic resonance (EPR) data obtained from the same set of samples, show that the $S_2 \rightarrow S_3$ transition, in contrast to the $S_0 \rightarrow S_1$ and $S_1 \rightarrow S_2$ transitions, does not involve a Mn-centered oxidation. This is rationalized by manganese μ-oxo bridge radical formation during the $S_2 \rightarrow S_3$ transition.

Using extended X-ray absorption fine structure (EXAFS) spectroscopy, the local environment of the Mn atoms in the S_0 state has been structurally characterized. These results show that the Mn–Mn distance in one of the di-μ-oxo-bridged Mn–Mn moieties increases from 2.7 Å in the S_1 state to 2.85 Å in the S_0 state. Furthermore, evidence is presented that shows three di-μ-oxo binuclear Mn_2 clusters may be present in the OEC, which is contrary to the widely held theory that two such clusters are present in the OEC.

The EPR properties of the S_0 state have been investigated and a characteristic 'multiline' signal in the S_0 state has been discovered in the presence of methanol. This provides the first direct confirmation that the native S_0 state is paramagnetic. In addition, this signal was simulated using parameters derived from three possible oxidation states of Mn in the S_0 state.

The dichroic nature of X-rays from synchrotron radiation and single-crystal Mn complexes have been exploited to selectively probe Mn-ligand bonds using XANES and EXAFS spectroscopy. The results from single-crystal Mn complexes show that dramatic dichroism exists in these complexes, and are suggestive of a promising future for single-crystal studies of PS II.

To Mel

Table of Contents

Table of Figures

Acknowledgments

I have been exceedingly fortunate to have not just one but three advisors to guide me through my career as a graduate student. Vittal Yachandra, Ken Sauer, and Mel Klein deserve a great deal of credit for everything that they have done for me over the past five years. Vittal has been a vital resource for his qualities ranging from his vast experimental and theoretical knowledge of X-ray spectroscopy to his never-ending enthusiasm to discuss data and their implications on a daily basis. I have also appreciated all of our discussions that deviate from scientific pursuits, such as the absurdity of the U.S. Senate and the tale of the snake cutting in line to get an aliquot of elixir.

I have learned a lot from Ken throughout my graduate career. He has been instrumental in teaching me how to write clearly and effectively and making sure that all of the scientific questions get addressed. If one is looking for a role model in academia, one need look no further than Ken.

I cannot overemphasize how grateful I am to have been associated with Mel. He was a consummate role model as a mentor, scientist, colleague, and friend. I will always value our conversations in which he taught me about the physics of EPR and X-ray absorption spectroscopy. I will always think of him, and I will consider myself successful if, as he did, I have his kind of enthusiasm and leadership by example throughout my career. I hope that I have and will continue to make him proud.

The experiments described in Chapter 2, Chapter 3, and Chapter 4 would not have been possible if I was not working with a colleague like Johannes Messinger. His remarkable abilities to design experiments and interpret their results were invaluable, as

well as his encyclopedic knowledge of the photosynthetic literature. I truly enjoyed the two years we spent working on experiments together.

I should emphasize that the work described in this thesis is highly collaborative, and is only made possible by the entire research group working together to achieve success in the lab and at the beamline. Without their input, it would not have been possible to complete any of the experiments that are described in this thesis. Carmen Fernandez played a critical role in the difficult task of bringing the flash experiments described in Chapter 2 to fruition. Roehl Cinco and Henk Visser were instrumental for their tireless effort in making the X-ray spectroscopy happen on the beamline. I have also enjoyed interacting with them throughout my graduate career and hope that they aren't too bothered by minor events such as finding one's iBook covered in politically oriented bumper stickers. I would also like to thank the other members of the group for both their help with experiments and making the Calvin lab an enjoyable place to work: Shelly Pizarro, Annette 'kugelschreiber' Rompel, Emanuele Bellacchio, Matthew Latimer, and Karen McFarlane (a.k.a. Karen McFanlore or Karen McFachara).

Finally, I would like to thank Michelle for her continual support and friendship. I would also like to extend my deepest gratitude to my parents for their continual encouragement and for demonstrating the value of hard work and doing things right.

Chapter 1 : Introduction

The advent of oxygen-evolving photosynthesis is perhaps the most important event to have occurred in evolution. It was only through the conversion of Earth's anaerobic atmosphere[1] to an aerobic atmosphere 2 – 3 billion years ago[2-4] that evolution of eukaryotic life forms became possible. This conversion was accomplished by photosynthetic organisms which harnessed the energy present in photons of sunlight and stored it in the form of readily accessible molecules such as dioxygen, NADPH

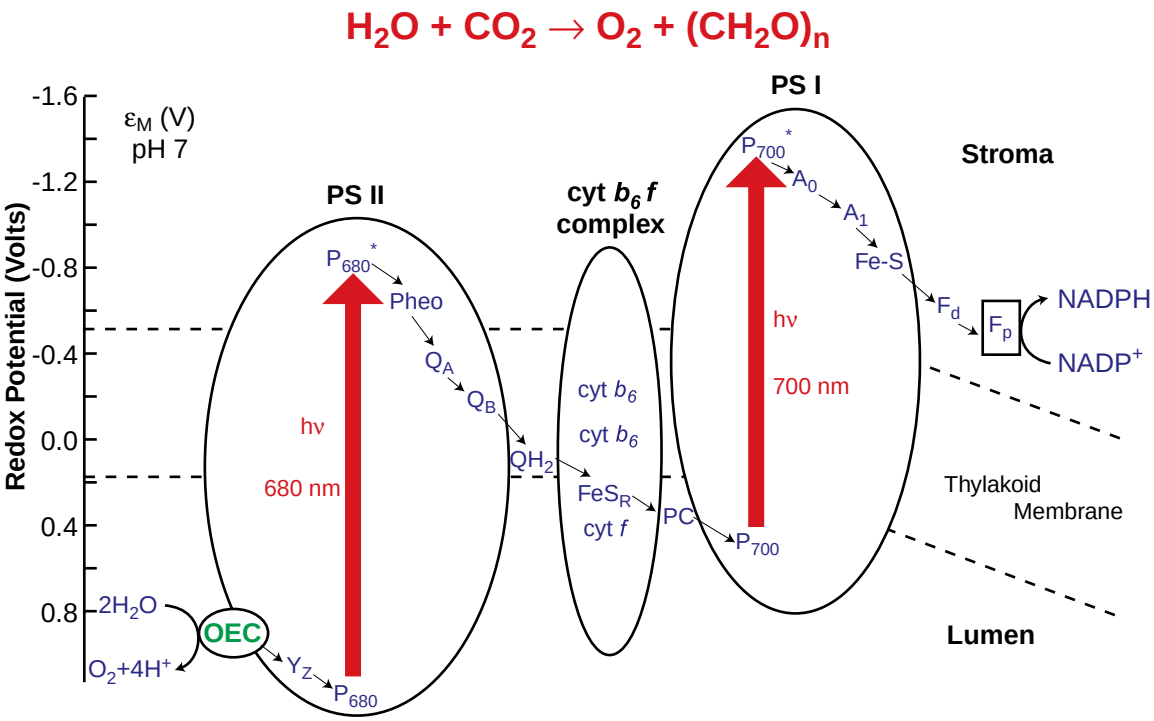

Figure 1-1: Z-scheme for photosynthetic electron flow, as adapted from Miller et al.[11] H_2O is the primary electron donor, and a series of charge-transfer steps provide the energy necessary for electron transport through the photosynthetic electron-transport chain. The terminal acceptor for the electrons is $NADP^+$; the resulting NADPH is used as reducing equivalents in the dark reactions in the Calvin cycle (where carbon fixation occurs). The equation above the Z-scheme describes the net reaction of photosynthesis.

(nicotinamide adenine dinucleotide phosphate), ATP (adenosine triphosphate), carbohydrates, and lipids. This process is summarized by the equation in Figure 1-1 and consists of two major groups of reactions: the light reactions and the dark reactions. The light reactions are schematically summarized in Figure 1-1; these reactions use light energy to oxidize water to dioxygen, generate a proton gradient across the thylakoid membrane, and generate reducing equivalents in the form of NADPH.[5] The potential generated by the proton gradient is then used by a membrane-bound complex, known as the ATP synthase, to generate ATP.[6,7] The dark reactions of photosynthesis use the reducing equivalents available in NADPH as well as ATP to fix CO_2 into carbohydrates, generating biomass in a process known as the Calvin-Bassham cycle.[8-10]

The driving force behind photosynthetic electron transport is the absorption of visible-light photons by the photosynthetic reaction centers photosystem II (PS II) and photosystem I (PS I). This absorption process provides the necessary free energy to transport electrons from water, the primary electron donor, to $NADP^+$, the terminal electron acceptor, and generates a proton gradient in the process. Each of these reaction centers is a large multi-subunit membrane-bound complex; PS II has a molecular weight of 300 – 400 kDa,[12] and the active form of PS I, a trimer, has a molecular weight of 1000 kDa.[13] These large reaction-center complexes trap photons with their large chlorophyll (Chl) antenna systems and transfer the absorbed energy to a designated cluster of Chl molecules (P_{680} in PS II and P_{700} in PS I).

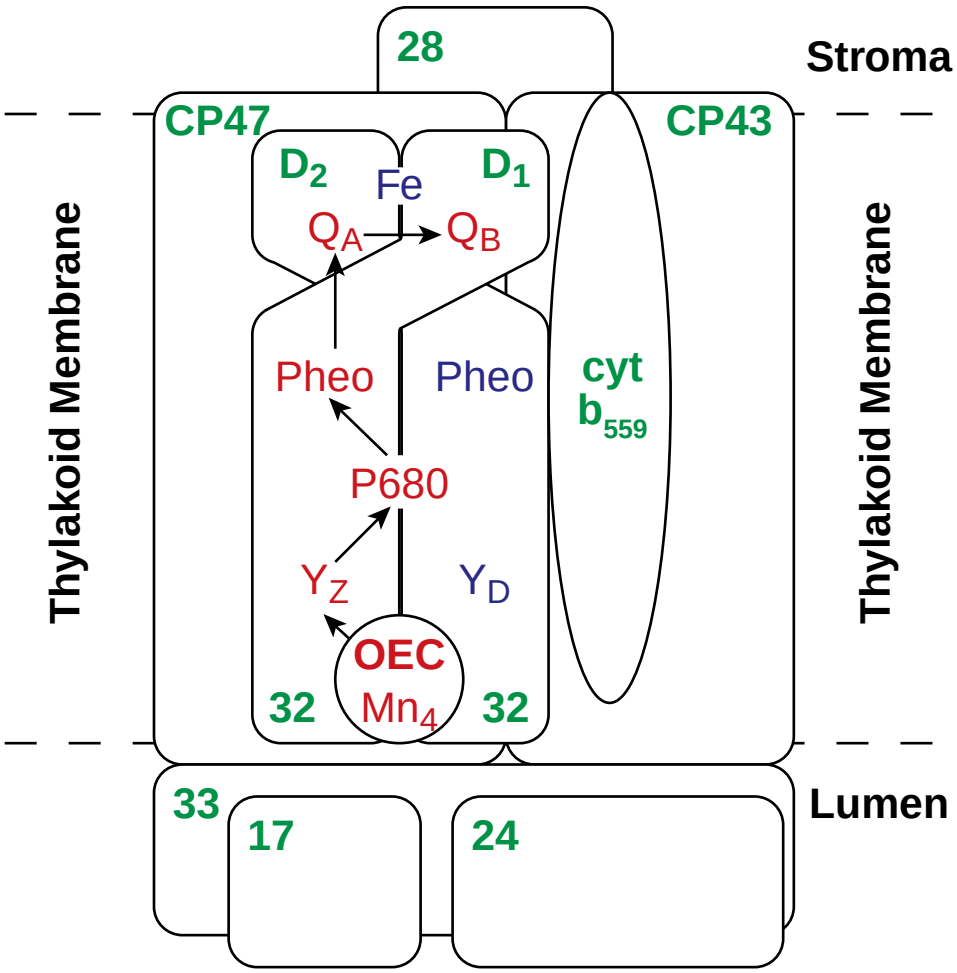

Figure 1-2: Schematic diagram of PS II. The labeled cofactors are described in the text. The chlorophyll-containing CP43, CP47, and 28 kDa polypeptides are primarily involved in light harvesting. The 33, 24, and 17 kDa extrinsic polypeptides play a role in the stabilization of the OEC and its associated cofactors. The 32 kDa D_1 and D_2 polypeptides provide many of the ligands to the OEC and also contain the redox-active tyrosines Y_Z and Y_D. The function of the cytochrome b_{559} subunit is unknown at present. Adapted from Debus.[14]

Absorption of the energy from the incident photon promotes P_{680} (or P_{700} in PS I) to an excited state. The excited state is dissipated very rapidly (3 – 20 ps for P_{680}^* reduction,[15,16] 1 – 2 ps for P_{700}^* reduction[17-20]) by transfer of an electron to a series of acceptor molecules. Figure 1-2 shows the electron transport path that exists in PS II.

After transfer to a pheophytin, the electron is sequentially transferred through two redox-active plastoquinone molecules, Q_A and Q_B. Once Q_B is doubly reduced, it is released from PS II into the thylakoid membrane and is oxidized by the next component in the electron transport chain, the cyt b_6f complex.

To fill the hole that is left behind after P_{680} oxidation, a redox-active tyrosine residue Y_Z (Tyr-161 from the D1 polypeptide[21,22]) becomes oxidized. Y_Z is quickly (0.07 – 1.4 ms[23-25]) reduced by the oxygen-evolving complex (OEC), which is bound to PS II. To reduce Y_Z, the OEC is able to extract electrons from water through a concerted 4-electron oxidation as shown in Eq. 1-1:

$$2H_2O \rightarrow O_2 + 4e^- + 4H^+ \qquad \text{Eq. 1-1}$$

If the OEC were to perform this reaction in a series of one-electron steps, highly reactive intermediates such as peroxide and superoxide would be formed.[26] To couple the one-electron chemistry of the reaction center with the four-electron chemistry of water oxidation, the Mn-containing OEC cycles through 5 redox states, S_0 through S_4, where the index denotes the number of oxidizing equivalents stored on the OEC.[27] Only when four oxidizing equivalents have been stored in the S_4 state is dioxygen formed, which avoids the release of harmful water-oxidation intermediates.

The OEC performs a vital and thermodynamically unfavorable reaction that has been extremely difficult to mimic with metal-containing model complexes.[28-30] Thus, the OEC has been the subject of intense study for over 30 years in an attempt to derive insight into the mechanism of water oxidation by the OEC.[14,31-40] The relevant kinetic and thermodynamic parameters as the OEC cycles through the various S-states have been of interest,[23-25,41,42] but the critical element to understanding water oxidation is knowledge of

both the structure of the OEC and the oxidation states of Mn for each of the intermediate S-states. Electron paramagnetic resonance (EPR) techniques[11,35,43,44] have provided important contributions towards this goal, especially in the identification of paramagnetic Mn species in each of the S-states.[45-54] However, structural information about the OEC from EPR experiments is usually only available indirectly through interpretation of the *g* values and hyperfine values obtained through simulation of experimental spectra.

X-ray spectroscopy, however, is a very powerful technique for addressing both

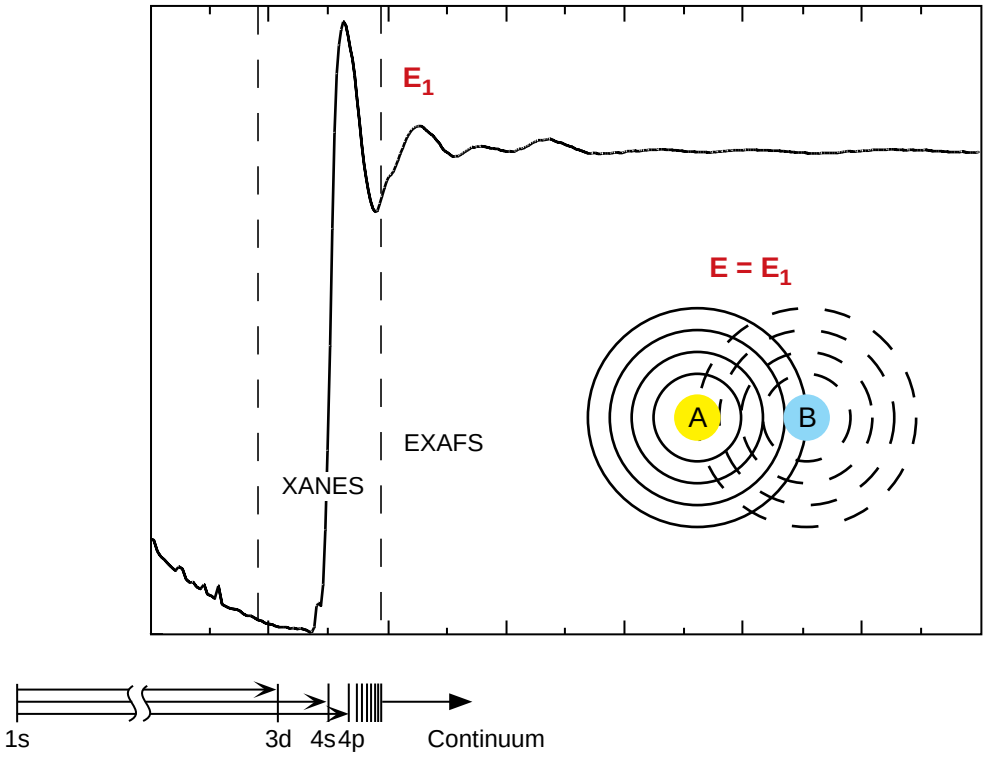

Figure 1-3: Mn K-edge X-ray absorption spectrum of PS II. The XANES region contains information about the oxidation states of Mn, and the EXAFS region contains structural information about the local environment surrounding Mn. The EXAFS interference pattern arises from a final-state interference effect from backscattering off neighboring atoms (B). At an X-ray energy E_1, the interference is constructive; thus, an increase in X-ray absorption is seen. See text for more details.

structural and oxidation-state questions. Figure 1-3 shows that the Mn K-edge X-ray absorption spectrum of PS II contains two main parts: the XANES (X-ray absorption near-edge structure) region and the EXAFS (extended X-ray absorption fine structure) region. Information about the oxidation states of Mn can be obtained from the XANES region, which is primarily the $1s \rightarrow 4p$ transition in Mn[55] and is sensitive to Mn oxidation-state changes through core-hole shielding effects.[56] Beyond the XANES absorption edge, EXAFS oscillations appear; these are due to a final-state interference effect from photoelectrons that are backscattered off neighboring atoms, as seen in Figure 1-3.[57] These oscillations contain information about the number of backscatterers present and the identity of the backscattering atoms; they also contain extremely accurate information about the absorber-backscatterer distances ($\bullet$ 0.02 Å error) in the frequency of the oscillations.

The seminal EXAFS and XANES experiments on the OEC were performed 20 years ago by Kirby et al.[58] and Goodin et al.,[59] respectively. The conclusion from the EXAFS experiments was that di-μ-oxo-bridged binuclear Mn_2 moieties are a prominent structural motif in the S_1 state of the OEC (the dark-stable state), while the conclusion from the XANES experiments was that Mn is oxidized during the $S_1 \rightarrow S_2$ transition. Many subsequent XANES and EXAFS experiments have provided additional oxidation-state and structural information for the OEC in other S-states.[36,38,40] However, the difficulty of generating relatively pure samples in S-states other than the dark-stable S_1 state and the S_2 state has hampered subsequent studies, which are crucial to a mechanistic understanding of water oxidation by the OEC.

This thesis addresses these problems on two fronts. By preparing samples enriched in each of the S-states S_0, S_1, S_2, and S_3, the presence or absence of Mn oxidation during each S-state transition has been addressed. This has been done using XANES spectroscopy as well as a novel X-ray spectroscopic technique, Kβ X-ray emission spectroscopy (Kβ XES) and is described in Chapter 2. These results can be explained by the conclusion that not all of the S-state transitions contain Mn-based oxidations.

Chapter 3 describes the structural characterization of the S_0 state using EXAFS spectroscopy on samples generated through single-flash turnover. This is the most difficult S-state to generate in high purity. The conclusions from these experiments show that some of the di-μ-oxo-bridged Mn–Mn distances are longer in the S_0 state than they are in the S_1 state. In addition, some surprising conclusions can be drawn from the experimental EXAFS results – specifically that three di-μ-oxo bridges may be present – that suggest additional structural possibilities for the OEC which have not been previously considered in detail.

Chapter 4 describes the characterization of the S_0 state using EPR spectroscopy in which a distinctive 'multiline' EPR signal has been detected in the S_0 state, thereby confirming the paramagnetic nature of the S_0 state. This signal was then simulated under various assumptions for the oxidation states of Mn in the S_0 state.

Chapter 6 describes the future directions for this research, which will likely be centered around the recently discovered X-ray crystallographic structure of PS II at 3.8 Å resolution.[60] To prepare for future studies of single crystals of PS II, single crystals of several Mn model complexes were studied using XANES and EXAFS spectroscopy to

exploit the dichroic nature of single crystals and synchrotron radiation; this is described in Chapter 5.

Chapter 2 : Absence of Mn-centered oxidation in the $S_2 \rightarrow S_3$ transition: insights from XANES and Kβ XES and implications for the mechanism of photosynthetic water oxidation

Abstract

A key question for the understanding of photosynthetic water oxidation is whether the four oxidizing equivalents necessary to oxidize water to dioxygen are accumulated on the four Mn ions of the oxygen evolving complex (OEC), or whether some ligand-centered oxidations take place before the formation and release of dioxygen during the $S_3 \rightarrow [S_4] \rightarrow S_0$ transition. Progress in instrumentation and flash sample preparation allowed us to apply Mn Kβ X-ray emission spectroscopy (Kβ XES) to this problem for the first time. The Kβ XES results, in combination with Mn X-ray absorption near-edge structure (XANES) and electron paramagnetic resonance (EPR) data obtained from the same set of samples, show that the $S_2 \rightarrow S_3$ transition, in contrast to the $S_0 \rightarrow S_1$ and $S_1 \rightarrow S_2$ transitions, does not involve a Mn-centered oxidation. Based on new structural data from the S_3 state, manganese μ-oxo bridge radical formation is proposed for the $S_2 \rightarrow S_3$ transition, and three possible mechanisms for the O–O bond formation are presented.

Introduction

Most life on earth is critically dependent on the presence of dioxygen in the atmosphere. Almost all of this dioxygen has been generated through photosynthetic oxygen evolution by the oxygen evolving complex (OEC) in photosystem II (PS II).[14,35,61] PS II is a ~500 kDa multi-subunit membrane protein complex whose primary function is to generate charge separation across the membrane using the energy present in photons of sunlight. The energy from this charge separation is then used to oxidize water to dioxygen in the OEC, and eventually to generate ATP and NADPH. The OEC contains four Mn atoms and two essential cofactors, Ca^{2+} and Cl^-. Using the energy from the light-induced charge separation in the PS II reaction center, the OEC couples the 4-electron chemistry of water oxidation with the 1-electron photochemistry of the reaction center by sequentially storing oxidizing equivalents in a series of S-states S_i ($i = 0 - 4$), where i denotes the number of oxidizing equivalents stored (Figure 2-1).[27] Once four oxidizing equivalents have been stored (S_4), the OEC evolves dioxygen. This accumulation process avoids the release of harmful water oxidation intermediates such as superoxide or peroxide.

The mechanism by which the OEC generates dioxygen from water has been the

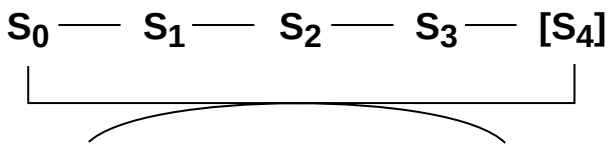

Figure 2-1: S-state scheme originally proposed by Kok et al.[27]

subject of intense study. Several possible mechanisms for this reaction have been proposed;[36,37,40,62-70] however, some key mechanistic questions are still unresolved. Knowledge of the structures of the Mn cluster and the oxidation states of Mn and other components as the OEC advances through the S-states is crucial to understanding the mechanism of water oxidation. In the absence of a high-resolution X-ray crystal structure of PS II, the primary spectroscopic tool for structural analysis of the S-states has been extended X-ray absorption fine structure (EXAFS) spectroscopy. Based on EXAFS data, the Mn cluster has been proposed to be a cluster consisting of at least two di-μ-oxo bridged Mn moieties and one mono-μ-oxo bridge Mn moiety.[34,71] However, the EXAFS data provide few constraints on how these motifs are arranged in the OEC; thus, several possible topological models exist.[40,72,73] Recently, a crystal structure at 3.8 Å resolution has been reported for an oxygen-evolving PS II preparation from *Synechococcus elongatus*.[60] The current data lack sufficient resolution to define an exact structure of the OEC in the S_1 state, but suggest an asymmetric 'Y' shape of the cluster. Based on ^{55}Mn ENDOR data from the S_2-state multiline EPR signal,[44,74] continuous-wave EPR simulations of the S_2-state EPR multiline signal,[75,76] and density functional theory (DFT) calculations,[77] structural models with a monomer-trimer arrangement of the Mn ions have been proposed, while a recent simulation of the S_2-state multiline EPR signal is consistent with a diamond-like structure.[78] Further work is required to define the overall structure of the OEC, but the Mn–Mn and Mn–Ca vectors determined by EXAFS spectroscopy will serve as a basis for any proposed structure.

EXAFS data reveal that the structure of the Mn cluster is not static; instead, distance changes are observed during some S-state transitions. The EXAFS spectra of the dark-stable S_1 state show two to three 2.7 Å Mn–Mn distances and one 3.3 Å Mn–Mn

distance, characteristic of two to three di-μ-oxo bridges and one mono-μ-oxo bridge, respectively.[72,79] Advancement to the S_2 state does not change the EXAFS spectrum; however, in the S_0 state one of the 2.7 Å distances increases in length by 0.1 – 0.2 Å, and the 2.7 Å distances increase in the S_3 state to 2.8 Å and 3.0 Å, indicating changes in the di-μ-oxo bridges.[69,80-82]

Several different spectroscopic methods have been used to address the oxidation states of Mn as a function of S-state. Electron paramagnetic resonance (EPR) spectroscopy has shown that the S_0 and S_2 states are paramagnetic, exhibiting multiline EPR signals,[45,46,50,51,83] and that the S_1 state has a parallel polarization EPR signal.[47-49,84] This suggests that Mn is oxidized during the $S_0 \rightarrow S_1$ and $S_1 \rightarrow S_2$ transitions. Other EPR studies of the power-saturation behavior of a redox-active tyrosine in photosystem II, Y_D^{ox}, which is sensitive to the presence of relaxing centers such as the Mn cluster, show that the half-saturation power $P_{1/2}$ changes during the $S_0 \rightarrow S_1$ and $S_1 \rightarrow S_2$ transitions, but remains unchanged during the $S_2 \rightarrow S_3$ transition.[85] This led to the suggestion that, unlike the $S_0 \rightarrow S_1$ and $S_1 \rightarrow S_2$ transitions, the $S_2 \rightarrow S_3$ transition proceeds without Mn oxidation. A direct pulsed electron spin echo measurement of the Y_D^{ox} T_1 relaxation time, which has intrinsic and dipolar contributions, shows the same trends with S-state as the continuous-wave EPR measurements.[86] Nuclear magnetic resonance proton relaxation enhancement (NMR-PRE) measurements, which measure the increased relaxation rate of the bulk water due to rapid exchange with water bound to a transition metal such as Mn, also led to the same conclusion, in particular with regard to the $S_2 \rightarrow S_3$ transition not involving Mn oxidation.[87] In addition, UV absorption difference spectroscopy has been used to address this question. By measuring small changes in absorbance between

S-states, difference spectra are obtained which have been interpreted by some groups to suggest that Mn is oxidized on each S-state transition, contrary to the conclusions from other methods.[88-90] However, the interpretation of these UV absorption difference spectra to derive insight about Mn oxidation is not straightforward.[91,92]

X-ray spectroscopic techniques are ideally suited to address questions about oxidation state, because the element in question, Mn, can be selectively probed with essentially no interference from other cofactors or the protein matrix. X-ray absorption near-edge structure (XANES) spectroscopy is the most well-known of these techniques and has been used extensively in the field of metalloproteins to investigate the oxidation states of redox-active metals in metalloprotein active sites.[56,59,93-100] The principal component in XANES spectra is a $1s \rightarrow 4p$ absorption edge in Mn. The pioneering application of XANES to PS II was performed by Goodin et al. in the early 1980s.[59] This study, which was extremely difficult because of the low Mn concentration in PS II samples (• 1 mM), showed that the Mn K-edge in the S_1 state is shifted to higher energy in the S_2 state. Dramatic improvements in detector technology and cryostat cooling capabilities have made XANES experiments routine for most concentrated metalloproteins, and the collection of XANES spectra from dilute, single-flash saturable PS II samples is now achievable. Three different groups have investigated the oxidation states of Mn for the S_0, S_1, S_2, and S_3 states using XANES. Based on shifts in the absorption edge, or lack thereof, Roelofs et al. proposed that Mn is oxidized during the $S_0 \rightarrow S_1$ and $S_1 \rightarrow S_2$ transitions, but is not oxidized during the $S_2 \rightarrow S_3$ transition.[98] In contrast, Ono et al.[101] and Iuzzolino et al.[102] interpret their XANES results to indicate that Mn is oxidized during each S-state transition, although one group (Ono et al.) reported no

independent S-state determination for their samples and the other group (Iuzzolino et al.) had significant S-state inhomogeneity in their samples.

The conflicting results in the literature concerning the $S_2 \rightarrow S_3$ transition, some which support and some which disagree with Mn oxidation occurring during this transition, have led to two different types of proposed O_2 evolution mechanisms, with one type[36,37,40,66,67,70] incorporating the oxidation of ligand or substrate in the S_3 state, and the other type[65,68,103] invoking Mn oxidation during the $S_2 \rightarrow S_3$ transition. As expected, fundamental differences in the chemistry of O–O bond formation and O_2 evolution exist between the two types of mechanisms. Clearly, if the nature of the $S_2 \rightarrow S_3$ transition is unambiguously identified, it will narrow the range of possible mechanisms for O_2 evolution, leading to a clearer understanding of this important process.

By the application of an independent X-ray spectroscopic technique, Kβ X-ray emission spectroscopy (Kβ XES), this chapter provides a new approach to contribute to the resolution of the true nature of the $S_2 \rightarrow S_3$ transition. It has been known for over 60 years that Kβ XES is sensitive to the number of unpaired 3d electrons of the fluorescing atom;[104-107] due to improvements in instrumentation, it has recently been possible to apply this technique to dilute, biologically relevant samples such as PS II.[108,109] Kβ XES monitors the Mn $3p \rightarrow 1s$ fluorescence, which is sensitive to spin state, and therefore oxidation state (*vide infra*) through a 3p – 3d exchange interaction.[107] This is an indicator of oxidation-state sensitivity that is different from XANES, which is sensitive to oxidation state through 1s core-hole shielding effects.[56] In this chapter, the investigation of the oxidation states of Mn in each of the intermediate S-states (S_0 through S_3) using Kβ XES and XANES spectroscopy on the same sets of samples that have been characterized

by EPR is reported, and it is concluded that Mn is oxidized on the $S_0 \rightarrow S_1$ and $S_1 \rightarrow S_2$ transitions, while ligand/substrate oxidation occurs during the $S_2 \rightarrow S_3$ transition in lieu of a Mn-centered oxidation. By combining these data with structural information from EXAFS spectroscopy, three possible mechanisms for O–O bond formation by the OEC are proposed.

Materials and Methods

PS II membranes were prepared from fresh spinach leaves by a 2 min incubation of the isolated thylakoids with the detergent Triton X-100 and subsequent centrifugation.[110,111] The pellets were then resuspended to a chlorophyll (Chl) concentration of 9.5 mg Chl/mL in a 30 % (v/v) glycerol buffer (pH 6.5, 50 mM MES, 15 mM NaCl, 5 mM $MgCl_2$, 5 mM $CaCl_2$) and stored as aliquots at -80° C until used. Chl concentrations were calculated as described in Porra et al.[112] Inductively-coupled plasma/atomic emission spectroscopy (ICP/AES) was used to determine the Mn concentration in a sample of known Chl concentration; this provided a ratio of Mn/Chl for the PS II preparation used in these experiments. Information on the number of Chl per reaction center (RC) was determined from the average oxygen yield per flash for this preparation using a Clark-type electrode under the following experimental conditions:[113] 1 and 4 Hz flash frequency, 100 Xenon flashlamp flashes per group, T = 21° C, electron acceptors: 1 mM $[Fe(CN)_6]^{3-}$, 0.2 mM PPBQ (phenyl-1,4-benzoquinone), and 0.5 mM DCBQ (2,5-dichloro-p-benzoquinone). From the average oxygen yield per flash and the known Chl concentration, the Chl/RC ratio was calculated using the knowledge that O_2 is evolved every 4^{th} flash and assuming that the miss and double-hit parameters are small and approximately equal for the Xenon flash lamp under these conditions and can therefore be neglected. By combining the Mn/Chl ratio determined from ICP/AES with the Chl/RC ratio determined from flash-induced oxygen evolution, a ratio of 4.3 ± 0.2 Mn/RC was calculated for the preparation used in this study.

To prepare samples for the X-ray experiments, a frequency-doubled Nd-YAG laser system (Spectra-Physics PRO 230-10, 800 mJ/pulse at 532 nm, 9 ns pulse width)

was used to illuminate PS II samples from both sides simultaneously. The setup shown in Figure 2-2 allowed us to double the sample concentration used in earlier studies[98,101] while still maintaining flash saturation. The laser was operated continuously at 10 Hz, and flashes were selected using an external shutter (model LSTX-Y3, nm Laser Products, Inc.).

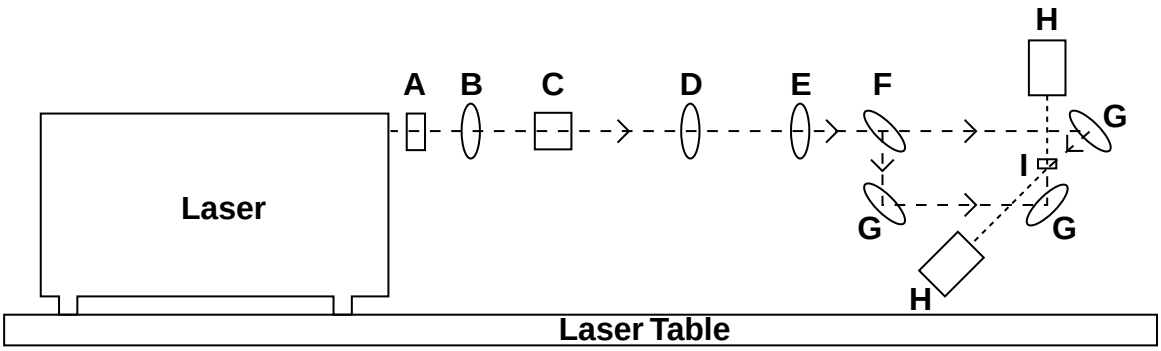

Figure 2-2: Schematic diagram of the setup of laser illumination of flash samples as viewed from the side. The laser output from the Spectra-Physics PRO 230-10 was modified using the following components, as labeled in the diagram: A) shutter; B) 1/4-wave plate; C) polarizing beamsplitter cube; D) f = -250 mm cylindrical lens; E) f = 1000 mm cylindrical lens; F) 50 % transmittance beamsplitter; G) mirror; H) beam stop; I) PS II flash sample.

Before flash illumination, 1 mM of recrystallized PPBQ, an exogenous electron acceptor of PS II, was added at 21° C from a 50 mM stock solution in dimethyl sulfoxide and mixed. Lexan sample holders (22 x 3.2 x 0.8 mm inner dimensions) were evenly filled with 40 µL aliquots of PS II at 4° C under dim green light and then used for flash illumination.

All samples were enriched in the $S_1Y_D^{ox}$ state (except for 'no preflash', NPF, samples) with one preflash followed by a 30 min dark-adaptation at 21° C. This preflash procedure oxidizes the fast electron donor Y_D and thereby minimizes S-state scrambling

due to the back-reaction with the S_2 and S_3 states between the flashes in the subsequent flash train. The samples were then illuminated with 0 to 6 flashes ('0F' to '6F' samples) at 1 Hz frequency. After the last flash, each sample was frozen immediately (< 1 s) in liquid nitrogen to trap its S-state composition. Three sets of >35 samples each were prepared and used within 10 days for the experiments. The dimensions of the Lexan sample holders allowed us to measure EPR spectra of every sample that was later used for X-ray experiments.

To verify that the laser flash illumination procedure did not damage the PS II samples, Mn(II) EPR spectra were collected for several 6F samples; they showed that almost no Mn(II) (<1.5 %) was released by seven laser flashes. For further confirmation, four of the 6F samples were dark-adapted for 40 minutes at room temperature after quantitation of their S_2-state multiline EPR signal amplitudes, and were then advanced to the S_2 state by continuous illumination at 190 K. The resulting normalized S_2-state multiline EPR signal amplitudes were identical to that obtained from the 1F samples.

After all S_2 EPR multiline signal and X-ray measurements were completed, the Mn content of each sample was quantitated by releasing the bound Mn as Mn(II) using the external reductant NH_2OH. 10 μL of a freshly prepared 1.0 M NH_2OH solution was layered onto the surface of each sample, and the samples were allowed to incubate at room temperature for 30 minutes. The Mn(II) six-line EPR spectrum (I = 5/2 for ^{55}Mn, 100 % natural abundance) was then measured for each sample using the parameters described below.

EPR spectra were collected on a Varian E-109 spectrometer with an E-102 microwave bridge and stored using Labview running on a Macintosh G3 computer. Samples were maintained at cryogenic temperatures using an Air Products Heli-tran

liquid helium cryostat. Spectrometer conditions were as follows: S_2 EPR multiline signal: 2800 ± 500 G scan range, 25,000 or 40,000 gain, 30 mW microwave power, 9 K temperature, 32 G modulation amplitude, 100 kHz modulation frequency, 2 min/scan, 2 or 4 scans per sample, 0.25 sec time constant, 9.26 GHz microwave frequency; Mn(II): 3300 ± 1000 G scan range, 16,000 gain, 10 μW microwave power, 20 K temperature, 32 G modulation amplitude, 100 kHz modulation frequency, 2 min/scan, 1 scan per sample, 0.25 sec time constant. MLS amplitudes were determined from the low-field and high-field peak-to-trough measurements for each designated peak. The Mn(II) six-line EPR signal amplitudes were determined using the low-field peak-to-trough measurements for the 2^{nd}, 3^{rd}, and 6^{th} hyperfine lines.

XANES spectra were recorded on beamline 7-3 at SSRL (Stanford Synchrotron Radiation Laboratory) essentially as in Roelofs et al.[98] The synchrotron ring SPEAR was operated at 3.0 GeV at a current of 50 – 100 mA. Energy resolution of the unfocused incoming X-rays was achieved using a Si(220) double-crystal monochromator, which was detuned to 50 % of maximal flux to attenuate harmonic X-rays. A N_2-filled ion chamber (I_0) was mounted in front of the sample to monitor incident beam intensity. An incident X-ray beam of 1 mm x 11 mm dimensions with a flux of approximately 3.5×10^{10} photons/sec. was used for the XANES experiments. The samples were placed at an angle of 45° relative to the X-ray beam and were kept at 10 ± 1 K in a He atmosphere at ambient pressure using an Oxford CF-1208 continuous-flow liquid He cryostat. The X-ray absorption spectra were collected as fluorescence excitation spectra[114] using a 13-element energy-resolving detector from Canberra Electronics,[115] and were referenced by I_0. Typical counts in the Mn fluorescence window for the central channel were 100 counts/sec at 6500 eV (below the Mn K-edge) and 320 counts/sec at

6600 eV (above the Mn K-edge). Spectra were collected at 10 eV/point from 6400 to 6520 eV with a collection time of 1 second per point, at 0.2 eV/point from 6520 to 6580 eV with a collection time of 3 seconds per point, and at 10 eV/point from 6580 eV to 7100 eV with a collection time of 1 second per point. Three vertical positions of 1 mm height each were used for each sample, and only 2 or 3 scans were collected at each separate position to minimize and monitor radiation damage. A third scan at each position was taken for fewer than 25 % of the XANES samples. The samples were protected with a shutter from the beam at all times unless a measurement was in progress. Collection of an energy-reference spectrum was achieved by placing a $KMnO_4$ sample between two N_2-filled ion chambers I_1 and I_2, which were positioned behind the PS II sample, and collecting a $KMnO_4$ absorption spectrum concurrently with PS II data collection. The narrow pre-edge line (FWHM • 1.7 eV) at 6543.3 eV was subsequently used for energy calibration.[116] For the XANES spectra, 41 – 49 scans (2 – 3 scans per position, 3 positions per sample) were averaged per flash number for the 0F – 3F spectra, and 11 – 13 scans (2 – 3 scans per position, 3 positions per sample) were averaged per flash number for the 4F – 6F spectra. After removal of a linear background, the XANES data were normalized by fitting a quadratic polynomial to the EXAFS region (6570 – 7100 eV) and assigning the intensity of the extrapolated polynomial to 1.0 at 6563 eV. Second derivatives between 6535 and 6575 eV were calculated for each point by fitting a cubic polynomial to a range of ± 3 eV around that point and computing the 2nd derivative of the polynomial.

Kβ emission spectra were recorded on beamline 10-2 at SSRL using a crystal array spectrometer with • 1 eV energy resolution.[109] The PS II samples were positioned

with an angle of 15° between the surface of the sample and the incident X-ray beam and were kept in an Oxford CF1208 cryostat at a temperature of 10 ± 1 K under an ambient pressure He atmosphere. An incident X-ray beam (10.45 keV) of 1 mm x 4 mm dimensions and a flux of approximately 7×10^{11} photons/sec (~10x higher energy absorption per unit of sample volume than for XANES) were used.

The crystal array monochromator contained eight 8.9 cm-diameter spherically-curved Si(440) crystals mounted on a movable table; the crystals were placed in an arc at a radial distance r = 85 cm from the sample. An energy-resolving Ge detector was mounted on a moveable platform positioned below the sample and cryostat in an approximate Rowland circle geometry. Bragg diffraction from the crystals allowed the detection of X-ray fluorescence from PS II at specific wavelengths of the broadband X-ray fluorescence spectrum. By moving the crystals and Ge detector vertically, the Bragg angle between the X-ray fluorescence and the Si crystal normal could be changed, thereby changing the wavelength of detection.

The samples were protected with a fast pneumatic shutter from X-ray exposure during all spectrometer movements. To minimize and quantitate the effect of photoreduction, the following scan protocol was used. The $K\beta_{1,3}$ main peak (6483.6 – 6497.3 eV) was initially scanned twice (5 sec/point, 6 min scans, ~0.2 eV step size) and was then measured a third time after the Kβ' region (6467.4 – 6483.6 eV, 19.5 min scan) and the high energy region (6496.5 – 6510.9 eV, 11 min scan) were collected. 33 – 39 separate scans (3 positions per sample, 11 – 13 separate samples) per flash number were collected for the first $K\beta_{1,3}$ scans (shown in Figure 2-7B). The total number of counts from all of the first $K\beta_{1,3}$ scans at all three positions was 8100 – 9000 counts per flash

number. Similar counts were obtained from the second $K\beta_{1,3}$ scans; however, fewer third $K\beta_{1,3}$ scans were collected, and only 2400 – 3600 counts were obtained. Only the data from the first $K\beta_{1,3}$ scans at each position were used for the spectra shown in Figure 2-7B. The calibration of the instrument was checked periodically with a MnF_2 sample and was found to be invariant over the entire run.

The following data reduction was performed on the raw Kβ emission spectra of PS II: a) subtraction of a linear background (less than 10 % of the peak intensity of ~9000 counts) arising from Compton scattering and other fluorescence emission (mostly Fe Kα). The linear background was chosen so as to align the PS II data with those of highly concentrated Mn oxides in the low (<6470 eV) and high (>6505 eV) energy regions. The fluorescence intensities in these low and high energy regions are invariant with oxidation state (see Figure 2-6). b) The individual data points were binned (step size varied from 0.1 eV to 0.24 eV) into groups of 9 or 5 points in the tails and 2 points in the $K\beta_{1,3}$ peak. c) The spectra were splined onto a grid of 0.1 eV energy steps to facilitate the calculation of 1st-moment (<E>) values. d) The spectra were then normalized by assigning the integrated area from 6467.9 eV to 6510.4 eV to be 1; this had no effect on the 1st-moment value. The 1st-moment values were calculated between 6485 and 6495 eV using the formula shown in Eq. 2-1:

$$1^{st}\ \text{moment} = \sum_j \frac{E_j \cdot I_j}{I_j} \qquad \text{Eq. 2-1}$$

where E_j and I_j are the energies and fluorescence intensities, respectively, of the j^{th} point.

Results

EPR

Characterization of the samples using EPR spectroscopy is a critical aspect of these experiments, because it is the only way to determine S-state composition as a function of flash number for the same samples that are subsequently used in the X-ray experiments. Starting from dark-adapted samples, the S_2-state multiline EPR signal is maximal after 1 flash and oscillates with a period of four as a function of flash number; thus the S_2-state multiline EPR signal can be used to characterize the S-state distribution of samples given 0 to 6 flashes. The S_2-state multiline EPR signal was measured on each of 109 separate samples given no preflashes (NPF) or given 0, 1, 2, 3 4, 5, or 6 flashes.

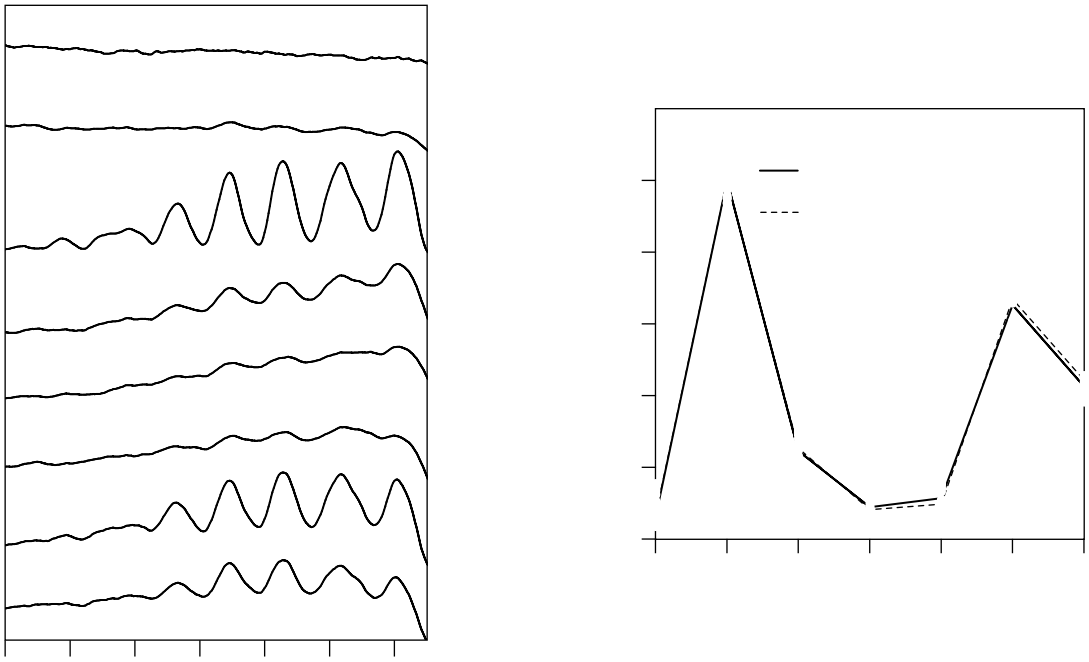

Figure 2-3: S_2-state multiline EPR signal oscillation pattern. **(A)** EPR difference spectra (flash sample minus buffer spectrum) of the low-field side of the S_2 multiline. The spectra shown are the average of all samples used in this study. Spectra from 2, 23, 23, 18, 19, 9, 7, and 8 samples were averaged for the NPF, 0F, 1F, 2F, 3F, 4F, 5F, and 6F spectra, respectively. They are normalized to their total Mn contents, which were determined as described in Materials and Methods. The sloping baseline that is apparent at high field is due to a flash-induced background signal in the Lexan sample holders. This signal was shown in flashed empty sample holders to be a very broad EPR signal with no hyperfine structure. Thus, it does not affect the quantitations of the S_2-state multiline EPR signal hyperfine peaks. **(B)** The S_2-state multiline EPR signal amplitudes obtained from the designated peaks in Figure 2-3A are shown as a function of flash number (solid line). The data points are measurements on the spectra from individual samples and are normalized to the Mn content in each sample (see Materials and Methods). The best fit to S_2-state multiline EPR signal oscillation pattern (Fit #4 in Table 2-1) is shown as a dashed line. All S_2-state multiline EPR signal amplitudes were normalized to the average 1F S_2-state multiline EPR signal amplitude.

Figure 2-3A shows the difference spectra (sample minus buffer) obtained by averaging all samples of a given flash number. These spectra are normalized according to the total Mn content of each sample (see the Materials and Methods section). A deep period-four oscillation is observed with maxima on the first and fifth flashes, indicating that there is very little dephasing of S-state advancement with flashes and an initial S-state population of almost 100 % S_1. The signal-to-noise ratio of these average spectra allows a reliable quantitation of even the small S_2-state multiline EPR signal amplitudes in the 0F, 3F, and 4F samples. This can be seen by the comparison to the EPR spectrum of the NPF sample, which has no S_2-state multiline EPR signal. For each spectrum shown in Figure 2-3A, the four designated S_2-state multiline EPR signal peaks were quantitated (see the Materials and Methods section); the results are shown as the solid line in Figure 2-3B, with the 1F value normalized to 100 %. In addition, the S_2-state multiline EPR signal quantitations for each sample are shown as filled circles in Figure 2-3B.

Due to factors such as redox equilibria between the cofactors in PS II,[117] it is inevitable that some dephasing occurs while the OEC is advanced through the various S-states. The original Kok model explains this by assuming two parameters: the miss probability (α) accounts for the percentage of centers that do not advance in each flash and the double-hit probability (β) describes the percentage of centers that make two turnovers in a single flash ($S_i \rightarrow S_{i+2}$).[27,118] Double hits are caused by the long (~100 μs) tail of the 3 – 5 μs Xe flashlamp pulses commonly used;[119] the rates of S-state turnovers are in most cases limited by the $Q_A^- \rightarrow Q_B$ or $Q_A^- \rightarrow Q_B^-$ electron transfers, which are on the same time scale as the tail of the Xe flashlamp pulse. The short (9 ns) Gaussian-

shaped pulses from Nd-YAG lasers do not have these tails, making double hits negligible for laser flash illumination. According to the Kok model, a sample that is initially 100 % in the S_1 state will have an S-state distribution of α % S_1, (100 - α - β) % S_2, and β % S_3 population after the first flash. This analysis can be extended for subsequent flashes to the point where the complete S-state distribution as a function of flash number can be easily derived if the quantities α and β are known. This model has been used to calculate the S-state population for each flash number and have compared the calculated S_2-state values to the measured amplitudes shown in Figure 2-3B. Using a Microsoft Excel spreadsheet and a least-squares minimization routine, the error between the calculated and measured S_2-state populations is minimized using α and β as adjustable parameters.

A systematic approach has been used to extract a reliable S-state distribution from the S_2-state multiline EPR signal oscillation pattern. The results from applying the original Kok model to the experimental data in Figure 2-3B are shown as Fit #1 in Table 2-1. The value of β was set to 0 for this fit because the pulse width of the laser used in the experiment (9 ns) is at least 5 orders of magnitude faster than the $Q_A^- \rightarrow Q_B$ or $Q_A^- \rightarrow Q_B^-$ electron transfers and 3 orders of magnitude faster than the $Q_A^- \rightarrow Fe^{3+}$ electron transfer (*vide infra*), thus eliminating the possibility of double hits.[119] A noticeable improvement in the fit, shown in Fit #2, is obtained by varying the initial S_2-state percentage in addition to α. This is justified because there is a discernible (8.4 %) S_2-state multiline EPR signal for the 0F samples due to the presence of PPBQ during the preflash treatment. Exogenous quinones such as PPBQ are known to extend the S_2- and S_3-state lifetimes by minimizing recombination reactions with the acceptor side, and are necessary to obtain deep S_2-state multiline EPR signal oscillation patterns in isolated

Table 2-1: Fits to the S_2 multiline EPR signal oscillation pattern. The S_2 multiline EPR signal oscillation pattern shown as a solid line in Figure 2-3B was fit with an (extended) Kok model: α , β are the miss and double-hit parameters, respectively, and I. C. gives the percentage of 'impaired centers' (see Results for details). The fit error and fit quality were calculated as follows: Fit Error = $\Sigma(\text{residual}^2)$ and Fit Quality = (fit error)/(7 - # of free parameters).

Fit #	α	Initial S_2	I. C.	β	Fit Error	Fit Quality
1	11.4 %	–	–	–	197	33
2	11.7 %	7.9 %	–	–	64	13
3	11.6 %	6.7 %	–	1.5 %	42	11
4	**10.8 %**	**5.7 %**	**4.7 %**	**–**	**10.5**	**3**

PS II membranes.[120,121] Because Lexan sample holders, which allowed the EPR and X-ray spectroscopy to be performed on the same samples, and not EPR tubes were used to hold the PS II samples, PPBQ could not be added and mixed into each sample after the preflash and was therefore added to the entire PS II aliquot before the preflash treatment. The possibility of double hits was also considered; but, as expected (*vide supra*), the inclusion of double hits, shown in Fit #3, does not significantly improve the fit quality.

However, none of these 3 fits properly accounts for the small but significant S_2-state multiline EPR signal amplitudes for the 3F and 4F samples. It is therefore necessary to use 'extended Kok models', whereby additional dephasing parameters are used to explain the 3F and 4F S_2-state multiline EPR signal amplitudes. Several phenomena aside from α and β can lead to dephasing of S-state advancement. One possibility is the initial presence of some reduced tyrosine Y_D, which can rapidly

recombine with the S_2 and S_3 states during the time between the flashes, oxidizing Y_D to Y_D^{ox} and reducing the Mn cluster.[122] However, the preflash protocol that was used converts Y_D to Y_D^{ox} in nearly all centers, as shown by a lack of an increase in the Y_D^{ox} EPR signal with increasing flash number (data not shown); thus, this reaction cannot account for the observed S_2-state multiline EPR signal amplitudes in the 3F and 4F samples. Another scenario concerns the presence of a certain percentage of acceptor-impaired centers. It has been shown that, even in whole plant leaves, in some PS II centers the acceptor-side quinone Q_A^- is oxidized with a $t_{1/2}$ of $2-3$ seconds and that full recovery takes up to 100 seconds;[123,124] thus these centers are effectively blocked from multiple turnovers with a flash frequency of 1 Hz. In addition, much higher S_2-state multiline EPR signal amplitudes are observed for the 3F and 4F samples in the absence of PPBQ (data not shown); thus, it is reasonable to consider acceptor-side limitations. For simplicity, this was modeled as a variable percentage of centers which advance with the normal miss parameter α for the first flash, but cannot advance on any subsequent flashes; thus, the miss parameter for these centers for subsequent flashes is 100 %. More complex fits taking reoxidation kinetics or miss factors smaller than 100 % for the impaired centers into account were considered. However, these yielded almost identical fits with essentially the same S-state distributions for the various flash numbers (data not shown). Therefore, the increased number of parameters was not justified. Fit #4 in Table 2-1 shows that including these 'impaired centers' as a fit parameter significantly improves the fit. The dashed line in Figure 2-3B represents the best fit to the data that was obtained, Fit #4, with a 10.8 % miss parameter, 5.7 % of the centers initially in the S_2 state, and 4.7 % impaired centers. To obtain maximal error limits, similar fits were made to a 'most

damped' pattern and a 'least damped' pattern that were constructed using the respective higher and lower ends of the standard deviations from the individual S_2-state multiline EPR signal measurements shown in Figure 2-3B (see Table 2-2 for details).

Using the fit parameters from Fit #4, the S-state distribution of samples given 0, 1, 2, 3, 4, 5, and 6 flashes have been calculated and are shown in Table 2-2. As expected, the 0F, 1F, 2F, and 3F samples are predominantly in the S_1, S_2, S_3, and S_0 states,

Table 2-2: S-state composition of samples given 0 to 6 flashes. The numbers were calculated using Fit 4 in Table 2-1. The maximum error in S-state populations is obtained from fits to a 'least-damped' and a 'most-damped' oscillation pattern, which were obtained using the high or low ends of the standard deviations calculated from the individual data points in Figure 2-3B. The 'least damped' pattern used the following standard deviations: 0F: low, 1F: high, 2F: low, 3F: low, 4F: low, 5F: high, 6F: low, while the 'most damped' pattern used the following standard deviations: 0F: high, 1F: low, 2F: high, 3F: high, 4F: high, 5F: low, 6F: high.

	S_0	S_1	S_2	S_3
0F	0.0 ± 0.0	**94.3** ± 3	5.7 ± 3	0.0 ± 0.0
1F	0.0 ± 0.0	10.2 ± 0.9	**84.7** ± 3	5.1 ± 1.7
2F	4.5 ± 0.6	1.6 ± 0.6	21.5 ± 4	**72.4** ± 5
3F	**65.2** ± 5	4.6 ± 0.4	7.0 ± 3	23.2 ± 1.2
4F	27.7 ± 1.3	**59.0** ± 4	8.3 ± 1.1	5.0 ± 0.5
5F	7.5 ± 1.1	31.5 ± 1.7	**56.8** ± 1.8	4.2 ± 1.0
6F	4.6 ± 1.0	10.5 ± 1.8	37.6 ± 4	**47.3** ± 5

respectively, and the deep S_2-state multiline EPR signal oscillation pattern that was obtained contributes to a fairly high S-state purity for the 0F – 3F samples. The information in Table 2-2 is necessary to extract pure S-state X-ray spectra from the measured X-ray spectra of samples given 0 – 3 flashes. It should be emphasized that the S-state distributions calculated from Fit #2 (the standard Kok model) are well within the maximum error limits shown in Table 2-2, indicating that, while the inclusion of impaired centers improves the fit to the S_2-state multiline EPR signal oscillation data, under these conditions, they have a negligible effect on the overall S-state distributions and the resulting pure S-state spectra.

XANES

The XANES spectra from samples given 0 – 3 flashes are shown in the upper portion of Figure 2-4A. The edge shift that is apparent between the 0F and 1F spectra indicates that Mn oxidation occurs during the $S_1 \rightarrow S_2$ transition. However, it is less clear that there is a significant shift between the 1F and 2F spectra, suggesting that Mn is not oxidized as the OEC proceeds from the S_2 to the S_3 state. As expected, the edge position shifts to lower energy between the 2F and 3F spectra, reflecting mainly the $S_3 \rightarrow [S_4] \rightarrow S_0$ transition. However, due to 23 % of the centers being in the S_3 state in the 3F spectra, the edge position is at a higher energy than would be expected for the pure S_0 state.

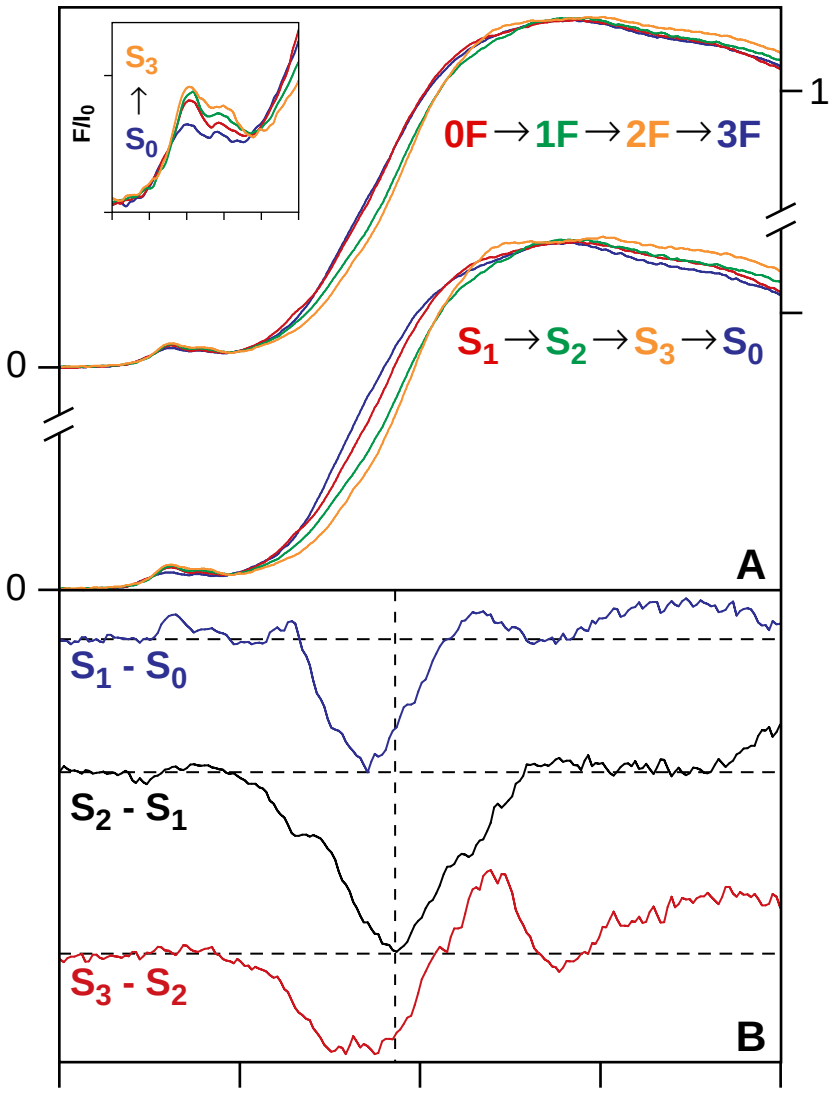

Figure 2-4: Mn K-edge XANES spectra of flash-illuminated PS II samples. **(A)** Pure S-state spectra (bottom) were obtained from the flash spectra (top) by deconvolution using the inverse of the S-state distribution matrix in Table 2, as described in the text. The pre-edge region (principally a 1s → 3d transition) for the S_0–S_3 states is shown in the inset. **(B)** S-state XANES difference spectra. The spectra are multiplied by a factor of 5 and are vertically offset for clarity. The horizontal dashed lines show the zero value for each difference spectrum.

Using the known S-state distributions shown in Table 2-2 for the flash samples, the flash spectra can be deconvoluted to obtain the pure S-state spectra as follows. The S-state distributions in Table 2-2 describe the flash spectra as a linear combination of pure S-state spectra, as shown in Eq. 2-2:

$$\begin{pmatrix} 0F \\ 1F \\ 2F \\ 3F \end{pmatrix} = \underbrace{\begin{pmatrix} 0 & 0.943 & 0.057 & 0 \\ 0 & 0.102 & 0.847 & 0.051 \\ 0.045 & 0.016 & 0.215 & 0.724 \\ 0.652 & 0.046 & 0.07 & 0.232 \end{pmatrix}}_{M} \cdot \begin{pmatrix} S_0 \\ S_1 \\ S_2 \\ S_3 \end{pmatrix} \qquad \text{Eq. 2-2}$$

By inverting the S-state distribution matrix M, pure S-state spectra can be obtained from flash spectra according to Eq. 2-3:

$$M^{-1} \cdot \begin{pmatrix} 0F \\ 1F \\ 2F \\ 3F \end{pmatrix} = \begin{pmatrix} S_0 \\ S_1 \\ S_2 \\ S_3 \end{pmatrix} \qquad \text{Eq. 2-3}$$

Eq. 2-3 was used to deconvolute the XANES spectra given 0 – 3 flashes, shown in the upper portion of Figure 2-4A, into the pure S-state spectra, shown in the lower portion of Figure 2-4A. It is clear from these pure S-state spectra that the edge position shifts to higher energy during both the $S_0 \rightarrow S_1$ and $S_1 \rightarrow S_2$ transitions, confirming previous conclusions that Mn oxidation occurs during both of these S-state transitions.[59,80,98] However, the S_2- and S_3-state XANES spectra show a much smaller edge shift than the $S_1 \rightarrow S_2$ transition, as well as a change in the shape of the edge between the S_2 and S_3 states. The S-state difference spectra (Figure 2-4B) show these differences prominently. The fact that the shape and position of the S_3 - S_2 difference spectrum is unlike that of the S_2 - S_1 or S_1 - S_0 difference spectrum indicates that the chemistry of the

$S_2 \rightarrow S_3$ transition is not the same as the $S_0 \rightarrow S_1$ and $S_1 \rightarrow S_2$ transitions, where Mn oxidation is thought to occur on each step. One possible explanation for this is that a species other than Mn is oxidized during the $S_2 \rightarrow S_3$ transition. However, it is difficult to confirm this hypothesis based solely on XANES difference spectra (as shown in Visser et al.[125]) or based on visual comparisons between the spectra as shown in Figure 2-4A. Instead, an analysis method that has been proven through comparisons to model complexes, such as the 2nd-derivative method (*vide infra*), should be used to derive insight into oxidation-state changes.

Further information about edge shape and position can be obtained by taking the 2nd derivative of the XANES spectrum.[34,55,59,71,93,95,126-131] Figure 2-5 shows the 2nd derivatives of the pure S-state spectra from Figure 2-4A compared to the 2nd derivatives for each

Table 2-3: 2nd-derivative inflection point energy (IPE) values for the S_0, S_1, S_2, and S_3 states. The numbers were calculated using Fit #4 in Table 2-1. The maximum IPE error in S-state populations is obtained by calculating S-state distributions from fits to a 'least-damped' and a 'most-damped' oscillation pattern, and then using those S-state distribution matrices to deconvolute the flash spectra in Figure 2-4A into pure S-state spectra.

	2nd-derivative IPE values
S_0	6550.8 ± 0.1
S_1	6552.9 ± 0.1
S_2	6554.0 ± 0.1
S_3	6554.3 ± 0.1

flash sample. The spectra of the individual flash samples, shown in Figure 2-5A, demonstrate the reproducibility achieved in this experiment. In addition, the S-state homogeneity of the flash samples (see Table 2-2) is reflected in the similarity between the 2nd derivatives of the experimentally obtained flash-sample spectra (Figure 2-5A) and the deconvoluted S-state spectra (Figure 2-5B). The edge positions for each of the S-states have been quantitated by measuring the inflection point energy (IPE), given by the zero-crossing of the 2nd derivative; the results are shown in Table 2-3. Extensive model compound studies have shown that, without exception in the study of more than 13 sets of compounds, when Mn is oxidized by one electron in a set of Mn model compounds with similar ligands, the IPE shifts $1-2$ eV to higher energy upon Mn oxidation, regardless of nuclearity.[34,125] Thus, the shifts in the IPE values of 2.1 eV and 1.1 eV during the $S_0 \rightarrow S_1$ and $S_1 \rightarrow S_2$ transitions, respectively, confirm that Mn oxidation occurs during each of these transitions. However, the IPE shift for the $S_2 \rightarrow S_3$ transition is only 0.3 eV, confirming under improved conditions the earlier results of Roelofs et al.,[98] and providing strong evidence that a Mn-based oxidation does not occur during this transition. It is noteworthy that a comparison of the IPE values from the 2nd derivatives of the 1st and 2nd XANES scans for each flash number shows no change within experimental error (< 0.1 eV); therefore, X-ray photoreduction did not affect the XANES experiments (data not shown).

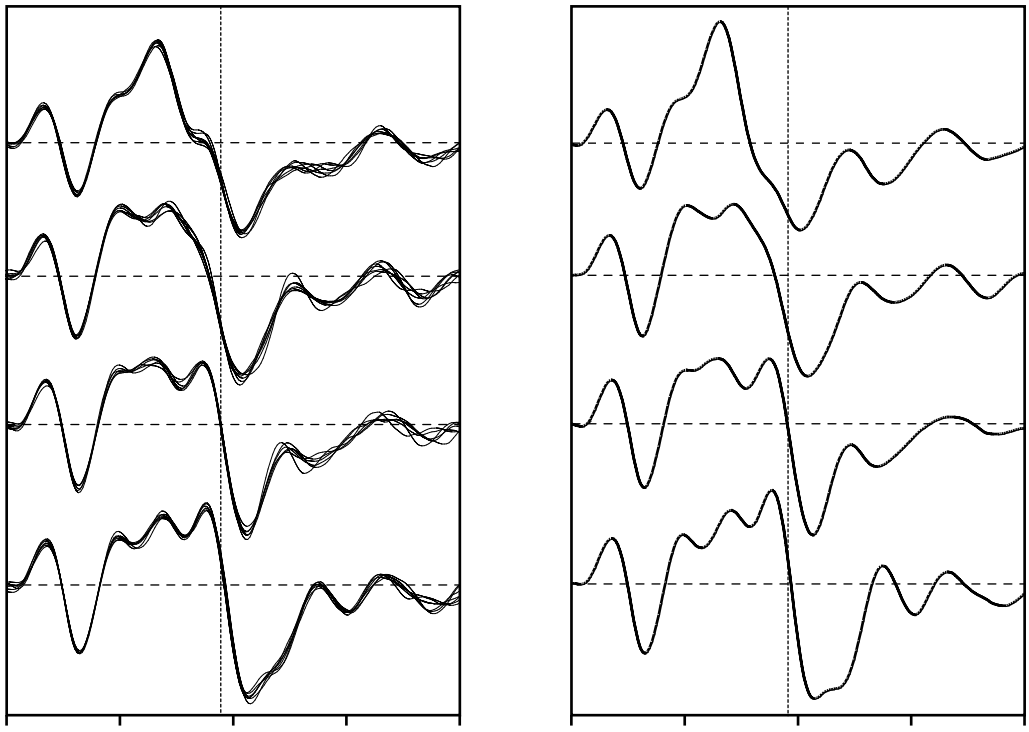

Figure 2-5: 2nd derivatives of Mn K-edge XANES spectra. **(A)** Samples given 0, 1, 2, or 3 flashes. The individual 2nd-derivative spectra from 7, 6, 7, and 7 samples given 0, 1, 2, or 3 flashes, respectively, are shown. The dashed vertical line marks the average inflection point energy for the 1F spectra. The individual edge spectra from which these 2nd derivatives were calculated were used to generate the composite XANES flash spectra shown in the upper portion of Figure 2-4A. **(B)** Deconvoluted S-state spectra. These spectra are the 2nd derivatives of the S-state XANES edge spectra shown in the lower portion of Figure 2-4A. The dashed vertical line is at the inflection point energy for the S_2-state spectrum. Because of the high S-state purity of the flashed samples, the deconvoluted S-state spectra are quite similar to the experimentally obtained flash spectra shown in part A of this figure.

The inset of Figure 2-4A shows the pre-edge (1s $\rightarrow$ 3d) transitions for each of the S-states S_0 , S_1, S_2, and S_3. This formally dipole-forbidden transition contains information about the oxidation state and geometry[56] of Mn in the OEC. Analysis of these features in mononuclear metalloproteins with Fe at the active site[96,132-137] and Fe model complexes[138]

has proven useful in determining the coordination number and oxidation state of Fe. The pre-edge region in the inset of Figure 2-4A shows changes with S-state; the most prominent change occurs between the S_0 and S_1 states. It also shows the quality of the XANES spectra from this experiment. The analysis of the pre-edge region is complicated by the tetranuclear nature of the Mn cluster; the majority of such studies to date have dealt with mononuclear systems, and some studies have been done on homovalent binuclear complexes. Further investigations of the pre-edge region from PS II and Mn model compounds will aid in interpretation of the $1s \rightarrow 3d$ features in Mn model compounds and metalloenzymes.

Kβ emission spectroscopy

Shown in Figure 2-6 are the Kβ emission spectra of $Mn(IV)O_2$, $Mn_2(III)O_3$, and Mn(II)O, which illustrate the features of Kβ emission spectra and their sensitivity to the oxidation states of Mn. Although a more detailed analysis of these spectra requires the use of ligand-field multiplet calculations,[107] a qualitative understanding of the spectra can be obtained without these calculations. The Kβ emission spectra in Figure 2-6 consist of two main features: the Kβ' peak at ~6475 eV and the $K\beta_{1,3}$ peak at ~6490 eV. The separation of these two features is due to the exchange interaction of the unpaired 3d electrons with the 3p hole in the final state of the $3p \rightarrow 1s$ fluorescence transition.[139,140] The spin of the unpaired 3d valence electrons can be either parallel (Kβ') or antiparallel ($K\beta_{1,3}$) to the hole in the 3p level. Furthermore, the Kβ features are broadened by the finite lifetimes for the initial and final states as well as spin-orbit and multiplet splittings.

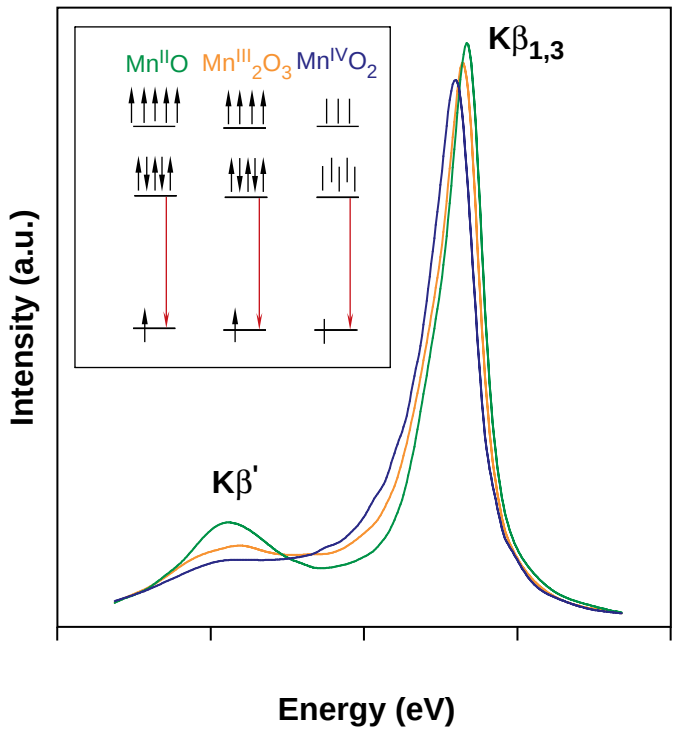

Figure 2-6: Kβ spectra of Mn oxides. This figure shows the changes in the Kβ spectrum due to Mn oxidation. The inset shows a pictorial representation of the Kβ fluorescence transition for each of the oxides. The spectra were normalized by the integrated area under the spectra, as described in Materials and Methods.

In the case of the Kβ' line, the final-state lifetime is much shorter compared to the $K\beta_{1,3}$ line and hence the structure is broader and has a smaller peak intensity.[141]

As the oxidation state of Mn increases from Mn(II) to Mn(III) to Mn(IV), fewer unpaired 3d valence electrons are available to interact with the 3p hole; thus, the magnitude of the 3p – 3d exchange interaction becomes smaller, leading to a decrease in the Kβ' – $K\beta_{1,3}$ splitting. The consequence is that, if one focuses only on the more intense $K\beta_{1,3}$ emission peak, it shifts to lower energy as Mn is oxidized. Whereas the Kβ emission spectrum is sensitive to oxidation state through a 3p – 3d exchange interaction, the independent technique of XANES spectroscopy is sensitive to oxidation state through

a different mechanism: core-hole shielding effects. This is why, upon Mn oxidation, $K\beta_{1,3}$ emission spectra shift to lower energy, while XANES spectra shift to higher energy.

In general, Kβ XES is sensitive to the spin state of the fluorescing atom, and not its oxidation state, because the magnitude of the 3p – 3d exchange interaction is governed by the number of unpaired 3d electrons. However, for the situations relevant for PS II, i.e. Mn(II), Mn(III), and Mn(IV) ions in a high-spin configuration, the oxidation state is directly correlated to the spin state.

The shifts in the $K\beta_{1,3}$ emission peaks can be quantitated using a 1^{st}-moment analysis described in Eq. 2-1, which in essence calculates the 'center of mass' of the $K\beta_{1,3}$ spectrum along the energy axis within the integration limits used. As Mn is oxidized from Mn(II) to Mn(III) in the oxide series, the 1^{st} moments (<E>) shift to lower energy by 0.30 eV. The Mn(III) $\rightarrow$ Mn(IV) <E> shift of 0.33 eV is similar. It should be emphasized that these shifts are much larger than those expected for PS II, because each of the Mn atoms in the oxide samples is changing oxidation state. However, in PS II maximally 1 out of 4 Mn atoms in the OEC is oxidized during each S-state transition (except $S_3 \rightarrow [S_4] \rightarrow S_0$).

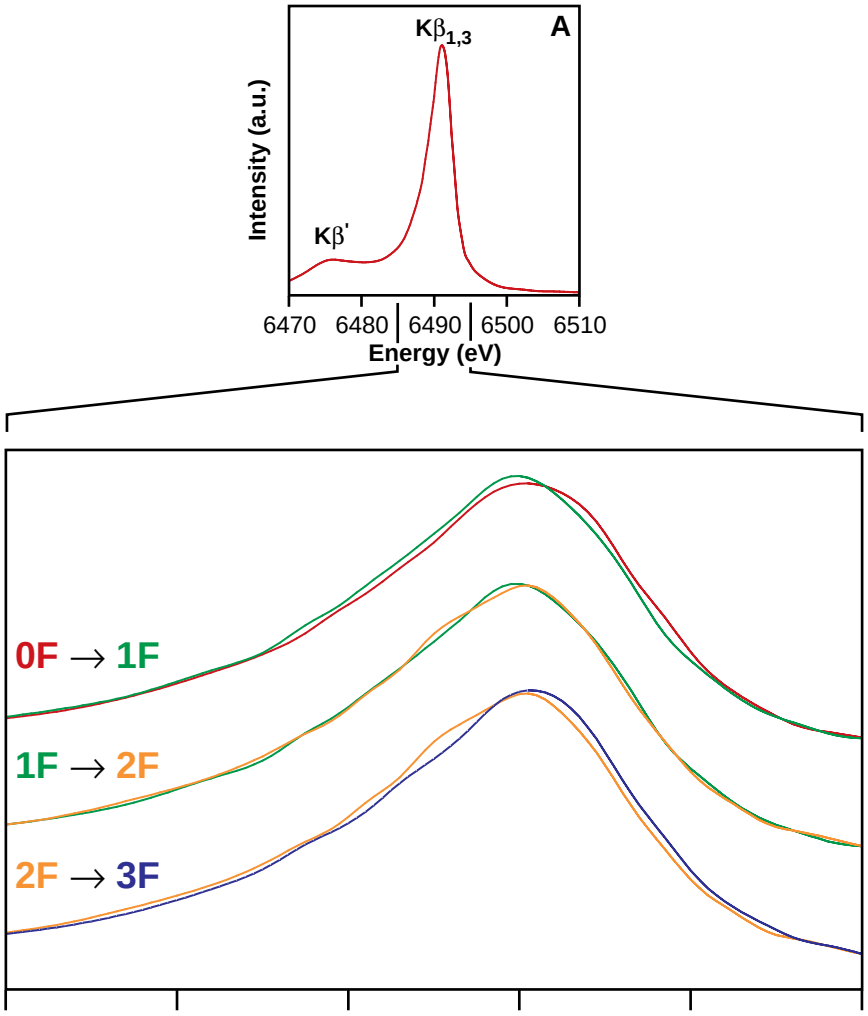

Figure 2-7: Kβ spectra of PS II flash samples. **(A)** The composite Kβ spectrum from 15 individual 0F PS II samples. This spectrum has been reconstructed from piecewise scans of the high-energy tail, $K\beta_{1,3}$, and Kβ' regions on each sample, as explained in Materials and Methods. **(B)** Overplots of the $K\beta_{1,3}$ spectra of the 0F, 1F, 2F, and 3F PS II samples. The spectra were normalized as described in Materials and Methods. The sum spectra of the first $K\beta_{1,3}$ scans (6 minute scan time each) at each sample position are shown. The magnitude of the first-moment shift for $Mn_2(III)O_3 \rightarrow Mn(IV)O_2$ is significantly larger than the first-moment shift for the $S_1 \rightarrow S_2$ transition, where only 1 Mn out of 4 is being oxidized.

The composite Kβ emission spectrum from 15 individual 0F samples is shown in Figure 2-7A. This spectrum has been reconstructed from piecewise scans of the high-energy tail, $K\beta_{1,3}$, and Kβ' regions on each sample, as explained in the Materials and Methods section. Figure 2-7B shows the main $K\beta_{1,3}$ emission peak for the 0F, 1F, 2F, and 3F samples. Only the first six-minute $K\beta_{1,3}$ emission scan of each position was used for these spectra, which are the average of 33 – 39 separate scans (3 positions per sample, 11 – 13 separate samples) per flash number. It is evident that the $K\beta_{1,3}$ emission peak shifts to lower energy for the 1F sample relative to the 0F sample, reflecting the Mn oxidation that occurs during the $S_1 \rightarrow S_2$ transition. However, there is no clear shift between the 1F and 2F samples, which is again suggestive that Mn is not oxidized during the $S_2 \rightarrow S_3$ transition. The large shift in the opposite direction (to higher energy) between the 2F and 3F spectrum is expected, because Mn is reduced during the $S_3 \rightarrow [S_4] \rightarrow S_0$ transition. The flash spectra have been deconvoluted to generate pure S-state spectra as described earlier, and the calculated $K\beta_{1,3}$ emission spectra for the S_0, S_1, S_2, and S_3 states are shown in Figure 2-8. The pure S-state $K\beta_{1,3}$ emission spectra are quite similar to the $K\beta_{1,3}$ emission spectra from the flash samples shown in Figure 2-7B due to the high degree of S-state purity of the flash samples. Based on the spectra shown in Figure 2-8, the 1st-moment shift observed for the $S_1 \rightarrow S_2$ transition, where 1 Mn out of 4 is oxidized, is 0.06 eV. In contrast, the 1st-moment shift for the $S_2 \rightarrow S_3$ transition is only 0.02 eV.

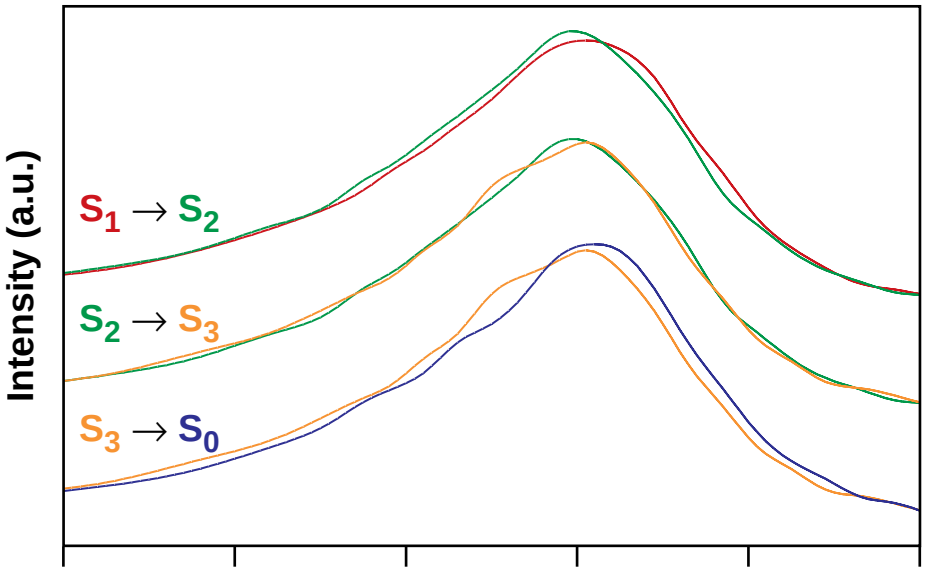

Figure 2-8: Overplots of the normalized (area under the peak) $K\beta_{1,3}$ spectra of PS II samples in the S_0, S_1, S_2, and S_3 states. These spectra were generated by deconvoluting the flash spectra shown in Figure 2-7, as described in the text.

The changes in the $K\beta_{1,3}$ emission spectra can also be visualized as difference spectra. This was done by smoothing the pure S-state spectra (shown in Figure 2-8) by fitting a cubic polynomial of 3 eV width around each point, and then performing the subtractions to generate the S-state difference spectra shown in Figure 2-9. The derivative-shaped S_1 - S_0 and S_2 - S_1 difference spectra show that the $K\beta_{1,3}$ peak shifts to lower energy during both the $S_0 \rightarrow S_1$ and $S_1 \rightarrow S_2$ transitions. This reinforces the earlier conclusions that Mn oxidation occurs during both of these transitions. However, the derivative-shaped feature is noticeably absent in the S_3 - S_2 difference spectrum, thus confirming that the $S_2 \rightarrow S_3$ transition proceeds without Mn oxidation.

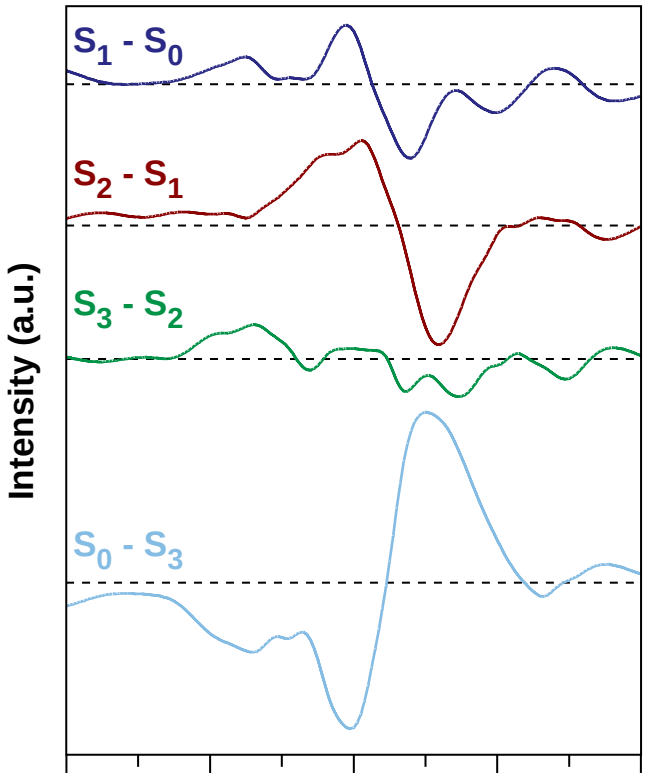

Figure 2-9: Kβ difference spectra of PS II. The Kβ spectra from Figure 2-8 were smoothed by fitting a cubic polynomial of 3 eV width to each point, and were then subtracted to generate the spectra shown.

The Kβ XES protocol was carefully designed to minimize and examine the effects of radiation damage to the samples. As described in the Materials and Methods section, three $K\beta_{1,3}$ emission scans were taken at each sample position. Figure 2-10 shows the 1st-moment values for the 0F, 1F, 2F, and 3F samples as a function of X-ray exposure time. The dashed lines show the fits to the data points for each flash number assuming 1st-order kinetics for the photoreduction process. The fits show the relative radiation damage susceptibility for each flash number, as well as an extrapolated 'zero exposure time' moment for each flash number. Figure 2-10 shows that the radiation damage rate

for the 2F samples is significantly less than that of the 0F, 1F, or 3F samples. This finding excludes the possibility that the extremely small <E> shift between the 1F and 2F samples could be caused by a faster photoreduction of the S_3 state compared to the S_2 state.

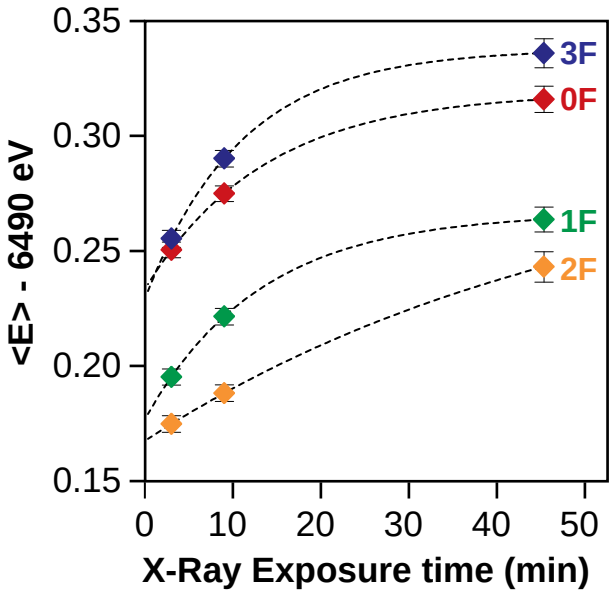

Figure 2-10: 1st moments of the $K\beta_{1,3}$ peaks of the PS II flash samples as a function of X-ray exposure time. The 1st moments were calculated for the energy range shown in Figure 2-7B. Symbols are the data points and the dashed lines are first-order fits. The error bars reflect the statistical error for each measurement and are based on the total number of counts.

Discussion

Oxidation states of the Mn cluster based on XANES spectroscopy and Kβ emission spectroscopy

XANES spectroscopy has been widely used for nearly 25 years to address the oxidation states of redox-active metals in metalloprotein active sites.[56,59,93-100] In addition to XANES, this work applies Kβ XES for the first time to single-flash saturable concentrations (~150 μM Mn) of PS II, thus providing an important independent determination of the Mn redox states in each of the accessible S-states of the OEC in PS II.

By combining the information available from the XANES spectra (Figure 2-4 and Figure 2-5) with the Kβ emission spectra (Figure 2-8 and Figure 2-9) and literature data, the presence or absence of Mn oxidation during each S-state transition will be addressed in more detail, and oxidation states for the four Mn ions in each S-state, S_0, S_1, S_2, and S_3, will be proposed.

$S_1 \rightarrow S_2$ transition

As detailed in the Results section, the Mn K-edge XANES spectra and the $K\beta_{1,3}$ emission spectra confirm the presence of Mn oxidation during the $S_1 \rightarrow S_2$ transition, consistent with earlier XANES studies.[59,98,102] The principal pieces of evidence supporting this conclusion are the 1.1 eV shift in the XANES 2nd-derivative IPE values, the shift in the $K\beta_{1,3}$ peak to lower energy by 0.06 eV, and the derivative-shaped $K\beta_{1,3}$ difference spectrum.

This conclusion is corroborated by several other spectroscopic studies[59,85-90,98] and is also confirmed by EPR spectroscopic measurements. The observation of a multiline EPR signal in the S_2 state during a conventional perpendicular-polarization EPR experiment[50,51] is most consistent with a transition between odd-electron (Kramers) states. The S_1 state has no perpendicular polarization-detectable EPR signals; however, EPR signals are detectable in parallel-polarization EPR experiments,[47-49,84] which is consistent with the S_1 state being an even-electron (non-Kramers) state. Therefore, these EPR signals are consistent with Mn being oxidized from an even-electron to an odd-electron state during the $S_1 \rightarrow S_2$ transition.

Simulations of the EPR signals from the S_2 state also provide insight into the absolute Mn oxidation states in the S_2 state. S_2-state EPR multiline signal simulations by Hasegawa et al.[75,76] and ^{55}Mn ENDOR spectroscopy on the S_2 state by Britt and co-workers[44,74] are most consistent with the oxidation states of $Mn_4(III,IV_3)$; however, simulations by Zheng et al.[142] are most consistent with $Mn_4(III_3,IV)$ as the oxidation states of Mn in the S_2 state. The presence of high-valent Mn atoms in the active OEC is not surprising, because it was established early on that Mn(II) atoms could be incorporated into Mn-depleted photosystem II centers only via light-induced oxidation of Mn in a process called photoactivation.[143-145] The reverse reaction, i.e. a chemical reduction of the OEC, has led to the discovery of an S_{-3} state.[146] The stability of the S_{-3} state (hours) has been interpreted[70] to favor $Mn_4(II_2,III_2)$ over $Mn_4(II_4)$ for the Mn redox states in the S_{-3} state, assuming that S_{-3} state formation involves only Mn reduction.[146] This is consistent with $Mn_4(III,IV_3)$ as the Mn oxidation states in the S_2 state.

If the S_2 state is proposed to be either in the $Mn_4(III,IV_3)$ or the $Mn_4(III_3,IV)$ oxidation states, then the oxidation states of Mn in the S_1 state must be either $Mn_4(III_2,IV_2)$ or $Mn_4(III_4)$, which are both one-electron reductions from the oxidation-state proposals for the S_2 state. Although the oxidation state of $Mn_4(III_4)$ for the S_1 state has been suggested by one group,[147] the 2nd derivative of the XANES spectrum for the S_1 state shows that its edge shape is unlike the edge shape observed for Mn(III) complexes; when the 2nd-derivative XANES spectrum for the S_1 state is fit using Mn(III) and Mn(IV) model compounds, it cannot be fit well using only Mn(III) model compounds.[71,148] Furthermore, inspection of the only available set of tetranuclear Mn complexes with all O ligation, four distorted Mn_4 (III_3,IV) cubanes, shows XANES IPE values at ~6551 eV for these complexes,[73] consistent with the S_0-state XANES IPE of 6550.8 eV and lower than the S_1-state XANES IPE of 6552.9 eV. Thus, this indicates that the oxidation states of Mn in the S_1 state are $Mn_4(III_2,IV_2)$, not $Mn_4(III_4)$.

In addition, a reductant treatment of PS II core particles with hydroquinone (a two-electron reductant) leads predominantly to the formation of the S_{-1} state, which is two electrons reduced relative to the S_1 state. The XANES spectrum from samples in the S_{-1} state is best fit with a $Mn_4(II_2,IV_2)$ oxidation state.[148] An oxidation-state assignment of $Mn_4(III_2,IV_2)$ is also consistent with recent Kβ XES experiments on the S_1 state. In fitting the $K\beta_{1,3}$ emission spectrum for the S_1 state, Bergmann et al.[108] found that the best fit to the experimental data was obtained using equal amounts of the $K\beta_{1,3}$ emission spectra from Mn(III) and Mn(IV) model compounds; the fit was significantly worse if only Mn(III) or only Mn(IV) was used for the fit.[108]

It is therefore most likely that the oxidation states for Mn are $Mn_4(III_2,IV_2)$ in the S_1 state and $Mn_4(III,IV_3)$ in the S_2 state. The oxidation of Mn(III) to Mn(IV) during this transition is reflected in the 1.1 eV shift in the XANES IPE value (Table 2-3) and the shift of -0.06 eV in the 1st moment of the Kβ emission spectra (Figure 2-8). The S_2 - S_1 difference spectra shown in Figure 2-4B (XANES) and Figure 2-9 (Kβ XES) also confirm that Mn is oxidized during this transition. Thus, these changes in the IPE and 1st-moment values, as well as their corresponding difference spectra, provide an internal standard for a Mn(III) → Mn(IV) oxidation within the OEC.

$S_0 \rightarrow S_1$ transition

The Mn K-edge XANES spectra for these S-states, displayed in Figure 2-4A, and the 2nd derivatives (Figure 2-5B) show a clear shift of 2.1 eV (as determined by the 2nd-derivative IPE values) in the XANES edge position during the $S_0 \rightarrow S_1$ transition. In addition, the S_1 - S_0 Kβ XES difference spectrum, shown in Figure 2-9, is derivative-shaped, which is indicative of Mn oxidation during this transition. Because the S_1 state has Mn oxidation states of $Mn_4(III_2,IV_2)$, as detailed above, the changes in the X-ray spectroscopic data could be due to either a Mn(II) → Mn(III) oxidation or a Mn(III) → Mn(IV) oxidation.

Because the S_1 - S_0 XANES and Kβ XES difference spectra (Figure 2-4B and Figure 2-9) are somewhat different from the S_2 - S_1 difference spectra, this suggests that the $S_0 \rightarrow S_1$ transition most likely reflects a Mn(II) → Mn(III) oxidation. The S_1 - S_0 XANES difference spectrum shown in Figure 2-4B contains positive features in the 6545 – 6565 eV range, unlike the S_2 - S_1 XANES difference spectrum. This includes the

pre-edge region, which shows that the S_0-state XANES spectrum has a lower pre-edge intensity than the S_1-state XANES spectrum (also seen in the inset in Figure 2-4A). In addition, the S_1 - S_0 and S_2 - S_1 Kβ XES difference spectra shown in Figure 2-9 are not identical; the magnitude of the S_1 - S_0 Kβ XES difference spectrum is smaller than that of the S_2 - S_1 difference spectrum (as determined by integration of the absolute value of the difference spectrum). The shape of the XANES edge is different for the S_0-state and S_1-state spectra; this is shown in part by the peak at 6548 eV in the 2nd derivative of the S_0-state XANES spectrum (Figure 2-5B). This is suggestive of the presence of Mn(II), based on comparison to the 2nd derivatives of Mn(II)-containing model compounds. The significantly larger shift in the 2nd-derivative IPE values for the $S_0 \rightarrow S_1$ transition compared to the $S_1 \rightarrow S_2$ transition is also indicative for a Mn(II) $\rightarrow$ Mn(III) oxidation. This is based on the finding that, for homologous sets of model compounds, the shifts in the IPE value for Mn(II) $\rightarrow$ Mn(III) oxidations are usually larger than those seen for Mn(III) $\rightarrow$ Mn(IV) oxidations. However, in agreement with Roelofs et al.,[98] but in contrast to Iuzzolino et al.,[102] no 'Mn(II) shoulder' is observed in the pure S_0-state XANES spectrum (Figure 2-4A).

Other spectroscopic studies[45,46,80,83,85-90] concur that Mn oxidation occurs during the $S_0 \rightarrow S_1$ transition. In addition, one possible explanation of the greater spectral width of the S_0-state EPR multiline signal compared to the S_2-state EPR multiline signal is that Mn(II) is present in the S_0 state,[45,46,83] which suggests a Mn(II) $\rightarrow$ Mn(III) oxidation for the $S_0 \rightarrow S_1$ transition. The presence of Mn(II) in the S_0 state may also explain why Y_D^{ox} can oxidize the S_0 state to the S_1 state, but not the S_1 state to the S_2 state.[120]

The Kβ XES and XANES difference spectra, in addition to other spectroscopic data are consistent with the assignment of the $S_0 \rightarrow S_1$ transition as a Mn(II) $\rightarrow$ Mn(III) oxidation. Therefore, the oxidation states of Mn in the S_0 state are proposed to be $Mn_4(II,III,IV_2)$, which change upon Mn oxidation to $Mn_4(III_2,IV_2)$ in the S_1 state.

$S_2 \rightarrow S_3$ transition

The most controversial S-state transition has been the $S_2 \rightarrow S_3$ transition (see Introduction). Most debate has focused on whether this transition is a Mn-centered[65,68,101-103] or ligand-centered[36,40,66,67,69,70,98] oxidation. In addition, a redox isomerism between Mn and ligands has been proposed for the S_3 state.[37] If Mn were to be oxidized during the $S_2 \rightarrow S_3$ transition, the oxidation would have to be a Mn(III) $\rightarrow$ Mn(IV) transition. A Mn(IV) $\rightarrow$ Mn(V) transition is unlikely to occur with Mn(III) still present in the complex given the proposed reactivity of the Mn(V) ion, although a $Mn_4(IV_4) \rightarrow Mn_4(IV_3,V)$ transition has been proposed for the $S_3 \rightarrow [S_4]$ transition.[103] Thus, it would be expected that the XANES and Kβ XES difference spectra, as well as the observed shifts in the XANES IPE values and the Kβ emission spectra 1st-moment values, would be essentially identical to the $S_1 \rightarrow S_2$ transition, where a Mn(III) $\rightarrow$ Mn(IV) oxidation also occurs. However, as described below, the spectroscopic results for the $S_2 \rightarrow S_3$ transition are completely different from those of the $S_1 \rightarrow S_2$ transition.

The XANES results from Figure 2-4 and Figure 2-5 provide strong support for a ligand-based oxidation of the OEC occurring during the $S_2 \rightarrow S_3$ transition, based on the small (0.3 eV) shift in the XANES 2nd-derivative IPE values. This finding is consistent

with earlier XANES studies by Roelofs et al.[98] The fact that the S_3 - S_2 XANES difference spectrum is significantly different from the S_2 - S_1 difference spectrum (Figure 2-4B) is inconsistent with a Mn(III) $\rightarrow$ Mn(IV) oxidation occurring during the $S_2 \rightarrow S_3$ transition. Instead, the S_3 - S_2 XANES difference spectrum shows how the shape of the XANES edge changes between the S_2 and S_3 states, which is consistent with a ligand-based oxidation (*vide infra*).

Changes in the XANES spectrum similar to those observed during the $S_2 \rightarrow S_3$ transition are also observed in a different enzymatic system, galactose oxidase, as well as in model compounds that mimic its structure and reactivity. Galactose oxidase, a metalloenzyme with a mononuclear Cu active site, is known to catalyze the two-electron aerobic oxidation of alcohols to aldehydes.[149] The anaerobic and one-electron oxidized forms of the enzyme contain Cu^{I} and Cu^{II} in the active site, respectively. However, instead of a Cu^{III} ion, the two-electron oxidized form of the enzyme is known to contain a phenoxyl radical coordinated to a Cu^{II} atom. When monitored using XANES spectroscopy, the XANES edge was clearly shifted to higher energy between the Cu^{I} and Cu^{II} forms of the enzyme. However, comparison of the Cu^{II} and Cu^{II}–$O^{\cdot}$ forms of the enzyme showed that the edge shape was slightly different and the edge position was in fact shifted to slightly lower energy.[150] This trend is also seen in Cu^{II}–phenoxyl radical model complexes, where the Cu^{II}–$O^{\cdot}$ complex has a different XANES edge shape from that of the corresponding Cu^{II} complex, but essentially the same edge position.[55,151] In addition, DFT calculations support the formation of Cu^{II}–$O^{\cdot}$ in both the enzyme and the model complexes.[152]

The same situation occurs in the OEC during the $S_2 \rightarrow S_3$ transition, where the edge shape changes but the edge position is minimally affected. Therefore, based on the XANES data, it is reasonable to suggest that, as is formed in galactose oxidase, a ligand radical is formed in the S_3 state in lieu of Mn oxidation; this will be denoted by $Mn_4(III,IV_3)^{\cdot}$.

This interpretation of the XANES data is strongly reinforced by the Kβ emission spectra and Kβ XES difference spectra from Figure 2-8 and Figure 2-9, respectively. The difference spectra clearly show that the derivative-shaped difference spectrum that is expected if Mn is oxidized, as in the $S_0 \rightarrow S_1$ and $S_1 \rightarrow S_2$ transitions, is absent in the $S_2 \rightarrow S_3$ transition. In addition, the <E> value of 6490.157 eV for the S_3 state argues against Mn oxidation during the $S_2 \rightarrow S_3$ transition, because it is inconsistent with a $Mn_4(IV_4)$ oxidation state, which is required for the S_3 state if Mn is oxidized during the $S_2 \rightarrow S_3$ transition. Comparison of the S_3-state <E> value to the <E> values from 18 different monomeric, dimeric, trimeric, and tetrameric Mn(IV) model compounds with different ligands, including Cl^-, shows that the S_3-state <E> value is higher than the <E> value for any of the Mn(IV) compounds studied (average <E> = 6490.00 eV, highest <E> = 6490.10 eV). It is difficult to explain this result unless Mn(III) is still present in the S_3 state, which means that, based on the $Mn_4(III,IV_3)$ redox states derived for the S_2 state (*vide supra*), a Mn-based oxidation cannot occur during the $S_2 \rightarrow S_3$ transition.

Effects of structural changes on the XANES and Kβ XES data

This section will consider in detail whether structural changes and/or ligand rearrangements during the $S_2 \rightarrow S_3$ transition could compensate for Mn oxidation in the

Kβ emission and XANES spectra. This is of particular interest due to the proposed structural changes during the $S_2 \rightarrow S_3$ transition[153,154] which were recently confirmed by direct distance measurements from EXAFS experiments.[69] The detailed considerations described below show that it is unlikely that a structural change could mask the effects of Mn oxidation during the $S_2 \rightarrow S_3$ transition in the OEC.

The work by Visser et al.[125] compares the XANES spectra from two Mn_2(III,IV) binuclear complexes with different ratios of aromatic to non-aromatic ligands and different μ-oxo bridges. This comparison shows that drastic ligand rearrangements can affect the observed XANES edge shape and position to a greater degree than changes in oxidation state.

However, the Kβ XES results from the work of Visser et al.[125] show that, while the previously mentioned Mn complexes have different XANES 2nd-derivative IPE values for complexes in the same Mn oxidation state, the Kβ XES 1st-moment values are essentially identical for the two different binuclear complexes in the same Mn oxidation state. This shows that, if a large change in ligand environment were to occur without a change in oxidation state, the Kβ emission spectra 1st-moment values should be largely unaffected.

Could ligand rearrangement prevent the observation of a Mn-centered oxidation in the XANES spectra pertaining to the $S_2 \rightarrow S_3$ transition? Several lines of evidence argue against this proposition. In Mn model compounds, dramatic ligand effects are seen when several aromatic ligands are substituted for aliphatic ligands and vice versa.[125,155] This is because, with aromatic ligands, additional $1s \rightarrow {}^{*}$ transitions are present just below the main $1s \rightarrow 4p$ XANES transition;[156] this shifts the XANES edge position to

lower energy with respect to complexes with aliphatic ligands. These 1s $\rightarrow$ * transitions are absent with aliphatic ligands, because they have occupied, not unoccupied, * ligand orbitals. The Mn cluster in PS II has very few aromatic ligands; therefore, the contribution of 1s $\rightarrow$ * transitions to the PS II XANES spectra should be negligible. The possibility of tyrosine ligands to the Mn cluster has been ruled out by site-specific mutagenesis experiments;[157] 1 – 2 histidines, out of ~24 total ligands to Mn, are ligated to the Mn cluster in the S_2 state.[158-160] There is no evidence from EXAFS spectroscopy for the binding of more histidine ligands in the S_3 state. If additional histidine binding occurred, histidine multiple-scattering features would appear in the Fourier transform of the S_3-state EXAFS data; they are not present in the experimental spectra.[69,161] Therefore, the effects of aromatic ligands do not need to be considered in interpreting the XANES spectra of the S-states of the OEC.

Another possible ligand substitution or rearrangement is that Cl^-, an essential cofactor for oxygen evolution,[162,163] could be bound in the S_3 state and not in the S_2 state. This is consistent with ^{35}Cl NMR experiments by Preston et al.[164] and UV absorbance experiments by Wincencjusz et al.[165] which show that, in these preparations, Cl^- is required for the $S_2 \rightarrow S_3$ and $S_3 \rightarrow [S_4] \rightarrow S_0$ transitions, but not for the $S_0 \rightarrow S_1$ and $S_1 \rightarrow S_2$ transitions. Further evidence comes from EXAFS spectroscopy experiments on oriented PS II membranes in the S_3 state which show a Fourier peak at a distance of ~2.2 Å from Mn.[166] Based on comparison to model compounds, this is consistent with Cl^- binding to Mn in the S_3 state.[167] However, some experiments have been interpreted to suggest that Cl^- binds to the Mn cluster prior to the formation of the S_3 state.[52,168-172]

If Cl^- were only to bind in the S_3 state, its effect on the Mn K-edge XANES spectrum of PS II can be estimated by examining data from sets of Mn model compounds with and without Cl^- bound. Pizarro et al.[167] have examined sets of dimeric and trimeric Mn model complexes which are essentially identical except for the exchange of Cl^- for oxygen-containing ligands. In the dimeric complex (two Cl^- per two Mn), the edge shape changes somewhat when the Cl^- ligands are replaced by an acetate bridge, but the 2^{nd}-derivative IPE values are essentially unchanged. In the trimeric complex, which contains one Cl^- per three Mn atoms, replacing Cl^- with OH^- causes even less of a change in the edge shape, and the 2^{nd}-derivative IPE values are again quite similar. The effect on PS II is expected to be even less, because, if Cl^- is bound to Mn in the S_3 state, the ratio would most likely be one Cl^- to four Mn. Thus, it is unlikely that Cl^- binding in the S_3 state could offset the effects of a hypothetical Mn oxidation during the $S_2 \rightarrow S_3$ transition.

The most likely structural change occurring during the $S_2 \rightarrow S_3$ transition is the modification of the di-μ-oxo bridges. This is based on EXAFS spectroscopic data from the S_3 state that show the Mn–Mn distances changing from 2.7 Å in the S_2 state to ~2.8 and 3.0 Å in the S_3 state.[69,82] Although the distance increase is not enough to justify a conversion from a di-μ-oxo to mono-μ-oxo motif (a 3.3 – 3.6 Å Mn–Mn distance would be necessary[173]), the effects of a modification of the di-μ-oxo bridges on the Mn K-edge XANES spectrum is well modeled by a series of Mn complexes in which the di-μ-oxo bridges of a dimeric Mn_2(IV,IV) complex were successively protonated, which increased the Mn–Mn distance from 2.7 Å to 2.8 Å and 2.9 Å, respectively.[174] These complexes showed some changes in edge shape, but almost no change in edge position

(2nd-derivative IPE values of 6553.5 eV, 6553.2 eV, and 6553.3 eV for 0, 1, or 2 μ-oxo bridge protonations, respectively) due to di-μ-oxo bridge protonation. It is therefore unlikely that a hypothetical oxidation-state change during the $S_2 \rightarrow S_3$ transition could be masked by the lengthening of the Mn–Mn distances in the S_3 state, or any other plausible ligand substitutions or rearrangements.

Furthermore, the Kβ XES results from the work of Visser et al.[125] show that, if a large change in ligand environment were to occur without a change in oxidation state, the Kβ emission spectra 1st-moment values should be largely unaffected. Thus, it is even more unlikely that a hypothetical oxidation-state change could be masked in the spectra from two independent X-ray spectroscopic techniques, XANES and Kβ emission spectroscopy.

Comparison to other XANES studies

Much of the controversy surrounding the $S_2 \rightarrow S_3$ transition is due to the conflicting results among earlier XANES studies of the S-states generated using single-flash turnover. The current XANES study represents a significant improvement in three important areas: a) a high sample concentration was used, which resulted in a large improvement of the signal-to-noise ratio relative to earlier data, b) due in part to laser flash illumination, a deep S_2 EPR multiline oscillation with no double hits was achieved; this largely removes ambiguities in the deconvolution of the measured XANES spectra into the pure S-state XANES spectra, and c) the monitoring and minimization of radiation damage. Another difference between the studies is the way in which the data are analyzed; this is discussed in detail in the Appendix. The 2nd-derivative method has been

used for determination of XANES edge energy positions based on the following criteria: a) it is insensitive to linear background subtraction and normalization, b) it has been used successfully by several groups for 25 years to determine the oxidation state of metal ions in metalloproteins and model complexes (see the Results section) and c) in addition to the edge position, detailed information on the edge shape is provided.

For the following comparison of various XANES studies, it is very important to keep in mind that without an accurate determination of the S-state composition of the flash samples, no meaningful conclusions can be drawn about the Mn oxidation-state changes during the various S-state transitions. To achieve an accurate S-state deconvolution, the S_2-state EPR multiline signal must be measured for all the samples used for the XANES experiments and a deep S_2-state EPR multiline signal oscillation must be obtained. Otherwise, several different dephasing mechanisms can be invoked, each of which yields different S-state compositions for the flashed samples and different 'pure' S-state spectra.

Ono et al. study[101]

This was the pioneering XANES study on flashed samples; unfortunately, no independent data on the S-state composition of the PS II samples were provided, which precludes a unique determination of the S-state XANES edge energies (*vide supra*). Among the four existing XANES studies, it is the only one in which the flash-sample XANES spectra (i.e. before deconvolution into pure S-states) show a Mn K-edge shift between the 1F and the 2F samples which is of approximately the same magnitude as the 0F to 1F shift. Because this study does not provide an independent characterization of the S-state composition of their samples, this behavior can be explained if the actual miss

parameter is significantly larger than the reported miss parameter of 9 %. A high miss factor in this study could be caused by: a) the low energy per pulse of the laser, i.e. non-saturating illumination, b) the absence of exogenous electron acceptors, such as PPBQ, and c) a significantly higher Y_D content in the samples than the 25 % that was assumed (up to 75 % Y_D has been observed[175,176]). Furthermore, the pure S-state edge energies were determined by fitting the oscillation pattern of the half-height energies, not by deconvolution (or fitting) of the flash spectra. This is problematic, because the edge shapes are not the same for each S-state (see the lower portion of Figure 2-4A).

Roelofs et al. study[98]

Roelofs et al. observed IPE shifts between S-states similar to those reported here. As is the case in the present study, the S_2-state multiline EPR signal oscillation pattern from Roelofs et al. showed a deep period four oscillation, which greatly reduced the error introduced by deconvolution. A possible concern about the data from Roelofs et al. is that the reported IPE values are consistently lower than those shown in Table 2-3 by

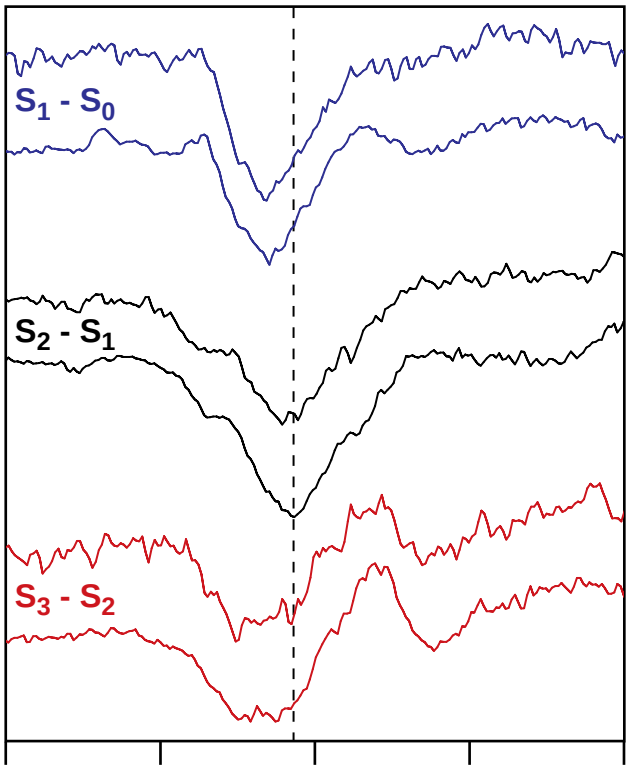

Figure 2-11: Comparison of Mn K-edge XANES difference spectra of PS II samples in the S_0, S_1, S_2, and S_3 states from the present study (also shown in Figure 2-4B) and from the work of Roelofs et al.[98] In each set of XANES difference spectra, the difference spectrum from the work of Roelofs et al.[98] is presented above the difference spectrum from the present study. The XANES difference spectra have been vertically offset for clarity.

approximately 0.5 – 0.7 eV for the S_0, S_2, and S_3 states and by 1.2 eV for the S_1 state. One hypothetical explanation of this discrepancy, as suggested by Iuzzolino et al.,[102] is that the samples in the Roelofs et al. study had some free Mn(II) present. This possibility was tested by adding in fractional amounts of a $Mn(II)_{(aq)}$ XANES spectrum or a spectrum from a Mn(II)-containing model compound to the XANES spectra obtained in the present study. Neither of these scenarios reproduced the XANES spectra shown in Roelofs et al.; as expected, the 2nd derivatives of the simulated spectra showed an intense feature at 6545 eV which is absent in the Roelofs et al. data. Therefore, the lower XANES IPE values for the Roelofs et al. data cannot be attributed to the presence of Mn(II) in the samples. It is possible that either of two factors, differing cryoprotectant concentrations (50 % glycerol in the Roelofs et al. data, 30 % glycerol in the present study) or a small (< 5 % of the total signal) feature in the I_0 spectrum of the Roelofs et al. data, contributed to the observed difference in the XANES IPE values. However, as shown in Figure 2-11, the XANES difference spectra from the work of Roelofs et al. are, aside from a lower signal-to-noise ratio, almost identical to the difference spectra from the present study for each of the S-state transitions. Therefore, the study by Roelofs et al. provides strong support to the XANES spectra from the present study.

Iuzzolino et al. study[102]

In contrast to the data from Ono et al.,[101] the raw data from Iuzzolino et al. qualitatively agree well with the data from the present study and the data from Roelofs et al.[98] In all three studies, a clear Mn K-edge shift is seen between the 0F and 1F spectra, while very little change in edge position is observed between the 1F and the 2F samples. In addition, the IPE of the 0F (S_1) sample from Iuzzolino et al. is essentially identical to

the IPE measured in the present study. However, after deconvolution, Iuzzolino et al. find that the shift between S_2- and S_3-state spectra is of the same size or even larger (depending on analysis method) than the shift between the S_1 and S_2 states; the opposite is true in the current study. A reasonable explanation for this 'after deconvolution' discrepancy is that Iuzzolino et al. have used a double-hit parameter, 11 – 15 %, that is too large; typical values of 2 – 5 % are found with similar Xe flash lamps.[146,177] The edge position of the S_3 state is especially sensitive to the double-hit parameter, because this factor determines what percentage of the S_0 state is subtracted from the 2F spectrum. Because the S_0 state has a far lower edge position than the S_3 state, even a small error in the S_0-state population of the 2F sample has a significant effect on the calculated S_3-state edge position. This uncertainty does not exist when a Nd-YAG laser is used for flash illumination, because these laser pulses are too short (ns) to cause multiple turnovers. In addition, the S_2-state multiline EPR signal oscillation patterns achieved by Iuzzolino et al. are quite damped; therefore, many different fits to the S_2-state multiline EPR signal oscillation patterns can be invoked, creating considerable uncertainty in the subsequently deconvoluted S-state spectra. As detailed in the Appendix, it can be shown that, if a different deconvolution is used, a significantly smaller edge shift for the $S_2 \rightarrow S_3$ transition compared to the $S_1 \rightarrow S_2$ transition is obtained for the Iuzzolino et al. data. Therefore, the differences between the conclusions from Iuzzolino et al. and those from the current study are largely due to an incorrect deconvolution by Iuzzolino et al. of their fairly damped S_2-state multiline EPR signal oscillation pattern and, to a smaller extent, the use of the integral method for edge energy determination (see Appendix for details).

Summary of Mn oxidation states in PS II

Figure 2-12 summarizes the Kβ XES and XANES flash patterns from the present study that lead to the conclusions about Mn oxidation states. Both spectroscopies show a clear shift in the spectra between the 0F and 1F samples, indicating that Kβ emission and XANES spectroscopies confirm the presence of Mn oxidation during the $S_1 \rightarrow S_2$ transition. The small change between the 2F and 3F samples in both spectroscopies provides strong support for the $S_2 \rightarrow S_3$ transition proceeding without a Mn-based oxidation. On the next transition, $S_3 \rightarrow [S_4] \rightarrow S_0$, dioxygen is released, shifting the position of the 3F spectra to lower energy for XANES spectroscopy and higher energy for Kβ XES. These flash patterns are explained by the proposed oxidation states of the Mn cluster in the S_0, S_1, S_2, and S_3 states, as shown in Figure 2-13. Consistent with earlier proposals,[36,98,178] these oxidation states are: S_0: $Mn_4(II,III,IV_2)$, S_1: $Mn_4(III_2,IV_2)$, S_2: $Mn_4(III,IV_3)$, S_3: $Mn_4(III,IV_3)^{\cdot}$.

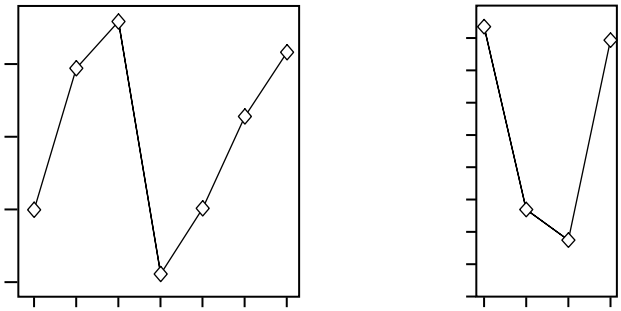

Figure 2-12: **(A)** Oscillation of XANES inflection point energies (I.P.E.) of the 0F to 6F samples. **(B)** Oscillation of first moments (<E>) of the Kβ spectra from the 0F to 3F samples (4F to 6F were not collected). The extrapolated <E> values for zero X-ray exposure time from Figure 2-10 are shown.

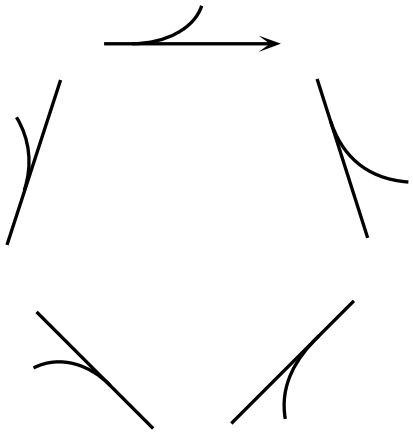

Figure 2-13: S-state scheme for oxygen evolution based on the proposal by Kok et al.[27] The proposed oxidation states of Mn in each of the S-states S_0–S_3 based on the results from Kβ emission and XANES spectroscopy are shown. For the S_3 state, it is proposed that the oxidizing equivalent is stored mainly on a direct ligand to Mn, most likely a μ-oxo bridge, and little of this spin density is present on Mn. The oxidation of a terminal ligand is less likely because of the observed lengthening of the Mn–Mn distances in the S_3 state.[69]

Implications for the mechanism of photosynthetic water oxidation

Recent EXAFS data on the S_3 state show a lengthening of the Mn–Mn distances relative to the S_2 state, with one 2.7 Å di-μ-oxo bridged Mn–Mn distance increasing to 3.0 Å.[69] To achieve a lengthening of Mn–Mn distances by 0.3 Å in di-μ-oxo bridged units, the bond strength of the μ-oxo bridges must be drastically decreased. This can be achieved by protonation or oxidation of the bridging oxygens. Protonation of both bridges is known to increase the di-μ-oxo Mn–Mn distance from 2.7 Å to ~2.9 Å.[174] It is, however, very unlikely (and inconsistent with the external proton release pattern of PS II[68,179]), that protonation occurs when the complex becomes oxidized. Oxidation of

one of the μ-oxo bridges is an even more drastic way to reduce the strength of the μ-oxo bridge than protonation, and would explain the experimentally determined 3.0 Å Mn-Mn distance in the S_3 state. Consistent with previous proposals,[36,69] it is concluded that a μ-oxo bridge becomes oxidized in the S_3 state.

Because the XANES and Kβ XES experiments are performed at 10 K to minimize photoreduction, the possibility should be considered of a temperature-dependent equilibrium[92] whereby the S_3 state is trapped in a Mn(III)-L$^{\bullet}$ configuration at low temperatures, but at room temperature a Mn(IV)-L configuration exists.[180] Thus, neither a structural change occurring between the S_2 and S_3 states nor the presence of a radical in the S_3 state would be seen in experiments performed at physiological temperatures. However, both phenomena have indeed been seen in experiments performed at room temperature. NMR-PRE experiments performed at 17° C do not support a Mn-based oxidation for the $S_2 \rightarrow S_3$ transition (see Introduction). The $S_2 \rightarrow S_3$ transition has been shown to have a high reorganization energy based on the temperature dependence of the activation energy for this transition[181] and the S_3 state is 10 – 20x less reactive than the S_2 state towards exogenous reductants;[154] both experiments support a structural change occurring at room temperature. Furthermore, the presence of a radical in the S_3 state at physiological temperatures is supported by recent studies by Ioannidis et al.[182] comparing the reactivity of NO• towards the S_2 and S_3 states at 18° C. These studies showed that the S_3 state is reduced by NO• to the S_1 state five times faster than the S_2 state is reduced. This rate increase is especially significant given the 10 – 20x restricted access of substrate molecules to the OEC in the S_3 state, as shown by the above-

mentioned experiments[154] with exogenous reductants. This is consistent with NO• acting as a radical trapping agent and the S_3 state containing some radical character.

DFT calculations by Per Siegbahn provide additional support for the presence of a radical in the S_3 state.[77] These calculations show that it is energetically unfavorable to oxidize Mn during the $S_2 \rightarrow S_3$ transition relative to the formation of a ligand radical in the S_3 state. Furthermore, this energetic preference only exists if the ligand radical is present as a μ-oxo bridge radical.

The data in this study are therefore best interpreted to show that a ligand-centered rather than a Mn-centered oxidation takes place during the $S_2 \rightarrow S_3$ transition. Based on this result, the mechanistic proposals invoking a Mn oxidation during the $S_2 \rightarrow S_3$ transition that were mentioned in the Introduction can be excluded.

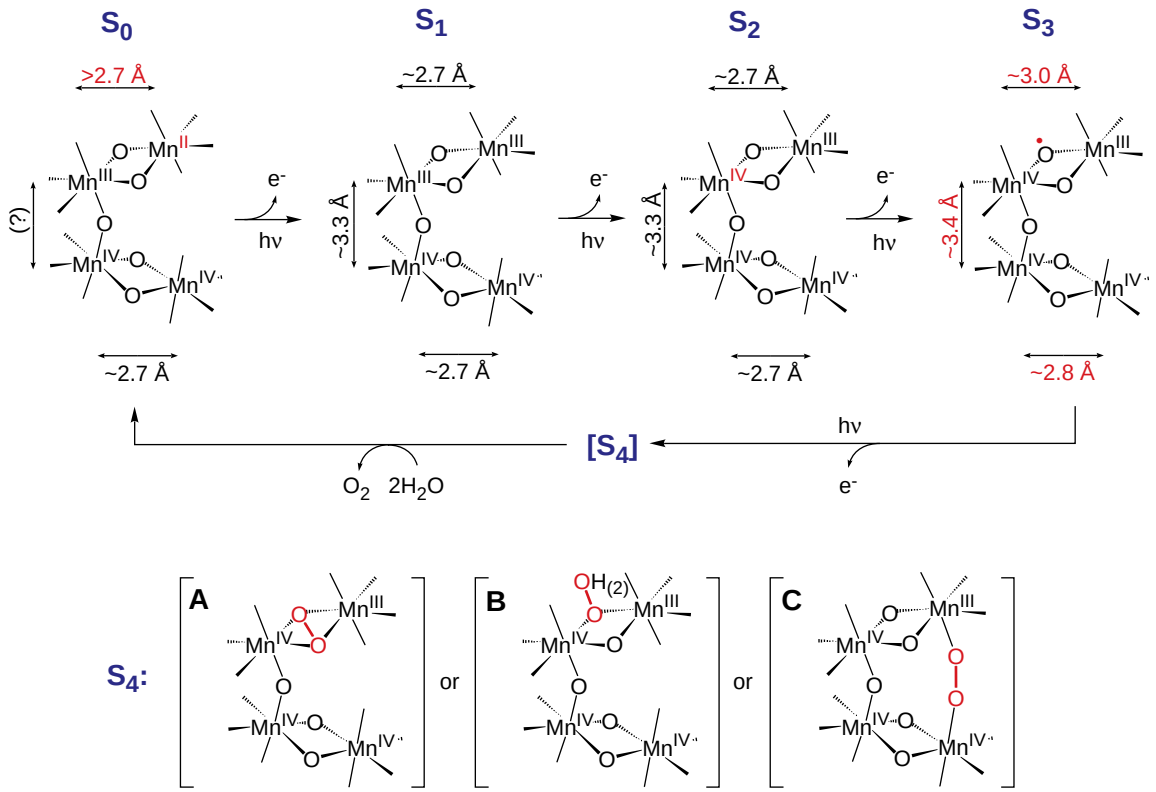

Figure 2-14: Summary of changes in Mn oxidation states and Mn–Mn distances during photosynthetic water oxidation. During the $S_0 \rightarrow S_1$ transition, a Mn(II) $\rightarrow$ Mn(III) oxidation causes the decrease of the Mn–Mn distance. In the $S_1 \rightarrow S_2$ transition, one Mn(III) is oxidized to Mn(IV), and the Mn–Mn distances do not change. During the $S_2 \rightarrow S_3$ transition, a μ-oxo bridge is oxidized, which triggers the increase in Mn–Mn distances. In the $S_3 \rightarrow [S_4] \rightarrow S_0$ transition, a short-lived peroxo intermediate is formed in the S_4 state. **(A)**, **(B)**, and **(C)** are 3 options for O–O bond formation in the S_4 state. The peroxo intermediate is further oxidized to O_2, and two water molecules bind to regenerate the S_0 state. For clarity, Y_Z, the cofactors Ca^{2+} and Cl^-, and terminal Mn ligands are not shown. Mn–Mn distances were determined by EXAFS spectroscopy.[36,81,161] As mentioned in DeRose et al.,[72] Cinco et al.,[73] and Robblee et al.,[40] other possible topological models exist for the OEC; similar mechanisms that can be proposed for each of these alternative topological models should be considered equally viable.

The proposed μ-oxo bridge radical in the S_3 state can be rationalized in the context of any of several possible models for the OEC. It is important to emphasize that the spatial arrangement of the Mn atoms in the OEC is not definitively known. It has been

stated for some time[72] that several topological models (shown as A, E, F, and G in Figure 4 from DeRose et al.[72]) are considered equally possible based on EXAFS data. Although one of the possible topological models is shown in Figure 2-14, similar mechanisms can be proposed using the other topological models, and should all be considered equally viable. Although Ca^{2+} and Cl^{-} are not included in Figure 2-14 for clarity, it should be emphasized that these essential cofactors of oxygen evolution are nonetheless involved in the mechanism of oxygen evolution. Three different possibilities for the O–O bond formation in the S_4 state are shown in Figure 2-14A-C: A) Upon the $S_3 \rightarrow S_4$ transition, the neighboring μ-oxo bridge also becomes oxidized and the O–O bond is formed between the two μ-oxo radicals (Figure 2-14A).[36,40,69] B) The O–O bond is formed between the μ-oxo bridge radical and either an unbound water molecule[40,69] (Figure 2-14B) or a terminal water ligand. C) In the S_4 state, the μ-oxo bridge radical migrates to a terminal hydroxo group and forms the O–O bond with a second terminal Mn-$O^{\cdot}$ that is formed by oxidation through Y_Z^{ox} (Figure 2-14C).[70] All three options for the S_4 state generate O_2 which is derived from inequivalent oxygen atoms in the S_3 state, as shown by $^{16}O/^{18}O$ water-exchange measurements on the S_3 state.[183,184] In addition, a recent $H_2{}^{16}O/H_2{}^{18}O$ FTIR experiment has shown the presence of an exchangeable di-μ-oxo-bridge in the S_1 and S_2 states[185] and another recent $H_2{}^{16}O/H_2{}^{18}O$ FTIR experiment has detected the presence of an asymmetrically hydrogen-bonded H_2O molecule in the S_1 and S_2 states.[186] Although the former result is consistent with options A and B in Figure 2-14 and the latter result is consistent with options B and C, it is not directly known at the present time whether or not either of the aforementioned species participate in oxygen evolution.

The formation of a μ-oxo bridge radical in the S_3 state in lieu of Mn oxidation could be viewed as the onset of water oxidation. Storing this radical on the μ-oxo bridge prevents premature O–O bond formation and possible release of reactive intermediates, which could damage the polypeptides of PS II.

Appendix

Deconvolution of the of the S_2-state EPR multiline oscillation pattern of Iuzzolino et al. study using an extended Kok model

Iuzzolino et al.[102] fit their S_2-state multiline EPR signal oscillation patterns using the original Kok model (see the Results section) with only miss and double-hit parameters as variables; values of 22 % and 11 % (or 14 % and 15 % in samples not used for the XANES experiments) are obtained for the miss and double-hit parameters, respectively. The value of 11 % (or 15 %) is exceedingly large for double hits induced by Xe flashlamps with 3 – 5 μs full width at half maximum; typical values are in the range of 2 – 5 %, depending on conditions.[146,177] This indicates that the simple Kok fit approach is not sufficient and that an extended Kok model needs to be invoked that takes into account a) impaired centers and b) high double hits on every second flash.

As described in the Results section, it has been shown that a fraction of impaired centers can exist in PS II centers.[123,124] Under the assumption of 5 % impaired centers and an initial S_2-state population of 2 % after dark-adaptation (estimated from the S_2-state EPR multiline oscillation pattern presented in Figure 1 of Iuzzolino et al.), the S_2-state multiline EPR signal oscillation pattern of Iuzzolino et al. can be fit using a 20 % miss parameter and a 6 – 9 % double-hit parameter. This leads to a reduction of the calculated S_0-state population in the 2F sample from 15.4 % to 9 – 13 %. The large effect on the calculated edge position shifts of this apparently small reduction in the calculated S_0 population can be roughly estimated using data from the Iuzzolino et al. study. One 'extreme' fit presented in Table 2 from Iuzzolino et al. assumes similar miss (18.7 %) and

double hit (7.3 %) parameters to those found above. Using these parameters, an initial S_2-state population of 2 %, and no impaired centers, an S_0-state population of 10.8 % is calculated for the 2F sample; this is within the range of the fit described above. As shown in Iuzzolino et al., deconvolution using their 'extreme' fit results in the edge shifts between the S-state XANES spectra, as determined using the 'integral' method for edge position determination, being comparable to the data in this study, i.e. a larger shift is observed for the $S_1 \rightarrow S_2$ transition than for the $S_2 \rightarrow S_3$ transition.

In addition to impaired centers, the possibility of high double hits on every second flash should be considered for the Iuzzolino et al. data. It is well documented (and has also been observed in this study (data not shown)) that, in the presence of PPBQ, a reductant-induced oxidation of the non-heme iron occurs on every other flash.[187,188] Because of the fast $Q_A^- \rightarrow Fe^{3+}$ electron transfer, this results in a larger double-hit parameter in every second flash if Xe flashlamps (μs) are used. As mentioned earlier, double hits are not a concern with Nd-YAG lasers.[119] This effect was also included in the extended Kok model, and fits were obtained with $\beta_{1,3,5}$ = 9 % and $\beta_{2,4,6}$ = 3 % (other parameters as above). However, this did not significantly improve the fits nor did the calculated percentage of the S_0 state in the 2F sample change significantly. Nonetheless, this shows that a reasonable double-hit parameter can be obtained if impaired centers and different even/odd flash double hits are taken into account. In contrast to the double-hit parameter, however, the miss parameter stays high in all of the fits, which indicates non-saturating illumination conditions.

It should be emphasized that, for the S_2-state multiline EPR signal oscillation pattern of Iuzzolino et al., neither the presence of impaired centers nor the occurrence of

higher double hits on every second flash can be unambiguously proven through fits to their S_2-state multiline EPR signal oscillation pattern. The inclusion of these parameters in the above fits is solely guided by independent data from the literature and the fact that, without these additional parameters, unrealistically high values for the double-hit parameter are obtained. The uncertainty present in the Iuzzolino et al. data would have been largely avoided if a deep S_2-state multiline EPR signal oscillation pattern had been obtained in that study.

Comparison of different methods for XANES edge energy determination

Previous studies have used three different methods to calculate XANES edge energy positions for each S-state of the OEC. Ono et al.[101] used the energy at which the X-ray absorption is half its maximal value, known as the 'half-height' method, in their study. To interpret changes in oxidation states with this method, the shape of the XANES spectrum should be unchanged during a comparison, which is not true for the S-state spectra (see Figure 2-4A). This method is also highly sensitive to noise in the data, because it is a measurement at a single point and is affected by uncertainty due to noise at the top of the edge. In addition, the spectral information present in the 2^{nd}-derivative spectra is absent with the half-height method.

Roelofs et al.[98] calculated the zero-crossing value of the 2^{nd} derivative of the XANES spectrum ('2^{nd} derivative' method) in their study. Although this method is sensitive to the width of the polynomial used for calculation of the 2^{nd} derivative, several important advantages exist with this method: a) it is insensitive to linear background subtraction and normalization, b) it has been used successfully by several groups for 25 years to determine the oxidation state of metal ions in metalloproteins and model

complexes (see the Results section) and c) in addition to the edge position, detailed information on the edge shape is also provided. However, the width of the polynomial used for calculation of the 2nd derivative must be properly chosen to find an appropriate balance between the reduction of noise in the spectrum (at higher polynomial widths) and retention of spectral structure (at lower polynomial widths); the IPE value and shape of the spectrum are dependent on this choice, which is largely guided by analysis of model compound data. Roelofs et al. (and the current study) used a 6 eV width for the polynomial, which has successfully been used to analyze model compound data.[34,125] Extensive model compound studies have shown that, without exception in the study of more than 13 sets of compounds, when Mn is oxidized by one electron in a set of Mn model compounds with similar ligands, the IPE shifts 1 – 2 eV to higher energy upon Mn oxidation, regardless of nuclearity. When the polynomial width is decreased to 3 – 4 eV, the noise envelope on the 2nd derivatives becomes significant, especially for the PS II data, making the IPE values unreliable.

Iuzzolino et al.[102] used an 'integral' method in which the 1st moment is calculated on the absorption axis between a chosen set of limits, and the X-ray energy value corresponding to the calculated 1st-moment absorption value is reported. Although this method is superior to the half-height method in that the value reported attempts to take into account the shape of the edge, the calculated value is highly dependent on the arbitrary choice of limits, particularly if the shape of the XANES spectrum changes during the comparison (*vide infra*). In addition, errors in normalization and background removal affect the reported values, and the spectral information present in the 2nd-derivative spectra is absent with the integral method. In most cases, use of the integral method with homologous sets of Mn model compounds in different Mn oxidation

states shows trends which are similar to those seen when the 2nd-derivative method is used (6 eV polynomial width). However, when Mn oxidation occurs in these complexes, the edge shape is essentially unchanged.

The 2nd-derivative method has been used in the current study and by Roelofs et al.,[98] and the conclusions from the current study are unaffected if the polynomial width for the 2nd derivative is altered between 5 eV and 8 eV. In particular, the IPE shift for $S_2 \rightarrow S_3$ transition is always < 40 % of the IPE shift for the $S_1 \rightarrow S_2$ transition. However, at lower polynomial widths, noise prevents a reliable determination of the edge energies, and at higher polynomial widths, too many 2nd-derivative features are lost. This relatively large insensitivity of the 2nd-derivative method towards the choice of the polynomial width lends support to the conclusions about the Mn oxidation states in PS II based on this procedure.

However, when the integral method is used, the changes in the shape of the XANES edge that occur during the $S_0 \rightarrow S_1$ and $S_2 \rightarrow S_3$ transitions are of concern. This is because the conclusions about oxidation-state changes, or lack thereof, are strongly dependent on a subjective choice of limits for the 1st-moment calculation for the XANES spectra of the OEC. Use of the same integration limits as Iuzzolino et al.,[102] I = 0.15 to 1, gives the following results: $S_1 - S_0$: 0.4 eV, $S_2 - S_1$: 0.8 eV, $S_3 - S_2$: 0.5 eV. However, integration limits of I = 0.15 to 0.7 give different results: $S_1 - S_0$: 0.5 eV, $S_2 - S_1$: 0.7 eV, $S_3 - S_2$: 0.7 eV, and continuing the integration to the top of the edge (I = 0.15 – T.O.E.) again produces different results: $S_1 - S_0$: 0.3 eV, $S_2 - S_1$: 0.9 eV, $S_3 - S_2$: 0.3 eV.

A more intuitive understanding of why these trends change so dramatically is provided by the XANES difference spectra in Figure 2-4A. The choice of different

integration limits selects for different regions of the spectra; this can leave out significant differences between S-states that are shown in the difference spectra. Furthermore, it is difficult to identify criteria to use that would recommend a particular choice of integration limits, because the use of any of the three integration limits above seems to show reasonable trends when applied to sets of Mn model complexes in which Mn is oxidized. Thus, because the conclusions from applying the integral method on XANES spectra in the current study are critically dependent on the choice of limits, this method cannot be used in this study to provide reliable conclusions about oxidation states of Mn in the OEC.

Chapter 2 Acknowledgments

This research was supported by the National Institutes of Health (GM-55302, GM-44891-5, and GM-48145), and the Director, Office of Basic Energy Sciences, Division of Energy Biosciences of the U.S. Department of Energy (DOE), under Contract DE-AC03-76SF00098. Profs W. H. Armstrong, G. Brudvig, G. Christou, G. C. Dismukes, J.-J. Girerd, R. N. Mukherjee, V. L. Pecoraro, and K. Wieghardt are thanked for providing model compounds, Prof. G. Renger is thanked for the flash-induced oxygen evolution measurements, Dr. Elodie Anxolabéhère-Mallart is thanked for assistance with data collection at SSRL, and Dr. S. Mills is thanked for assistance in performing the ICP/AES measurements. Synchrotron radiation facilities were provided by the Stanford Synchrotron Radiation Laboratory (SSRL) which is operated by the Department of Energy, Office of Basic Energy Sciences. The SSRL Biotechnology Program is supported by the National Institutes of Health, National Center of Research Resources, Biomedical Technology Program, and by the Department of Energy, Office of Biological and Environmental Research.

Chapter 3 : The S_0 state of photosystem II: Is there heterogeneity in the Mn–Mn distances? Determination by EXAFS spectroscopy.

Introduction

The biological generation of oxygen by the oxygen-evolving complex (OEC) in photosystem II (PS II) is arguably one of nature's most important biosynthetic reactions. To perform the 4-electron oxidation of water to dioxygen, the Mn-containing OEC cycles through 5 intermediate S-states, S_0 through S_4, as shown in Figure 2-1 in Chapter 2. This proposal by Kok et al.[27] in 1970 has led to intense study to identify the nature of each of the quasi-stable S-states S_0, S_1, S_2, and S_3 to derive insight about the mechanism of water oxidation in the OEC. Because the S_1 state is the dark-stable state,[27] this S-state is relatively easily studied in the form of concentrated, dark-adapted samples. The discovery that the S_2 state could be prepared essentially quantitatively by low-temperature (190 K) illumination[189] allowed similar studies to be performed on the S_2 state as had been done on the S_1 state. However, the remaining S-states, the S_0 state and the S_3 state, required single-flash saturation techniques. Because this was possible only with dilute samples (•5 mg Chl/mL, prior to the experiments detailed in Chapter 2), the experimental horizons for these S-states were not very promising, especially for X-ray spectroscopic experiments. This has severely limited experimental studies; hence, much less is known about the S_0 and S_3 states than is known about the S_1 and S_2 states.

Most of the information about OEC structure and Mn oxidation states has come from electron paramagnetic resonance (EPR) and X-ray spectroscopic studies of the S_1 and S_2 states. EPR spectroscopy has shown that the S_2 state is paramagnetic, exhibiting

either a multiline EPR signal[50,51] or a broad signal centered at $g = 4.1$.[52,53] In addition, the S_1 state has a parallel-polarization EPR signal.[47-49,84] These signals have been interpreted as arising from a Mn cluster with a nuclearity of four,[75,76,142,190] although other interpretations exist.[191,192]

Two forms of X-ray spectroscopy, X-ray aborption near-edge structure (XANES) spectroscopy and extended X-ray absorption fine structure (EXAFS) spectroscopy, have provided a wealth of information about the oxidation states of Mn in the OEC and the structure of the OEC, respectively, in the S_1 and S_2 states. This is largely due to the inherent element specificity of X-ray spectroscopy. XANES spectroscopy mainly monitors the $1s \rightarrow 4p$ transition in Mn,[55] which is sensitive to Mn oxidation-state changes through core-hole shielding effects.[56] Consistent with the EPR spectroscopic data, XANES experiments have indicated that Mn is oxidized during the $S_1 \rightarrow S_2$ transition.[59,98,101,102] In addition, the results from Chapter 2 show that this conclusion is confirmed by another X-ray spectroscopic technique, Kβ X-ray emission spectroscopy.

EXAFS spectroscopy has been widely applied in the studies of metalloprotein active sites to provide detailed structural information about the coordination environment around the active-site metal(s).[57,193-195] Unlike X-ray crystallography, this technique does not require long-range order; EXAFS experiments can be performed on frozen solutions. EXAFS oscillations exist at energies above the absorption edge of Mn and are due to a final-state interference effect from photoelectrons that are backscattered off neighboring atoms.[57] These oscillations contain information about the number of backscatterers present and the identity of the backscattering atoms; they also contain extremely accurate information about the absorber-backscatterer distances (• 0.02 Å error) in the frequency

of the oscillations. Fourier transformation of the EXAFS oscillations generates a radial distribution function of backscattering atoms;[196] this provides a pictorial representation of the environment surrounding the absorbing atom. The EXAFS oscillations can be quite accurately described theoretically[197,198] and can be fit using the available theory to extract the three parameters mentioned above.

The pioneering EXAFS study of the OEC was performed by Kirby et al.[58] shortly after the advent of user facilities designed to exploit synchrotron radiation. This study showed that there was a remarkable similarity between the EXAFS spectrum of the PS II-containing chloroplasts and the EXAFS spectrum of a di-μ-oxo-bridged Mn complex $Mn_2(III,IV)O_2$(2,2'-bipyridine). Specifically, the Fourier peak corresponding to the 2.7 Å Mn–Mn distance in the di-μ-oxo Mn_2(III,IV) complex was also seen in the chloroplast spectra, which led to the suggestion that a di-μ-oxo-bridged Mn_2 moiety also exists in the OEC. This was confirmed by several subsequent EXAFS studies of PS II[71,72,199-203] that also detected a short 1.8 Å Mn–O distance characteristic of μ-oxo-bridged metal clusters;[204] EXAFS studies that detected a 2.7 Å Mn–Mn interaction but failed to detect the short 1.8 Å Mn–O distance[79,205] were later shown to have been performed on samples that contained significant amounts of adventitious Mn(II).[14,34,148]

These findings firmly established that the OEC in PS II is comprised of di-μ-oxo-bridged Mn_2 clusters. Technical improvements in instrumentation led to the detection of an additional scatterer at 3.3 Å from Mn.[71,72,79,202,205] This interaction has been interpreted as containing contributions from both Mn–Mn and Mn–Ca interactions at 3.3 – 3.4 Å.[206,207] These findings were incorporated into a structural model for the OEC proposed by Yachandra et al.[34,71] shown in Figure 3-1 which contains two di-μ-oxo Mn–Mn moieties connected by a mono-μ-oxo Mn–Mn moiety. The structural building blocks

derived from EXAFS spectroscopy have since been prerequisite structural elements in virtually any proposed model.[36,37,40,65,66,70,103] However, these models have suffered from the relative paucity of structural information about the S_0 and S_3 states, because these S-states are relatively difficult to generate with the homogeneity and concentration that are required for many XAS experiments.

Early XAS experiments by Guiles et al.[80,208] with the S_0 and S_3 states used chemical treatments to get around the problem of low concentrations. However, the S-states generated in this manner were designated as S_0^* and S_3^* to emphasize that they are generated through chemical treatment and are thus not native S-states. The S_3^* state was prepared using a high-potential quinone PPBQ (see Chapter 2) to oxidize the non-heme Fe^{2+} on the acceptor side to Fe^{3+}. This allowed a 2-electron turnover during continuous illumination in the presence of the Q_B inhibitor DCMU (3-(3,4-dichlorophenyl)-1,1-dimethyl urea). The S_0^* state was prepared by adding the chemical reductant NH_2OH to a

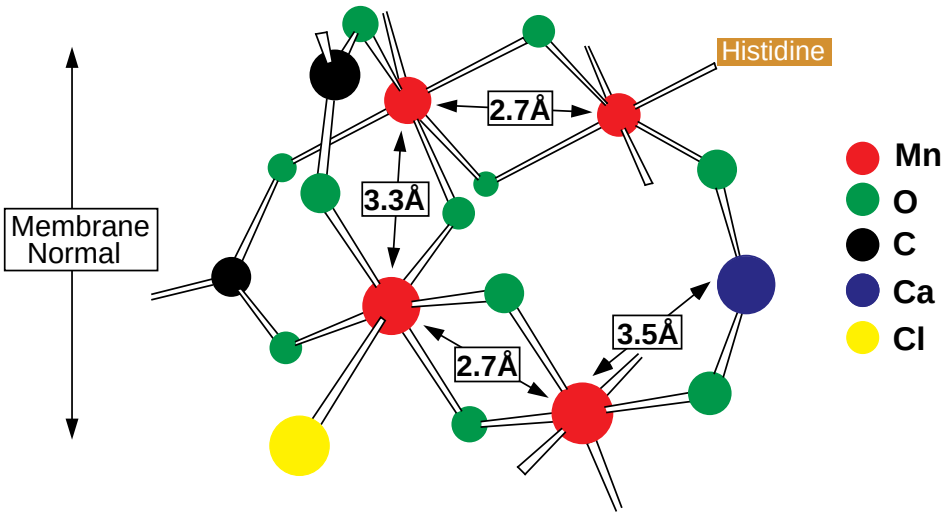

Figure 3-1: A proposed topological model shown in Cinco et al.[206] for the structure of the OEC in PS II. This model incorporates the distance constraints from EXAFS spectroscopy as described in the text.

concentration of 40 μM in S_1-state samples, producing a reduced state called the S_0^* state. Although they were hampered by low signal-to-noise ratios and the uncertainty about the relationship between the chemically generated S^*-states and the native S-states, these experiments provided the first suggestions from XAS that heterogeneity may exist in the 2.7 Å Mn–Mn distances in the S_0 and S_3 states in the form of a reduced amplitude of Fourier peak II in the S_0^* and S_3^* states relative to that in the S_1 state; this heterogeneity is not seen in the S_1- or S_2-state EXAFS spectra.

Further XAS studies on single-flash saturable samples have extended the work of Guiles et al.[208] on the S_3 state, and have provided additional information about the structure around and oxidation states of the Mn atoms in the OEC immediately before the release of dioxygen. The XANES experiments by Roelofs et al.[98] and the experiments shown in Chapter 2 demonstrate that Mn is most likely not oxidized during the $S_2 \rightarrow S_3$ transition. Furthermore, EXAFS experiments by Liang et al.[69] showed that the Mn–Mn distances of 2.7 Å in the S_1 and S_2 states increase to ~2.85 and 3.0 Å in the S_3 state, indicating that a significant structural change is occurring during the $S_2 \rightarrow S_3$ transition. These studies have been reinforced by recent experiments by Fernandez and co-workers[161] on oriented samples in the S_3 state, where these two Mn–Mn distances were also seen and were found to be dichroic. In addition, it was calculated that the 2.85 Å and 3.0 Å Mn–Mn vectors have distinctly different projections onto the membrane normal, implying that they are oriented at different angles within the membrane-bound OEC.

The S_0 state has been studied even less than the S_3 state, especially in terms of X-ray spectroscopy. The study by Guiles et al. using chemical reductants to generate the S_0^* state[80] was repeated in similar experiments on reduced S-states by Riggs-Gelasco

et al.,[203] who also observed a decrease in the amplitude of the 2.7 Å Mn–Mn Fourier peak. This was interpreted by Riggs-Gelasco et al. as a reduction in the number of Mn–Mn vectors instead of the appearance of distance heterogeneity. However, the native S_0 state prepared using single-flash turnover has not been extensively examined using EXAFS spectroscopy due to the difficulties in collecting EXAFS spectra from single-flash saturable samples, although a preliminary report has appeared.[81]

The signal-to-noise requirement for XANES spectroscopy is lower than that required for EXAFS spectroscopy; this has enabled three different research groups to collect and analyze XANES spectra of samples in the S_0 state. Single-flash turnover experiments similar to those described in Chapter 2 have been performed by Ono et al.,[101] Roelofs et al.,[98] and Iuzzolino et al.[102] All three groups, as well as the conclusions from Chapter 2, are in agreement that Mn is oxidized during the $S_0 \rightarrow S_1$ transition. As described in Chapter 2, the XANES difference spectra (Figure 2-4B) support the assignment of this transition to a Mn(II) $\rightarrow$ Mn(III) oxidation. This is mainly due to the fact that the shape of the S_1 - S_0 difference spectrum is different from the shape of the S_2 - S_1 difference spectrum, where a Mn(III) $\rightarrow$ Mn(IV) oxidation is known to occur (see Chapter 2).

The discovery of a multiline signal in the S_0 state provides further evidence for Mn oxidation during the $S_0 \rightarrow S_1$ transition. This signal was first discovered by Messinger et al.[83] in the S_0^* state produced by chemical reduction with NH_2OH, and an essentially identical signal was subsequently discovered by Messinger et al.[45] (see Chapter 4) and by Åhrling et al.[46] in the native S_0 state generated by single-turnover flashes. A later study showed that this signal can also be generated in PS II isolated from

the cyanobacterium *Synechococcus elongatus*.[209] Unlike the Åhrling et al. study, the latter Messinger et al. study[45] incorporated a protocol to increase the sample concentration and avoid EPR spectral contamination from the S_2-state EPR multiline signal. This protocol consisted of generating the S_0 state under single-flash saturable conditions, adding the reagent FCCP (carbonyl cyanide 4-(trifluoromethoxy) phenylhydrazone) to the samples, and subsequently concentrating through centrifugation. Addition of FCCP had two major benefits. First, the S_2 and S_3 states were rapidly deactivated by FCCP to the S_1 state,[210] eliminating EPR signals from either of those two S-states. Second, FCCP accelerated the reduction of the redox-active tyrosine Y_D^{ox},[211] which decreased decay of the S_0 state into the S_1 state through oxidation by Y_D^{ox}.[120]

In this chapter, this method of preparing samples in the native S_0 state has been extended to perform EXAFS spectroscopic experiments on the S_0 state of PS II generated through single-flash turnover. These experiments show that distance heterogeneity in the 2.7 Å Mn–Mn distances most likely exists in the S_0 state, which can be explained through a combination of the presence of Mn(II) and the protonation of a di-μ-oxo-bridged Mn–Mn moiety. Furthermore, curve fitting of the EXAFS data from the S_0 state leads to the intriguing possibility that three di-μ-oxo-bridged Mn–Mn moieties may exist in the OEC instead of the two di-μ-oxo-bridged Mn–Mn moieties that are widely used in proposed structural models for the OEC.[34,36,65,66,71,74,77]

Materials and Methods

PS II membranes were prepared from fresh spinach leaves by a 2 min incubation of the isolated thylakoids with the detergent Triton X-100.[110,111] The samples were then resuspended to a chlorophyll (Chl) concentration of 6.5 mg Chl/mL in sucrose buffer (pH 6.5, 400 mM sucrose, 50 mM MES, 15 mM NaCl, 5 mM $MgCl_2$, 5 mM $CaCl_2$) and stored as aliquots at -80° C until used. Chl concentrations were calculated as described in Porra et al.[112]

To prepare samples enriched in the S_0 state, a frequency-doubled Nd-YAG laser system (Spectra-Physics PRO 230-10, 800 mJ/pulse at 532 nm, 9 ns pulse width) was used to illuminate the PS II samples. The laser was operated continuously at 10 Hz, and flashes were selected using an external shutter (model LSTX-Y3, nm Laser Products, Inc.).

Before flash illumination, the PS II membranes were diluted to a concentration of 1 mg Chl/mL in sucrose buffer, and 3 mL of this solution was transferred in darkness into each of 20 tissue culture flasks (Falcon 3014, 50 mL, 25 cm^2 growth area) that were kept on ice. The Nd-YAG beam was redirected and diffused such that the laser beam could illuminate the entire growth area of the flask from below. Sample illumination under these conditions was proven to be saturating by separate experiments in which the Chl concentration was reduced to 0.5 and 0.25 mg Chl/mL, and no increase in the yield of the S_0 state formed in 3-flash (3F) samples relative to the experiments described herein was seen (data not shown). Each sample was given one pre-flash and was dark-adapted for 90 minutes on ice.

After dark-adaptation, PPBQ (phenyl-1,4-benzoquinone; 50 mM in MeOH) was added to each flask to a final concentration of 25 µM, and 3 flashes were applied at 1 Hz frequency to each flask. Immediately after the flashes, FCCP (carbonyl cyanide 4-(trifluoromethoxy) phenylhydrazone; 5 mM in MeOH) was added to each flask to a final concentration of 1 µM. This accelerated the deactivation of the S_2 and S_3 states of PS II to the S_1 state[210] and reduced Y_D^{ox}, the stable tyrosine radical of PS II.[211] The latter reaction essentially eliminates the main path for the decay of the S_0 state, which is the oxidation of the S_0 state to the S_1 state by Y_D^{ox}.[120] This reaction has a half-life of 30 minutes at 5° C.[177] In addition to FCCP, MeOH was added to each flask to a final concentration of 3 % v/v, which enabled the detection of the S_0 EPR multiline signal in these samples.[45,46,83] The samples were then collected and centrifuged at 4° C for 30 min at 48000x *g*. The concentrated PS II membranes were then put into Lexan sample holders (22 x 3.2 x 0.8 mm inner dimensions) and were frozen at 77 K for EPR and X-ray experiments. It took a total of 50 minutes to complete the protocol from the point of applying three flashes to the sample and freezing the samples at 77 K. Control samples in the S_1 state were prepared in an identical fashion except that the application of 3 laser flashes to each tissue culture flask was not performed.

EPR spectra were collected on a Varian E-109 spectrometer with an E-102 microwave bridge and stored using Labview running on a Macintosh G3 computer. Samples were maintained at cryogenic temperatures using an Air Products Heli-tran liquid helium cryostat. Spectrometer conditions were as follows: S_2 EPR multiline signal: 2700 ± 2000 G scan range, 6300 gain, 30 mW microwave power, 8 K temperature, 32 G modulation amplitude, 100 kHz modulation frequency, 4 min/scan, 1 scan per sample, 0.25 sec time constant, 9.26 GHz microwave frequency. MLS amplitudes were

determined from the low-field and high-field peak-to-trough measurements for each designated peak in Figure 3-2. PS II centers in the S_1 state were advanced to the S_2 state by continuous illuminations performed at low temperature. The illuminations were performed with a 600 W lamp, and a 5 % w/v $CuSO_4$ solution was used as an IR filter. Samples were placed in a tall test tube which was suspended in a 200 K dry ice/ethanol bath. An unsilvered dewar contained the 200 K bath and enabled the low-temperature illuminations.

XANES and EXAFS spectra were recorded on beamline 7-3 at SSRL (Stanford Synchrotron Radiation Laboratory). The synchrotron ring SPEAR was operated at 3.0 GeV at 50 – 100 mA beam current. Energy resolution of the unfocused incoming X-rays was achieved using a Si(220) double-crystal monochromator, which was detuned to 50 % of maximal flux to attenuate harmonic X-rays. A N_2-filled ion chamber (I_0) was mounted in front of the sample to monitor incident beam intensity. An incident X-ray beam of 1.4 mm x 11 mm dimensions (1 mm x 11 mm for XANES) with a flux of approximately 3.5×10^{10} photons/sec was used for the EXAFS experiments; the total photon flux on the sample was 1.6×10^9 photons/sec/mm^2 of sample. The samples were placed at an angle of 45° relative to the X-ray beam and were kept at 10 ± 1 K in a He atmosphere at ambient pressure using an Oxford CF-1208 continuous-flow liquid He cryostat. The X-ray absorption spectra were collected as fluorescence excitation spectra[114] using a 13-element energy-resolving detector from Canberra Electronics,[115] and were referenced by I_0. Typical counts in the Mn fluorescence window for the central channel were 200 counts/sec at 6500 eV (below the Mn K-edge) and 1300 counts/sec at 6600 eV (above the Mn K-edge).

XANES spectra were collected at 0.2 eV/point from 6520 to 6580 eV with a collection time of 3 sec per point, and at 10 eV/point from 6580 eV to 7100 eV with a collection time of 1 sec per point. The EXAFS spectra were collected at 3 eV/point from 6400 to 6540 eV with a collection time of 1 sec per point, 0.25 eV/point from 6540 to 6550 eV with a collection time of 1 sec per point, and at 1 eV/point from 6550 eV to 6576 eV with a collection time of 1 sec per point. The EXAFS region was collected with points evenly spaced every 0.05 $Å^{-1}$ in *k*-space from 2.05 $Å^{-1}$ to 12 $Å^{-1}$, with E_0 assigned as 6563 eV. The time of collection was weighted using a cubic function from a minimum of 1 sec per point at low *k* values to a maximum of 10 sec per point at high *k* values.

Two sample regions of 1.4 mm height were used for the EXAFS scans, and 8 scans were collected from each separate region. To monitor radiation damage, XANES spectra were collected before and after the EXAFS scans using a sample region of 1 mm height which included the sample region used for the EXAFS scans. The samples were protected with a shutter from the beam at all times unless a measurement was in progress. Collection of an energy-reference spectrum was achieved by placing a $KMnO_4$ sample between two N_2-filled ion chambers, I_1 and I_2, which were positioned behind the PS II sample, and collecting a $KMnO_4$ absorption spectrum concurrently with PS II data collection. The narrow pre-edge line (FWHM • 1.7 eV) at 6543.3 eV was subsequently used for energy calibration.[116] For the EXAFS spectra, 16 scans (8 scans per region, 2 regions per sample) were averaged per sample for each of six 3F samples and six control samples in the S_1 state.

After removal of a linear background, the XANES spectra were normalized by fitting a quadratic polynomial to the EXAFS region (6570 – 7100 eV) and adjusting the value of the extrapolated polynomial to 1.0 at 6563 eV. Second derivatives were

calculated between 6535 and 6575 eV for each point of the XANES spectra by fitting a cubic polynomial to a range of ± 3 eV around that point and computing the 2nd derivative of the polynomial.

Data reduction of the EXAFS spectra was performed by removal of a linear pre-edge background, followed by normalization of the edge jump by fitting a quadratic polynomial to the EXAFS region (6570 – 7100 eV) and assigning the intensity of the extrapolated polynomial to 1.0 at 6563 eV. The resulting spectra were then divided by the tabulated free-atom absorption values from McMaster et al.[212] Residual background removal was obtained by fitting a quadratic polynomial to the region between 6750 eV and 7100 eV and subtracting the resulting polynomial from the entire EXAFS spectrum. Conversion of EXAFS spectra into *k*-space was performed using the formula in Eq. 3-1:

$$k\ (\text{Å}^{-1}) = \sqrt{\frac{2m_e}{\hbar^2}(E - E_0)} \qquad \text{Eq. 3-1}$$

where k is the photoelectron momentum (Å^{-1}), also referred to as the photoelectron wavevector; m_e is the electron mass; $\hbar = h/2$, where h is Planck's constant, and E_0 is the threshold energy for photoelectron production. Although the value of E_0 was fixed at 6563 eV for the *k*-space conversion, subsequent curve-fitting using the EXAFS equation (Eq. 3-2) treated E_0 as a variable parameter. The *k*-space spectra were then multiplied by k^3 to generate k^3-weighted EXAFS spectra; this largely offsets the damping of the EXAFS oscillations seen in the non-k^3-weighted *k*-space spectra. As shown below in Eq. 3-2, this is mainly due to the $1/(kR^2)$ amplitude dependence of the EXAFS oscillations and the fact that the *ab initio* amplitude function $f_{eff_j}(\pi, k, R_j)$ is dependent roughly on $1/k^2$.[193] Because low-frequency background contributions were apparent in the Fourier

transforms of the uncorrected spectra as peaks at $R' < 1$ Å, further background removal of a 5-domain spline in k^3-space was necessary.

To simplify the curve-fitting procedure, the individual Fourier peaks I, II, and III were isolated and fit separately by applying a Hamming window to the first and last 15 % of the chosen range, leaving the middle 70 % untouched. In addition, the Fourier peaks were isolated and fit in pairs (I + II, II + III) to minimize possible distortions from isolating closely spaced Fourier peaks separately. However, as mentioned by Latimer et al.[207], there is a tradeoff in doing this, because the fits to pairs of Fourier peaks are dominated by the contribution from the larger peak, making it difficult to reliably extract information from the smaller Fourier peak. This is particularly relevant for fits to peaks II and III.

Curve fitting was performed using *ab initio*-calculated phases and amplitudes from the program FEFF 5.05 from the University of Washington.[197,213] These *ab initio* phases and amplitudes were used in the EXAFS equation,[214-217] shown as Eq. 3-2:

$$\chi(k) = S_0^{\,2} \sum_j \frac{N_j}{kR_j^{\,2}} f_{eff_j}(\pi, k, R_j) e^{-2\sigma_j^{\,2}k^2} e^{-2R_j/\lambda_j(k)} \sin(2kR_j + \phi_{ij}(k)) \qquad \text{Eq. 3-2}$$

$S_0^{\,2}$ is an amplitude reduction factor due to shake-up/shake-off processes at the central atom(s). This factor was set to 0.85 for all fits based on fits to model compounds.[73] The neighboring atoms to the central atom(s) are then divided into j shells, with all atoms with the same atomic number and distance from the central atom grouped into a single shell. Within each shell, the coordination number N_j denotes the number of neighboring atoms in shell j at a distance of R_j from the central atom. $f_{eff_j}(\pi, k, R_j)$ is the *ab initio* amplitude function for shell j, and the Debye-Waller term $e^{-2\sigma_j^{\,2}k^2}$ accounts for damping due to static and thermal disorder in absorber-backscatterer distances. A larger Debye-Waller

factor σ_j reflects increased disorder, and leads to an exponential damping of the EXAFS oscillations. The mean free path term $e^{-2R_j/\lambda_j(k)}$, which depends on *k*, reflects losses due to inelastic losses in the scattering process, where $\lambda_j(k)$ is the electron mean free path.[217] $\lambda_j(k)$ was calculated by *ab initio* methods with FEFF 5.05. The oscillations in the EXAFS spectrum are reflected in the sinusoidal term $\sin(2kR_j + \phi_{ij}(k))$, where $\phi_{ij}(k)$ is the *ab initio* phase function for shell *j*. This sinusoidal term shows the direct relationship between the frequency of the EXAFS oscillations in *k*-space and the absorber-backscatterer distance.

Eq. 3-2 was used to fit the experimental Fourier isolates using *N*, *R*, and σ^2 as variable parameters. No firm theoretical basis exists to guide the choice of E_0 for Mn K-edges; thus, uncertainty in E_0 translates into uncertainty in *k*-space values, as shown in Eq. 3-1. Therefore, E_0 was also treated as a variable parameter. To reduce the number of free parameters in the fits, the value of E_0 was constrained to be equal for all shells in the fit. This was shown by O'Day et al.[218] to be a valid constraint when using FEFF phases and amplitudes.

N values are defined as shown in Eq. 3-3:

$$N = \frac{\text{total number of Mn} - \text{backscatterer vectors}}{\text{number of Mn atoms per OEC}} \qquad \text{Eq. 3-3}$$

Hence, coordination numbers are evaluated on a per Mn basis and are dependent on the stoichiometry of Mn atoms in the OEC. It is well established that an active OEC contains four Mn atoms;[200,219-230] a report of six Mn per PS II[231] was most likely due to an uncorrected high residual Mn content in inactive centers present in the samples.[14] On a 4 Mn/PS II basis, *N* values for Mn–Mn interactions in the OEC come in multiples of 0.5,

because each Mn–Mn interaction contains two Mn–backscatterer interactions. Other Mn–backscatterer interactions come in multiples of 0.25, *i.e.* an *N* value of 2 in a Mn–O shell is interpreted as two O neighbors to each Mn atom.

Fit quality was evaluated using two different fit parameters, Φ and ε^2. Φ is described in Eq. 3-4:

$$\Phi = \sum_{1}^{N} \left(\frac{1}{s_i} \right)^2 [\chi^{expt}(k_i) - \chi^{calc}(k_i)]^2 \qquad \text{Eq. 3-4}$$

where *N* is the total number of data points collected, $\chi^{expt}(k_i)$ is the experimental EXAFS amplitude at point *i*, and $\chi^{calc}(k_i)$ is the theoretical EXAFS amplitude at point *i*. The normalization factor s_i is given by Eq. 3-5:

$$\frac{1}{s_i} = \frac{k_i^3}{\sum_{j}^{N} k_j^3 \left| \chi^{expt}(k_j) \right|} \qquad \text{Eq. 3-5}$$

The ε^2 error takes into account the number of variable parameters *p* in the fit and the number of independent data points N_{ind}, as shown in Eq. 3-6:[232,233]

$$\varepsilon^2 = \left\lceil \frac{N_{ind}}{N_{ind} - p} \right\rceil N^{-1} \Phi \qquad \text{Eq. 3-6}$$

N is the total number of data points collected, and the number of independent data points N_{ind} is estimated from the Nyquist sampling theorem, as shown in Eq. 3-7:

$$N_{ind} = \frac{2 \Delta k \Delta R}{\pi} \qquad \text{Eq. 3-7}$$

•***k*** is the *k*-range of the data (3.5 – 11.5 Å^{-1}) and •***R*** is the width of the Fourier-filtered peak in Å. ε^2 provides a gauge of whether the addition of another shell to the fit is

justified. If, upon addition of a second shell, the normalized fit error Φ does not decrease sufficiently to statistically justify the inclusion of the additional shell, ε^2 will increase.

The most reliable parameter from the fit is definitely the Mn–backscatterer distance *R*. Typical errors for *R* values are in the range of 2 %, while errors in *N* values are significantly higher, often up to 30 %.[234] Therefore, when examining the results of the fits to the EXAFS oscillations, more emphasis should be placed on the more accurate *R* values than the less accurate *N* values.

Results

EPR

It is critical that an independent determination of the S-state distribution of the 3F samples is performed using EPR spectroscopy; the deconvolution of the 3F XANES and EXAFS spectra to obtain the spectra of the 'pure' S_0 state is dependent on a proper EPR characterization. Because FCCP was added to the samples immediately after the flashes, any centers that remain in the S_2 or S_3 states after the flash treatment are rapidly deactivated to the S_1 state,[210] as explained in the Materials and Methods section. Therefore, the calculated S-state distribution will contain PS II centers in only the S_0 and S_1 states. In separate experiments, it was discovered that increasing the FCCP concentration 10-fold (to 10 μM) caused a ~25 % reduction of the S_1 state in the dark to the S_0 state and possibly the S_{-1} state (data not shown). To confirm that the FCCP concentration used in this study (1 μM) was not of sufficient concentration to cause reduction of the S_1 state, the S_2-state EPR multiline signal was measured from parallel S_1-state samples with and without FCCP that had been continuously illuminated at 200 K. The fact that identical normalized S_2-state EPR multiline signal amplitudes were obtained from both types of samples provides further confidence in the EPR characterization of the S-state distribution.

During the preparation of the XAS samples, eight identical 3F samples and eight identical S_1-state samples were prepared. From these 16 samples, two S_1-state samples and two 3F samples were set aside for EPR characterization. Because the samples that were set aside for EPR characterization are identical to the respective samples used in the

XAS experiments, the S-state distribution that was determined for the samples characterized by EPR can also be used to deconvolute the XANES and EXAFS spectra for the XAS samples.

The S_2-state multiline EPR signal generated by continuous illumination (CI) at 190 K of the 3F and S_1-state samples is shown in Figure 3-2. At 190 K, all S-state transitions aside from the $S_1 \rightarrow S_2$ transition are kinetically blocked.[121] This means that, in the 3F sample, the S_0 state cannot advance to the S_1 state during this illumination procedure; thus the 3F CI samples will have a smaller normalized S_2-state multiline EPR signal than will the S_1-state CI samples. In addition, because the spectra shown in Figure 3-2 are difference spectra (after CI - before CI), the presence of the S_0-state multiline EPR signal,[45,46,83] which was visible in the 3F samples before CI (data not shown), will not affect the quantitations of the S_2-state multiline EPR signal. To correct for differences in sample volume, the measured S_2-state multiline EPR signals for each sample were normalized by the magnitude of their respective non-heme Fe^{2+} signal.

The results of the EPR characterization study are shown in Table 3-1. Because one of the S_1-state samples generated noisy EPR spectra, it was not used for the calculations shown in Table 3-1. The ratio of the induced S_2-state multiline EPR signal in the 3F sample relative to that induced in the control S_1-stae sample (50 %) corresponds to the percentage of centers originally in the S_1 state in the 3F sample. Therefore, the S-state distribution assigned to the samples in the current study is 50 % S_0, 50 % S_1. This S-state distribution will be used in subsequent deconvolutions of the XANES and EXAFS spectra of 3F samples.

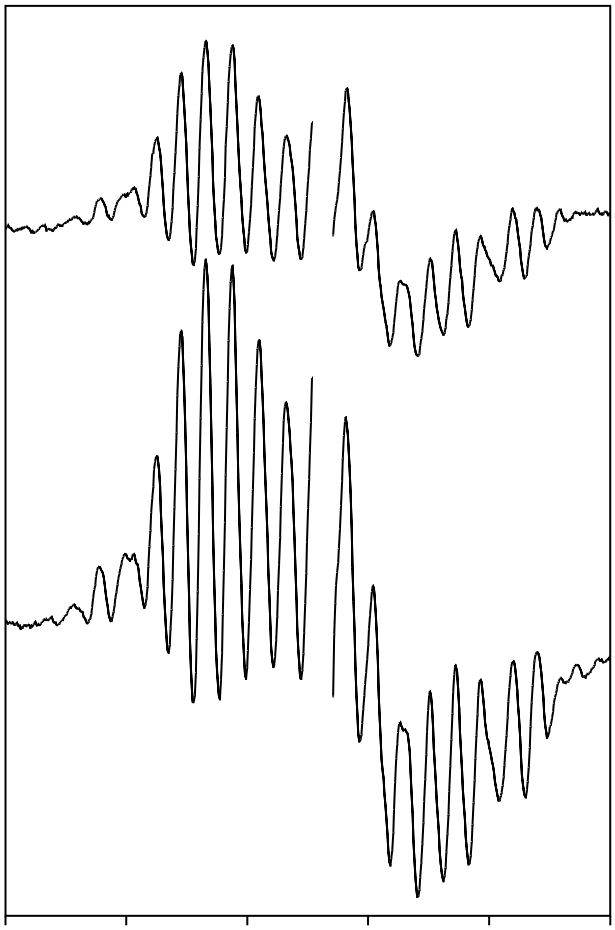

Figure 3-2: Use of the S_2-state multiline EPR signal to quantitate the S_0:S_1 ratio in 3F samples. A 3F sample and a control S_1-state sample were continuously illuminated (CI) at 200 K for 60 min; the spectra shown above are light - dark spectra. The illumination temperature was low enough that only the $S_1 \rightarrow S_2$ transition could proceed; the $S_0 \rightarrow S_1$ transition was cryogenically blocked. The amplitude of the S_2 multiline EPR signal was then measured using the marked peaks. The central region corresponding to Y_D^{ox} has been deleted for clarity. The ratio of the induced S_2-state multiline EPR signal in the 3F sample relative to that induced in the control S_1 sample (50 %) corresponds to the percentage of centers in the S_1 state in the 3F sample before CI. The addition of FCCP ensures that the only S-states in the 3F sample are the S_0 state and the S_1 state; therefore, the remaining 50 % of the centers are poised in the S_0 state. This S-state distribution is used when deconvoluting the EXAFS spectra of the 3F samples.

Table 3-1: S-state distribution results from measurements of the induced S_2-state multiline EPR signal in 3F samples and control S_1-state samples. The spectra used in the calculation of the values for Sample S_0 #2 are shown in Figure 3-2.

Sample	3F CI / S_1 CI	S_0-state population
S_0 #1	0.487	51.3 %
S_0 #2	0.498	50.2 %

Using samples with 9.5 mg Chl/mL, a greater S_0-state percentage (65 % according to Table 2-2) was obtained in the 3F samples in the experiments described in Chapter 2 than the S_0-state percentage reported in the current chapter. The smaller S_0-state percentage is most likely due to the oxidation of some of the centers in the S_0 state by external oxidants during the 30 min centrifugation and subsequent sample handling or through oxidation by Y_D^{ox} residues which have not yet been reduced. However, the slightly lower percentage of centers in the S_0 state for the S_0-state EXAFS experiments is necessary to obtain highly concentrated PS II samples for EXAFS studies.

XANES

The primary purpose of the XANES spectra was to monitor the progress of photoreduction during the EXAFS experiments. This was performed by collecting two XANES scans before and after eight EXAFS scans and monitoring the shift in the 2^{nd}-derivative IPE value between the sets of XANES scans. For the 3F samples and the S_1-state samples, the effects of photoreduction were quite small. The 2^{nd}-derivative IPE values for the S_1-state samples and the 3F samples shifted to lower energy by 0.2 –

0.4 eV. Although these shifts are slightly larger than those seen in the flash studies detailed in Chapter 2, the effects on the EXAFS data are expected to be far less than the effects on the XANES data. Figure 3-17 in the Appendix shows that there is very little difference in the k^3-space spectra if the 1st set of four EXAFS scans from each region of the sample are compared to the 2nd set of four EXAFS scans from each region of the sample. In addition, there was no discernible difference in the fits to the EXAFS data for the two spectra shown in Figure 3-17 (data not shown).

The XANES spectra collected during the S_0-state EXAFS experiments are shown in Figure 3-3A, and the 2nd derivatives of the XANES spectra are shown in Figure 3-3B. The shift in the 2nd-derivative IPE values is 2.5 eV, which is slightly larger than the 2.1 eV shift for the flash studies shown in Chapter 2. However, the shapes of the XANES 2nd-derivative spectra shown in this chapter are similar to those shown in Chapter 2 as well as to those reported in Roelofs et al.[98]

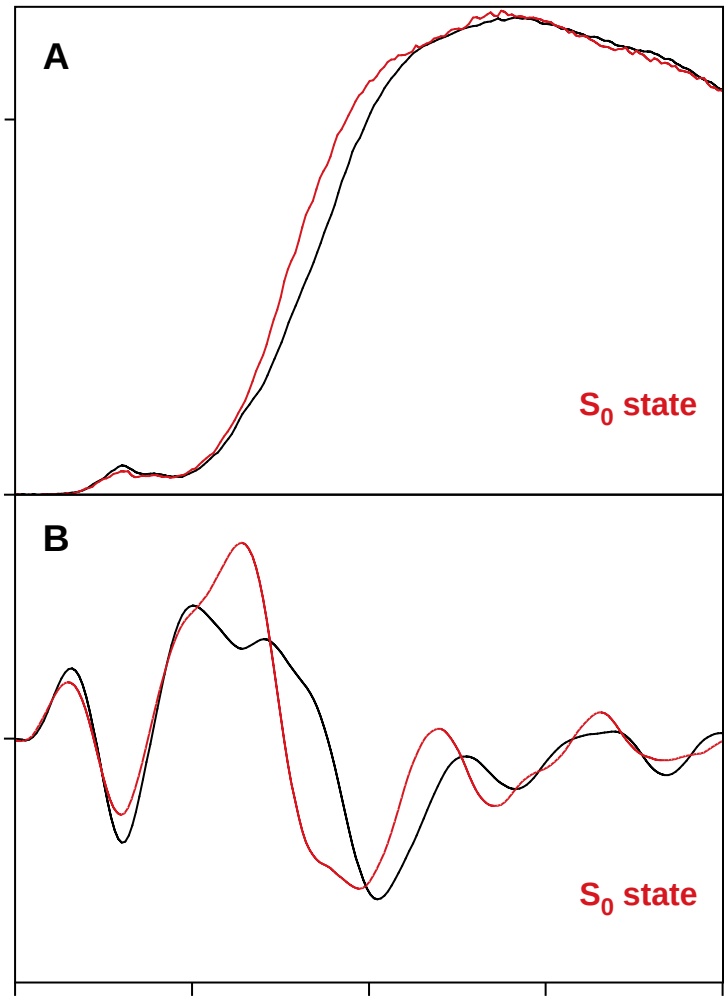

Figure 3-3: XANES spectra of samples in the S_0 and S_1 states. **(A)** The S_1-state XANES spectrum shown above (average of 10 scans) was subtracted from the 3F XANES spectrum (average of 10 scans) to generate the S_0-state spectrum that is shown. The deconvolution information from Figure 3-2 and Table 3-1 was used for the subtraction. **(B)** 2^{nd} derivatives of the XANES spectra of samples in the S_0- and S_1-states. A polynomial of 6 eV width fit around each point was used for the analytical calculation of the 2^{nd}-derivative spectra. The IPE value for the S_0-state spectrum is 6550.2 eV, and the IPE value for the S_1-state spectrum is 6552.7 eV.

k^3-space spectra and Fourier transforms

Figure 3-4 shows the average Mn K-edge EXAFS spectra from six 3F samples and six samples in the S_1 state. Deconvolution of the 3F spectrum using the S-state distribution calculated from Figure 3-2 (shown in Table 3-1 as 50 % S_0, 50 % S_1) yields the EXAFS spectrum of the pure S_0 state, which is also shown in Figure 3-4. The deconvolution was performed using normalized *E*-space spectra before conversion into

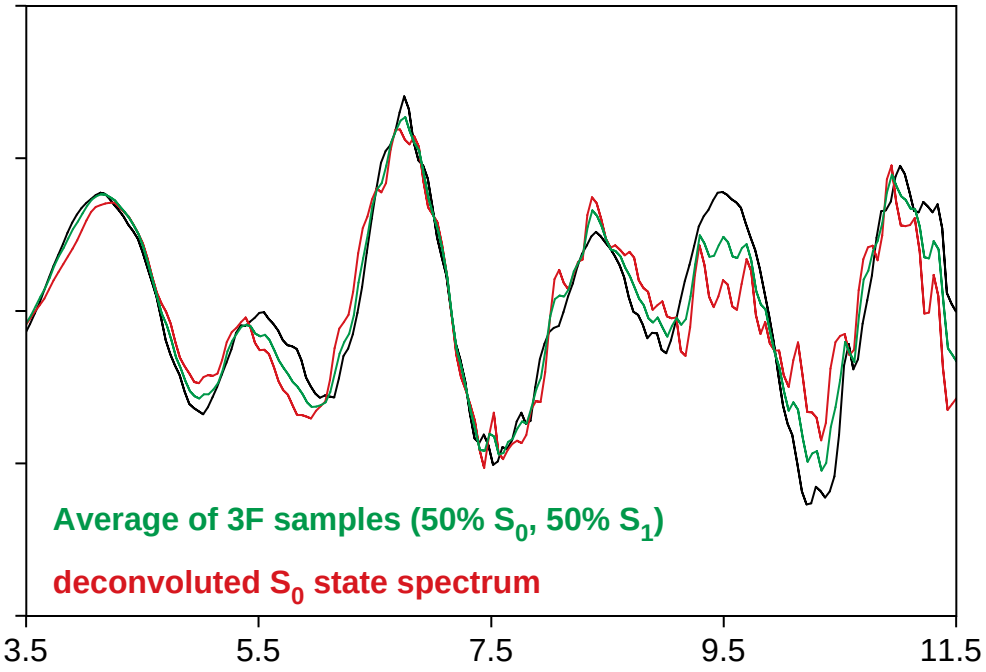

Figure 3-4: Average Mn K-edge EXAFS spectra from samples given 3 flashes (green) and samples in the S_1 state (black). Six 3F samples and six S_1-state samples were averaged for each spectrum. The deconvoluted S_0-state spectrum shown above in red was calculated from the 3F spectrum and the S_1-state spectrum using the quantitations from Figure 3-2 and Table 3-1 (50 % S_0, 50 % S_1).

k^3-space. If the deconvolution was performed after both the 3F spectrum and the S_1 state were converted into *k*-space, the results were virtually identical (see Figure 3-15 and Figure 3-16 in the Appendix). The most noticeable change between the S_0-state and S_1-state spectra is that the resolution of EXAFS oscillations in the S_1 state between $k = 8.5$ and 11 $Å^{-1}$ is decreased in the S_0 state. This loss of resolution can be explained by an increase in distance heterogeneity in the S_0 state relative to the S_1 state, which leads to destructive interference at higher *k* values of EXAFS oscillations of slightly different frequencies. This phenomenon has also been seen in other S-states that have heterogeneity in the Mn–Mn distances, such as the S_0^* state,[80] the S_2–$g = 4.1$ state,[235] the NH_3-treated S_2 state,[236] the F^--treated S_2 state,[237] and the S_3 state.[69,161] Each of the six 3F samples that were used to generate the average spectrum shown in Figure 3-4 was deconvoluted separately using the average S_1-state EXAFS spectrum to generate six independent S_0-state EXAFS spectra; the results are shown in Figure 3-5. This figure shows that the loss of resolution of the EXAFS oscillations that is seen in the average spectrum is also seen in the spectra from the six individual samples.

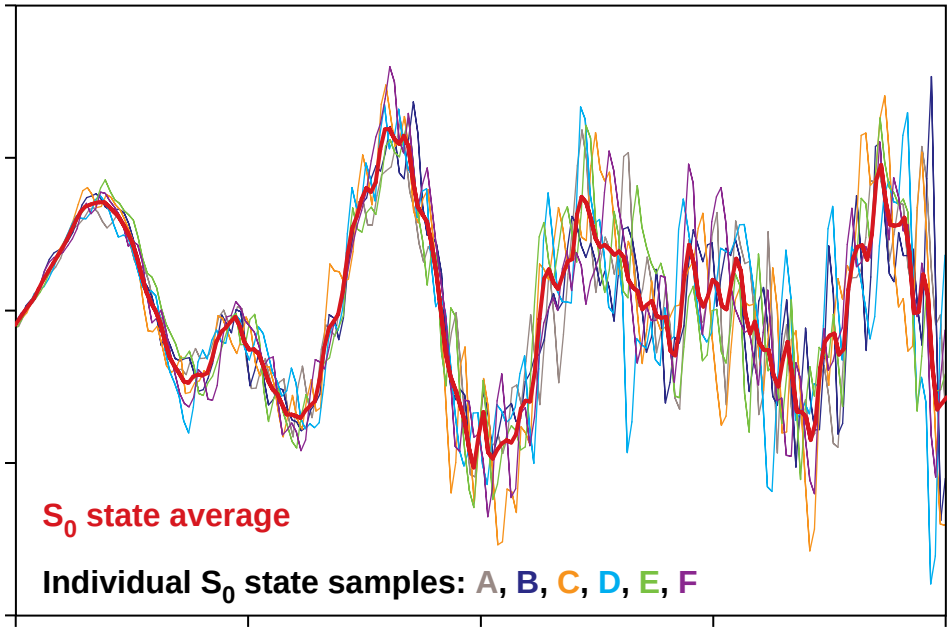

Figure 3-5: Mn K-edge EXAFS spectra of the S_0 state from six separate 3F samples. Each 3F spectrum was individually deconvoluted as described in Figure 3-4 to generate the six pure S_0-state spectra shown above. The S_0-state spectrum from Figure 3-4 is shown as a red line for comparison.

By performing a Fourier transform on the k^3-space spectra, a graphical representation of the environment surrounding the Mn atoms in PS II is obtained as a radial distribution function.[196] Figure 3-6 shows the Fourier transforms from the 3F, S_0-state, and S_1-state k^3-space spectra shown in Figure 3-4. Three prominent peaks, labeled as Peaks I, II, and III in Figure 3-6, exist in the Fourier transforms. Peak I corresponds to first-shell Mn–O interactions arising from μ-oxo-bridging and terminal ligands. Peak II arises from Mn–Mn backscattering in di-μ-oxo-bridged Mn_2 moieties. Peak III contains contributions from both mono-μ-oxo-bridged Mn–Mn and mono-μ-oxo-bridged Mn–Ca moieties.

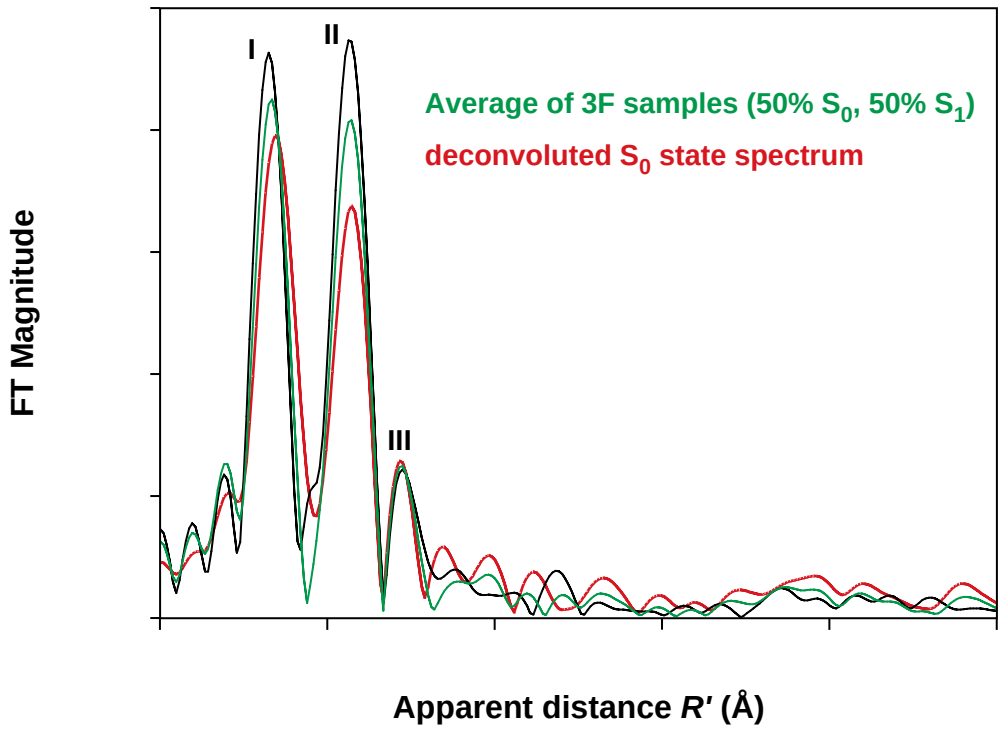

Figure 3-6: Fourier transforms of the average Mn K-edge EXAFS spectra shown in Figure 3-4. The Fourier transform corresponding to the S_1 state is shown in black, the Fourier transform corresponding to the 3F samples is shown in green, and the Fourier transform corresponding to the pure S_0 state is shown in red.

Although Peak III is relatively invariant between the S_0 and S_1 states, Peaks I and II show significant differences between the S_0 and S_1 states. Peak I is at a longer apparent distance and has a slightly lower peak amplitude in the S_0 state relative to the S_1 state. This implies some sort of increase in distance and/or distance heterogeneity in the Mn–O distances in the S_0 state relative to the S_1 state. In the S_0 state, Peak II is approximately 30 % lower in amplitude than in the S_1 state. This consequence of the aforementioned loss in resolution of EXAFS oscillations in the *k*-space spectrum of the S_0 state was also seen in the previously mentioned studies of other S-states that have heterogeneity in the Mn–Mn distances.[69,80,161,235-237] This provides compelling evidence that structural changes

are occurring during the $S_0 \rightarrow S_1$ transition that reduce the heterogeneity of the 2.7 Å Mn–Mn distances.

Curve fitting of EXAFS spectra

Although the Fourier transforms shown in Figure 3-6 provide the basis for drawing compelling qualitative conclusions about structural changes during the $S_0 \rightarrow S_1$ transition, reliable quantitative results can be obtained by fitting the experimental data using the EXAFS equation (Eq. 3-2), as described in the Materials and Methods section. The Fourier isolates of Peaks I, II, and III are shown in Figure 3-7, Figure 3-8, and Figure 3-9, respectively; these isolates show the k^3-space contributions to the Fourier

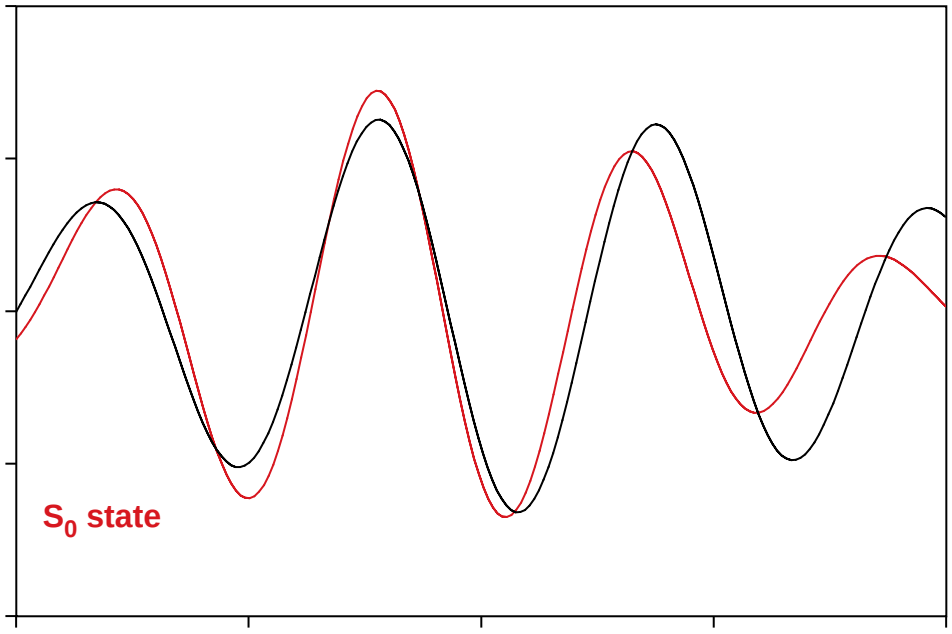

Figure 3-7: Fourier isolates from Peak I of the Fourier transforms shown in Figure 3-6. The S_0 state is shown in red and the S_1 state is shown in black. The difference in the frequency of the EXAFS oscillations between the two S-states is evident.

peak of interest. The increase in the apparent distance of Peak I in the Fourier transforms of the S_0 state relative to the S_1 state is evident in the increase in frequency of the EXAFS oscillations in the S_0-state Fourier isolate relative to that of the S_1-state Fourier isolate, as shown in Figure 3-7. For Peak II, the Fourier isolates in Figure 3-8 show that the amplitude of the S_0-state Fourier isolate is significantly smaller than the amplitude of the corresponding S_1-state Fourier isolate. Because the amplitude envelope for the S_0-state Fourier isolate is significantly different from that of the S_1 state, it is unlikely that the decrease in Peak II amplitude can be explained by a decrease in the number of Mn–Mn interactions in the S_0 state relative to the S_1 state, which should not change the amplitude envelope. A more likely explanation, which was explained earlier, is that this could indicate the presence of distance heterogeneity in the Mn–Mn distances in the S_0 state. If the •*R* value is smaller than the theoretical resolution limit of 0.14 Å (see Appendix for details), the observed damping of the amplitude function would occur, although the fit results shown in the Curve Fitting section show that the calculated distance separation from the fits is close to the theoretical resolution limit (*vide infra*). In order to see a beat in the Fourier isolates at the proposed distance separation in the S_0 state, the EXAFS spectrum would have to be collected to higher *k* values. Unfortunately, the K-edge absorption of Fe occurs at a *k* value of approximately 12 $Å^{-1}$. Because there are three Fe atoms per OEC (two copies of cytochrome b_{559} and one non-heme Fe^{2+})[238] and extra Fe can be present in the preparation depending on isolation conditions,[226] this eliminates the possibility of collecting data at higher *k* values.

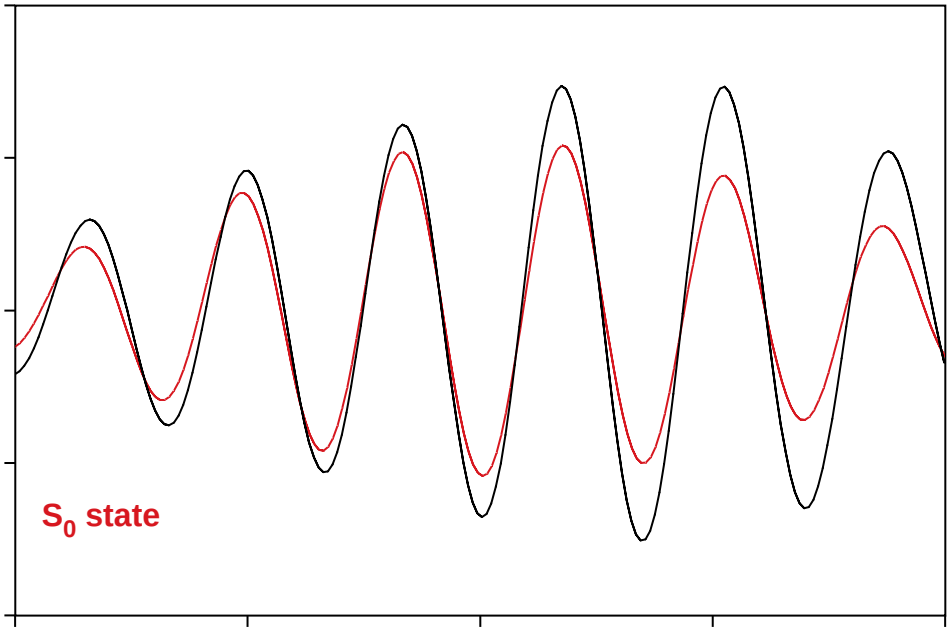

Figure 3-8: Fourier isolates from Peak II of the Fourier transforms shown in Figure 3-6. The S_0 state is shown in red and the S_1 state is shown in black. The difference in the amplitude envelope of the EXAFS oscillations between the two S-states is evident, and can be explained by the presence of two different Mn–Mn distances with a small (< 0.2 Å) separation in distance.

The Fourier isolates from Peak I and Peak II from each individual S_0-state data set are shown in Figure 3-10 and Figure 3-11, respectively. These Fourier isolates show that the trends seen in the Fourier isolates generated from the Fourier transform of the average S_0-state spectrum are also seen the Fourier isolates generated from each individual sample. Specifically, the differences in the amplitude envelope and frequency of the S_0 and S_1-state Peak I Fourier isolates shown in Figure 3-7 are also seen in the individual sample spectra shown in Figure 3-10. In addition, the differences in the amplitude envelope of the S_0 and S_1-state Peak II Fourier isolates shown in Figure 3-8 that was interpreted as possible distance heterogeneity are also seen in the individual sample

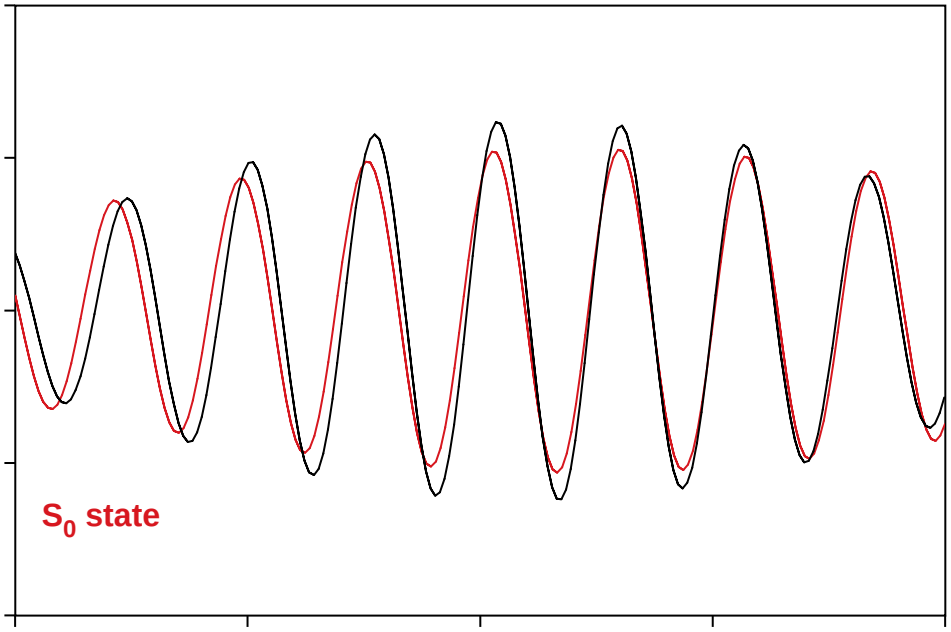

Figure 3-9: Fourier isolates from Peak III of the Fourier transforms shown in Figure 3-6. The S_0 state is shown in red and the S_1 state is shown in black.

spectra shown in Figure 3-11. Even before the curve-fitting procedures are applied, the consistency mentioned above greatly increases confidence in the conclusions.

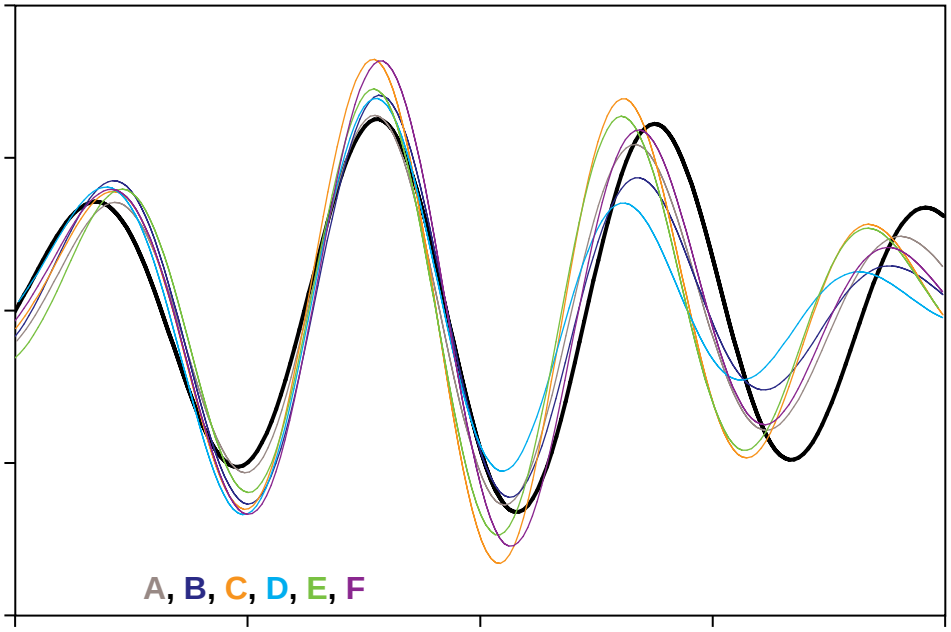

Figure 3-10: Fourier isolates from Peak I of the Fourier transforms generated from each of the six individual S_0-state spectra shown in Figure 3-5. The average S_1-state spectrum is shown in black. The difference in the amplitude envelope frequency of the EXAFS oscillations between the two S-states is evident.

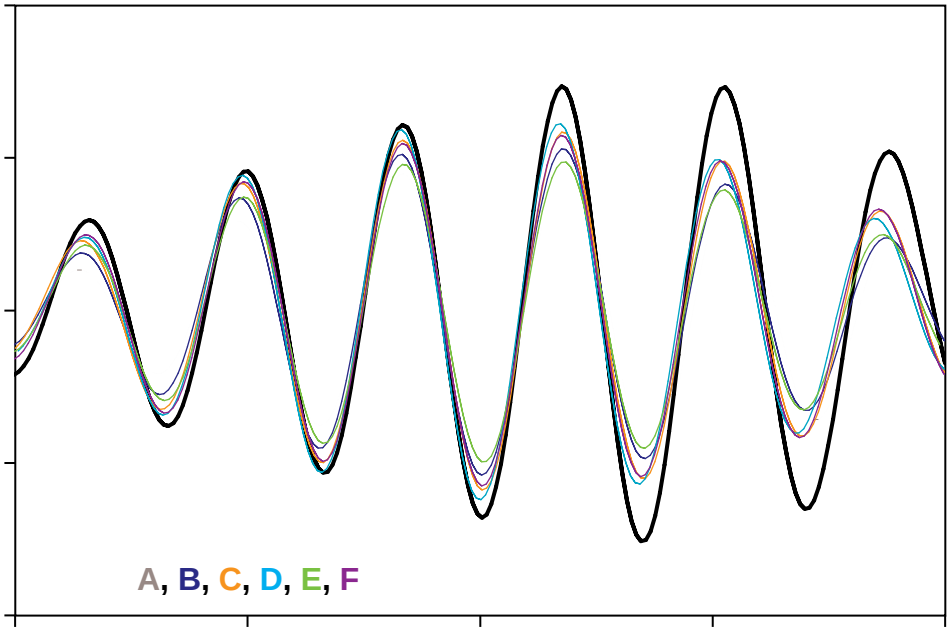

Figure 3-11: Fourier isolates from Peak II of the Fourier transforms generated from each of the six individual S_0-state spectra shown in Figure 3-5. The average S_1-state spectrum is shown in black. The difference in the amplitude envelope of the EXAFS oscillations between the two S-states is evident, and can be explained by the presence of two different Mn–Mn distances in the S_0 state with a small (< 0.2 Å) separation in distance.

Peak I

Fits to Peak I are known to be dominated by the short 1.8 Å bridging Mn–O distances,[72] although more terminal Mn–O distances exist than bridging Mn–O distances. Using one Mn–O shell, it is not surprising that Fits #1 – 8 in Table 3-2 show that the S_0 state is best fit by a 1.86 Å Mn–O distance. This is a longer distance than the corresponding fit to the S_1-state spectrum (Fit #9 in Table 3-2), which is 1.83 Å. Furthermore, the Debye-Waller disorder parameter is larger in the S_0 state relative to the S_1 state by a factor of 2 – 3. This indicates an increase in disorder in the Mn–O distances

in the S_0 state relative to the S_1 state, which could be due to either an increase in overall disorder in Mn–O distances or the presence of longer terminal Mn–O distances in the S_0 state. The latter hypothesis would be consistent with the presence of a Mn(II) atom in the S_0 state, which would be expected to have longer Mn–O bridging and terminal distances.[239-241]

To account for the two different types of Mn–O distances (bridging and terminal), two-shell fits to Peak I were attempted, although some previous studies have been unable to detect the presence of the terminal Mn–O shell.[73] Fits #10 and #11 in Table 3-2 show one fit minimum for a 2-shell fit to Peak I for the S_0 state and the S_1 state. A significant improvement in fit error Φ is seen for the two shell fit. However, these two-shell fit minima are quite shallow; essentially identical fit error values were obtained if the *N* and

Table 3-2: One- and two-shell simulations of Fourier peak I of the S_0-state samples. Fit #7 corresponds to the average of the fit parameters from Fits #1 – 6, while Fits #8 and #10 are fits to the average S_0-state spectrum.

Fit #	sample	shell	*R* (Å)	*N*	σ^2 (Å^2)	$\bullet E_0$ [b]	Φ (x 10^{-3})	ε^2 (x 10^{-5})
1	S_0 A	Mn–O	1.85	2.5[c]	0.003	-20	0.89	0.81
2	S_0 B	Mn–O	1.85	2.5[c]	0.005	-19	0.53	0.45
3	S_0 C	Mn–O	1.87	2.5[c]	0.003	-18	0.64	0.54
4	S_0 D	Mn–O	1.87	2.5[c]	0.006	-17	0.41	0.31
5	S_0 E	Mn–O	1.88	2.5[c]	0.004	-14	0.74	0.70
6	S_0 F	Mn–O	1.85	2.5[c]	0.004	-20	0.65	0.53
7	Average	Mn–O	1.86	2.5[c]	0.004	-18	0.64	0.56
8	S_0 Grand Add	Mn–O	1.86	2.5[c]	0.005	-18	0.62	0.41
9	S_1	Mn–O	1.83	2.5[c]	0.002	-20	1.41	1.54
10[*]	S_0 Grand Add	Mn–O	1.86	2.5[c]	0.005	-20	0.35	0.58
		Mn–O	2.24	3.5[c]	0.025[d]			
11[*]	S_1	Mn–O	1.83	2.5[c]	0.004	-20	1.13	5.92
		Mn–O	2.06	3.5[c]	0024			

[a]fit parameters and quality-of-fit parameters are described in Materials and Methods; [b]$\bullet E_0$ was constrained to be equal for all shells within a fit; [c]parameter fixed in fit; [d]upper limit for parameter; [*]see text for details

Debye-Waller values for the terminal Mn–O shell were both much smaller (0.5 – 1.0 and ~0.002 Å^2, respectively), or were both at an intermediate value. Irrespective of the *N* and σ^2 values, however, the *R* values for the terminal Mn–O distances in the S_0 and S_1 states were much more precise. The terminal Mn–O shell for the S_0 state required a long 2.2 – 2.3 Å distance for an acceptable fit, compared to the 2.0 – 2.1 Å distance that was required for the S_1 state. A logical extension of this fit, if Mn(II) is present in the S_0 state, is to attempt a three-shell fit that separates the bridging Mn–O distances, the Mn(II) terminal Mn–O distances, and the terminal Mn–O distances from the other three Mn atoms into separate shells. However, this resulted in an under-determined fit as calculated by Eq. 3-6 because of the limited width of the Fourier peak (see Eq. 3-7).

A reasonable conclusion from the fits to Peak I is that there is an increase in the Mn–O distances in the S_0 state relative to the S_1 state, which is also seen in the Fourier isolates shown in Figure 3-7 and Figure 3-10, and the Fourier transforms shown in Figure 3-6. This can be accounted for by a 0.03 Å increase in the average bridging Mn–O distance in the S_0 state relative to the S_1 state and the presence of some longer 2.2 – 2.3 Å terminal Mn–O distances in the S_0 state. Both of these conclusions are consistent with the presence of a Mn(II) atom in the S_0 state.

Peak II

Relative to Peaks I and III, fits to Peak II are well-known to have deep fit minima and thus produce the most reliable information about neighbors to Mn in the OEC.[72] Fits #1 – 9 in Table 3-3 show the results from fitting one Mn–Mn shell to Peak II in both

Table 3-3: One- and two-shell simulations of Fourier peak II from the S_0-state samples. Fits #7 and #16 correspond to the average of the fit parameters from Fits #1 – 6 and #10 – 15, respectively, while Fits #8 and #17 are fits to the average S_0-state spectrum.

Fit #	sample	shell	R (Å)	N	σ^2 (Å^2)	$\bullet E_0$ [b]	Φ (x 10^{-3})	ε^2 (x 10^{-5})
1	S_0 A	Mn–Mn	2.71	0.94	0.003	-20	0.60	0.84
2	S_0 B	Mn–Mn	2.72	1.30	0.005	-20	0.38	0.50
3	S_0 C	Mn–Mn	2.73	1.37	0.004	-19	0.19	0.29
4	S_0 D	Mn–Mn	2.74	1.55	0.005	-16	0.25	0.37
5	S_0 E	Mn–Mn	2.73	1.25	0.005	-17	0.25	0.40
6	S_0 F	Mn–Mn	2.74	1.37	0.004	-16	0.23	0.42
7	Average	Mn–Mn	2.73	1.30	0.004	-18	0.32	0.47
8	S_0 Grand Add	Mn–Mn	2.72	1.30	0.005	-19	0.27	0.41
9	S_1	Mn–Mn	2.72	1.25	0.002	-19	0.58	0.64
10	S_0 A	Mn–Mn	2.70	0.98	0.002[c]	-20	0.36	0.92
		Mn–Mn	2.85	0.31	0.002[c]			
11	S_0 B	Mn–Mn	2.71	1.05	0.002[c]	-17	0.25	0.56
		Mn–Mn	2.85	0.46	0.002[c]			
12	S_0 C	Mn–Mn	2.73	1.16	0.002[c]	-15	0.12	0.37
		Mn–Mn	2.86	0.42	0.002[c]			
13	S_0 D	Mn–Mn	2.74	1.20	0.002[c]	-13	0.15	0.46
		Mn–Mn	2.87	0.53	0.002[c]			
14	S_0 E	Mn–Mn	2.73	1.02	0.002[c]	-13	0.13	0.50
		Mn–Mn	2.87	0.44	0.002[c]			
15	S_0 F	Mn–Mn	2.74	1.19	0.002[c]	-12	0.13	0.70
		Mn–Mn	2.88	0.46	0.002[c]			
16	Average	Mn–Mn	2.725	1.10	0.002[c]	-15	0.19	0.58
		Mn–Mn	2.86	0.44	0.002[c]			
17	S_0 Grand Add	Mn–Mn	2.72	1.08	0.002[c]	-15	0.17	0.53
		Mn–Mn	2.86	0.44	0.002[c]			
18	S_1	Mn–Mn	2.74	1.54	0.002[c]	-13	0.49	0.76
		Mn–Mn	2.90	0.51	0.002[c]			

[a]fit parameters and quality-of-fit parameters are described in Materials and Methods; [b]$\bullet E_0$ was constrained to be equal for all shells within a fit; [c]parameter fixed in fit

the S_0 and S_1 states. Both the S_0 state and the S_1 state can be fit with a Mn–Mn distance of 2.72 Å and a coordination number *N* between 1.25 and 1.5. The reduced amplitude of Peak II in the S_0 state that is seen in Figure 3-6 is manifested in the one-shell fits as an increased Debye-Waller disorder parameter of 0.004 – 0.005 $Å^2$. This is over twice as large as the Debye-Waller parameter for the S_1 state and may indicate that two different Mn–Mn distances exist in the S_0 state which are fit by only one shell in these fits. In addition, other systems with heterogeneity in the 2.7 Å Mn–Mn distances, such as the S_0^* state,[80] the S_2–*g* = 4.1 state,[235] the NH_3-treated S_2 state,[236] the F^--treated S_2 state,[237] and the S_3 state,[69,161] all show increased Debye-Waller parameters when one Mn–Mn shell is fit to two Mn–Mn distances. Therefore, it is reasonable to split Peak II into two separate Mn–Mn distances.

Fits #10 – 18 in Table 3-3 show improvements in the fits for the S_0 state if Peak II is treated as two separate Mn–Mn distances. Attempts to fit the second shell as a Mn–C shell and the first shell as a Mn–Mn shell produced significantly higher fit error values than the one-shell Mn–Mn fits; thus this scenario is considered unlikely. With two separate Mn–Mn distances, the fit error Φ decreased by 40 % for the two-shell fit in the S_0 state relative to the one-shell fit, indicating that splitting the Mn–Mn distances is a valid approach. However, the improvement in Φ for the S_1 state is only 15 % for the same approach; thus a two-shell fit is questionable for the S_1 state. When separated into two shells, the S_0 state is fit well by Mn–Mn distances of 2.72 and 2.86 Å, a distance heterogeneity •***R*** of 0.14 Å. However, the coordination numbers from the two-shell fits for the S_0 state are quite surprising. Virtually all of the proposed models for the structure of the OEC,[34,36,65,66,71,74,77] including the one shown in Figure 3-1, incorporate two di-μ-oxo

Mn–Mn distances; if Eq. 3-3 is used to calculate the predicted *N* value, the result is an *N* value of 1. Furthermore, if one of these distances were to increase in the S_0 state, one would expect that the *N* values for the two shells in the two-shell fit would be equal. However, the results from Table 3-3 show that this is not the case. The N_1:N_2 ratio for the 2-shell fits is approximately 2:1, and the total *N* value $N_1 + N_2$ is approximately 1.5. Thus, using Eq. 3-3, these results predict that three di-μ-oxo Mn–Mn distances exist, and that one of them is larger in the S_0 state relative to the S_1 state. However, because the ε^2 value increases when going from a one-shell to a two-shell fit, it is possible that these fits are underdetermined, which can be remedied by reducing the number of free parameters.

Table 3-4: One- and two-shell simulations of Fourier peak II from the S_0-state samples in which N_1 and N_2 for the 2 shells were fixed in either a 1:1 or a 2:1 ratio. Fits #7 and #16 correspond to the average of the fit parameters from Fits #1 – 6 and #10 – 15, respectively, while Fits #8 and #17 are fits to the average S_0-state spectrum.

Fit #	sample	shell	R (Å)	N	σ^2 (Å^2)	$\bullet E_0$ [b]	Φ (x 10^{-3})	ε^2 (x 10^{-5})
1	S_0 A	Mn–Mn	2.67	0.47[d]	0.002[c]	-20	0.60	0.83
		Mn–Mn	2.74		0.002[c]			
2	S_0 B	Mn–Mn	2.67	0.64[d]	0.002[c]	-20	0.36	0.47
		Mn–Mn	2.77		0.002[c]			
3	S_0 C	Mn–Mn	2.68	0.68[d]	0.002[c]	-19	0.18	0.28
		Mn–Mn	2.77		0.002[c]			
4	S_0 D	Mn–Mn	2.70	0.76[d]	0.002[c]	-16	0.23	0.34
		Mn–Mn	2.80		0.002[c]			
5	S_0 E	Mn–Mn	2.68	0.61[d]	0.002[c]	-17	0.23	0.38
		Mn–Mn	2.78		0.002[c]			
6	S_0 F	Mn–Mn	2.69	0.68[d]	0.002[c]	-16	0.22	0.40
		Mn–Mn	2.79		0.002[c]			
7	Average	Mn–Mn	2.68	0.59[d]	0.002[c]	-18	0.30	0.45
		Mn–Mn	2.77		0.002[c]			
8	S_0 Grand Add	Mn–Mn	2.68	0.64[d]	0.002[c]	-19	0.26	0.39
		Mn–Mn	2.77		0.002[c]			
9	S_1	Mn–Mn	2.71	0.63[d]	0.002[c]	-19	0.58	0.63
		Mn–Mn	2.73		0.002[c]			
10	S_0 A	Mn–Mn	2.68	0.89[e]	0.002[c]	-20	0.48	0.67
		Mn–Mn	2.81	0.44[e]	0.002[c]			
11	S_0 B	Mn–Mn	2.71	1.02[e]	0.002[c]	-17	0.26	0.34
		Mn–Mn	2.84	0.51[e]	0.002[c]			
12	S_0 C	Mn–Mn	2.71	1.01[e]	0.002[c]	-17	0.14	0.21
		Mn–Mn	2.82	0.50[e]	0.002[c]			
13	S_0 D	Mn–Mn	2.73	1.16[e]	0.002[c]	-14	0.16	0.24
		Mn–Mn	2.86	0.58[e]	0.002[c]			
14	S_0 E	Mn–Mn	2.72	0.98[e]	0.002[c]	-13	0.15	0.24
		Mn–Mn	2.86	0.49[e]	0.002[c]			
15	S_0 F	Mn–Mn	2.72	1.06[e]	0.002[c]	-14	0.16	0.29
		Mn–Mn	2.84	0.53[e]	0.002[c]			
16	Average	Mn–Mn	2.71	1.02[e]	0.002[c]	-16	0.22	0.33
		Mn–Mn	2.84	0.51[e]	0.002[c]			
17	S_0 Grand Add	Mn–Mn	2.71	1.00[e]	0.002[c]	-16	0.19	0.29
		Mn–Mn	2.84	0.50[e]	0.002[c]			
18	S_1	Mn–Mn	2.70	0.89[e]	0.002[c]	-19	0.58	0.63
		Mn–Mn	2.75	0.44[e]	0.002[c]			

[a]fit parameters and quality-of-fit parameters are described in Materials and Methods; [b]$\bullet E_0$ was constrained to be equal for all shells within a fit; [c]parameter fixed in fit; [d]the N_1:N_2 ratio was fixed to 1:1 for this fit; [e]the N_1:N_2 ratio was fixed to 2:1 for this fit

The results from Table 3-4 address the concerns about the ε^2 values and expand on the possible inequality between N_1 and N_2. The fits presented in Table 3-4 fix the N_1:N_2 ratio to either 1:1 (Fits #1 – 9) or 2:1 (Fits #10 – 18). Those in which the N_1:N_2 ratio for the S_0 state was fixed to 1:1 do not compare favorably to the single-shell fits from Table 3-3. This is because the fit error values Φ for the two-shell fits are virtually identical to those for the one-shell fits, despite the addition of a second Mn–Mn shell. In addition, the *R* values for the first shell of the two-shell fits are quite low (below 2.7 Å). However, Fits #10 – 17 from Table 3-4 show a significant improvement if, as suggested from the fits from Table 3-3 in which the N values were allowed to vary, the N_1:N_2 ratio is fixed to 2:1. The improvement in both Φ and ε^2 is significant, approximately 30 % relative to the one-shell fit. Furthermore, the N_1 and N_2 values for all of the S_0-state fits are almost exactly 1 and 0.5, respectively, which are exactly the predicted values for a system with three Mn–Mn μ-oxo-bridged motifs. The Mn–Mn distances for these S_0-state fits are quite similar to those from Table 3-3, with R_1 = 2.71 Å and R_2 = 2.84 Å (•***R*** = 0.13 Å). It is important to note that, regardless of which N_1:N_2 ratio was applied, there was no improvement in Φ or ε^2 for the S_1-state two-shell fits relative to the single-shell fits, indicating that, if three Mn–Mn 2.7 Å distances exist in the S_1 state, there is no resolvable distance heterogeneity in these experiments.

Because the proposed distance heterogeneity in the S_0 state (0.13 – 0.14 Å) is so close to the theoretical resolution limit of 0.14 Å, it is not possible to unequivocally prove that there are two different Mn–Mn distances present in the S_0 state. This resolution limit is defined as the ability to see a k^3-space beat in the Peak II Fourier isolate, and can be improved if data can be collected to higher *k* values (see Appendix for a detailed

discussion of the calculation of theoretical resolution limits). Thus, it is theoretically possible to explain the EXAFS data from the S_0 state in terms of an overall increase in site inhomogeneity for the 2.7 Å distances. This is a different disorder scenario from the presence of two different Mn–Mn distances, which would be expected to have very little site inhomogeneity. However, it is difficult to rationalize a proposed increase in site inhomogeneity in the S_0 state without increasing the Mn–Mn distances.

Peak III

Curve-fitting results for Peak III are shown in Table 3-5. The fit results for the individual S_0-state samples were essentially identical to those shown in Table 3-5 for the S_0 Grand Add fit (data not shown). Although the fit minima are much more shallow than those for fits to Peak II, it is still possible to address some relevant questions about Peak III, specifically the chemical nature of the backscatterers that contribute to this peak. A comparison of Fits #1 and #2, as well as Fits #4 and #5, shows that the fit results

Table 3-5: One- and two-shell simulations of Fourier peak III from the S_0-state samples.

Fit #	sample	shell	R (Å)	N	σ^2 (Å^2)	$\bullet E_0$ [b]	Φ (x 10^{-3})	ε^2 (x 10^{-5})
1	S_0 Grand Add	Mn–Mn	3.33	0.5[c]	0.004	-12	0.28	0.75
2	S_0 Grand Add	Mn–Ca	3.39	0.5[c]	0.002	-13	0.35	0.94
3	S_0 Grand Add	Mn–Mn Mn–Ca	3.36 3.58	0.5[c] 0.25[c]	0.002[c] 0.002[c]	-7	0.13	0.35
4	S_1	Mn–Mn	3.36	0.5[c]	0.003	-6	0.17	0.24
5	S_1	Mn–Ca	3.41	0.5[c]	0.002	-7	0.28	0.40
6	S_1	Mn–Mn Mn–Ca	3.37 3.57	0.5[c] 0.25[c]	0.002[c] 0.002[c]	-2	0.08	0.12

[a]fit parameters and quality-of-fit parameters are described in Materials and Methods; [b]$\bullet E_0$ was constrained to be equal for all shells within a fit; [c]parameter fixed in fit

are significantly better if Peak III is fit with a Mn–Mn rather than a Mn–Ca distance. This provides convincing evidence for the presence of a 3.3 Å mono-μ-oxo Mn–Mn distance. Fits #3 and #6 show that the fit error parameters Φ and ε^2 drop by a sizeable amount, approximately 50 %, if an additional Mn–Ca interaction is added to the mono-μ-oxo Mn–Mn interaction. Attempts to fit Peak III with a combination of a Mn–Mn shell and a Mn–C shell or a combination of a Mn–Ca shell and a Mn–C shell resulted in fit errors that were 2 – 3 fold higher than those for a combination of a Mn–Mn shell and a Mn–Ca shell (data not shown). A similar increase in error was observed if the *N* value for Fit #1 or Fit #4 in Table 3-5 was fixed to 1.0 to assess the possibility of two or more 3.3 Å Mn–Mn interactions or if Peak III was fit with only a Mn–C shell (data not shown). In addition, attempts to fit Peak III with one Mn–Mn shell ($N = 0.5$) and two Mn–Ca shells ($N = 0.5$) resulted in fit errors that were 20 – 50 % higher than those shown for Fits #3 and #6 in Table 3-5. As shown in the Fourier transforms from Figure 3-6, Peak III is essentially invariant between the S_0 state and the S_1 state. Thus, it is not surprising that the fits are quite similar between the S_0 and S_1 states. The Fourier isolate from Figure 3-9 shows a very small frequency shift between the S_0 and S_1 states which is manifested in slightly smaller (0.02 – 0.03 Å) distances in the S_0 state relative to the S_1 state. However, these changes may be too small to be significant.

All of the previous fits to Peak I, Peak II, and Peak III were also applied to the average 3F EXAFS spectrum (50 % S_0, 50 % S_1) to examine the effects of the subtraction procedure. Because of the high signal-to-noise ratio achieved in this experiment, it is unlikely that the fit results presented in Table 3-2, Table 3-3, Table 3-4, and Table 3-5 are the result of noise introduced into the data during the subtraction procedure. The fits to

the 3F EXAFS spectra confirmed this, as the fit results were halfway between those reported above for the S_0 state and those reported above for the S_1 state (data not shown).

As mentioned in the Materials and Methods section, the possibility was examined that the Fourier isolation technique is generating artifacts in the data, although most of the Fourier peaks in Figure 3-6 are well-separated, which minimizes any distortion artifacts from the isolation procedure. This was done by isolating the Fourier peaks as pairs (Peaks I+II and Peaks II+III) and comparing the obtained curve-fitting results to those obtained when the peaks were isolated individually. As shown in Table 3-6 and Table 3-7 in the Appendix, no major changes in the fit results are obtained by fitting the Fourier peaks as pairs relative to the fits to the individual Fourier peaks; thus, it is rather unlikely that the fit results presented in Table 3-2, Table 3-3, Table 3-4, and Table 3-5 are affected by Fourier isolation artifacts.

Discussion

Mn–Mn distance heterogeneity in the OEC

As mentioned in the Introduction, pioneering EXAFS experiments in the late 1970s by Kirby et al.[58] showed that a major structural motif in the OEC is the di-μ-oxo-bridged binuclear Mn_2 cluster. This was confirmed by several subsequent EXAFS studies.[71,72,79,199-202,205] Later studies with improved instrumentation were able to detect the additional presence of mono-μ-oxo Mn–Mn and mono-μ-oxo Mn–Ca motifs at a longer distance.[71,72,79,202,205,207]

EXAFS studies of the S_1 and S_2 states revealed that all of the di-μ-oxo-bridged Mn–Mn moieties have essentially the same Mn–Mn distance of ~2.7 Å. This distance is consistent with those found in numerous studies of di-μ-oxo-bridged Mn_2(III,IV) and Mn_2(IV,IV) complexes.[58,64,242] This provides strong evidence that the 2.7 Å distance detectable in the EXAFS spectra of the S_1 and S_2 states originates from di-μ-oxo-bridged Mn_2(III,IV) and/or Mn_2(IV,IV) moieties.

However, other states of the OEC, including those generated by treatments with oxygen-evolution inhibitors or those generated by Ca^{2+}-depletion, show that many, but not all, of these states contain Mn–Mn distance heterogeneity which affects the amplitude and, in some cases, the position of Peak II in the Fourier transforms. It is well-established that the native S_2 state can exist in two forms: the multiline state[50,51] and the $g = 4.1$ state.[52,53] Recently, it was established that 820 nm photons could convert the multiline state into the $g = 4.1$ state, and it was proposed that this occurs by a valence-swapping mechanism whereby an electron is transferred from a Mn(III) ion to a Mn(IV)

ion.[243,244] A comparative EXAFS study by Liang et al.[235] of the S_2 state in both of these magnetic configurations showed that, while the multiline form of the S_2 state showed no 2.7 Å Mn–Mn distance heterogeneity, one of the Mn–Mn distances in the $g = 4.1$ form of the S_2 state lengthened to 2.85 Å. It is difficult, however, to rationalize the observed distance increase, because the Mn_2(III,IV) and Mn_2(IV,IV) di-μ-oxo motifs both have Mn–Mn distances of ~2.7 Å.[36,173,204]

Inhibitors of oxygen evolution such as F^- and NH_3 can also lead to Mn–Mn distance heterogeneity in the OEC. PS II centers treated with F^- cannot advance past the S_2 state and, when poised in the S_2 state, exist almost exclusively in the $g = 4.1$ state.[52,170] EXAFS spectroscopy on the F^--treated S_2 state shows that, as in the native S_2–$g = 4.1$ state, one of the di-μ-oxo-bridged Mn–Mn distances increases in length to 2.8 – 2.85 Å.[237] Unless F^- is incorporated into the OEC as a bridging ligand, it is not easy to explain the observed lengthening of the Mn–Mn distance in F^--treated samples.

Treatment of PS II centers with NH_3 also inhibits oxygen evolution, and an 'NH_3-altered' multiline is observed for these centers when poised in the S_2 state.[245] Pulsed EPR spin echo measurements with $^{15}NH_3/^{14}NH_3$ have elucidated that NH_3 is bound to Mn in the S_2 state,[246] and the asymmetry parameter η derived from these ESEEM measurements is more consistent with the binding of NH_3 in a bridging position.[246] Thus, it was proposed that NH_3 replaces one of the μ-oxo bridges in one of the di-μ-oxo Mn–Mn cores. In addition, a Mn model complex $[Mn_2(O)(NH_2)(phen)_4]^{4+}$ (phen = 1,10-phenanthroline) that was synthesized by Frapart and co-workers[247] showed that an amido group can be incorporated as a bridging ligand in a μ-oxo-μ-amido Mn_2 complex.

EXAFS studies of the NH_3-treated S_2 state by Dau et al.[236] are consistent with this hypothesis, because these NH_3-treated samples show that one of the di-μ-oxo Mn–Mn bridges increases in length in the S_2 state to 2.87 Å. Furthermore, the X-ray dichroism for this vector is different from the dichroism of the remaining Mn–Mn vectors.[236] This behavior can be rationalized by the fact that an O^{2-} bridge is expected to have a shorter Mn-ligand bond than NH_2^- based on the electrostatic argument of a difference in charge of the ligand. For the NH_2^- case, the longer Mn-ligand bond is expected to cause the observed increase in the Mn–Mn distance.

Another method of inhibiting oxygen evolution is to deplete PS II samples of the essential cofactor Ca^{2+}. Ca^{2+}-depleted samples are often referred to as S'-states, and can be poised in the S_1' or S_2' states. Aside from exhibiting an altered multiline signal relative to Ca^{2+}-reconstituted samples,[248,249] these S'-states are essentially structurally identical to the native S-states as determined by EXAFS spectroscopy and show no detectable Mn–Mn distance heterogeneity in Peak II.[250] In addition, an S_3' state can be prepared from Ca^{2+}-depleted samples by continuous illumination at 4° C[248,249] which, based on ESEEM and ENDOR spectroscopic data,[251-253] is more accurately described as an $S_2Y_Z^{\cdot}$ state. The conclusions from EXAFS spectroscopic studies of the $S_2Y_Z^{\cdot}$ state show that this S'-state not structurally different from the other S'-states or the native S_1 and S_2 states.[250] Thus, unlike other inhibited S-states, the S'-states do not exhibit measurable Mn–Mn distance heterogeneity.

Although the electron on $Y_Z^{\cdot}$ in the $S_2Y_Z^{\cdot}$ state cannot be transferred to Mn or Mn ligands in Ca^{2+}-depleted samples, this can occur in native samples to generate the S_3 state, which is quite different from either the S_2 state or the $S_2Y_Z^{\cdot}$ state. The first EXAFS study of an S_3-like state was the study by Guiles et al.[208] of the S_3^* state generated by reductant-

induced oxidation of the non-heme Fe^{2+}. The results from this study showed that the amplitude of Peak II is lower in the S_3^* state than in the S_2 state, which was interpreted as arising from Mn–Mn distance heterogeneity in the S_3^* state. Subsequent studies observed the same behavior in the native S_3 state generated by two single-turnover flashes.[69,161] In these subsequent studies, the Mn–Mn distances were observed to increase from 2.7 Å to 2.8 Å and 3.0 Å. In light of XANES and Kβ spectroscopic studies which were best explained by the oxidizing equivalent not being localized on Mn in the S_3 state (see Chapter 2),[98,161] the observed changes in distance were best explained by the presence of a μ-oxo-bridged oxyl radical in the S_3 state.[36,69] The decrease in bond order from converting a μ-oxo (O^{2-}) bridge into an oxyl radical ($O^{\bullet-}$) can explain the observed lengthening of the Mn–Mn distance in the S_3 state. Furthermore, the presence of an oxyl radical provides a mechanism for storing an oxidizing equivalent on the OEC in the S_3 state without contradicting the XANES and Kβ spectroscopic results that are inconsistent with Mn oxidation during the $S_2 \rightarrow S_3$ transition (see Chapter 2).[98,161]

As described above, the S_1, S_2, and S_3 states, as well as several inhibited S-states, have all been structurally characterized using EXAFS. However, the results from the current chapter represent the first EXAFS characterization of the native S_0 state. A previous study by Guiles et al.[80] characterized a chemically reduced S-state called the S_0^* state, and provided evidence for Mn–Mn distance heterogeneity in that S-state in the form of a lower Peak II amplitude in the S_0^* state. Although the EPR spectra from these S-states are essentially identical (see Chapter 4),[45] it has not been proven that the chemically generated S_0^* state and the native S_0 state produced by three single-turnover flashes are indeed the same species.

The results from the current chapter show that the S_0 state has a noticeable reduction in the amplitude of Peak II in the Fourier transform relative to the S_1 state, as seen in Figure 3-6. This is also evident in the reduced amplitude of the Fourier isolates from Peak II shown in Figure 3-8 and Figure 3-11. Curve-fitting analyses of the Peak II Fourier isolates (shown in Table 3-3 and Table 3-4) show that the differences in Peak II between the S_0 and S_1 states can be explained by the existence of Mn–Mn distance heterogeneity in the S_0 state in the form of Mn–Mn distances at ~2.7 Å and ~2.85 Å. These results provide the first evidence that structural changes occur during the $S_0 \rightarrow S_1$ transition in the OEC, which can be rationalized by a combination of two effects: μ-oxo bridge protonation and the presence of Mn(II)

The evidence for the involvement of μ-oxo bridge protonation in the S_0 state comes from an EXAFS spectroscopic study by Baldwin et al.[174] of a series of Mn_2(IV,IV) di-μ-oxo-bridged complexes in which the μ-oxo bridges were successively protonated. The results from this study showed that the Mn–Mn distance increases from 2.7 Å to 2.8 Å to 2.9 Å with 0, 1, or 2 μ-oxo bridge protonations, respectively. This can be explained by the fact that protonation of a μ-oxo bridge lowers the Mn–O bond order, which causes an increase in the Mn–Mn distance. Although protonation was considered to be unlikely for the S_3 state because of the high redox states of the Mn ions and the fact that the bound water has already been partially deprotonated,[68] protonation of a μ-oxo bridge could easily occur in the S_0 state, especially if substrate water is incorporated into a bridging position as an OH^- bridging ligand.

Recent experimental results from Geijer et al.[254] can be interpreted to suggest that protonation indeed plays a role in determining the Mn–Mn distances. This group

examined the effect of pH on the intensity of the S_0-state EPR multiline signal (see Chapter 4)[45,46,83] and observed a parabolic dependence of the S_0-state EPR multiline signal intensity with pH whereby the intensity was maximal at pH 6.0 but was lower by up to 75 % at acidic and alkaline pH values. Furthermore, this effect was essentially reversible. One possible explanation provided by Geijer et al.,[254] and originally suggested by Baldwin et al.[174] to explain the results from their study of model complexes, is that the protonation state of a μ-oxo bridge is changing the Mn–Mn distance and thereby changing the magnitude of the antiferromagnetic exchange coupling in the binuclear Mn_2 moiety; this would explain the disappearance of the S_0-state EPR multiline signal at acidic or alkaline pH values.

Another effect that could increase the Mn–Mn distance is the presence of Mn(II). It is well-known that the Mn–ligand distances are longer for Mn(II) complexes than they are for Mn(III) and Mn(IV) complexes,[239-241] and the XANES and Kβ spectroscopic data from Chapter 2 are consistent with the presence of Mn(II) in the S_0 state. However, no Mn model complexes have been reported which contain a di-μ-oxo-bridged Mn(II) atom. The closest analogs which have been structurally characterized are Mn_2(II,II) and Mn_2(II,III) di-μ-phenoxyl-bridged complexes which have Mn–Mn distances of 3.2 – 3.4 Å.[255-259] In addition, a di-μ-hydroxo-bridged Mn_2(II,II) complex with a Mn–Mn distance of 3.31 Å has been characterized.[260] The long Mn–Mn distance in these complexes is most likely due to a combination of the nature of the bridging ligands and the oxidation states of the Mn ions; a di-μ-oxo-bridged moiety that incorporates Mn(II) would be expected to have a shorter Mn–Mn distance due to the presence of the μ-oxo bridges.

It is possible that both of these scenarios, the presence of Mn(II) and μ-oxo bridge protonation, occur in the S_0 state. However, the conclusions from the Baldwin et al. study[174] show that protonation of one di-μ-oxo bridge alone may be enough to explain the observed Mn–Mn distance increase in the S_0 state, and protonation of a di-μ-oxo bridge is consistent with the conclusions from the S_0-state EPR multiline signal pH dependence study by Geijer et al.[254] It is also possible that the presence of Mn(II) in lieu of μ-oxo bridge protonation is enough to explain the experimental data for the S_0 state, but this cannot currently be proven by comparisons to model complexes.

Are there three di-μ-oxo bridges present in the OEC?

The results presented in this chapter lead to a most surprising conclusion: it is possible that three, not two, di-μ-oxo Mn–Mn moieties are present in the OEC. The fits to Fourier Peak II in the S_0 state shown in Table 3-3 do not distribute the coordination numbers N_1 and N_2 equally between the 2.7 Å and the 2.85 Å shells; an equal distribution would be consistent with the presence of two di-μ-oxo Mn–Mn moieties. Instead, the distribution of N values from the fits is in a 2:1 ratio with N_{tot} ~1.5, and, as shown in Table 3-4, a head-to-head comparison of a 2:1 ratio and a 1:1 ratio for N_1:N_2 shows that 2:1 is clearly better than 1:1. In a significant portion of the available literature, however, there has been the assumption that two di-μ-oxo Mn–Mn moieties are present in the OEC.

Because the possibility that three di-μ-oxo Mn–Mn moieties exist in the OEC has not been seriously considered until now, it would be productive to re-examine the data already in the literature under the premise of three di-μ-oxo Mn–Mn moieties. This is most convincingly done for S-states in which Mn–Mn distance heterogeneity exists, because the N_1:N_2 ratio for these S-states can be examined, which is more reliable than the

total *N* value. These S-states include the S_0^* state,[80] the S_2–*g* = 4.1 state,[235] the NH_3-treated S_2 state,[236] the F^--treated S_2 state,[237] and the S_3 state.[69,161]

The earliest EXAFS study that revealed Mn–Mn distance heterogeneity was the study of the S_0^* state by Guiles et al.[80] The best fit to Peak II in the S_0^* state, shown in Table III from Guiles et al.,[80] is one Mn–Mn shell at 2.69 Å with an *N* value of 1.0, and another Mn–Mn shell at 2.87 Å with an *N* value of 0.5. Although these fits were done using an early fitting method called 'fine adjustment based on models'[261] instead of using *ab initio* FEFF calculations,[197,213] the N_1:N_2 ratio and the magnitude of the *N* values are both consistent with three di-μ-oxo-bridged Mn–Mn moieties.

Several alternative forms of the S_2 state have been studied using EXAFS spectroscopy, and all of them show the expected inequivalence in N_1 and N_2 for three di-μ-oxo bridges. Liang et al.[235] studied the S_2–*g* = 4.1 state, and the results from Table 4B of Liang et al.[235] are that the best fit to the S_2–*g* = 4.1 state is with two Mn–Mn shells at 2.72 Å and 2.85 Å. The *N* value for the first shell is 0.76, almost twice as high as the *N* value for the second shell of 0.44. This is again consistent with three di-μ-oxo-bridged Mn–Mn moieties and, as before, if three di-μ-oxo-bridged Mn–Mn moieties exist, only one of the Mn–Mn distances changes relative to the S_1 state.

Dau et al.[236] and DeRose et al.[237] used EXAFS spectroscopy to investigate the S_2 state under conditions of F^- inhibition and NH_3 inhibition, respectively. The best fit to Peak II from the NH_3-treated samples is shown in Table 1 from Dau et al.[236] as two Mn–Mn shells, one at 2.71 Å and another at 2.86 Å. The N_1 and N_2 values from this fit are inequivalent at 0.75 and 0.5, respectively, which is more consistent with three di-μ-oxo bridges than two. F^--inhibited S_2-state samples studied by DeRose et al.[237] also behave in a similar fashion. The best fit to Peak II in F^--inhibited S_2-state samples, shown in

Table 2 from DeRose et al.,[237] is with two Mn–Mn shells at 2.71 Å and 2.85 Å. The *N* values from this fit are also inequivalent, with N_1 = 0.8 and N_2 = 0.4. The re-evaluation of the results from the inhibited S_2 states is best explained by one of three di-μ-oxo Mn–Mn bridges increasing in distance in the inhibited S_2 states.

Recent studies of the S_3 state by Liang et al.[69] are also consistent with the presence of three di-μ-oxo Mn–Mn moieties. In the native S_3 state produced by two single-turnover flashes, the Mn–Mn distances increase from 2.7 Å to 2.82 Å and 2.95 Å in a two-shell fit (Table 1B from Liang et al.[69]). The N values for the two-shell fit are 0.7 and 0.4 for N_1 and N_2, respectively, demonstrating that the data from the S_3 state, like the other S-states detailed above, is quite consistent with the presence of three di-μ-oxo-bridged Mn_2 moieties. As seen above, none of the S-states which exhibit distance heterogeneity are best fit by an equal *N* value for both Mn–Mn shells; the fit results from these S-states are in fact more consistent with a 2:1 N_1:N_2 ratio (where N_1 corresponds to the shorter distance), as seen in the data from the current chapter.

Mechanistic and structural consequences

The data from the current chapter and a reinterpretation of data already in the literature raise the possibility that the OEC contains three di-μ-oxo bridges. This has serious consequences for the vast majority of the proposed structural models of the OEC that are in the literature,[34,36,65,66,69,71,74,77,78] because almost all of these structural models contain only two di-μ-oxo Mn–Mn motifs. However, as originally pointed out in 1994 by DeRose et al.,[72] and subsequently by Cinco et al.[73] and Robblee et al.,[40] several possible structural models can be constructed from the constraints available from EXAFS. These

possibilities are shown as structures A through K in Figure 3-12, although most of these have only two 2.7 Å Mn–Mn distances.

Several mechanisms for oxygen evolution have been proposed based on the topological structure from structure A in Figure 3-12.[36,65,69] The only reason for this preference is that structure A is one of the simplest possible models. In fact, simulations of EPR spectra from the S_2 state are improved using a different topology which rationalizes the strong exchange coupling between two di-μ-oxo Mn–Mn moieties. Peloquin et al.[74] prefer structures E or F in Figure 3-12, while Hasegawa et al.[76,78] prefer a model similar to but not identical to structure G in Figure 3-12.

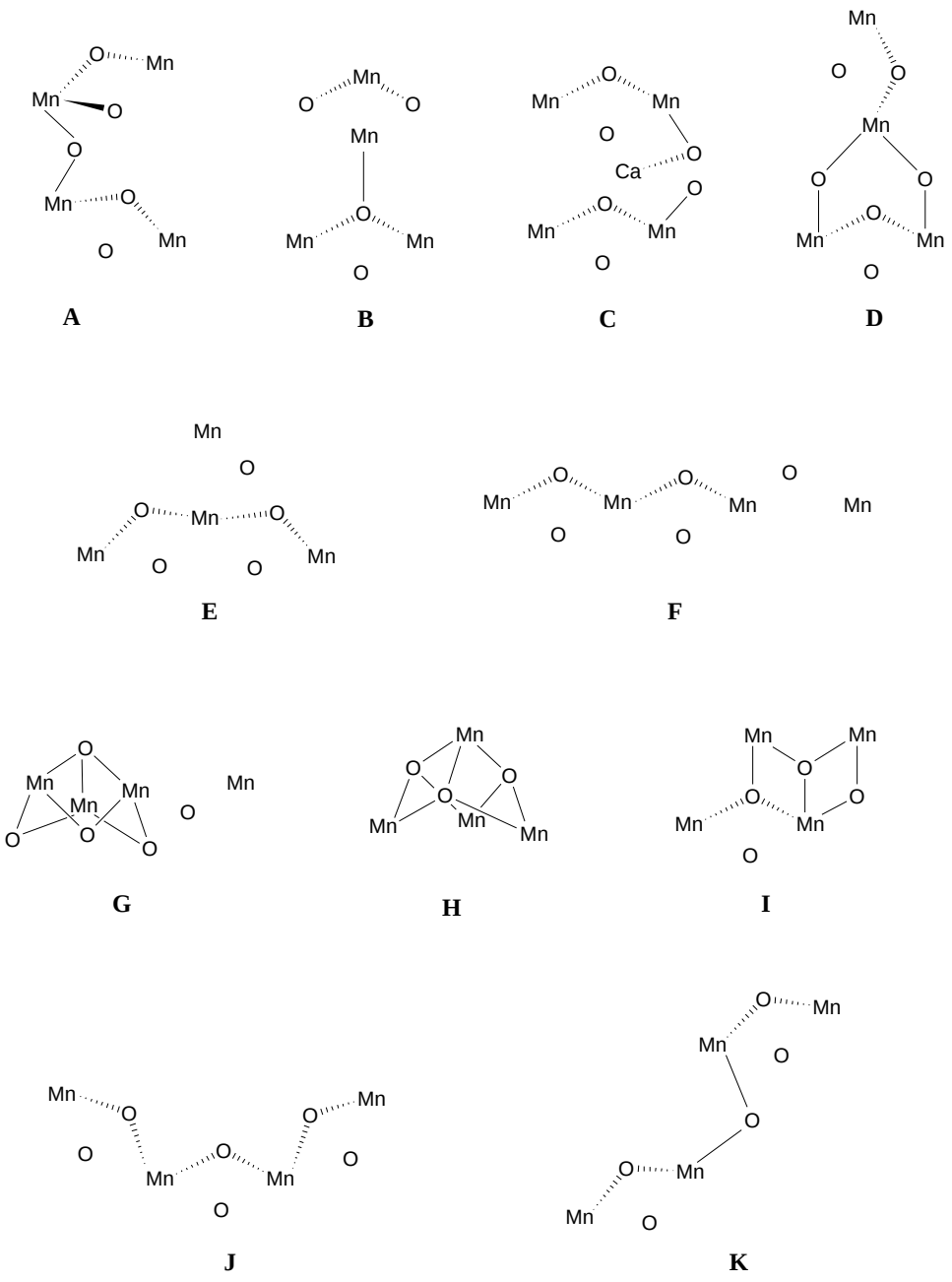

Figure 3-12: Possible structural models for the active site of the OEC in PS II. Adapted from DeRose et al.,[72] Cinco et al.,[73] and Robblee et al.[40]

Some of the structures in Figure 3-12 are less likely using criteria other than the number of 2.7 Å di-μ-oxo Mn–Mn motifs. Structure B in Figure 3-12 contains two 3.3 Å Mn–Mn distances; this is unlikely based on the fits to Peak III described in the Results

section, which are more consistent with one such distance. Structure C and variations thereof consisting of two isolated di-μ-oxo Mn–Mn moieties are preferred by Pace and co-workers based on their EPR simulations,[192,262,263] but structure C is not widely accepted on the basis of EPR simulations by other groups[44,74,264] and EXAFS data.[250] The fits to Peak III shown in Table 3-5 also disagree with structure C, because fits to Peak III that do not include Mn are consistently and significantly worse than those that include Mn. Structure D is disfavored for the same reason that was set forth for structure B, *i.e.* two 3.3 Å Mn–Mn distances are considered unlikely. Structure H, with three 3.3 Å Mn–Mn distances is even more unlikely than structures B and D, as shown by the EXAFS spectra from a similar set of complexes, a series of distorted cubanes.[73]

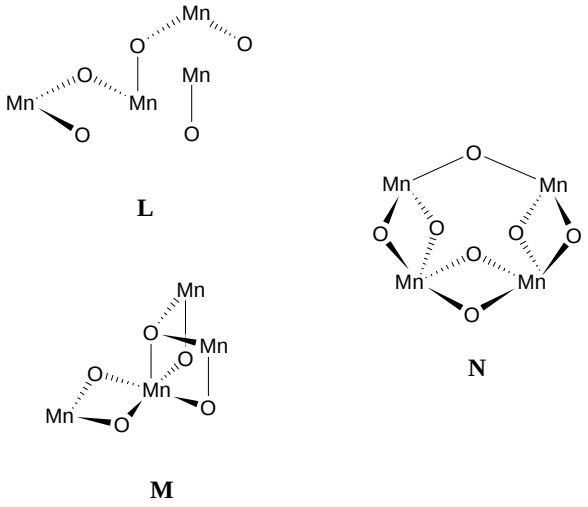

Figure 3-13: Modified structural models for the active site of the OEC in PS II. Structures L and M are modifications of structure I from Figure 3-12, and structure N is a modification of structure J from Figure 3-12.

Structures I and J, with two and zero 3.3 Å Mn–Mn distances, respectively, are not consistent in their current form with the EXAFS data, which is best fit with one 3.3 Å Mn–Mn distance (see Table 3-5), However, they can be modified slightly, as shown in

Figure 3-13, to make them consistent with the EXAFS data. By slightly changing the arrangement of the Mn and oxygen atoms in structure I (Figure 3-12), structures L and M in Figure 3-13 can be created. These topological structures are quite similar to the one proposed by Siegbahn based on density functional theory calculations,[77] although Ca is not included in structures L and M and is an integral part of the Siegbahn model. By adding a mono-μ-oxo Mn–Mn bridge to structure J (Figure 3-12), structure N in Figure 3-13 can be created. Thus, structure G from Figure 3-12 and structures L, M, and N from Figure 3-13 are the favored structures for a topological model of the OEC based on the insights developed from the EXAFS spectroscopic results in this chapter.

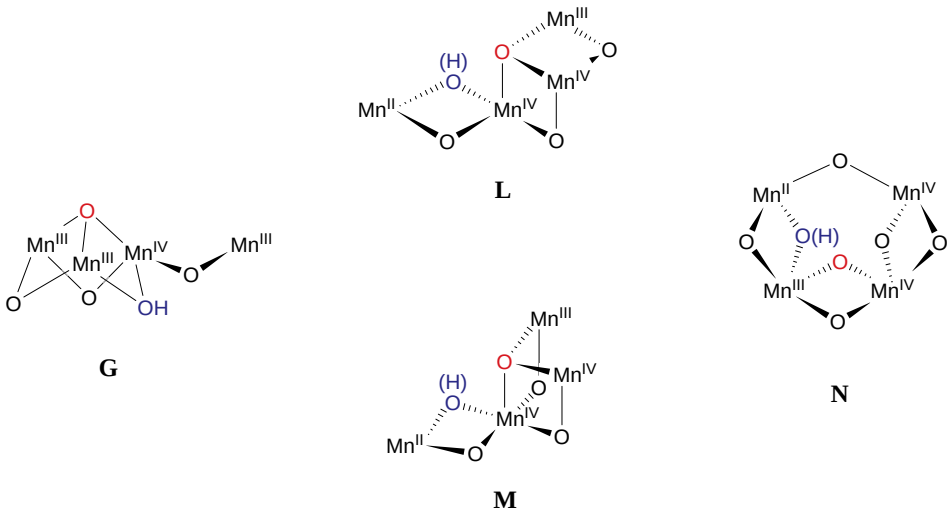

Figure 3-14: Structural models for the active site of the OEC in the S_0 state. Basic structures are taken from Figure 3-13 and Figure 3-12. The di-μ-oxo moiety giving rise to the 2.85 Å Mn–Mn distance in each model contains a μ-oxo or μ-hydroxo bridge colored in blue; the two remaining di-μ-oxo Mn–Mn distances are 2.7 Å. The site of the proposed oxyl radical in the S_3 state is denoted in red for each model (see text for details).

Using the three topological models presented in Figure 3-13 plus structure G from Figure 3-12 as a framework, four possibilities for the structure and oxidation states of Mn in the S_0 state are shown in Figure 3-14. Each model incorporates the conclusions from

the EXAFS experiments detailed in this chapter and the conclusions about oxidation states presented in Chapter 2. The detailed description of each model and how each model accounts for the experimental data from the OEC is presented below.

Of the four proposed models in Figure 3-14, structure G provides the best explanation of the results from EXAFS experiments on the S_3 state, which are that all of the 2.7 Å Mn–Mn distances in the S_2 state increase in distance in the S_3 state.[69] This was explained by Yachandra et al.[36] and Liang et al.[69] using structure A in Figure 3-12 as a structural framework and incorporating an oxyl radical in a μ-oxo bridging position in the S_3 state. This provided an explanation for an increase in distance of one di-μ-oxo-bridged Mn–Mn moiety from 2.7 Å in the S_2 state to 3.0 Å in the S_3 state, and it also rationalized the conclusion from XANES experiments[98] (which has since been reinforced by the XANES and Kβ XES experiments presented in Chapter 2) that no Mn-centered oxidation occurs during the $S_2 \rightarrow S_3$ transition. However, it was difficult to understand why, in structure A, the other di-μ-oxo Mn–Mn moiety also increased in distance in the S_3 state even though it was fairly isolated from the proposed oxyl radical. Thus, it would be more logical if the structure of the OEC was in fact more 'tied together' than is shown in structure A, which would more easily explain the lengthening of all di-μ-oxo Mn–Mn motifs in the S_3 state. If the topological model shown as structure G in Figure 3-14 is used, formation of an oxyl radical at the oxygen denoted in red in Figure 3-14 would cause all three di-μ-oxo Mn–Mn moieties to increase in distance, as seen in the S_3 state. O–O bond formation in the transient S_4 state could then occur between the oxyl radical and the oxygen denoted in blue in Figure 3-14.

In the S_0 state, the presence of Mn(II) and/or protonation of a μ-oxo bridge can account for the increase of one 2.7 Å Mn–Mn distance to 2.85 Å, as explained above. However, with structure G, the presence of Mn(II) in the S_0 state would cause two out of three 2.7 Å Mn–Mn distances to increase, not one out of three. Because this contradicts the results from the EXAFS experiments, the use of structure G necessitates assigning the oxidation states of Mn in the S_0 state as $Mn_4(III_3,IV)$ and protonating one of the μ-oxo bridges in the S_0 state (shown in blue in Figure 3-14). Although the XANES and Kβ XES spectra presented in Chapter 2 are easier to explain if Mn(II) is present in the S_0 state, Mn(II) is definitely not required, and $Mn_4(III_3,IV)$ is an acceptable alternative.

The remaining structures in Figure 3-14, structures L, M, and N, can all incorporate Mn(II) in the S_0 state and increase only one of the Mn–Mn distances. Because it is unclear from model chemistry if protonation of a μ-oxo bridge would be required, the proton is denoted in blue in Figure 3-14 as optional for all three models. The oxygen which becomes the oxyl radical in the S_3 state is shown in red for each structure. Because this oxygen is tri-μ-oxo-bridged in structures L and M, these two structures can more easily rationalize the increase in all Mn–Mn distances in the S_3 state than structure N, in which the oxyl-radical oxygen is part of only one di-μ-oxo bridge.

In each of the four structures shown in Figure 3-14, the O–O bond formation in the transient S_4 state is proposed to occur between the oxyl radical and the oxygen atom denoted in blue in Figure 3-14. An alternative for each structure is to form the O–O bond between the oxyl radical and either exogenous or terminally bound water or hydroxide, as shown for structure B in Figure 2-14 from Chapter 2.

In addition to the constraints imposed by considering the EXAFS and EPR data from the OEC, a preliminary structure of the OEC has been recently reported based on X-ray crystallographic data from PS II.[60,265] These data are most consistent with an OEC which is asymmetric and shaped somewhat like a pear. However, as confirmed by Mn and Sr EXAFS studies,[206,207] the OEC is most accurately described as a Mn/Ca heteronuclear cluster; therefore, Ca should be incorporated into each of the proposed structures in Figure 3-14 before they are compared with the results from X-ray crystallographic studies. If Ca were not included, structure N in Figure 3-14 would be considered unlikely because of its high symmetry. However, after including 1 – 2 Mn–Ca distances at ~3.4 Å, as required from the EXAFS experiments,[206,207] all four structures in Figure 3-14 can be made compatible with the 'pear' constraint.

Structures L and M are of particular interest if Ca is included, because this generates a pseudo Mn–Ca cubane as suggested by Siegbahn in his DFT-based mechanistic proposal.[77] However, one of the predictions from the Siegbahn mechanism is that the Mn–Ca distances should decrease by ~0.1 Å during each S-state transition. As shown by the curve-fitting results in Table 3-5, this is not borne out by the fits to the EXAFS data pertaining to the $S_0 \rightarrow S_1$ transition; however, the Mn–Ca distance is significantly longer than detected in previous experiments.[207] Nevertheless, many other predictions derived from this mechanism, such as the energetic preference for oxyl radical formation in lieu of Mn oxidation during the $S_2 \rightarrow S_3$ transition, are supported by experimental data.

The finding from the current study that it is likely that three di-μ-oxo Mn–Mn motifs exist in the OEC has profound effects on the structural and mechanistic questions

that exist about the mechanism of water oxidation in the OEC. The new topological models shown in Figure 3-13 and Figure 3-14 evolved from consideration of the results presented in this chapter and represent new structural possibilities for the OEC that have not been widely considered in previous studies. It is expected that significant insights will come from consideration of experimental data in terms of these new models. This will be particularly revealing for the interpretations of EXAFS data from oriented PS II membranes in various S-states[161,202,205,236] and the interpretation of the ENDOR, ESEEM, and continuous-wave EPR spectra from the S_2 and S_0 states.[44,74]

Appendix

Calculation of theoretical resolution limit in EXAFS

The ability of the EXAFS technique to resolve the presence of similar backscatterers at two closely separated distances is well known to be dependent on •***R***, the difference in absorber-backscatterer distances (Å), and •***k***, the width of the *k*-space EXAFS data set ($Å^{-1}$). When EXAFS oscillations from two backscatterers at closely separated distances are superimposed, the addition of the sinusoidal terms from Eq. 3-2 ($\sin[2kR_1]$ and $\sin[2kR_2]$, if the phase shifts are neglected) generates a local amplitude minimum in the *k*-space spectrum from the addition of 2 sine waves with different frequencies; this is commonly known as a beat. The magnitude of R_1 - R_2 determines at what value of *k* the beat will appear. This is shown by the trigonometric identity in Eq. 3-8:

$$\sin a + \sin b = 2\cos\left(\frac{a-b}{2}\right)\sin\left(\frac{a+b}{2}\right) \qquad \text{Eq. 3-8}$$

Eq. 3-9 shows the application of Eq. 3-8 to the current problem:

$$\sin 2kR_1 + \sin 2kR_2 = 2\cos\left(k\left[R_1 - R_2\right]\right)\sin\left(k\left[R_1 + R_2\right]\right) \qquad \text{Eq. 3-9}$$

The beat in the *k*-space spectrum arises from the $\cos\left(k\left[R_1 - R_2\right]\right)$ term in Eq. 3-9. When the operand of the cosine function, $k\left[R_1 - R_2\right]$, equals zero, the first beat will appear. This occurs when Eq. 3-10 is true:

$$k\left[R_1 - R_2\right] = \frac{\pi}{2} \qquad \text{Eq. 3-10}$$

Thus, the minimum •*R* necessary to see a beat in the *k*-space spectrum is most accurately depicted by Eq. 3-11, assuming that the *k*-space window is wide enough to see the beat:

$$\Delta R = \frac{\pi}{2k_{max}} \qquad \text{Eq. 3-11}$$

However, Eq. 3-11 is rarely[266,267] if ever quoted in recent literature[268-270] when the theoretical resolution limit is calculated; two other formulas are commonly seen instead. Eq. 3-12[57,217] and Eq. 3-13:[271-273]

$$\Delta R \Delta k \approx 1 \qquad \text{Eq. 3-12}$$

$$\Delta R \Delta k = \frac{\pi}{2} \qquad \text{Eq. 3-13}$$

A necessary assumption for Eq. 3-12 to be valid is that, for the *k*-range used in the experiments reported in this chapter, the minimum *k* value is 4.2 $Å^{-1}$, while a necessary assumption for Eq. 3-13 to be valid is that the minimum *k* value is 0 $Å^{-1}$. Because neither of these assumptions is valid for the data shown in this chapter, it is not surprising that three formulas, Eq. 3-11, Eq. 3-12, and Eq. 3-13, predict different minimum resolution limits. Eq. 3-11 predicts the correct resolution limit of 0.14 Å with data collected to $k = 11.5$ $Å^{-1}$; however, for a *k*-range of 3.5 – 11.5 $Å^{-1}$, Eq. 3-12 predicts a resolution limit of 0.125 Å, and Eq. 3-13 predicts a resolution limit of 0.2 Å. With the predicted Mn–Mn Peak II distance heterogeneity in the S_0 state of 0.1 – 0.15 Å based on curve-fitting results, it is important to relate this to the correct theoretical limit shown in Eq. 3-11 and avoid using the more commonplace but inappropriate formulas in Eq. 3-12 and Eq. 3-13. This is particularly important concerning Eq. 3-13, because k_{max} is significantly larger than •***k*** when EXAFS data analysis begins at $k = 3.5$ $Å^{-1}$.

Comparison of deconvolution methods for S_0-state EXAFS spectra

Deconvolution of the 3F EXAFS spectra into pure S_0-state EXAFS spectra can be performed in two ways. The S_1-state spectrum can be subtracted from the 3F spectrum after normalization in *E*-space and before conversion into k^3-space. Alternatively, the S_1-state spectrum can be subtracted from the 3F spectrum after both spectra have been converted into k^3-space using the methods detailed in the Materials and Methods section. Although the former method is preferred because only one round of background removal is performed to the S_0-state spectrum, the latter method is often used because the signal-to-noise ratio is often insufficient for subtraction before conversion into k^3-space. For the results presented in this chapter, the high signal-to-noise ratio permitted the

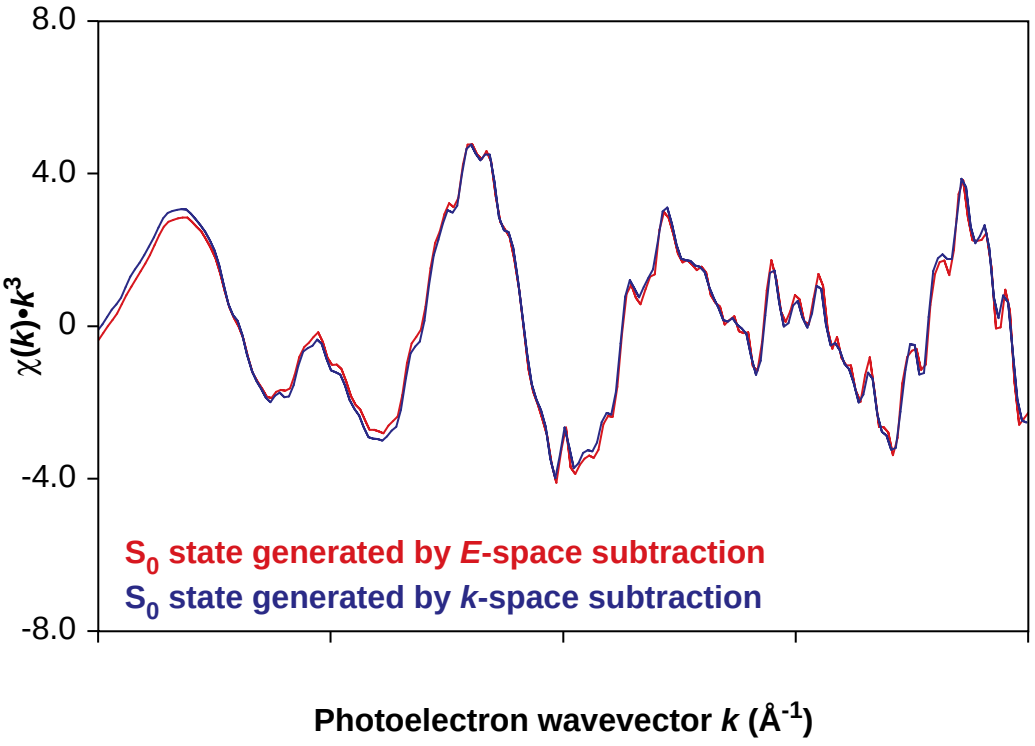

Figure 3-15: Mn K-edge EXAFS spectra of the S_0 state generated by deconvolution in *E*-space (red) and in k^3-space (blue). The data analysis of the S_0 state reported in this chapter is based on the deconvolution in *E*-space.

deconvolutions to be performed before conversion into k^3-space. However, to ensure that this was not affecting the data analysis, the deconvolution was performed after the conversion into k^3-space. Figure 3-15 and Figure 3-16 show that the resulting spectra are virtually identical. Furthermore, the curve-fitting results to the Fourier isolates generated from both of the S_0-state spectra shown in Figure 3-16 show virtually identical results for the two deconvolution methods (data not shown); thus, the choice of deconvolution method did not affect the data analysis.

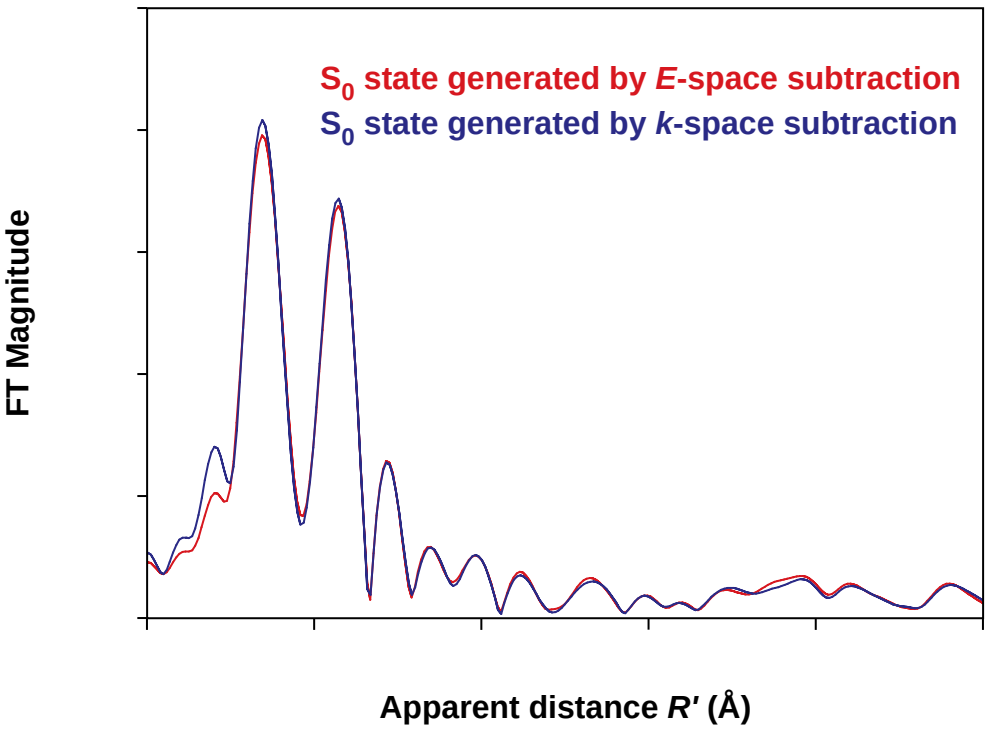

Figure 3-16: Fourier transforms of Mn K-edge EXAFS spectra from Figure 3-15 of the S_0 state generated by deconvolution in *E*-space (red) and in k^3-space (blue). The data analysis of the S_0 state reported in this chapter is based on the deconvolution in *E*-space.

Consideration of possible radiation damage effects

As described in the Materials and Methods section, the experimental protocol of the S_0-state EXAFS experiments was designed to minimize and monitor radiation damage by collecting only 8 EXAFS scans on each separate region of the sample. To evaluate the effects of possible radiation damage on the EXAFS spectra, the average k^3-space spectrum of the first set of EXAFS scans collected on each sample region of the 3F samples was compared to the average k^3-space spectrum of the second set of EXAFS scans collected on each sample region. Each set corresponded to four EXAFS scans, each of ~20 min duration. Figure 3-17 shows that there is very little change between the

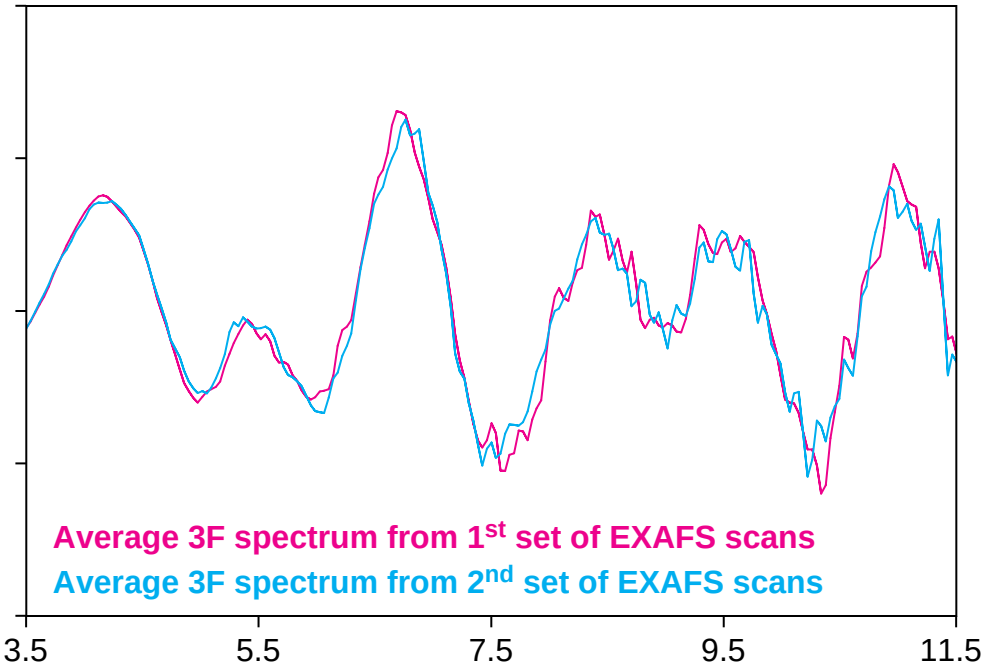

Figure 3-17: Average k^3-weighted EXAFS spectra from 3F samples showing the effects of radiation damage. The average spectrum from the first set of EXAFS scans on each region of the sample is shown in pink, and the average spectrum from the second set of EXAFS scans on each region of the sample is shown in light blue. Each set of spectra consisted of four EXAFS scans, each of ~20 min duration.

two k^3-space spectra from the 3F samples. Furthermore, the curve-fitting results from both of the spectra shown in Figure 3-17 are virtually identical (data not shown). Therefore, radiation damage effects are assumed to be minimal for the EXAFS spectra presented in this chapter.

Curve-fitting results from Peaks I+II and II+III

As mentioned in the Results section, the effects of possible Fourier isolation artifacts to the curve-fitting results was examined by isolating and fitting the Fourier peaks as pairs (Peaks I+II and Peaks II+III). As shown in Table 3-6 and Table 3-7, these results are essentially identical to those shown in Table 3-2, Table 3-3, Table 3-4, and

Table 3-6: Two- and three-shell simulations of Fourier peaks I and II from the S_0-state and S_1-state samples.

Fit #	sample	shell	R (Å)	N	σ^2 (Å^2)	$\bullet E_0$ [b]	Φ (x 10^{-3})	ε^2 (x 10^{-5})
1	S_0 Grand Add	Mn–O	1.85	2.5[c]	0.005	-20	0.67	0.66
		Mn–Mn	2.72	1.19	0.004			
2	S_0 Grand Add	Mn–O	1.85	2.5[c]	0.005	-20	0.65	0.64
		Mn–Mn	2.67	0.61[d]	0.002[c]			
		Mn–Mn	2.77		0.002[c]			
3	S_0 Grand Add	Mn–O	1.86	2.5[c]	0.005	-17	0.59	0.58
		Mn–Mn	2.71	1.05[e]	0.002[c]			
		Mn–Mn	2.84	0.53[e]	0.002[c]			
4	S_1	Mn–O	1.83	2.5[c]	0.002	-20	1.23	1.20
		Mn–Mn	2.72	1.19	0.004			
5	S_1	Mn–O	1.83	2.5[c]	0.005	-20	1.23	1.205
		Mn–Mn	2.71	0.60[d]	0.002[c]			
		Mn–Mn	2.71		0.002[c]			
6	S_1	Mn–O	1.86	2.5[c]	0.005	-20	1.23	1.20
		Mn–Mn	2.71	0.80[e]	0.002[c]			
		Mn–Mn	2.72	0.40[e]	0.002[c]			

[a]fit parameters and quality-of-fit parameters are described in Materials and Methods; [b]$\bullet E_0$ was constrained to be equal for all shells within a fit; [c]parameter fixed in fit; [d]the Mn–Mn N_1:N_2 ratio was fixed to 1:1 for this fit; [e]the Mn–Mn N_1:N_2 ratio was fixed to 2:1 for this fit

Table 3-5 for the S_1-state and S_0 Grand Add samples. This was also true for pairwise fits for each of the individual S_0-state spectra S_0A through S_0F (data not shown). Thus, the effects of the Fourier isolation procedure are found to be negligible for the fits presented in Table 3-2, Table 3-3, Table 3-4, and Table 3-5.

Table 3-7: Two- and three-shell simulations of Fourier peaks II and III.

Fit #	sample	shell	R (Å)	N	σ^2 (Å^2)	$\bullet E_0$ [b]	Φ (x 10^{-3})	ε^2 (x 10^{-5})
1	S_0 Grand Add	Mn–Mn	2.73	1.14	0.004	-18	0.25	0.33
		Mn–Mn	3.28	0.5[c]	0.005			
2	S_0 Grand Add	Mn–Mn	2.69	0.57[d]	0.002[c]	-17	0.25	0.33
		Mn–Mn	2.77		0.002[c]			
		Mn–Mn	3.28	0.5[c]	0.004			
3	S_0 Grand Add	Mn–Mn	2.71	0.94[e]	0.002[c]	-15	0.22	0.29
		Mn–Mn	2.83	0.47[e]	0.002[c]			
		Mn–Mn	3.31	0.5[c]	0.004			
4	S_0 Grand Add	Mn–Mn	2.73	1.10	0.003	-16	0.23	0.30
		Mn–Mn	3.26	0.5[c]	0.002[c]			
		Mn–Ca	3.45	0.25[c]	0.002[c]			
5	S_0 Grand Add	Mn–Mn	2.70	0.56[d]	0.002[c]	-16	0.23	0.30
		Mn–Mn	2.77		0.002[c]			
		Mn–Mn	3.27	0.5[c]	0.002[c]			
		Mn–Ca	3.45	0.24[c]	0.002[c]			
6	S_0 Grand Add	Mn–Mn	2.71	0.83[e]	0.002[c]	-15	0.21	0.28
		Mn–Mn	2.81	0.41[e]	0.002[c]			
		Mn–Mn	3.28	0.5[c]	0.002[c]			
		Mn–Ca	3.47	0.25[c]	0.002[c]			
7	S_1	Mn–Mn	2.72	1.05	0.001	-18	0.48	0.47
		Mn–Mn	3.23	0.5[c]	0.005			
8	S_1	Mn–Mn	2.73	0.63[d]	0.002[c]	-17	0.50	0.49
		Mn–Mn	2.73		0.002[c]			
		Mn–Mn	3.26	0.5[c]	0.002[c]			
9	S_1	Mn–Mn	2.73	0.84[e]	0.002[c]	-17	0.50	0.49
		Mn–Mn	2.73	0.42[e]	0.002[c]			
		Mn–Mn	3.26	0.5[c]	0.002[c]			
10	S_1	Mn–Mn	2.73	1.26	0.002[f]	-16	0.46	0.39
		Mn–Mn	3.24	0.5[c]	0.002[c]			
		Mn–Ca	3.42	0.25[c]	0.002[c]			
11	S_1	Mn–Mn	2.73	0.63[d]	0.002[c]	-16	0.46	0.46
		Mn–Mn	2.73		0.002[c]			
		Mn–Mn	3.24	0.5[c]	0.002[c]			
		Mn–Ca	3.43	0.25[c]	0.002[c]			
12	S_1	Mn–Mn	2.73	0.84[e]	0.002[c]	-16	0.46	0.46
		Mn–Mn	2.73	0.42[e]	0.002[c]			
		Mn–Mn	3.24	0.5[c]	0.002[c]			
		Mn–Ca	3.42	0.25[c]	0.002[c]			

[a]fit parameters and quality-of-fit parameters are described in Materials and Methods; [b]$\bullet E_0$ was constrained to be equal for all shells within a fit; [c]parameter fixed in fit; [d]the Mn–Mn N_1:N_2 ratio was fixed to 1:1 for this fit; [e]the Mn–Mn N_1:N_2 ratio was fixed to 2:1 for this fit; [f]if the Debye-Waller parameter for this fit was not fixed, it went to a chemically unreasonable value of 0 Å^2

Chapter 3 Acknowledgments

This research was supported by the National Institutes of Health (GM-55302), and the Director, Office of Basic Energy Sciences, Division of Energy Biosciences of the U.S. Department of Energy (DOE), under Contract DE-AC03-76SF00098. Synchrotron radiation facilities were provided by the Stanford Synchrotron Radiation Laboratory (SSRL) which is operated by the Department of Energy, Office of Basic Energy Sciences. The SSRL Biotechnology Program is supported by the National Institutes of Health, National Center of Research Resources, Biomedical Technology Program, and by the Department of Energy, Office of Biological and Environmental Research.

Chapter 4 : Discovery of the S_0-state EPR multiline signal in native samples

Introduction

The photosynthetic oxidation of water to molecular oxygen is energetically driven by light-induced charge separations in the reaction center of photosystem II (PS II). The reaction is catalyzed by a tetranuclear manganese cluster contained in the oxygen evolving complex (OEC). The OEC cycles through five different redox states termed S_0 to S_4, with S_1 being the dark-stable state. Oxygen is released during the $S_4 \rightarrow S_0$ transition.[36] The removal of one electron from the OEC on each S-state transition leads to the idea that alternate S-states should be paramagnetic because of their odd-electron number. The multiline EPR signal, which is the hallmark of the S_2 state, establishes the odd-electron character of the Mn cluster in S_2.[50,51] The S_1 state, one-electron reduced from S_2, is paramagnetic but of even electron number, and a non-Kramers EPR signal is observed in parallel-polarized EPR.[47-49] Because the S_0 state is reduced by one further electron, it is expected to be an odd-electron or Kramers state observable with conventional EPR. Hence, it was somewhat surprising that no EPR signal had been reported for this state. This problem was recently resolved by Messinger et al. who observed a new EPR multiline signal in an S_0^* state, an S_0-like state produced by reduction of the S_1 state by hydroxylamine or hydrazine.[83] The essential ingredient was the addition of 1.5 % methanol. In addition, Åhrling et al.[46] discovered an identical EPR multiline signal for the physiological S_0 state using more dilute samples which were turned over by saturating laser-flash excitation in the presence of 3 % methanol. Goussias et al.[274] found a different EPR multiline signal by incubation of S_1 samples with NO• at -30°C in the absence of methanol. This signal may originate from a different kind

of S_0 state or from NO• bound to the S_1 state. This chapter describes the observation of an EPR signal in a physiological S_0 state produced by three-flash illumination of dark-adapted PS II membranes. This EPR signal is sufficiently similar to that produced by NH_2OH treatment that, from the perspective of EPR, one need no longer distinguish the states prepared by the two methods. Furthermore, this chapter describes a broad EPR signal for the S_0 state in absence of methanol.

Materials and Methods

Dark-adapted spinach PS II membranes[110,111] were enriched in the S_0 state by the following flash procedure: aliquots of 3 mL volume were illuminated at a chlorophyll concentration of 1 mg/mL in ice-cold pH 6.5 buffer (5 mM $CaCl_2$, 5 mM $MgCl_2$, 15 mM NaCl, 50 mM MES, 400 mM sucrose) with one pre-flash (Xe flashlamp, 13 µs FWHM, 5 J per pulse; pathlength ~ 2 mm), further dark-adapted on ice for 90 – 120 min and illuminated with three Xe-flashes (0.5 Hz). Before centrifugation (30 min, 40,000x *g*, 4°C) 1.5 % methanol (v/v), 20 µM phenyl-*para*-benzoquinone (PPBQ; 50 mM in methanol or DMSO) and/or 2.5 µM carbonyl cyanide p-(trifluoromethoxy) phenylhydrazone (FCCP; 2.5 mM in ethanol) were added as indicated in Figure 4-1. The pellets (~30 mg Chl/mL) were transferred in the dark into special EPR Lucite holders of 120 µL volume and frozen in liquid N_2. PPBQ was added to oxidize the acceptor-side quinones of PS II, which otherwise produce iron-quinone EPR signals at $g = 1.9$ and 1.8.[275] FCCP was used to accelerate the deactivation of the S_2 and S_3 states of PS II to the S_1 state[210] and the reduction of the stable tyrosine radical of PS II,[211] Y_D^{ox}, which prevents the reaction $S_0 + Y_D^{ox} \rightarrow S_1 + Y_D^{red}$ ($t_{1/2}$ = 30 min, 5°C).[177] All measurements were recorded using a Varian E-109 X-band spectrometer with an E-102 microwave bridge and an Air Products helium flow cryostat. Instrument conditions: microwave power, 30 mW;

modulation frequency, 100 kHz; modulation amplitude, 20 G; time constant, 0.5 sec; scan time, 4 min.

Results and Discussion

Figure 4-1A shows the EPR difference spectrum from the S_0-state sample (minus S_1) prepared with FCCP, PPBQ, and methanol. A multiline signal clearly different from the well-known S_2-state EPR multiline signal (Figure 4-1B, same additions) is observed. Most of the peaks are out-of-phase between the two signals (for examples, see dashed lines in Figure 4-1). The average splitting of the hyperfine lines is very similar, about 85 – 90 G, but the values for the S_0-state signal occur over a wider range (70 – 110 G) than those for the S_2-state EPR multiline signal (80 – 100 G). Although it is difficult at the current signal-to-noise ratio to clearly identify the last peak at the high field side of the S_0-state EPR multiline signal, a careful study of the outer wings (see inset in Figure 4-1A) and a comparison of spectra obtained from several independent samples (data not shown) show that the total spectral breadth is 2200 – 2400 G and the total number of peaks is 24 – 26, compared to 18 – 20 reported for the S_2-state.[14,50] Therefore, the S_0-state EPR multiline signal is about 300 – 500 G wider than the S_2-state EPR multiline signal. This extra width is exclusively on the high field side of the S_0-state EPR multiline signal, which gives rise to an asymmetry of this EPR signal, indicative of an average g value below $g = 2.0$. In the absence of FCCP, mixtures of S_0-state and S_2-state EPR multiline signals were observed, which displayed in their outer low-field wings peaks of the S_0 multiline (data not shown). This indicates that the S_0-state EPR multiline signal can be generated in the absence of FCCP. The fraction of centers in the S_0 state in sample A (Figure 4-1) is about 50 %. This was determined by converting the residual S_1-state population into the S_2 state by 200 K illumination and comparison of the resulting S_2-state EPR multiline signal amplitude with that of sample B (Figure 4-1). FCCP does

not affect the amplitude of the S_2-state EPR multiline signal generated by 200 K illumination at the concentration used in this study (data not shown). The S_0-state minus S_1-state difference spectrum obtained in the absence of methanol is shown in Figure 4-1C. A broad ~2400 G wide signal with only poorly resolved hyperfine structure is observed, showing i) that methanol is important for observing the hyperfine lines and ii) that the S_0 state also has an EPR signal in the absence of methanol. The effect of methanol, a water analog, on the amplitude of the hyperfine peaks may be explained by binding at or near the Mn cluster and thereby hypothetically changing in a subtle way the hyperfine couplings of the involved Mn ions. Support for this speculation comes from the recent finding that methanol binds to a binuclear Mn(III, IV) complex[276] and that methanol binds to the S_2 state.[277] Alternatively, methanol may simply reduce the hyperfine linewidth through a reduction of inhomogeneity around the Mn cluster. Figure 4-1D displays a S_0^*-state EPR multiline signal from a sample prepared using NH_2OH as a reductant.[83] Only minor differences (if any) can be seen between the S_0- and S_0^*-state multiline signals. Based on this finding, the two states are proposed to be identical.

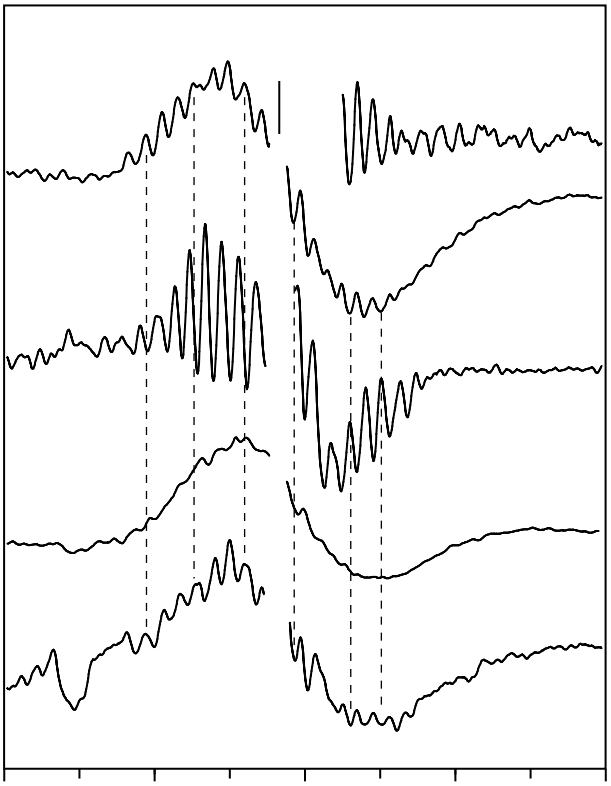

Figure 4-1: X-band EPR difference spectra from PS II membranes at 7 K: **(A)** physiological S_0 state minus S_1 state in presence of methanol (1.5 %, v/v), FCCP and PPBQ, average of 30 scans each; the inset (4x amplified) was obtained after subtraction of a three domain spline that was fit to that section of the EPR trace (this procedure removes the broad underlying signal); **(B)** S_2 state minus S_1 state with same additions, induced by 200 K continuous illumination (6 min), average of 25 scans each; **(C)** S_0 state minus S_1, both without methanol, but with PPBQ and FCCP addition, average of 15 scans each; **(D)** S_0^* state induced by NH_2OH incubation in presence of 1.5 % methanol (v/v) and 1 mM EDTA minus S_1 with the same additions, average of 15 scans each. For clarity, spectrum D is amplified by a factor of 3 relative to the other spectra; the asterisk in the spectrum labels a subtraction artifact that is probably due to different amounts of low-potential cytochrome b_{559}^{+} in the S_0^*-state sample compared to the S_1 control. The $g = 2$ regions containing the Y_D^{ox} radical signal were deleted for clarity. In FCCP-treated samples, the amplitude of the Y_D^{ox} signal was 15 – 30 % of the value from untreated samples.

The S_2 state has under certain conditions a second EPR signal at $g = 4.1$.[14,52,53] Difference spectra in the field range of 400 – 2400 G were therefore taken for the different S_0-state samples (± methanol). No indications for a $g = 4.1$ signal were found in any of the samples, but all displayed small reproducible changes at higher g values. These require further study to clarify their origin.

Mn K-edge XANES (X-ray absorption near edge structure) has been shown to directly reflect the oxidation state of the Mn, and the edge shifts exhibited upon S-state changes lend strong support to the model of one-electron oxidations of the Mn cluster for the $S_0 \rightarrow S_1$ and $S_1 \rightarrow S_2$ transitions. Based on comparison with X-ray absorption edge positions and shapes for model complexes, the following Mn redox states have been proposed for the different S-states of the OEC: S_0 (II, III, IV_2) or (III_3, IV), S_1 (III_2, IV_2), S_2 (III, IV_3), S_3 (III, IV_3)$^{\cdot}$.[98,101,148,201] It has been observed for binuclear Mn complexes[279] and in Mn catalase[280,281] that the spectral width of the EPR multiline signals is greater for the (II, III) than for the (III, IV) forms. The larger spectral width of the S_0-state EPR multiline signal compared to the S_2-state EPR multiline signal may therefore be indicative of a Mn^{II} center in the S_0 state.[83] To test this idea, simulations of the S_0 EPR multiline signal using previously employed values of the projected Mn hyperfine constants (Mn^{II}:

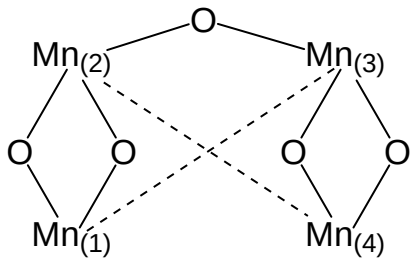

Figure 4-2: Schematic drawing of the presumed structure of the Mn cluster in PS II used for EPR spectral simulations. Solid lines represent chemical bonds, while the dashed lines indicate the spin coupling scheme used to obtain the spins S_{13} and S_{24} in the vector-coupling approach.

A' = 85 – 100 G, Mn^{III}: A' = 80 – 95 G and Mn^{IV}: A' = 70 – 85 G)[280,281] were performed using second-order perturbation theory.[50,278] The results for both binuclear and a C_{2v}-symmetric tetranuclear species (see Figure 4-2) with various combinations of oxidation states are presented in Table 4-1. Assuming a tetranuclear origin for the S_0-state EPR multiline signal, it was possible to simulate the main features of the S_0-state EPR multiline signal, i.e. the number of lines, the spectral width and the relatively weak hyperfine structure on top of a broad signal, within this simple model by using the average of any set of the calculated parameters (Table 4-1). The current level of simulation does not allow a further distinction between the (II, III_3), (II, III, IV_2) and (III, IV_3) oxidation states. In contrast, satisfactory simulations, especially of the broad 'underlying' feature, have not been achieved assuming isotropic (see Table 4-1) or axially symmetric *g* and A values for the (II, III) or (III, IV) binuclear clusters. However, in rhombic simulations with largely anisotropic *g* and A values, these features could be largely reproduced (see Table 4-2 and Figure 4-3 for examples of EPR simulations). Therefore, it is concluded that higher level simulations and measurements at other microwave frequencies are necessary to reveal the degree of anisotropy in the S_0 EPR multiline signal and to resolve the nature of the Mn cluster.

Table 4-2: Simulation parameters for EPR spectral simulation of the S_0-state EPR multiline signal. These values were used to generate the simulated EPR spectra shown in Figure 4-3.

the numbers in parentheses give the Mn oxidation states in the order $Mn_{(1)}$, $Mn_{(2)}$, $Mn_{(3)}$, $Mn_{(4)}$. The $|A_i|$ values were derived from the A_i values given in the text and from a general formula for the isotropic hyperfine coupling constants $A_i = A_i'(\mathbf{S}\cdot\mathbf{S}_1/S_1^2)(\mathbf{S}\cdot\mathbf{S}/S^2)$ for the Mn clusters[50,78] with $i = 1 - 4$ for a tetranuclear species (see Figure 4-2 for an illustration of the spin coupling scheme). The spectral width was calculated according to $3(|A_1| + |A_2|)$ for the binuclear systems and $3(|A_1| + |A_2| + |A_3| + |A_4|)$.

Tetranuclear cluster

parameter	(II,III$_3$)	(II,III,IV$_2$)	(III$_3$,IV)
g	1.9	1.9	1.9
$\|A_1\|$ (G)	188.5	192.5	145.5
$\|A_2\|$ (G)	117	117	145.5
$\|A_3\|$ (G)	142.5	96.5	117
$\|A_4\|$ (G)	117	77.5	77.5
linewidth (G)	40	40	40
spectral width (G)	3080	2640	2650
Figure 4-3 label	A	B	C

Binuclear cluster

	Axial		Rhombic	
parameter	(II,III)	(III,IV)	(II,III)	(III,IV)
g_x	1.9	1.9	1.7	1.7
g_y	1.9	1.9	1.8	1.85
g_z	2.0	2.0	2.0	2.0
$\|A_{1x}\|$ (G)	198	160	198	160
$\|A_{1y}\|$ (G)	198	160	214	173.5
$\|A_{1z}\|$ (G)	233	190	233	190
$\|A_{2x}\|$ (G)	107	70	107	70
$\|A_{2y}\|$ (G)	107	70	114.5	77
$\|A_{2z}\|$ (G)	127	85	127	85
linewidth (G)	30	30	30	30
spectral width (G)	1950	1470	2390	1960
Figure 4-3 label	D	E	F	G

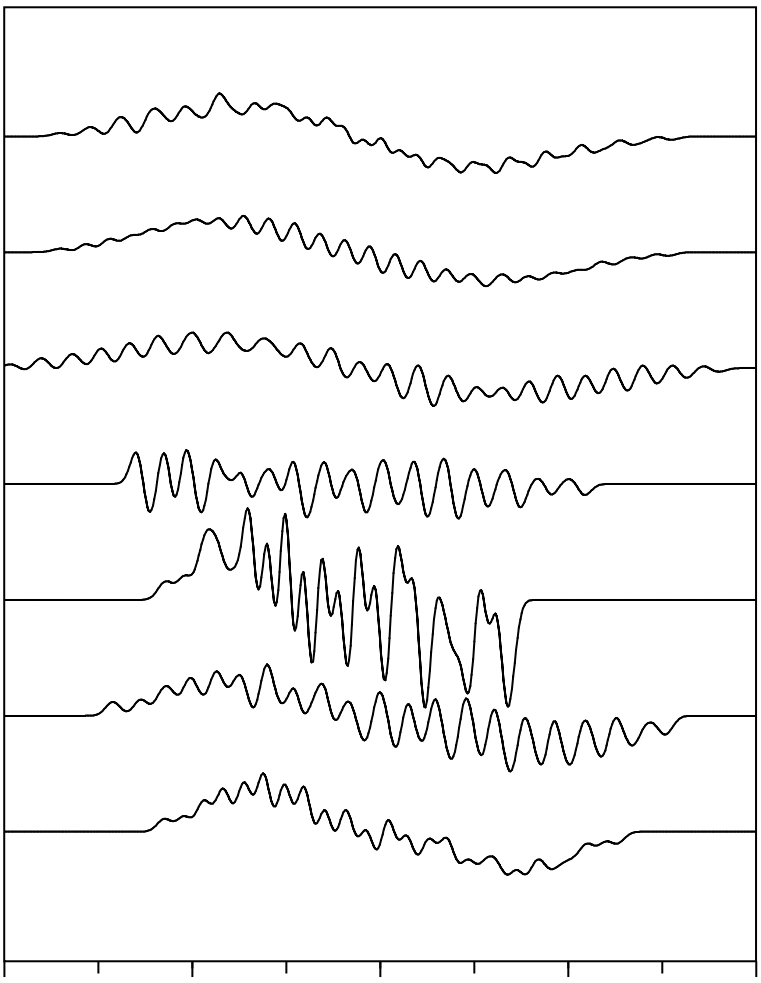

Figure 4-3: Simulated S_0-state EPR spectra using the parameters listed in Table 4-2 and the vector coupling scheme shown in Figure 4-2. All spectra have been normalized to a double-integral value of 1 except for spectrum D, which was normalized to a double-integral value of 0.2 for presentation purposes. Brief descriptions of the simulations are as follows: **(A)** $Mn_4(II,III_3)$ tetranuclear cluster simulation; **(B)** $Mn_4(II,III,IV_2)$ tetranuclear cluster simulation; **(C)** $Mn_4(III_3,IV)$ tetranuclear cluster simulation; **(D)** $Mn_2(II,III)$ binuclear cluster axial simulation; **(E)** $Mn_2(III,IV)$ binuclear cluster axial simulation; **(F)** $Mn_2(II,III)$ binuclear cluster rhombic simulation; **(G)** $Mn_2(III,IV)$ binuclear cluster rhombic simulation.

Chapter 5 : XANES and EXAFS studies of single-crystal Mn complexes

Introduction

Ever since the seminal EXAFS experiments by Kirby et al.[58] and XANES experiments by Goodin et al.[59] of Mn in the OEC, X-ray spectroscopic methods have been perhaps the most informative techniques that have been used to derive detailed information about the oxidation states of and the environment surrounding Mn in the OEC.[36,38,40] Information obtained using these techniques has been an integral component of proposed topological models of the OEC.[36,69,71,74,77] However, most of the X-ray spectroscopic studies were performed on randomly oriented PS II membranes; thus, no angle dependence of XANES or EXAFS features was observed.

One of the characteristic features about synchrotron radiation is that, when electrons or positrons travelling at relativistic speeds are directed into circular orbits by the magnetic field from bending magnets, beams of X-rays are emitted tangentially which are highly polarized in the plane of the orbit.[216,282,283] To exploit the plane-polarized nature of synchrotron radiation, PS II membranes can be oriented on a substrate such that the membrane planes are roughly parallel to the substrate surface. This imparts a one-dimensional order to these samples; while the *z* axis for each membrane (collinear with the membrane normal) is roughly parallel to the substrate normal, the *x* and *y* axes remain disordered. By collecting spectra at different angles between the substrate normal and the X-ray *E* vector, the dichroism of the absorber-backscatterer pair present in the oriented samples is reflected in and can be extracted from the resulting X-ray absorption spectra.

Several XAS studies on oriented PS II membranes have provided additional structural constraints that were not available from the studies on isotropic samples, mostly in terms of the orientation dependence of the Mn–Mn vectors in the di-μ-oxo-bridged Mn_2 motifs.[161,202,205,236] However, because the samples were ordered only in one dimension, the dichroism information was available only in the form of an angle with respect to the membrane normal. For EXAFS measurements, this means that the absorber-backscatterer vectors can lie anywhere on a cone defined by the angle the vector forms with the membrane normal.

Further refinement can be performed if samples with three-dimensional order, *i.e.* single crystals, are examined instead of oriented membranes. Single-crystal X-ray spectroscopy has been performed on single crystals of Cr=O porphyrin complexes,[284] dithiomolybdate single crystals,[285] and a series of single-crystal Cu(II) model complexes.[286] These studies, which focused on the XANES region of the spectrum, showed pronounced dichroism in the XANES region. The Cr=O complexes were particularly interesting because the dichroism measurements showed that the intense $1s \rightarrow 3d$ pre-edge transition was almost completely polarized along the Cr=O bond.[284] This was interpreted by Templeton et al.[287,288] in similar systems to be a transition between the 1s core level and an antibonding molecular orbital with metal d_{z^2} and oxygen p_z character.

Protein crystals have also been examined using single-crystal X-ray spectroscopy. Scott et al.[289] examined the Cu active site in a plastocyanin single crystal with the aim of selectively probing the long (2.90 Å from X-ray crystallography[290]) Cu–S(Met) bond. This is possible because the EXAFS amplitude is proportional to $\cos^2\theta$, where θ is the

angle between the X-ray *E* vector and the absorber-backscatterer vector.[282,287,289,291,292] This study was able to confirm the results from an earlier EXAFS study using isotropic samples[293] that the S(Met) ligand is not detectable by EXAFS, possibly due to uncorrelated vibrational motion of Cu and S; this reflects a weakly bonded situation. The contributions from the remaining ligands, two histidine ligands and a cysteine ligand, were shown to be dichroic, and the experimentally determined dichroism in the EXAFS spectra was consistent with the dichroism pattern calculated from the X-ray crystal structure.

This type of analysis can also be useful for systems where a high-resolution X-ray crystal structure is not available, such as PS II. These crystals have only become available recently,[60,265] and a preliminary X-ray crystal structure has been solved to 3.8 Å resolution.[60] Performing single-crystal EXAFS experiments can help to refine this low-resolution structure of the OEC by revealing information such as the angle(s) between the di-μ-oxo-bridged Mn–Mn vectors as well as the angles between the mono-μ-oxo Mn–Mn vector and the di-μ-oxo-bridged Mn–Mn vectors. This information is not currently available from the EXAFS experiments on oriented PS II membranes because of the 'cone' ambiguity mentioned above.

To prepare for subsequent experiments with PS II single crystals, three single-crystal Mn complexes were examined in the experiments detailed in this chapter. These consisted of two Mn(V) complexes, a Mn(V)–nitrido complex and a Mn(V)–oxo complex, as well as a di-μ-oxo-bridged binuclear Mn_2(III,IV) complex. All of these complexes exhibited noticeable dichroism in the EXAFS spectra, and the XANES features originating from the Mn(V)–nitrido and Mn(V)–oxo bonds were dramatically dichroic in the XANES spectra. The dichroism in the EXAFS spectra of the Mn(V)–

nitrido complex was fit for three orientations of the single crystal using single- and multiple-scattering EXAFS theory.

In addition to the single-crystal data from the above-mentioned Mn model compounds, it is desirable to examine the dichroism properties of a homologous set of Mn model complexes, such as the sets studied by Visser et al.[125] and Pizarro et al.[167] This would more closely replicate the scenario in PS II, where the OEC in the S_0, S_1, S_2, and S_3 states can be considered as a set of Mn complexes. Single crystals of a homologous set of Mn model complexes have been obtained from Prof. R. Mukherjee and co-workers which have been isolated in the Mn_2(III,III), Mn_2(III,IV), and Mn_2(IV,IV) oxidation states.[294-296] The di-μ-oxo Mn_2(III,IV) and Mn_2(IV,IV) complexes have identical ligands in both oxidation states, while the Mn_2(III,III) complex is mono-μ-oxo-bridged with an additional acetate bridge completing the ligation sphere; otherwise, the ligation is identical to the Mn_2(III,IV) and Mn_2(IV,IV) complexes.

Before the single crystals can be examined using X-ray absorption spectroscopy, characterization of the isotropic XAS spectra from these samples should be performed. The characterization of these complexes in their isotropic form using XANES and EXAFS and the similarities in the X-ray absorption spectra between compounds with different Mn oxidation states is reported.

Materials and Methods

The Mn model complexes were obtained from collaborators Dr. Jesper Bendix, Prof. Terrence Collins, and Prof. Jean-Jacques Girerd, who provided single crystals of $[Rh(en)_3]$ $[Mn(N)(CN)_5]\cdot H_2O$ (**1**) (en = 1,2-diaminoethane),[297] the macrocyclic Mn(V)–oxo complex (**2**),[298] and $[Mn_2(III,IV)O_2\ phen_4][(ClO_4)_3]$ (**3**) (phen = 1,10-phenanthroline), respectively. The structures of these compounds are shown in Figure 5-1. The homologous series of Mn complexes in different oxidation states was obtained from Prof. R. N. Mukherjee. These complexes have been structurally characterized as $[Mn_2(III,III)(\mu\text{-}O)(\mu\text{-}OAc)_2(MeL_2)][ClO_4]_2\cdot H_2O$ (**4**), $[Mn_2(III,IV)(\mu\text{-}O)_2(\mu\text{-}OAc)(MeL_2)][BF_4]_3\cdot 2MeCN$ (**5**), and $[Mn_2(IV,IV)(\mu\text{-}O)_2(\mu\text{-}OAc)(MeL_2)]$

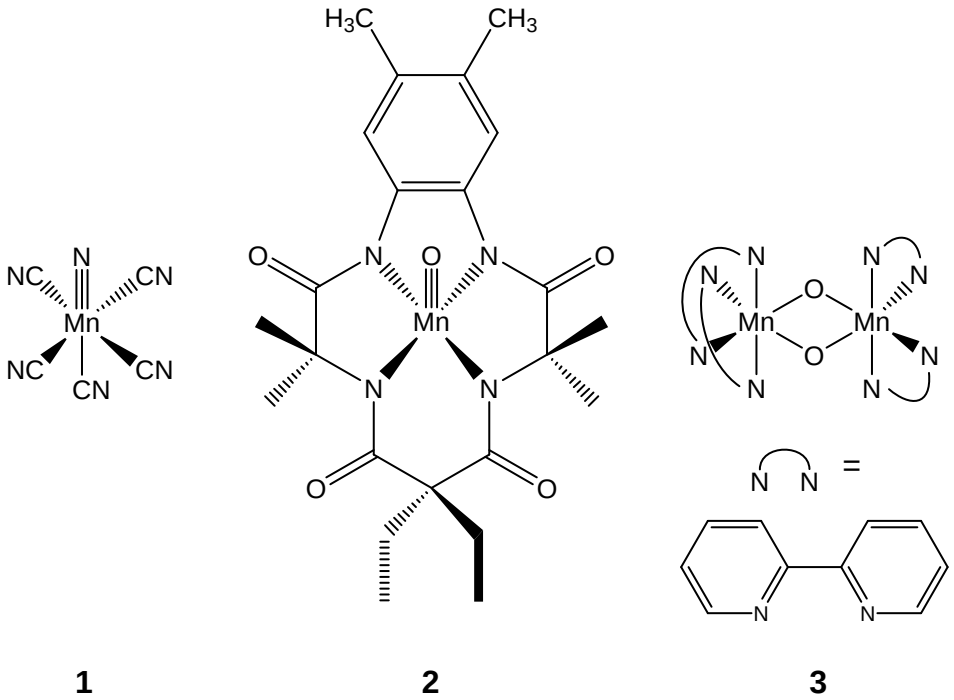

1 **2** **3**

Figure 5-1: Structures of the $[Mn(N)(CN)_5]^{3-}$ anion (**1**),[297] the macrocyclic Mn(V)–oxo complex (**2**),[298] and $[Mn_2(III,IV)O_2phen_4][ClO_4]$ (**3**) (phen = 1,10-phenanthroline).

$[ClO_4]_3 \cdot H_2O$ (**6**), where MeL = (2-pyridylmethyl)(2-pyridylethyl)methylamine.

The crystals were mounted on a Lucite® two-circle goniometer which was used in the work of Scott et al.[289] This two-circle goniometer permitted rotation around two perpendicular rotation axes ϕ and χ. These axes were defined as follows. The incoming X-ray beam is polarized in the laboratory *x*-*y* plane, as shown in the top view from Figure 5-2. The laboratory *z* axis is defined as an axis perpendicular to the plane of polarization of the X-ray *E* vector, and is the same axis as the rotation axis ϕ. The

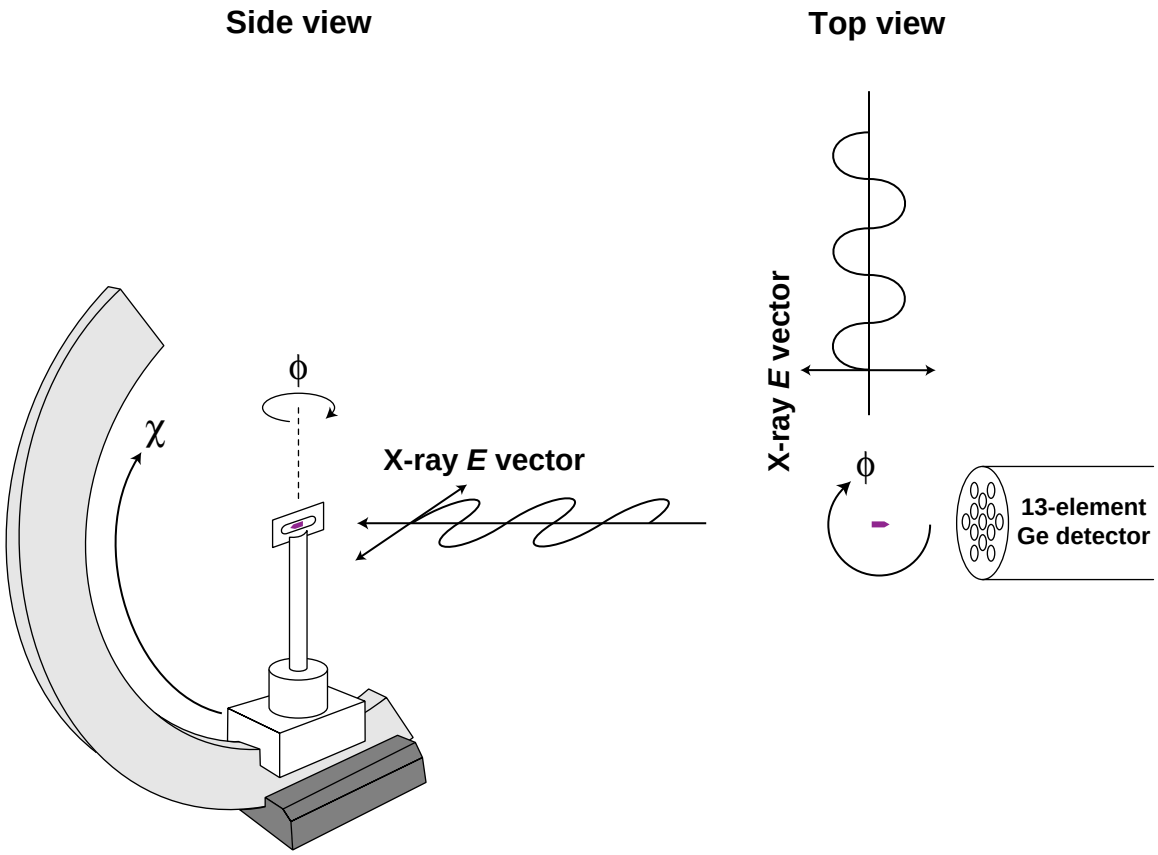

Figure 5-2: Schematic diagram of the two-circle goniometer illustrating the two angles of rotation ϕ and χ. The X-ray *E* vector is plane-polarized. For clarity, the 13-element Ge detector is omitted from the side view. The crystal in this diagram is at $\phi = 0°$ and $\chi = 0°$.

laboratory *x* axis is defined as the axis collinear with the X-ray *E* vector (pointing towards the Ge detector) and the laboratory *y* axis is defined as the direction of propagation of the X-rays. The crystals were mounted in the center of an Al sample holder using double-sided adhesive tape such that the long axis of the crystal was collinear with the long axis of the sample holder. The Al sample holder was then mounted onto the goniometer head such that the long axis of the crystal was parallel with the X-ray *E* vector and the laboratory *x* axis; this was defined as $\phi = 0°$.

It was not possible to collect spectra at an angle of $\phi = 90°$ because the Al sample holder blocked the incoming X-ray beam. Therefore, the second circle of the two-circle goniometer was used to make the long axis of the crystal perpendicular to the X-ray *E* vector. The goniometer arm could not lie along the laboratory *x* axis without blocking the Ge detector; thus, it was placed at a 45° angle to the *x* and *y* laboratory axes as shown in the side view of Figure 5-2. The second rotation axis χ lies at a 45° angle from the X-ray *E* vector in the plane of polarization of the X-rays. $\chi = 0°$ was defined as the angle that aligns the long axis of the crystal in the plane of polarization of the X-rays; the single crystal shown in the side view of Figure 5-2 is oriented at $\chi = 0°$.

A simplified explanation of the rotation axes ϕ and χ is that rotation by an arbitrary angle around ϕ rotates the crystal in the *x*-*y* plane, and rotation by an arbitrary angle around χ rotates the crystal out of the *x*-*y* plane. Alignment of the crystal and the X-ray beam was accomplished by moving the entire goniometer vertically and horizontally. Isotropic powder spectra were obtained by lightly grinding a single crystal in a mortal and pestle with 10-fold by weight excess of boron nitride.

XANES and EXAFS spectra were recorded at room temperature on beamline 7-3 at SSRL (Stanford Synchrotron Radiation Laboratory). The synchrotron ring SPEAR was operated at 3.0 GeV at 50 – 100 mA beam current. Energy resolution of the unfocused incoming X-rays was achieved using a Si(220) double-crystal monochromator, which was detuned to 50 % of maximal flux to attenuate harmonic X-rays. A N_2-filled ion chamber (I_0) was mounted in front of the sample to monitor incident beam intensity. An incident X-ray beam of 1 mm x 2 mm (for **1**) or 1 mm x 3 mm (for **2**, **3**) dimensions was used for the XANES and EXAFS experiments. The single-crystal X-ray absorption spectra were collected as fluorescence excitation spectra[114] using a 13-element energy-resolving detector from Canberra Electronics,[115] and were referenced by I_0. Typical counts in the Mn fluorescence window for the central channel were 300 counts/sec at 6500 eV (below the Mn K-edge) and 10,000 counts/sec at 6600 eV (above the Mn K-edge). The isotropic powder spectra were collected in a similar manner except that the count rate was too high to use an energy-resolving detector; thus, a non-energy-resolving ionization chamber known as a Lytle detector was used instead.[299]

Combination XANES/EXAFS spectra were collected at 3 eV/point from 6400 to 6535 eV with a collection time of 1 sec per point, 0.2 eV/point from 6535 to 6576 eV with a collection time of 1 sec per point, and at 1 eV/point from 6550 eV to 6576 eV with a collection time of 1 sec per point. The EXAFS region was collected with points evenly spaced every 0.05 $Å^{-1}$ in *k*-space from 2.05 $Å^{-1}$ to 12 $Å^{-1}$, with E_0 assigned as 6563 eV. The time of collection was weighted using a cubic function from a minimum of 1 sec per point at low *k* values to a maximum of 15 sec per point at high *k* values.

Collection of an energy reference spectrum was achieved by placing a $KMnO_4$ sample between two N_2-filled ion chambers, I_1 and I_2, which were positioned behind the PS II sample, and collecting a $KMnO_4$ absorption spectrum concurrently with PS II data collection. The narrow pre-edge line (FWHM • 1.7 eV) at 6543.3 eV was subsequently used for energy calibration.[116] Each spectrum presented in this chapter represents the average of 3 – 9 scans. Data reduction for the XANES and EXAFS spectra was performed as described in Chapter 3.

Curve fitting of the EXAFS spectra from single crystals of $[Rh(en)_3][Mn(N)(CN)_5]\cdot H_2O$ (**1**) was performed for the orientations $\phi = 0°$ $\chi = 0°$, $\phi = 45°$ $\chi = 0°$, and $\phi = 45°$ $\chi = 90°$ using the procedure described in Chapter 3 to isolate all of the Fourier peaks together (•***R'*** ~ 0 – 5 Å). These isolates were then fit using *ab initio*-calculated phases and amplitudes from the program FEFF 7.02 from the University of Washington.[197,213,300] These *ab initio* phases and amplitudes were calculated from the molecular structure of (**1**) described in Bendix et al.[297] and were used with the EXAFS equation (Eq. 3-2)[214-217] to calculate a theoretical EXAFS spectrum as explained in Chapter 3.

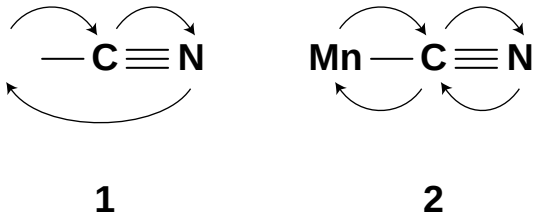

1 **2**

Figure 5-3: Possible multiple-scattering paths in the Mn(V)–nitrido complex (**1**).

Because the five cyano groups in (**1**) provide linear Mn–X–X scattering paths, it was important to take into account multiple-scattering effects in both the calculation of

ab initio phases and amplitudes and the fitting methodology.[218,301,302] The possible multiple-scattering paths are shown in Figure 5-3. Multiple-scattering effects are included in calculations performed by FEFF 7.02 in the form of an additional phase-and-amplitude file for each multiple scattering path. Because each additional path represents an additional shell in the fits, the number of free parameters must be kept to a reasonable number. This was performed by constraining the fits in a fashion similar to that performed by Laplaza et al.[302] such that each multiple-scattering shell had the same values for the fit parameters N, R, and σ^2 as the respective single-scattering path; as mentioned in Chapter 3, E_0 was constrained to be equal for all shells in a given fit.

Results

Mn(V)–nitrido single crystal (**1**)

The single crystals of the Mn(V)–nitrido complex have been well-characterized by Bendix et al.[297] and have crystallographic parameters that are particularly suited for this experiment. This complex crystallizes in the space group $P6_3$, with 6 molecules per unit cell. As shown in Figure 5-4, the Mn–nitrido bond for each molecule in the unit cell is nearly collinear with the crystallographic *c*-axis (the angle between each Mn–N vector and the crystallographic *c*-axis is only 9.4°).[297] In addition, the long axis of the crystal

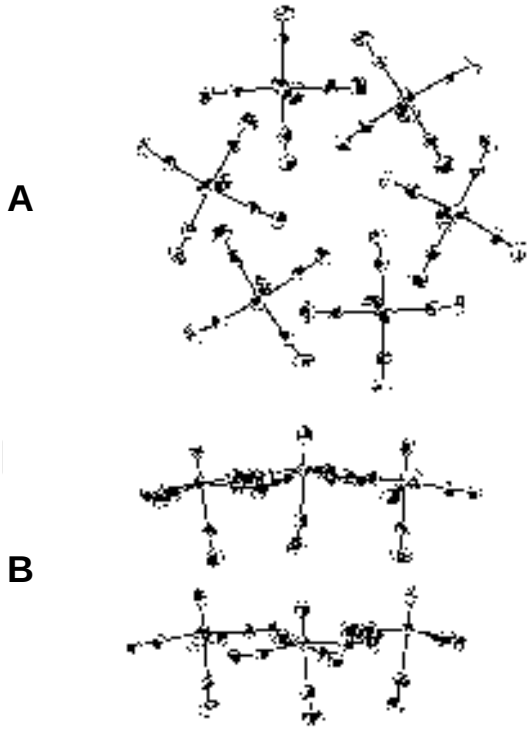

Figure 5-4: Diagram of the orientation of the $[Mn(N)(CN)_5]^{3-}$ anions (**1**) in the unit cell. (**A**) View along the *c* axis of the unit cell. (**B**) View perpendicular to the *c* axis of the unit cell.. Each Mn–nitrido vector makes a common angle of 9.4° with respect to the *c* axis of the unit cell. This figure was reproduced from Bendix et al.[297]

was found to coincide with the crystallographic *c*-axis.[297] This means that the Mn–N bond vector is essentially pointing along the long axis of the crystal; thus, the changes observed in the X-ray spectra can be correlated with the known orientation of the individual molecules within the macroscopic crystal.

It should be emphasized that not all crystals are optimal for single-crystal XAS. Several factors can result in crystals which are almost devoid of macroscopic dichroism. Aside from the case of molecules with high symmetry like T_d or O_h, which lack dichroic properties on a single-molecule basis, dichroic molecules in certain crystal-packing arrangements in the unit cell can produce a crystal without dichroic properties. For example, the $[Mn(N)(CN)_5]^{3-}$ anions could be arranged in a three-molecule unit cell such that the first molecule in the unit cell has the Mn–nitrido bond oriented along the unit cell *a*-axis, the second molecule has the Mn–nitrido bond oriented along the unit-cell *b*-axis, and the third molecule has the Mn–nitrido bond oriented along the unit-cell *c*-axis This scenario would make it impossible to choose two different orientations of the crystal to observe dichroism in any of the Mn–backscatterer vectors. It is also possible to envision similar scenarios in which the maximum possible dichroism observable from the single crystal is significantly less than is seen for the Mn(V)–nitrido complex. Furthermore, the relation between the crystallographic *a*-, *b*-, and *c*-axes and the macroscopic axes of the crystal needs to be determined from a diffraction pattern to specify the orientation of the unit cell in the X-ray beam. Fortunately, this relation was determined by Bendix et al.,[297] because the equipment necessary to collect and analyze a diffraction pattern was not available on the beamline used for these experiments.

XANES

Figure 5-5 shows the dichroism exhibited in the XANES spectra of the Mn(V)–nitrido single crystal (**1**) as the rotation angles ϕ and χ are changed. The intense pre-edge feature, which corresponds to bound 1s $\rightarrow$ 3d transitions,[56] is strongly dichroic, with the maximum intensity appearing when the Mn–N bond is collinear with the X-ray *E* vector. This is not surprising, because the normally dipole-forbidden 1s $\rightarrow$ 3d transition can gain significant intensity through mixing of the metal 3d orbitals with ligand 2p orbitals; a

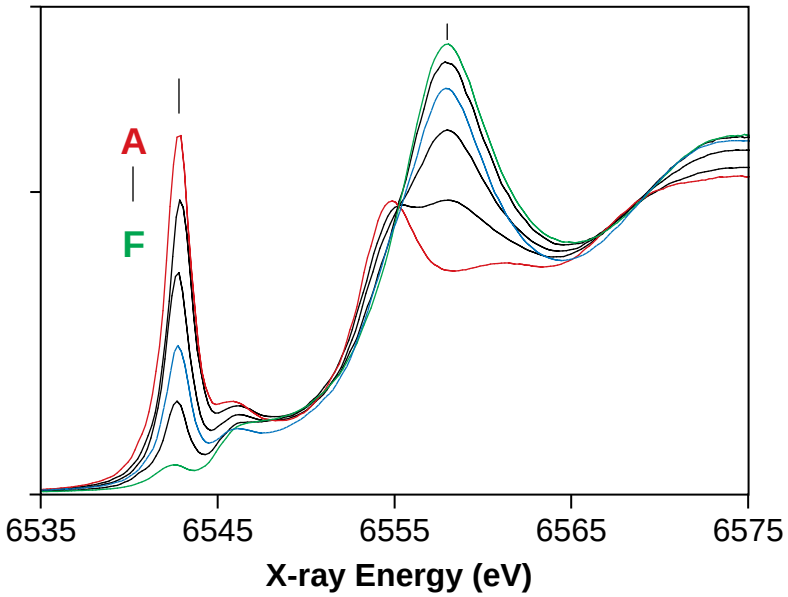

Figure 5-5: Mn K-edge XANES spectra of the Mn(V)–nitrido single crystal (**1**) as a function of the rotation angles ϕ and χ. The arrows show the direction that the spectral features change as ϕ is increased from 0° to 70°, thereby decreasing the overlap between the Mn–N bond and the X-ray *E* vector. The spectrum shown in red was collected at ϕ = 0° and χ = 0° (Mn–N bond aligned with the X-ray *E* vector), while the spectrum shown in green was collected at ϕ = 45° and χ = 90° (Mn–N bond aligned perpendicular the X-ray *E* vector),. The isotropic spectrum shown in blue was obtained from a polycrystalline sample. The specific orientation angles are as follows: **A**: ϕ = 0°, χ = 0° (red), **B**: ϕ = 30°, χ = 0°, **C**: ϕ = 45°, χ = 0°, **D**: polycrystalline sample (blue), **E**: ϕ = 70°, χ = 0°, **F**: ϕ = 45°, χ = 90° (green).

transition from the 1s level to an unoccupied molecular orbital with 2p character is then no longer dipole forbidden. This intense pre-edge transition was shown to occur in similar high-valent metal complexes, and was assigned to a transition between the 1s core level and an antibonding molecular orbital with metal d_{z^2} and ligand p_z character.[287,288] The intensity of this transition is minimized at the $\phi = 45°$, $\chi = 90°$ orientation, where the long axis of the crystal, and hence the Mn–N vectors, is oriented vertically and is orthogonal to the X-ray *E* vector. The non-zero amplitude of the pre-edge features is due to contributions from the other dipole-forbidden $1s \rightarrow 3d$ transitions and the fact that a 9.4° angle exists between the Mn–N vectors and the crystallographic *c*-axis. The apparent shift in the pre-edge peak in spectrum B ($\phi = 30°$, $\chi = 0°$) is an artifact of photoreduction (*vide infra*).

Spectrum D from Figure 5-5 (shown in blue) is from an isotropic sample, and was collected from a powdered single crystal. The pre-edge peak from this sample is much less intense (35.6 % less area) than the spectrum collected at $\phi = 0°$ and $\chi = 0°$ (shown in red in Figure 5-5), which provides maximum overlap between the X-ray *E* vector and the Mn–N bond. This is expected, because the isotropic sample contains Mn–N bonds in a sphere of all possible orientations. The amplitude of these features is weighted by $\cos^2\theta$, where θ is the angle between the Mn–backscatterer vector and the X-ray *E* vector. Thus, the $\cos^2\theta$ term must be averaged over all orientations in the sphere, which produces a weighting factor of $\frac{1}{3}$.[282,289] To properly compare the oriented single-crystal data with the data from isotropic samples, it is thus necessary to divide the oriented data by $3\cos^2\theta$. Keeping in mind that, at $\phi = 0°$ and $\chi = 0°$, the angle between the Mn–N bond and the

X-ray *E* vector is 9.4°, the calculated ratio of intensities (34.2 %) compares quite favorably to the experimental result of 35.6 %.

The main edge region, which contains the $1s \rightarrow 4p$ transition, is also strongly dichroic, presumably from multiple-scattering contributions from the five cyanide ligands to the Mn atom. This type of behavior has been seen in other compounds with many multiple-scattering paths[286] and was attributed to multiple-scattering features present in the main edge region.

EXAFS

Figure 5-6 shows the k^3-space EXAFS spectra of the Mn(V)–nitrido single crystal (**1**) for two combinations of the rotation angles ϕ and χ. Because of the favorable crystal habits and the anisotropic nature of the Mn(V)–nitrido single crystal (**1**), these spectra are very strongly dichroic. The spectrum shown in green in Figure 5-6 was collected at $\phi = 45°$ and $\chi = 90°$, which aligns the plane containing the equatorial cyano ligands with the plane of polarization of the X-rays and places the Mn–N bond and the axial cyano group orthogonal to the X-ray *E* vector. This orientation is thus dominated by C backscattering from the equatorial cyano groups and a strong multiple-scattering contribution from the collinear Mn–CN moieties in the equatorial plane.

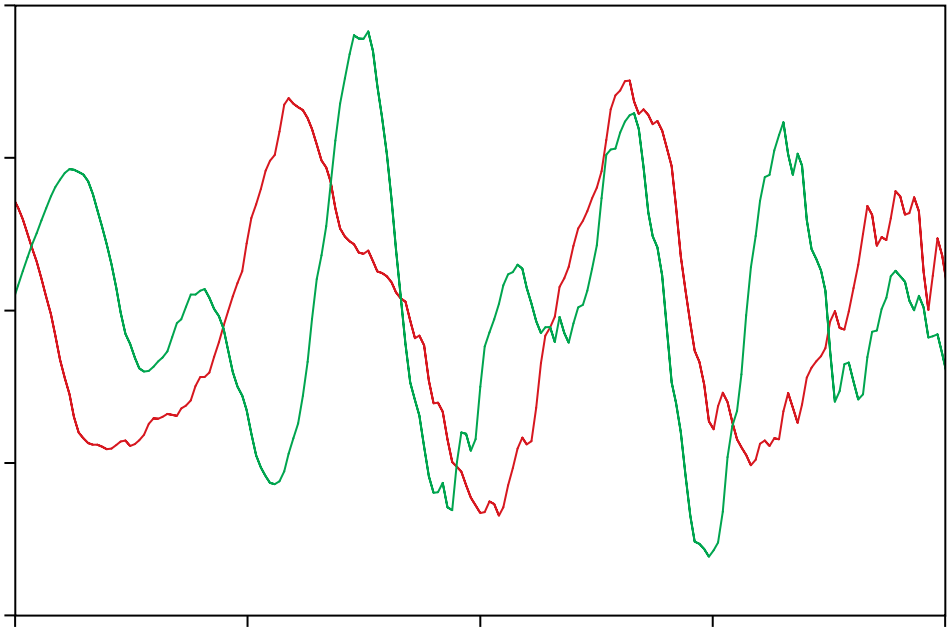

Figure 5-6: Mn k^3-space EXAFS spectra of the Mn(V)–nitrido single crystal (**1**) for two combinations of the rotation angles ϕ and χ. The spectrum shown in red was collected at $\phi = 0°$ and $\chi = 0°$, which provides maximum overlap between the Mn–N bonds and the X-ray *E* vector. The spectrum shown in green was collected at $\phi = 45°$ and $\chi = 90°$, which orients the Mn–N bonds nearly orthogonal to the X-ray *E* vector.

At the other extreme orientation, $\phi = 0°$ and $\chi = 0°$, the contributions from the equatorial cyano ligands is minimized and the dominating contribution to the k^3-space EXAFS spectrum is the short Mn(V)–nitrido bond. This is shown as the red spectrum in Figure 5-6, which is dominated by low-frequency EXAFS oscillations arising from Mn–N backscattering. An additional contributor to the EXAFS in this orientation is the axial Mn–CN group. However, because the Mn–C bond is ~0.25 Å longer than the equatorial Mn–C bonds and there are four equatorial cyano groups and only one axial group, the

contributions of the cyano groups in this orientation to the EXAFS spectrum is much less than are seen at $\phi = 45°$ and $\chi = 90°$.

Figure 5-7 shows the Fourier transforms of the k^3-space EXAFS spectra of the Mn(V)–nitrido single crystal (**1**) as a function of the rotation angles ϕ and χ. The intense peak at an apparent distance R' of 1.18 Å in the $\phi = 0°$, $\chi = 0°$ spectrum is due to backscattering from the nitrido atom, while the peak at an apparent distance R' of 1.53 Å

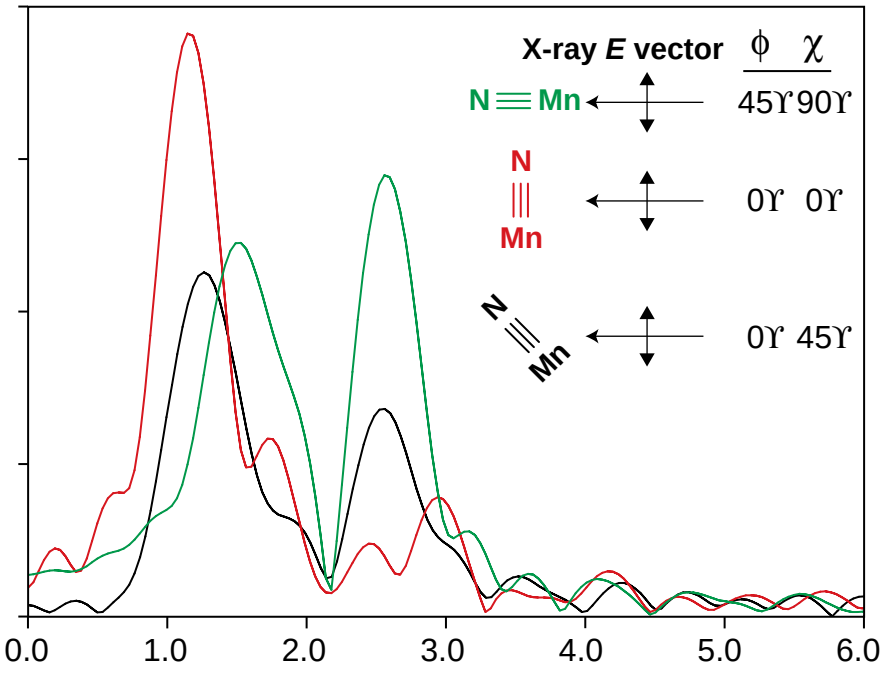

Figure 5-7: Fourier transforms of the k^3-space EXAFS spectra of the Mn(V)–nitrido single crystal (**1**) for three combinations of the rotation angles ϕ and χ. The spectrum shown in red was collected at $\phi = 0°$ and $\chi = 0°$, which provides maximum overlap between the Mn–N bonds and the X-ray *E* vector. The spectrum shown in green was collected at $\phi = 45°$ and $\chi = 90°$, which orients the Mn–N bonds nearly orthogonal to the X-ray *E* vector. The spectrum from an intermediate position, $\phi = 45°$ and $\chi = 0°$, is shown in black.

in the $\phi = 45°$, $\chi = 90°$ spectrum is due to backscattering from the four equatorial C atoms. The peak at $R' = 2.58$ Å arises from the N atoms in the equatorially bound cyano groups, and is strongly enhanced by multiple scattering mediated by the intervening collinear C atoms (see Figure 5-3). A rough estimate of the actual absorber-backscatterer distance can be obtained by adding ~0.5 Å to the apparent distances R' from the Fourier transform.

Curve-fitting analysis

A quantitative analysis of the angle dependence of the EXAFS spectra was achieved using the curve-fitting methodology described in the Materials and Methods section. Curve-fitting analysis was applied to the two extreme orientations of the Mn(V)–nitrido single crystal (**1**): $\phi = 0°$, $\chi = 0°$ (shown in red in Figure 5-7) and $\phi = 45°$, $\chi = 90°$ (shown in green in Figure 5-7). In addition, curve-fitting analysis was also applied to the intermediate orientation of $\phi = 45°$ and $\chi = 0°$. As expected, these results (which are detailed in the Appendix) were a convolution of those obtained at the extreme orientations.

Table 5-1 shows the curve-fitting results for the $\phi = 0°$, $\chi = 0°$ orientation. At this orientation, the major contributor to the EXAFS spectrum is the short Mn–N bond; thus, an acceptable fit is obtained with only a one-shell Mn–N fit (Fit #1 in Table 5-1). Further refinement can be obtained by incrementally including backscattering contributions from the axial Mn–C vector (Fit #2 in Table 5-1) and the nitrogen atom in the axial cyano group (Fit #3 in Table 5-1), as shown in Figure 5-8 and judged by the error parameters Φ and ε^2 in Table 5-1. Interestingly, the cyano nitrogen atom can contribute significantly to the EXAFS only by amplitude enhancement from a multiple-scattering path; of the two multiple-scattering paths in Figure 5-3, only path 1 contributed to the EXAFS in this orientation. Because N, a low-*Z* atom, is at a long distance from the absorbing atom for this scattering path, single-scattering paths provide almost no contribution to the EXAFS spectrum in this situation; as described in Chapter 3, there is a $1/(kR^2)$ dependence of the amplitude of the EXAFS oscillations. Because these spectra are from single crystals, the

Table 5-1: Simulations of the EXAFS spectra from the Mn(V)–nitrido single crystal (**1**) at an orientation of $\phi = 0°$, $\chi = 0°$. This orientation maximizes the contribution from the short (~1.5 Å) Mn–N vector.

Fit #	shell	path	R (Å)	N	σ^2 (Å^2)	$\bullet E_0$ [b]	Φ (x 10^{-3})	ε^2 (x 10^{-5})
1	Mn–N	–	1.57	3.28	0.003	-8	0.59	0.84
2	Mn–N	–	1.57	3.13	0.002	-8	0.35	0.22
	Mn–C	–	2.27	1.71	0.002[c]			
3	Mn–N	–	1.57	3.13	0.002	-8	0.20	0.14
	Mn–C	–	2.27	1.71	0.002[c]			
	Mn–N	1	3.47	2.58	0.002[c]			

[a]fit parameters and quality-of-fit parameters are described in Chapter 3 Materials and Methods, path = multiple-scattering path from Figure 5-3; [b]$\bullet E_0$ was constrained to be equal for all shells within a fit; [c]parameter fixed in fit

N values obtained from the fits cannot be correlated to a chemical structure using the same methodology that was used in Chapter 3. The EXAFS equation shown in Eq. 3-2 from Chapter 3 was derived for isotropic samples in which the absorber-backscatterer vectors lie in a sphere of all possible orientations. For spectra obtained from single crystals, the amplitude of these features is weighted by $\cos^2\theta$, where θ is the angle between the Mn–backscatterer vector of interest and the X-ray *E* vector; averaging over all possible orientations produces a weighting factor of $\frac{1}{3}$.[282,289] Thus, the *N* values from single-crystal data should be divided by $3\cos^2\theta$ to enable a meaningful comparison to *N* values from isotropic data. After this division is performed, Eq. 3-3 can be used to interpret *N* values, and the *N* value for the nitrido backscatterer agrees quite favorably with the expected value.

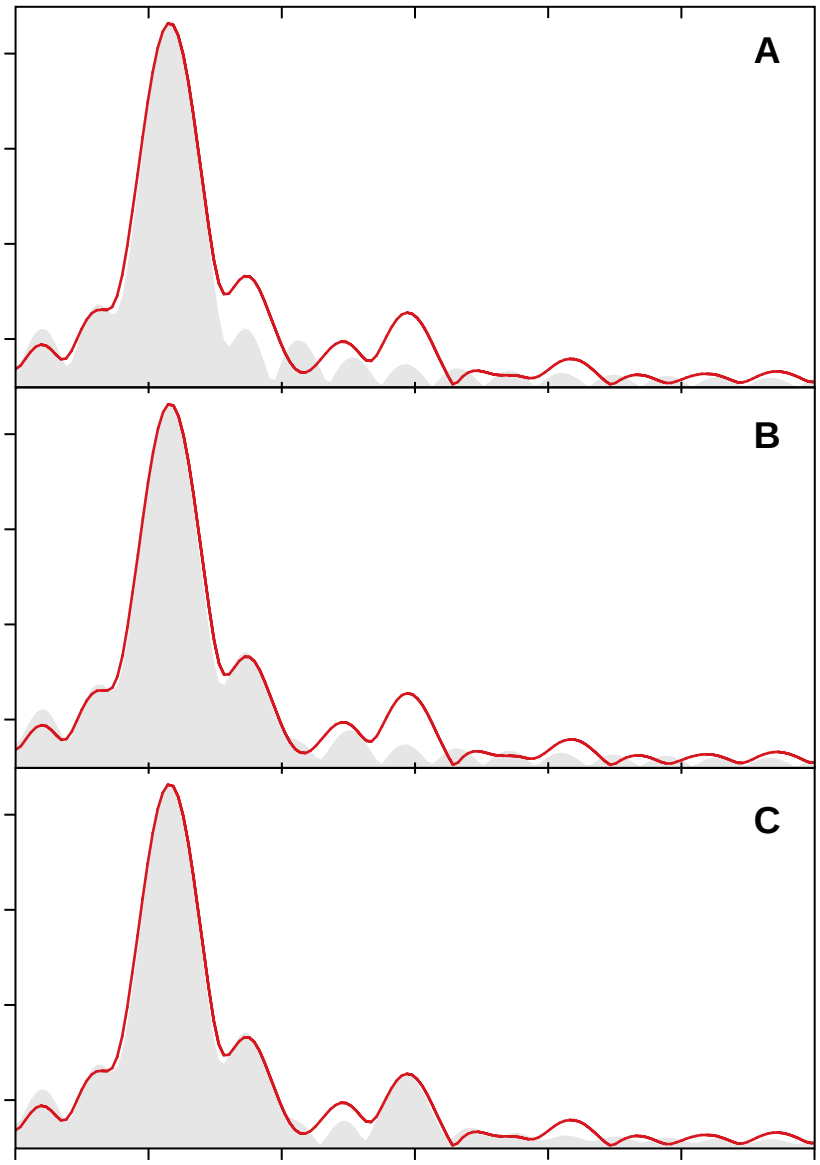

Figure 5-8: Curve-fitting results for various fits described in Table 5-1 to the k^3-space EXAFS spectra from the Mn(V)–nitrido single crystal (**1**) at an orientation of $\phi = 0°$ and $\chi = 0°$. For comparison purposes, the spectra are presented as Fourier transforms of the experimental spectra (red) and the various fits (gray) **(A)** Fit #1 from Table 5-1 (Mn–N); **(B)** Fit #2 from Table 5-1 (Mn–N + Mn–C); **(C)** Fit #3 from Table 5-1 (Mn–N + Mn–C + cyano Mn–N).

Table 5-2: Simulations of the EXAFS spectra from the Mn(V)–nitrido single crystal (**1**) at an orientation of $\phi = 45°$, $\chi = 90°$. This orientation minimizes the contribution from the short (~1.5 Å) Mn–N vector and maximizes the backscattering contributions from the equatorial cyano groups.

Fit #	shell	path	R (Å)	N	σ^2 (Å^2)	$\bullet E_0$ [b]	Φ (x 10^{-3})	ε^2 (x 10^{-5})
1	Mn–C	–	1.96	6.05	0.004	-16	4.72	2.72
2	Mn–C	–	1.96	5.85	0.004	-19	1.69	1.06
	Mn–N	–	3.2	7.0[e]	0.002[c]			
3	Mn–C	–	1.98	5.51	0.003	-11	0.37	0.23
	Mn–N	–	3.13[d]	6.51[d]	0.002[c,d]			
	Mn–N	1	3.13[d]	6.51[d]	0.002[c,d]			
	Mn–N	2	3.13[d]	6.51[d]	0.002[c,d]			

[a]fit parameters and quality-of-fit parameters are described in Chapter 3 Materials and Methods, path = multiple-scattering path from Figure 5-3; [b]$\bullet E_0$ was constrained to be equal for all shells within a fit; [c]parameter fixed in fit; [d]parameters constrained to be equal for designated shells in the fit; [e]upper limit for parameter

A particularly informative method of deriving insight into the various contributions to the EXAFS fits is to compare the Fourier transforms of the calculated EXAFS spectra for each fit to the experimentally determined EXAFS spectra. Figure 5-8 shows the comparison of the three fits from Table 5-1 (gray) to the experimental EXAFS spectrum (red). Fit #1 from Table 5-1 (Figure 5-8A) adequately accounts for the dominant Mn–N scattering in the EXAFS spectrum, but does not account for the peaks at higher R'. By including a Mn–C shell (Fit #2 from Table 5-1) for the axial cyano group, the shoulder on the large Mn–N peak is accounted for (Figure 5-8B), but it is necessary to add the multiple-scattering contributions from the axial cyano N (Fit #3 from Table 5-1) to obtain a significantly better fit to the spectrum (Figure 5-8C). By presenting the fits in the method shown in Figure 5-8, it is quite straightforward to assign features in the Fourier transform and assess the effects of multiple scattering.

At the other extreme orientation, $\phi = 45°$ and $\chi = 90°$, the contribution to the EXAFS of the short Mn–nitrido vector is minimal, and the spectrum is dominated by the contributions from the equatorial cyano groups. As shown in Fit #1 from Table 5-2, ignoring the contributions from Mn–N scattering paths leads to a poor fit of the experimental EXAFS; the second Fourier peak in Figure 5-9A is essentially unaccounted for. Fit #2 in Table 5-2 attempts to fit the second Fourier peak with a single-scattering Mn–N shell. Figure 5-9B shows that the resulting amplitude of the second Fourier peak in the fit is insufficient to account for the experimental data; this is also reflected in the high Φ and ε^2 values in Table 5-2. As Fit #2 from Table 5-2 shows, single-scattering theory predicts a significantly lower amplitude of this peak than is experimentally observed. One possible explanation of the high amplitude of the second Fourier peak could be that it is due to backscattering from higher *Z* atoms, such as a transition metal, at R > 3 Å. The characterization of these crystals by Bendix et al.[297] proved that this explanation is incorrect, because no metal atoms are visible from the Mn point-of-view in the samples at less than the EXAFS detection limit of 5 Å. Figure 5-9C shows that the inclusion of multiple-scattering shells nicely accounts for the amplitude of the second Fourier peak (Fit #3 in Table 5-2).

To explain the *N* values from these fits, it is important to emphasize that rotation of the crystal around the Mn–nitrido bond will not change the EXAFS spectrum; the projection of the four equatorial Mn–C or Mn–N vectors onto the X-ray *E* vector will always add up to a total of two Mn–C vectors and two Mn–N vectors. Thus, weighting by $3\cos^2\theta$ as described earlier yields an expected *N* value of ~6 for the curve-fitting results, which is borne out by the fits shown in Table 5-2.

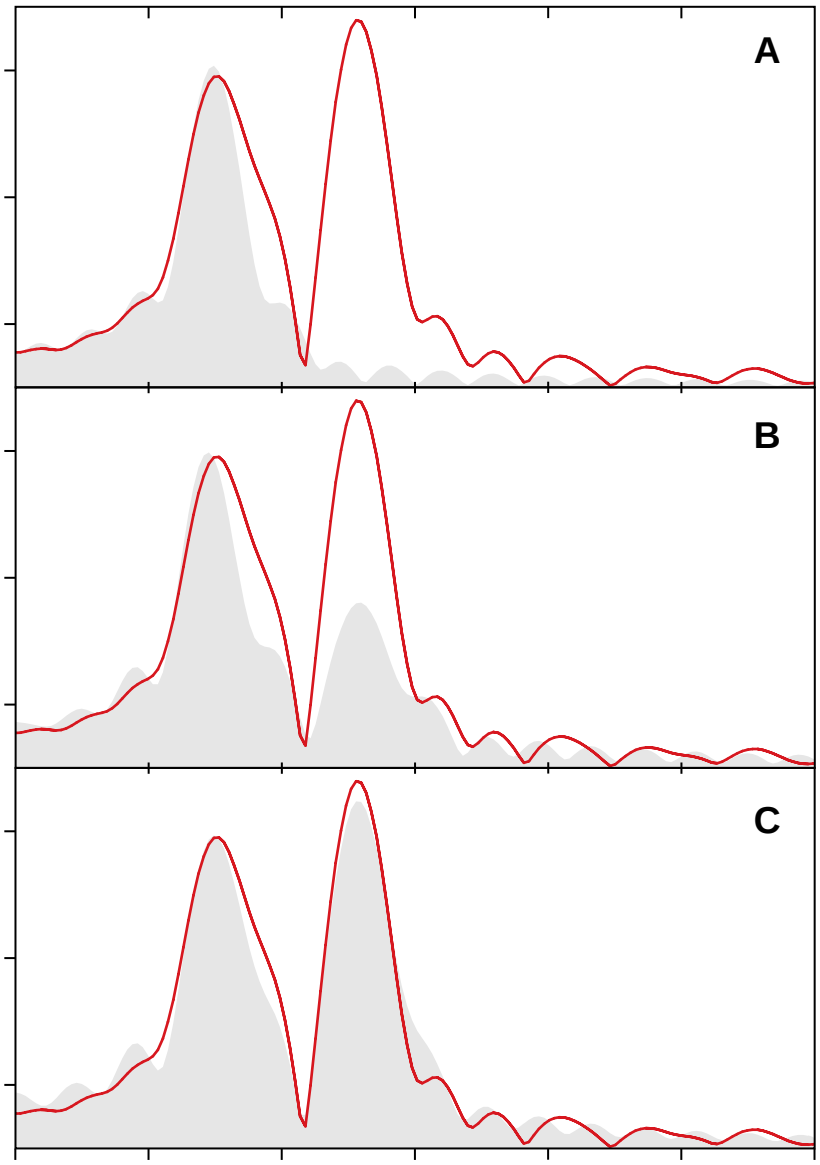

Figure 5-9: Curve-fitting results for various fits described in Table 5-2 to the k^3-space EXAFS spectra from the Mn(V)–nitrido single crystal (**1**) at an orientation of $\phi = 45°$ and $\chi = 90°$. For comparison purposes, the spectra are presented as Fourier transforms of the experimental spectra (red) and the various fits (gray) **(A)** Fit #1 from Table 5-2 (Mn–C); **(B)** Fit #2 from Table 5-2 (Mn–C + Mn–N single scattering); **(C)** Fit #3 from Table 5-2 (Mn–C + Mn–N single and multiple scattering).

Mn(V)–oxo single crystal (**2**)

XANES

Figure 5-10 shows the dichroism exhibited in the XANES spectra of the Mn(V)–oxo single crystal (**2**) as the rotation angles ϕ and χ are changed. As was seen for the Mn(V)–nitrido single crystal (**1**), a strongly dichroic pre-edge feature is seen for the Mn(V)–oxo complex; however, in contrast to the Mn(V)–nitrido single crystal, the pre-edge feature for the Mn(V)–oxo single crystal is more intense when the long axis of the crystal is oriented perpendicular to the X-ray *E* vector. This suggests that the Mn–O bond is oriented away from the long axis of the crystal. However, an absolute orientation

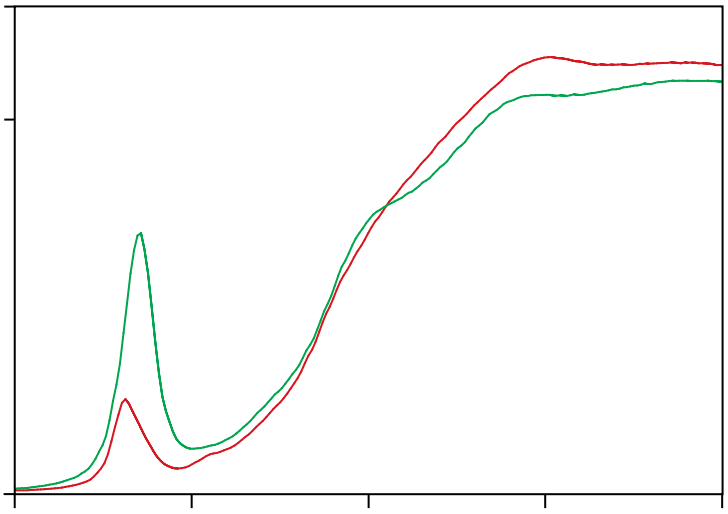

Figure 5-10: Mn K-edge XANES spectra of the macrocyclic Mn(V)–oxo single crystal (**2**) at two combinations of the rotation angles ϕ and χ. The spectrum shown in red was collected at $\phi = 0°$ and $\chi = 0°$ and the spectrum shown in green was collected at $\phi = 45°$ and $\chi = 90°$.

of the crystal could not be established because it is not known how the unit cell axes are related to the macroscopic crystal axes, and technical limitations precluded determining this relationship from a diffraction pattern (*vide supra*). Presumably, this pre-edge feature arises from transitions from the 1s core level to an antibonding molecular orbital with metal d_{z^2} and ligand p_z character.[287,288] Furthermore, the shape of the pre-edge peak changes significantly between the two orientations. Because of the short time of exposure to X-rays, it is unlikely that this difference is due to photoreduction effects. A more likely explanation is that there may be multiple pre-edge features in this complex, each with different dichroic properties.

The dichroism in the main edge region is much less dramatic than seen in Figure 5-5 for the Mn(V)–nitrido single crystal (**1**), which is partly because multiple-scattering contributions are much smaller for the Mn(V)–oxo complex (see Figure 5-1); multiple-scattering effects are strongly dependent on the collinearity of the absorber, backscatterer, and intervening atom, and are difficult to detect if the angle between these atoms is ~150° or less.[301]

EXAFS

Figure 5-11 shows the Fourier transforms of the k^3-space EXAFS spectra of the macrocyclic Mn(V)–oxo single crystal (**1**) for two combinations of the rotation angles ϕ and χ. The peak at an apparent distance R' of 1.5 Å in the $\phi = 0°$, $\chi = 0°$ spectrum (shown in red in Figure 5-11), which has a noticeable shoulder in the $\phi = 45°$, $\chi = 90°$ spectrum (shown in green in Figure 5-11), is mainly due to backscattering from the equatorial N ligands in the macrocycle. A shoulder appears at the orientation where the

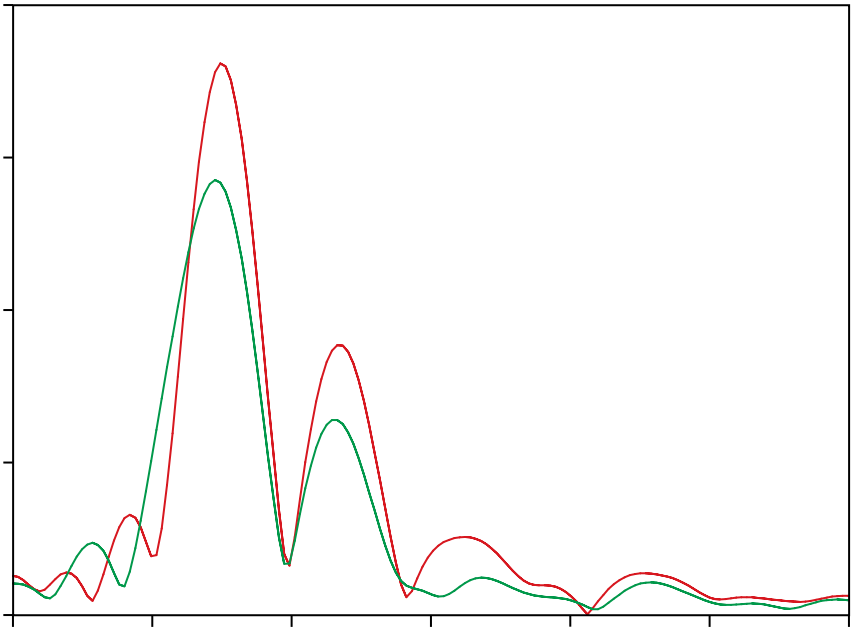

Figure 5-11: Fourier transforms of the k^3-space EXAFS spectra of the macrocyclic Mn(V)–oxo single crystal (**2**) for two combinations of the rotation angles ϕ and χ. The spectrum shown in red was collected at $\phi = 0°$ and $\chi = 0°$ and the spectrum shown in green was collected at $\phi = 45°$ and $\chi = 90°$.

pre-edge peak in Figure 5-10 becomes more intense ($\phi = 45°$, $\chi = 90°$); this reflects the appearance in the Fourier transform of backscattering from the short Mn–O distance. Because this complex does not have all the Mn–O bonds oriented in a nearly collinear fashion with the long axis of the crystal, as was the case for the Mn(V)–nitrido single crystal (**1**), the dichroism observed for the short (~1.5 Å) Mn–ligand distance is much smaller for the Mn(V)–oxo single crystal.

di-μ-oxo Mn_2(III,IV) single crystal (**3**)

XANES

Figure 5-12 shows the dichroism exhibited in the XANES spectra of the di-μ-oxo Mn_2(III,IV) single crystal (**3**) as the rotation angles ϕ and χ are changed. These XANES spectra are far less dichroic than those shown in Figure 5-5 and Figure 5-10 for the Mn(V)–nitrido single crystal (**1**) and the Mn(V)–oxo single crystal (**2**), respectively. Because an absolute orientation for this crystal could not be determined, it is possible that a different choice of the rotation angles ϕ and χ would produce increased dichroism in the XANES region. However, the maximum possible observable dichroism will be dictated

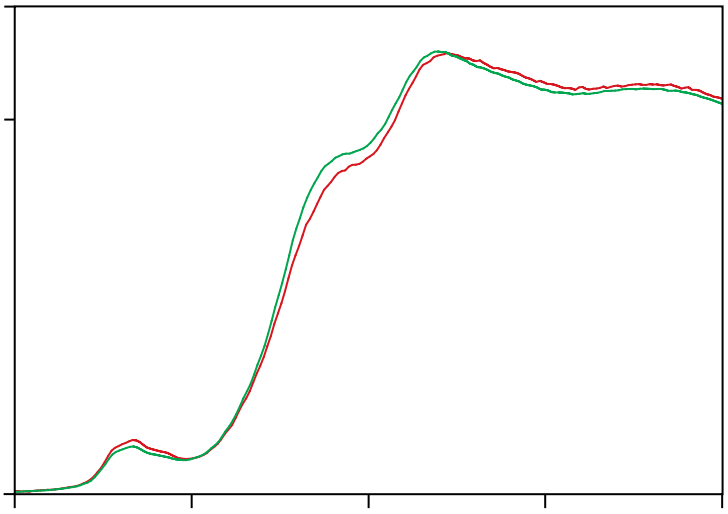

Figure 5-12: Mn K-edge XANES spectra of the di-μ-oxo Mn_2(III,IV) single crystal (**3**) at two combinations of the rotation angles ϕ and χ. The spectrum shown in red was collected at ϕ = 0° and χ = 0° and the spectrum shown in green was collected at ϕ = 45° and χ = 90°.

by how the di-μ-oxo Mn_2(III,IV) moieties are oriented within the unit cell.

EXAFS

Figure 5-13 shows the Fourier transforms of the k^3-space EXAFS spectra of the di-μ-oxo Mn_2(III,IV) single crystal (**3**) as a function of the rotation angles ϕ and χ. The peak at an apparent distance R' of 1.48 Å is mainly due to backscattering from the bridging di-μ-oxo ligands, and the peak at an apparent distance R' of 2.33 Å corresponds to Mn–Mn backscattering. While the XANES spectra shown in Figure 5-12 are not

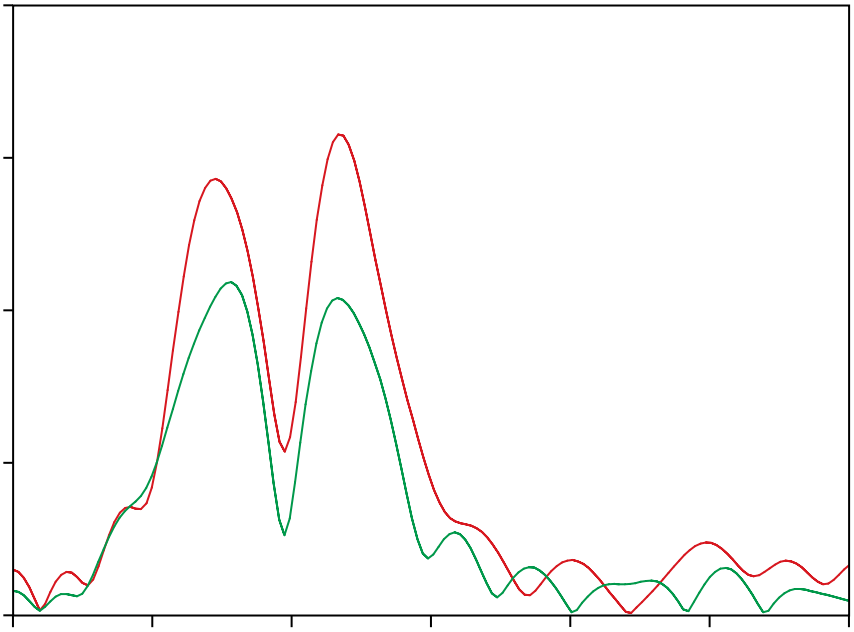

Figure 5-13: Fourier transforms of the k^3-space EXAFS spectra of the di-μ-oxo Mn_2(III,IV) single crystal (**3**) as a function of the rotation angles ϕ and χ. The spectrum shown in red was collected at ϕ = 0° and χ = 0° and the spectrum shown in green was collected at ϕ = 45° and χ = 90°. Note the change in the scale of the y-axis between this figure and those in Figure 5-7 and Figure 5-11

particularly dichroic, the EXAFS spectra taken at the same rotation angles ϕ and χ are much more dichroic. This is expected because the di-μ-oxo Mn–Mn moiety is planar;[303] thus, an orientation in which the X-ray *E* vector is parallel to the Mn–Mn vector will also maximize the contribution from the di-μ-oxo bridges. Conversely, an orientation in which the X-ray *E* vector is perpendicular to the Mn–Mn vector will minimize the contributions from both Mn–Mn backscattering and backscattering from the di-μ-oxo bridges, and the only remaining significant contributions will be from bridging ligands.

Examination of X-ray crystal structure data from similar compounds suggests that the di-μ-oxo Mn_2(III,IV) single crystal used in these studies will give rise to highly dichroic EXAFS spectra once the absolute crystal orientation can be calibrated and a judicious choice of the rotation angles ϕ and χ is made. Two similar complexes were crystallized by Stebler et al.,[303] the Mn_2(III,IV) complex with PF_6 counterions and the Mn_2(IV,IV) complex with ClO_4 counterions. Each molecule crystallized with four molecules in the unit cell (space group *Pbcn* for the PF_6 complex and $P2_1/c$ for the ClO_4 complex), and the planes formed by the di-μ-oxo Mn–Mn moieties of each molecule in the unit cell are all coplanar in each crystal. Therefore, it is reasonable to expect that such a situation exists for the di-μ-oxo Mn_2(III,IV) single crystal used in the current study; thus, proper choice of the rotation angles ϕ and χ should reveal even more dichroism in the EXAFS spectra than is observed in Figure 5-13.

A homologous set of Mn complexes in the Mn_2(III,III), Mn_2(III,IV), and Mn_2(IV,IV) oxidation states

XANES

The Mn K-edge XANES spectra of **4**, **5**, and **6** in the Mn_2(III,III), Mn_2(III,IV), and Mn_2(IV,IV) oxidation states are shown in Figure 5-14. The pre-edge region near 6542 eV shows significant changes when the mono-μ-oxo Mn_2(III,III) complex is oxidized to the di-μ-oxo Mn_2(III,IV) complex, but very little change when the di-μ-oxo Mn_2(III,IV) complex is oxidized to the di-μ-oxo Mn_2(IV,IV) complex. The pre-edge region is known to be extremely sensitive to the ligand geometry;[56] thus, it is not surprising that the changes in the pre-edge region in these complexes are dominated by the change in ligand environment of a mono-μ-oxo bridging compound to a di-μ-oxo bridging compound.

The shape of the main edge region also shows the most dramatic changes when the ligand environment is changed from mono-μ-oxo bridging moiety to a di-μ-oxo bridging moiety. However, in comparing the di-μ-oxo Mn_2(III,IV) complex to the di-μ-oxo Mn_2(IV,IV) complex, where the ligand environment is identical, the oxidation of

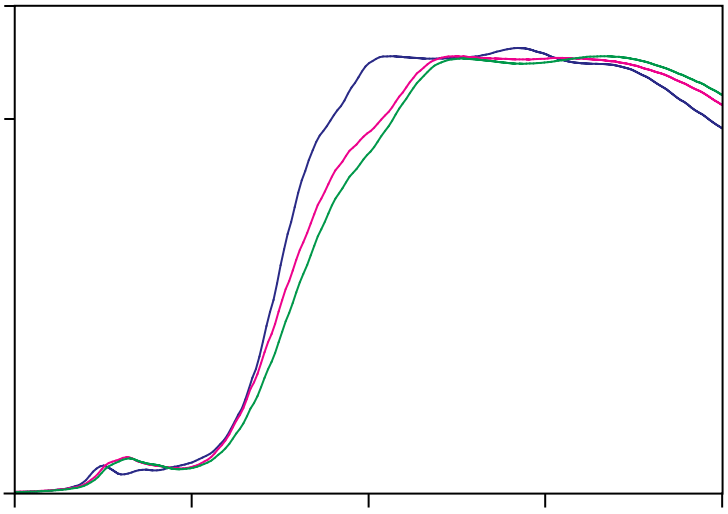

Figure 5-14: Mn K-edge XANES spectra of **4**, **5**, and **6** in the Mn_2(III,III) (blue), Mn_2(III,IV) (pink), and Mn_2(IV,IV) (green) oxidation states.

Mn causes a shift in the edge position to higher energy and there is almost no change in the shape of the edge. A similar trend is seen in the XANES spectra pertaining to the $S_1 \rightarrow S_2$ transition (see Figure 2-4 in Chapter 2).

EXAFS

The k^3-space EXAFS spectra of **4**, **5**, and **6** in the Mn_2(III,III), Mn_2(III,IV), and Mn_2(IV,IV) oxidation states, respectively, are shown in Figure 5-15. As was concluded from the examination of the XANES spectra in Figure 5-14, the greatest changes in the k^3-space EXAFS spectra occur between the mono-μ-oxo Mn_2(III,III) complex and the di-μ-oxo Mn_2(III,IV) complex. This is because the ~2.7 Å Mn–Mn backscattering which is present in di-μ-oxo-bridged Mn_2 moieties is absent in the mono-μ-oxo Mn_2(III,III) complex; thus, the k^3-space spectrum for the Mn_2(III,III) complex is much different from the k^3-space spectra for the Mn_2(III,IV) and the Mn_2(IV,IV) complexes. This is shown graphically in the Fourier transforms of these k^3-space spectra which are shown in Figure 5-16. The peak at an apparent distance R' = 2.3 Å in the Mn_2(III,IV) and the Mn_2(IV,IV) complexes reflects the contribution from Mn–Mn backscattering in the di-μ-oxo-bridged moiety. In the mono-μ-oxo Mn_2(III,IV) complex, the Mn–Mn backscattering peak has increased in apparent distance by ~0.5 Å, consistent with the presence of a mono-μ-oxo bridge.

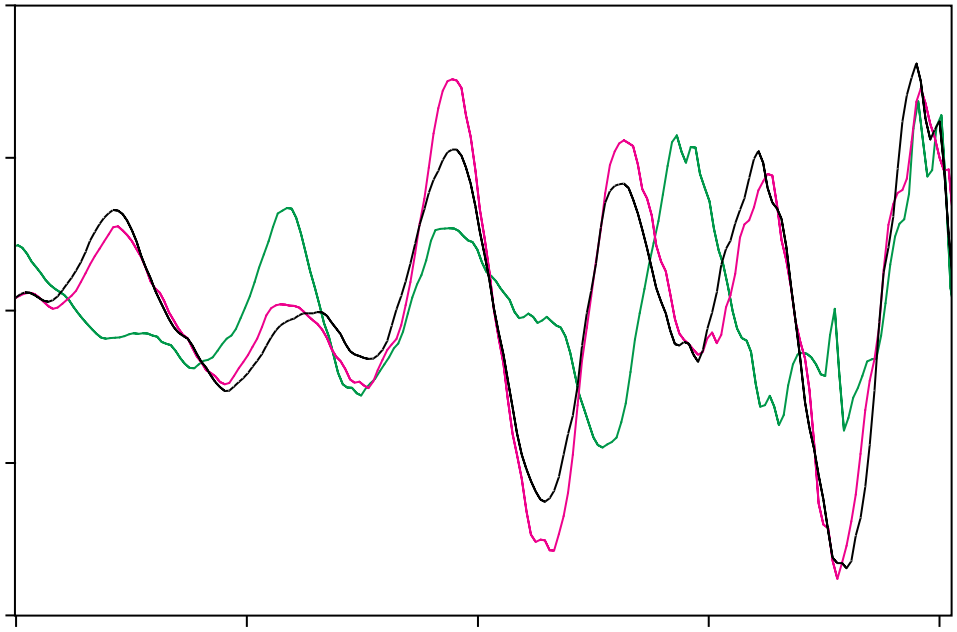

Figure 5-15: Mn k^3-space EXAFS spectra of **4**, **5**, and **6** the Mn_2(III,III) (blue), Mn_2(III,IV) (pink), and Mn_2(IV,IV) (green) oxidation states, respectively.

The first peak in Figure 5-16 corresponding to first-shell Mn–O/N ligands is also strongly affected by the presence of a di-μ-oxo bridge. It has been shown that the bridging oxygens in di-μ-oxo-bridged Mn–Mn moieties are by far the strongest contributor to the first-shell EXAFS due to their low static disorder, although a greater number of terminal Mn–O/N distances, albeit with a higher static disorder, exist.[72] The increase in apparent distance of the first peak in the mono-μ-oxo Mn_2(III,III) complex can be due to two factors. First, the Mn(III) Jahn-Teller distortion is expected to be twice as intense in the Mn_2(III,III) complex as it is in the Mn_2(III,IV) complex, which causes an increase in the first-shell distances to axial ligands. Another explanation is that the difference in the degree of static disorder between the bridging and terminal distances is

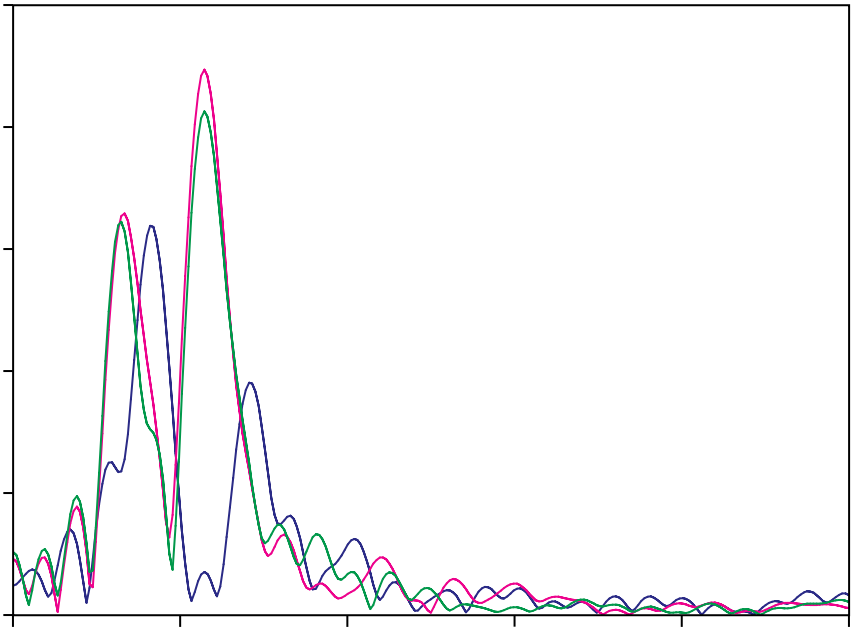

Figure 5-16: Fourier transforms of the Mn k^3-space EXAFS spectra of **4**, **5**, and **6** in the Mn_2(III,III) (blue), Mn_2(III,IV) (pink), and Mn_2(IV,IV) (green) oxidation states, respectively.

less in the Mn_2(III,III) complex than the Mn_2(III,IV) complex. However, neither of these scenarios would predict that the first-shell Fourier peak would be more intense in the Mn_2(III,III) complex than the Mn_2(III,IV) complex. In fact, a similar mono-μ-oxo Mn_2(III,III) complex with tacn (triazacyclononane) terminal ligands has been synthesized by Wieghardt et al.[304] and it was shown by DeRose et al.[72] to have a significantly reduced amplitude of the first- and second-shell Fourier peaks relative to the S_1 state of PS II.

Because single crystals have been obtained of all three of these complexes from Prof. Mukherjee, it will be possible to pursue oriented XAS studies with these samples in conjunction with the oriented studies of PS II single crystals.

Discussion

The ability to exploit the plane-polarized nature of synchrotron radiation has made possible the study of dichroism in oriented membranes,[161,202,205,236,305] single-crystal model complexes,[284-286] and single crystals of metalloproteins.[289] These studies have been able to significantly expand the X-ray absorption spectroscopic information available for these systems over what is gleaned from studies of isotropic samples.

Based on the results shown in this chapter, it is reasonable to expect that the study of single crystals of PS II will provide significant new information about the orientation of important structural motifs in the OEC. This is based on the significant dichroism observed in the single crystal studies of the three Mn complexes presented above. Of particular interest are the dichroic properties of the di-μ-oxo Mn_2(III,IV) single crystal (**3**) which show that the first and second Fourier peaks have quite similar dichroic properties. Thus, it is quite possible that the proper orientations of a PS II single crystal will show the same type of dichroism in Peaks I and II; this will greatly help in deriving insight into the relative orientations of the di-μ-oxo Mn–Mn motifs. This will also be extremely helpful in narrowing the possibilities for a topological model of the OEC that are shown in Figure 3-12 and Figure 3-13.

One of the issues that will need to be addressed for metalloprotein crystals is how to minimize radiation damage. The XANES spectra shown in Figure 5-5 from the Mn(V)–nitrido single crystal (**1**) show that susceptibility to radiation damage is a concern even for model complexes if they are exposed to the X-ray beam for a sufficient time. The spectrum in Figure 5-5 collected at $\phi = 30°$ and $\chi = 0°$ (pre-edge peak second from the top) was one of the last spectra collected on this crystal, and the pre-edge peak from

this transition is noticeably shifted to higher energy. This can be attributed to the effects of radiation damage, because the same trend was seen in separate scans at $\phi = 45°$ and $\chi = 0°$ which were taken near the beginning and the end of the experiment (data not shown); the experiment took over 24 hours to complete at room temperature. The radiation damage can be greatly reduced if a laminar flow of cold N_2 gas maintains the crystal temperature at ~100 K; such laminar-flow setups are already in place in all beamlines at SSRL dedicated to protein crystallography.

Further improvement can be obtained by using an image plate or an area detector to collect a diffraction pattern of a crystal mounted on the goniometer head. This eliminates the need to relate the unit cell axes with the macroscopic crystal axes, because the direction of the unit cell axes can be determined from the diffraction pattern if the space group of the crystal is known. By taking two diffraction patterns at two arbitrary angles 90° apart, the absolute orientation angles of the unit cell axes can be calculated; this provides an absolute calibration of the goniometer angles ϕ and χ and allows proper alignment of the X-ray *E* vector with the desired molecular vector(s).

These suggested improvements are being incorporated into a special single-crystal setup that can be installed in certain SSRL beamlines which will have a means of collecting diffraction patterns and cryo-cooling crystals. This will greatly reduce the two major problems mentioned above – absolute angle calibration and radiation damage – and will make it possible to perform single-crystal XAS studies on PS II.

Appendix

EXAFS curve-fitting of Mn(V)–nitrido single-crystal spectra from an intermediate orientation

The fitting procedure described in the main text for the extreme orientations of the Mn(V)–nitrido single crystal (**1**) can be extended to fit an intermediate orientation which contains contributions from almost all of the backscatterers present in the complex. Table 5-3 describes the fits to the EXAFS data at the intermediate orientation of $\phi = 45°$ and $\chi = 0°$. Fit #1 in Table 5-3 shows the attempt to fit this spectrum using only single-

Table 5-3: Simulations of the EXAFS spectra from the Mn(V)–nitrido single crystal (**1**) at an orientation of $\phi = 45°$ and $\chi = 0°$. This orientation contains contributions from both the short (~1.5 Å) Mn–N vector and the equatorial cyano groups.

Fit #	shell	path	R (Å)	N	σ^2 (Å^2)	$\bullet E_0$ [b]	Φ (x 10^{-3})	ε^2 (x 10^{-5})
1	Mn–C	–	1.94	4.42	0.004	-20	2.41	1.57
	Mn–N	–	3.08[d]	4.44[d]	0.004[d]			
	Mn–N	1	3.08[d]	4.44[d]	0.004[d]			
	Mn–N	2	3.08[d]	4.44[d]	0.004[d]			
2	Mn–N	–	1.60	1.70	0.003	5	2.89	1.81
	Mn–C	–	2.37	0.58	0.002[c]			
3	Mn–N	–	1.58	1.85	0.003	-1	1.61	1.16
	Mn–C	–	2.35	0.69	0.002[c]			
	Mn–N	1	3.20	3.70	0.002			
4	Mn–C	–	1.97	2.40	0.002[c]	-12	0.07	0.05
	Mn–N	–	3.13[d]	4.56[d]	0.005[d]			
	Mn–N	1	3.13[d]	4.56[d]	0.005[d]			
	Mn–N	2	3.13[d]	4.56[d]	0.005[d]			
	Mn–N	–	1.55	1.61	0.003			
	Mn–C	–	2.44	0.27	0.002[c]			

[a]fit parameters and quality-of-fit parameters are described in Chapter 3 Materials and Methods, path = multiple-scattering path from Figure 5-3; [b]$\bullet E_0$ was constrained to be equal for all shells within a fit; [c]parameter fixed in fit; [d]parameters constrained to be equal for designated shells in the fit

and multiple-scattering contributions from the equatorial cyano groups. As shown in Figure 5-17A, this adequately fits the backscattering contributions from the cyano N atoms, but poorly fits the low *R′* contributions to the first Fourier peak. Fit #2 in Table 5-3 uses only the single-scattering shells corresponding to the axial ligands; Figure 5-17B shows that this fits the low-*R′* portion of the first Fourier peak well, but cannot fit the second Fourier peak at all. Adding multiple-scattering contributions to this fit is a significant improvement (Fit #3 in Table 5-3, Figure 5-17C), but is mostly due to the fitting program attempting to fit the components of the EXAFS spectrum which are due to equatorial ligands with axial ligand parameters. Including shells for both the equatorial and axial ligands (Fit #4 in Table 5-3) provides an excellent fit to the experimental data, as shown in Figure 5-17D.

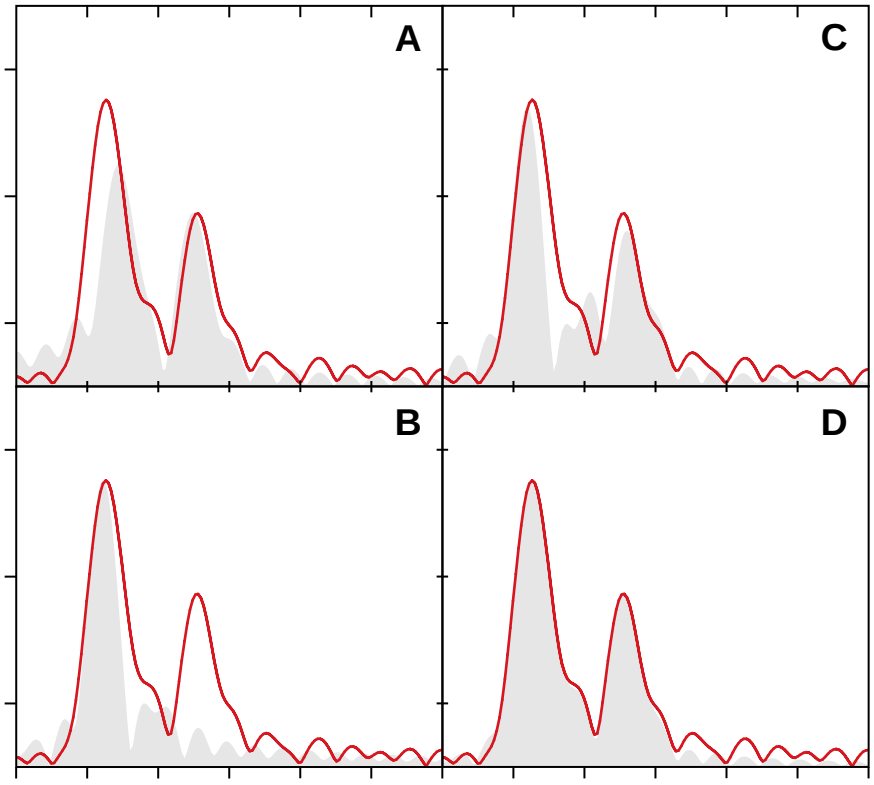

Figure 5-17: Curve-fitting results for various fits to the k^3-space EXAFS spectra from the Mn(V)–nitrido single crystal (**1**) at an orientation of $\phi = 45°$ and $\chi = 90°$. For comparison purposes, the spectra are presented as Fourier transforms of the experimental spectra (red) and the various fits (gray) **(A)** Fit #1 from Table 5-3; **(B)** Fit #2 from Table 5-3; **(C)** Fit #3 from Table 5-3; **(D)** Fit #4 from Table 5-3.

Chapter 5 Acknowledgments

This research was supported by the National Institutes of Health (GM-55302), and the Director, Office of Basic Energy Sciences, Division of Energy Biosciences of the U.S. Department of Energy (DOE), under Contract DE-AC03-76SF00098. Synchrotron radiation facilities were provided by the Stanford Synchrotron Radiation Laboratory (SSRL) which is operated by the Department of Energy, Office of Basic Energy Sciences. The SSRL Biotechnology Program is supported by the National Institutes of Health, National Center of Research Resources, Biomedical Technology Program, and by the Department of Energy, Office of Biological and Environmental Research. Dr. Jesper Bendix, Prof. Terrence Collins, Prof. Jean-Jacques Girerd, and Prof. R. N. Mukerjee are thanked for providing single-crystal Mn model complexes.

Chapter 6 : Future Directions

The conclusions presented in this thesis are suggestive of several additional experiments which can provide further insight into the structure of the OEC and the mechanism of oxygen evolution. Many of these experiments will take advantage of the higher Mn concentration in newly available single crystals of PS II from the research groups of Dr. Fromme and Prof. Witt in Berlin.[60,265] These preparations have 60 – 70 Chl per reaction center,[265] which is increased by a factor of about five relative to the preparations used for the experiments detailed in this thesis. Because the single-flash saturable concentration of Chl in this new preparation is still 9.5 mg/mL, this translates into a five-fold increase in the Mn concentration of single-flash saturable PS II samples.

Intriguing experiments for the future abound with these new Fromme/Witt PS II preparations and single crystals. It is now possible to use these new preparations to repeat the XANES and Kβ XES experiments detailed in Chapter 2 at a significantly higher Mn concentration. This will be most helpful for the Kβ XES experiments, which can now be performed with less X-ray exposure time, and a higher signal-to-noise ratio will be achieved. Furthermore, these experiments can now be done at the Advanced Photon Source (APS) in Argonne, IL, where the photon flux is increased by roughly a factor of 100 over that available at beamline 10-2 at SSRL. This means that, during the limited amount of beamtime available, a significantly larger number of samples will be able to be examined than were examined at beamline 10-2 at SSRL.

If the new Fromme/Witt PS II preparations are used, the total X-ray exposure per sample for the the Kβ XES experiments will be considerably reduced relative to the

experiments described in Chapter 2. This will improve confidence that the observed <E> shifts for the Kβ XES spectra detailed in Chapter 2 are not significantly affected by radiation damage. For the XANES experiments, the greatest benefit from the Fromme/Witt PS II preparations will be the significantly improved signal-to-noise ratio. This will make it easier to identify the individual features that contribute to the XANES spectrum using high-resolution 2nd derivatives. If these features can be reliably identified in the various S-states of the OEC as well as in Mn model complexes, it may be possible to gain a much deeper insight into the origin of the XANES transitions than is currently available. Currently, extracting oxidation-state information from XANES spectra is primarily based on qualitative interpretations of edge shape and using quantitative analysis methods like 2nd derivatives to calculate shifts in the overall position of the main XANES edge. With information about the position and number of individual transitions that form the main XANES edge, techniques like density functional theory can be used to assign these experimentally observed features to *ab initio*-calculated transitions between molecular orbitals. This type of interpretation could finally provide a firm theoretical basis for interpreting the XANES spectra of PS II much like the established theoretical basis that exists for interpreting EXAFS spectra.

The increased flux available at the APS can also be used to indirectly obtain an Mn L-edge XANES spectrum from PS II. It has been extremely difficult to collect Mn L-edge spectra because significant experimental problems occur with photons at the energy of the Mn L-edge absorption (~650 eV). The penetration depth of L-edge photons is only about 1 μm, and frost forming on the sample will instantly eliminate any Mn fluorescence. Furthermore, at these energies, almost any substance, including the sample,

significantly absorbs the incoming X-rays, so the experiments must be done in vacuum; radiation damage is thus a serious problem. Finally, the oxygen K-edge is only 100 eV lower in energy than the Mn L-edge; thus, superconducting energy-resolving detectors must be used to discriminate against the vast amount of oxygen Kα fluorescence that is present.[306]

These problems are particularly challenging in view of the potential of Mn L-edge spectra to provide detailed information about the Mn atoms in the OEC. In many ways, Mn L-edge spectra are superior to Mn K-edge spectra, because multiplet calculations[307] can be applied to L-edge spectra which are sensitive to the number of holes in the 3d level,[308] the oxidation state of Mn, and the spin state of Mn.[307] This is a rich amount of information about oxidation states relative to what is available from K-edge XANES spectra. L-edge spectra have already been obtained for a number of Fe, Cu, and Ni metalloproteins,[309-318] and have been fit using multiplet calculations to provide quantitative conclusions about the oxidation states of the metals involved. However, as detailed above, extending these experiments to Mn in PS II is not straightforward.

Most of the problems in L-edge spectroscopy are due to the intrinsic physical properties of <1 keV photons. Thus, the recent proposal by Prof. Stephen Cramer and co-workers that it may be possible to collect these L-edge spectra using hard X-rays is definitely worth investigating. This proposal is based on using a technique called resonant inelastic X-ray scattering (RIXS)[319] to collect an L-edge-like spectrum of Mn in PS II. RIXS involves exciting a pre-edge transition (1s $\rightarrow$ 3d) of the K shell using hard X-rays. Then, the high-resolution X-ray emission analyzer described in Chapter 2 can be tuned to detect the Kα fluorescence of Mn, which is a 2p $\rightarrow$ 1s transition. The final state

from this transition is a 2p hole, which is the same final state as the L-edge fluorescence ($3d \rightarrow 2p$). Thus, the resulting spectrum obtained using hard X-rays with RIXS should resemble a Mn L-edge emission spectrum. Furthermore, this technique offers an unprecedented opportunity to selectively excite into specific molecular orbitals with 3d character by tuning the incoming X-rays to look at a specific pre-edge transition; at least 2 – 3 resolvable pre-edge transitions are seen in the Mn K-edge spectrum of PS II, as shown in the inset of Figure 2-4A. This means that it would be possible to obtain 'nested' RIXS spectra which correspond to fluorescence from different molecular orbitals with 3d character.

A rough estimate of the expected signal-to-noise ratio for this experiment is actually quite promising, because the Mn Kβ fluorescence that was monitored in the experiments described in Chapter 2 is a factor of eight weaker than the Mn Kα fluorescence from these proposed experiments. However, the pre-edge transition shown in Figure 2-4A is formally dipole-forbidden, and in PS II is about ten times weaker than the main ($1s \rightarrow 4p$) XANES transition. Thus, the expected signal-to-noise ratio should be comparable to that observed for the Kβ XES spectra shown in Chapter 2. Furthermore, this experiment is dependent on the stability and energy resolution of the incoming X-ray beam. The beam needs to be monochromatic enough (•1 eV would be desirable) to selectively excite certain pre-edge transitions. In addition, any shift in energy of the incoming X-ray beam will be manifested as a shift in the observed L-edge-like spectra; this must be kept to a minimum to avoid unnecessarily broadening the spectral features.

The S_0-state EXAFS experiments described in Chapter 3 can be extended by using oriented S_0-state samples. This can be done by using the time after the flashes, which was used to concentrate the samples by centrifugation, instead to orient the S_0-state PS II membranes on a Mylar film. These samples can then be used in oriented EXAFS experiments to examine the dichroism of the 2.85 Å Mn–Mn vector separately from the 2.7 Å Mn–Mn vector(s) and extract the orientation of these Mn–Mn vectors with respect to the membrane plane. Using oriented samples to derive dichroism information has already been performed for samples in the S_3 state[161] and samples in the S_2 state which have been treated with NH_3;[236] these experiments have exploited the presence of Mn–Mn distance heterogeneity in the samples to deconvolute the dichroic properties of the longer and shorter Mn–Mn vectors.

The EPR experiments with the S_0-state multiline EPR signal detailed in Chapter 4 are being advanced by the examination of this signal using pulsed EPR methods in collaboration with the group of Prof. Britt at UC Davis and using high-field EPR spectroscopy in collaboration with the group of Prof. Lubitz at the TU-Berlin. The use of pulsed EPR methods such as ESEEM will provide further insight into the magnetic couplings present in the S_0 state and will significantly refine the fit possibilities presented in Chapter 4 for this signal. The use of high-field EPR will show how much *g* anisotropy is present in this signal; at the present time, it is not known to what degree hyperfine interactions and *g* anisotropy contribute to the splitting between the multiline peaks. If significant *g* anisotropy is present, the splitting between the multiline peaks will significantly increase at higher field, because *g* anisotropy is magnetic-field dependent while hyperfine interactions are not.

The single-crystal experiments with Mn model compounds that are detailed in Chapter 5 will be followed by similar experiments with single crystals of PS II from the Fromme and Witt groups in Berlin. The information gained by the experiments with model compounds will guide the subsequent studies of PS II, in which the hope is to specifically orient the di-μ-oxo-bridged Mn–Mn moieties in the OEC. This will lead to a significant refinement in the possibilities for the structure of the oxygen-evolving complex in PS II.

References

(1) Kasting, J. F. *Science* **1993**, *259*, 920-926.

(2) Doolittle, R. F.; Feng, D.-F.; Tsang, S.; Cho, G.; Little, E. *Science* **1996**, *271*, 470-477.

(3) Castresana, J.; Saraste, M. *Trends Biochem. Sci.* **1995**, *20*, 443-448.

(4) Martin, W. F. *BioEssays* **1996**, *18*, 523-527.

(5) Ort, D. R.; Yocum, C. F., Eds. *Oxygenic Photosynthesis; The Light Reactions.*; Kluwer Academic Publishers: Dordrecht, 1996; Vol. 4.

(6) Boyer, P. D. *Annu. Rev. Biochem.* **1997**, *66*, 717-749.

(7) Boyer, P. D. *Biochim. Biophys. Acta* **2000**, *1458*, 252-262.

(8) Calvin, M.; Benson, A. A. *Science* **1948**, *107*, 476-480.

(9) Calvin, M. *Angew. Chem., Int. Ed. Engl.* **1962**, *1*, 65-75.

(10) Bassham, J. A. *Sci. Amer.* **1962**, *206*, 1-15.

(11) Miller, A. F.; Brudvig, G. W. *Biochim. Biophys. Acta* **1991**, *1056*, 1-18.

(12) Satoh, K. In *Oxygenic Photosynthesis: The Light Reactions*; Ort, D. R., Yocum, C. F., Eds.; Kluwer Academic Publishers: Dordrecht, 1996; Vol. 4, pp 193-211.

(13) Witt, H. T. In *Oxygenic Photosynthesis: The Light Reactions*; Ort, D. R., Yocum, C. F., Eds.; Kluwer Academic Publishers: Dordrecht, 1996; Vol. 4, pp 363-375.

(14) Debus, R. J. *Biochim. Biophys. Acta* **1992**, *1102*, 269-352.

(15) Wasielewski, M. R.; Johnson, D. G.; Seibert, M.; Govindjee *Proc. Natl. Acad. Sci. U. S. A.* **1989**, *86*, 524-528.

(16) Durrant, J. R.; Hastings, G.; Joseph, D. M.; Barber, J.; Porter, G.; Klug, D. R. *Proc. Natl. Acad. Sci. U. S. A.* **1992**, *89*, 11632-11636.

(17) Trissl, H.-W.; Hecks, B.; Wulf, K. *Photochem. Photobiol.* **1993**, *57*, 108-112.

(18) Holzwarth, A. R.; Schatz, G.; Brock, H.; Bittersmann, E. *Biophys. J.* **1993**, *64*, 1813-1826.

(19) Hastings, G.; Kleinherenbrink, F. A. M.; Lin, S.; Blankenship, R. E. *Biochemistry* **1994**, *33*, 3185-3192.

(20) Hastings, G.; Kleinherenbrink, F. A. M.; Lin, S.; McHugh, T. J.; Blankenship, R. E. *Biochemistry* **1994**, *33*, 3193-3200.

(21) Debus, R. J.; Barry, B. A.; Sithole, I.; Babcock, G. T.; McIntosh, L. *Biochemistry* **1988**, *27*, 9071-9074.

(22) Metz, J. G.; Nixon, P. J.; Rögner, M.; Brudvig, G. W.; Diner, B. A. *Biochemistry* **1989**, *28*, 6960-6969.

(23) Babcock, G. T.; Sauer, K. *Biochim. Biophys. Acta* **1975**, *376*, 315-328.

(24) Razeghifard, M. R.; Klughammer, C.; Pace, R. J. *Biochemistry* **1997**, *36*, 86-92.

(25) Razeghifard, M. R.; Pace, R. J. *Biochim. Biophys. Acta* **1997**, *1322*, 141-150.

(26) Radmer, R.; Cheniae, G. In *Primary Processes of Photosynthesis*; Barber, J., Ed.; Elsevier Science Publishers: Amsterdam, 1977; Vol. 2, pp 303-348.

(27) Kok, B.; Forbush, B.; McGloin, M. *Photochem. Photobiol.* **1970**, *11*, 457-475.

(28) Geselowitz, D.; Meyer, T. J. *Inorg. Chem.* **1990**, *29*, 3894-3896.

(29) Naruta, Y.; Sasayama, M.-a.; Sasaki, T. *Angew. Chem., Int. Ed. Engl.* **1994**, *33*, 1839-1841.

(30) Limburg, J.; Vrettos, J. S.; Liable-Sands, L. M.; Rheingold, A. L.; Crabtree, R. H.; Brudvig, G. W. *Science* **1999**, *283*, 1524-1527.

(31) Sauer, K. *Acc. Chem. Res.* **1980**, *13*, 249-256.

(32) Babcock, G. T.; Barry, B. A.; Debus, R. J.; Hoganson, C. W.; Atamian, M.; McIntosh, L.; Sithole, I.; Yocum, C. F. *Biochemistry* **1989**, *28*, 9557-9565.

(33) Rutherford, A. W.; Zimmermann, J.-L.; Boussac, A. In *The Photosystems: Structure, Function and Molecular Biology*; Barber, J., Ed.; Elsevier Science Publishers: Amsterdam, 1992; Vol. 11, pp 179-229.

(34) Sauer, K.; Yachandra, V. K.; Britt, R. D.; Klein, M. P. In *Manganese Redox Enzymes*; Pecoraro, V. L., Ed.; VCH Publishers: New York, 1992; pp 141-175.

(35) Britt, R. D. In *Oxygenic Photosynthesis: The Light Reactions*; Ort, D. R., Yocum, C. F., Eds.; Kluwer Academic Publishers: Dordrecht, 1996; Vol. 4, pp 137-164.

(36) Yachandra, V. K.; Sauer, K.; Klein, M. P. *Chem. Rev.* **1996**, *96*, 2927-2950.

(37) Renger, G. *Physiol. Plant.* **1997**, *100*, 828-841.

(38) Penner-Hahn, J. E. *Struct. Bonding (Berlin)* **1998**, *90*, 1-36.

(39) Tommos, C.; Babcock, G. T. *Acc. Chem. Res.* **1998**, *31*, 18-25.

(40) Robblee, J. H.; Cinco, R. M.; Yachandra, V. K. *Biochim. Biophys. Acta* **2001**, *1503*, 7-23.

(41) Karge, M.; Irrgang, K.-D.; Renger, G. *Biochemistry* **1997**, *36*, 8904-8913.

(42) Renger, G.; Christen, G.; Karge, M.; Eckert, H.-J.; Irrgang, K. D. *JBIC* **1998**, *3*, 360-366.

(43) Vänngård, T.; Hansson, Ö.; Haddy, A. In *Manganese Redox Enzymes*; Pecoraro, V. L., Ed.; VCH Publishers: New York, 1992; pp 105-118.

(44) Britt, R. D.; Peloquin, J. M.; Campbell, K. A. *Annu. Rev. Biophys. Biomol. Struct.* **2000**, *29*, 463-495.

(45) Messinger, J.; Robblee, J.; Yu, W. O.; Sauer, K.; Yachandra, V. K.; Klein, M. P. *J. Am. Chem. Soc.* **1997**, *119*, 11349-11350.

(46) Åhrling, K. A.; Peterson, S.; Styring, S. *Biochemistry* **1997**, *36*, 13148-13152.

(47) Dexheimer, S. L.; Klein, M. P. *J. Am. Chem. Soc.* **1992**, *114*, 2821-2826.

(48) Yamauchi, T.; Mino, H.; Matsukawa, T.; Kawamori, A.; Ono, T.-a. *Biochemistry* **1997**, *36*, 7520-7526.

(49) Campbell, K. A.; Peloquin, J. M.; Pham, D. P.; Debus, R. J.; Britt, R. D. *J. Am. Chem. Soc.* **1998**, *120*, 447-448.

(50) Dismukes, G. C.; Siderer, Y. *Proc. Natl. Acad. Sci. U. S. A.* **1981**, *78*, 274-278.

(51) Hansson, Ö.; Andréasson, L.-E. *Biochim. Biophys. Acta* **1982**, *679*, 261-268.

(52) Casey, J. L.; Sauer, K. *Biochim. Biophys. Acta* **1984**, *767*, 21-28.

(53) Zimmermann, J.-L.; Rutherford, A. W. *Biochim. Biophys. Acta* **1984**, *767*, 160-167.

(54) Matsukawa, T.; Mino, H.; Yoneda, D.; Kawamori, A. *Biochemistry* **1999**, *38*, 4072-4077.

(55) DuBois, J. L.; Mukherjee, P.; Stack, T. D. P.; Hedman, B.; Solomon, E. I.; Hodgson, K. O. *J. Am. Chem. Soc.* **2000**, *122*, 5775-5787.

(56) Shulman, R. G.; Yafet, Y.; Eisenberger, P.; Blumberg, W. E. *Proc. Natl. Acad. Sci. U. S. A.* **1976**, *73*, 1384-1388.

(57) Yachandra, V. K. *Methods Enzymol.* **1995**, *246*, 638-675.

(58) Kirby, J. A.; Robertson, A. S.; Smith, J. P.; Thompson, A. C.; Cooper, S. R.; Klein, M. P. *J. Am. Chem. Soc.* **1981**, *103*, 5529-5537.

(59) Goodin, D. B.; Yachandra, V. K.; Britt, R. D.; Sauer, K.; Klein, M. P. *Biochim. Biophys. Acta* **1984**, *767*, 209-216.

(60) Zouni, A.; Witt, H. T.; Kern, J.; Fromme, P.; Kraus, N.; Saenger, W.; Ort, P., in press.

(61) Diner, B. A.; Babcock, G. T. In *Oxygenic Photosynthesis: The Light Reactions*; Ort, D. R., Yocum, C. F., Eds.; Kluwer Academic Publishers: Dordrecht, 1996; Vol. 4, pp 213-247.

(62) Brudvig, G. W.; Crabtree, R. H. *Proc. Natl. Acad. Sci. U. S. A.* **1986**, *83*, 4586-4588.

(63) Christou, G.; Vincent, J. B. *Biochim. Biophys. Acta* **1987**, *895*, 259-274.

(64) Pecoraro, V. L. In *Manganese Redox Enzymes*; Pecoraro, V. L., Ed.; VCH Publishers: New York, 1992; pp 197-231.

(65) Hoganson, C. W.; Babcock, G. T. *Science* **1997**, *277*, 1953-1956.

(66) Siegbahn, P. E. M.; Crabtree, R. H. *J. Am. Chem. Soc.* **1999**, *121*, 117-127.

(67) Haumann, M.; Junge, W. *Biochim. Biophys. Acta* **1999**, *1411*, 86-91.

(68) Schlodder, E.; Witt, H. T. *J. Biol. Chem.* **1999**, *274*, 30387-30392.

(69) Liang, W.; Roelofs, T. A.; Cinco, R. M.; Rompel, A.; Latimer, M. J.; Yu, W. O.; Sauer, K.; Klein, M. P.; Yachandra, V. K. *J. Am. Chem. Soc.* **2000**, *122*, 3399-3412.

(70) Messinger, J. *Biochim. Biophys. Acta* **2000**, *1459*, 481-488.

(71) Yachandra, V. K.; DeRose, V. J.; Latimer, M. J.; Mukerji, I.; Sauer, K.; Klein, M. P. *Science* **1993**, *260*, 675-679.

(72) DeRose, V. J.; Mukerji, I.; Latimer, M. J.; Yachandra, V. K.; Sauer, K.; Klein, M. P. *J. Am. Chem. Soc.* **1994**, *116*, 5239-5249.

(73) Cinco, R. M.; Rompel, A.; Visser, H.; Aromí, G.; Christou, G.; Sauer, K.; Klein, M. P.; Yachandra, V. K. *Inorg. Chem.* **1999**, *38*, 5988-5998.

(74) Peloquin, J. M.; Campbell, K. A.; Randall, D. W.; Evanchik, M. A.; Pecoraro, V. L.; Armstrong, W. H.; Britt, R. D. *J. Am. Chem. Soc.* **2000**, *122*, 10926-10942.

(75) Hasegawa, K.; Kusunoki, M.; Inoue, Y.; Ono, T.-a. *Biochemistry* **1998**, *37*, 9457-9465.

(76) Hasegawa, K.; Ono, T.-a.; Inoue, Y.; Kusunoki, M. *Chem. Phys. Lett.* **1999**, *300*, 9-19.

(77) Siegbahn, P. E. M. *Inorg. Chem.* **2000**, *39*, 2923-2935.

(78) Hasegawa, K.; Ono, T.-a.; Inoue, Y.; Kusunoki, M. *Bull. Chem. Soc. Jpn.* **1999**, *72*, 1013-1023.

(79) Penner-Hahn, J. E.; Fronko, R. M.; Pecoraro, V. L.; Yocum, C. F.; Betts, S. D.; Bowlby, N. R. *J. Am. Chem. Soc.* **1990**, *112*, 2549-2557.

(80) Guiles, R. D.; Yachandra, V. K.; McDermott, A. E.; Cole, J. L.; Dexheimer, S. L.; Britt, R. D.; Sauer, K.; Klein, M. P. *Biochemistry* **1990**, *29*, 486-496.

(81) Messinger, J.; Robblee, J. H.; Fernandez, C.; Cinco, R. M.; Visser, H.; Bergmann, U.; Glatzel, P.; Cramer, S. P.; Campbell, K. A.; Peloquin, J. M.; Britt, R. D.; Sauer, K.; Yachandra, V. K.; Klein, M. P. In *Photosynthesis: Mechanisms and*

Effects; Garab, G., Ed.; Kluwer Academic Publishers: Dordrecht, 1998; Vol. 2, pp 1279-1282.

(82) Liang, W.; Roelofs, T. A.; Olsen, G. T.; Latimer, M. J.; Cinco, R. M.; Rompel, A.; Sauer, K.; Yachandra, V. K.; Klein, M. P. In *Photosynthesis: from Light to Biosphere*; Mathis, P., Ed.; Kluwer Academic Publishers: Dordrecht, 1995; Vol. 2, pp 413-416.

(83) Messinger, J.; Nugent, J. H. A.; Evans, M. C. W. *Biochemistry* **1997**, *36*, 11055-11060.

(84) Campbell, K. A.; Gregor, W.; Pham, D. P.; Peloquin, J. M.; Debus, R. J.; Britt, R. D. *Biochemistry* **1998**, *37*, 5039-5045.

(85) Styring, S. A.; Rutherford, A. W. *Biochemistry* **1988**, *27*, 4915-4923.

(86) Evelo, R. G.; Styring, S.; Rutherford, A. W.; Hoff, A. J. *Biochim. Biophys. Acta* **1989**, *973*, 428-442.

(87) Sharp, R. R. In *Manganese Redox Enzymes*; Pecoraro, V. L., Ed.; VCH Publishers: New York, 1992; pp 177-196.

(88) Saygin, Ö.; Witt, H. T. *Biochim. Biophys. Acta* **1987**, *893*, 452-469.

(89) Kretschmann, H.; Dekker, J. P.; Saygin, Ö.; Witt, H. T. *Biochim. Biophys. Acta* **1988**, *932*, 358-361.

(90) Dekker, J. P. In *Manganese Redox Enzymes*; Pecoraro, V. L., Ed.; VCH Publishers: New York, 1992; pp 85-103.

(91) Lavergne, J. *Biochim. Biophys. Acta* **1987**, *894*, 91-107.

(92) Renger, G. *Photosynthetica* **1987**, *21*, 203-224.

(93) Cramer, S. P.; Eccles, T. K.; Kutzler, F. W.; Hodgson, K. O.; Mortenson, L. E. *J. Am. Chem. Soc.* **1976**, *98*, 1287-1288.

(94) Powers, L.; Blumberg, W. E.; Chance, B.; Barlow, C. H.; Leigh, J. S., Jr.; Smith, J.; Yonetani, T.; Vik, S.; Peisach, J. *Biochim. Biophys. Acta* **1979**, *546*, 520-538.

(95) Kirby, J. A.; Goodin, D. B.; Wydrzynski, T.; Robertson, A. S.; Klein, M. P. *J. Am. Chem. Soc.* **1981**, *103*, 5537-5542.

(96) Roe, A. L.; Schneider, D. J.; Mayer, R. J.; Pyrz, J. W.; Widom, J.; Que, L., Jr. *J. Am. Chem. Soc.* **1984**, *106*, 1676-1681.

(97) Kau, L. S.; Spira-Solomon, D. J.; Penner-Hahn, J. E.; Hodgson, K. O.; Solomon, E. I. *J. Am. Chem. Soc.* **1987**, *109*, 6433-6442.

(98) Roelofs, T. A.; Liang, W.; Latimer, M. J.; Cinco, R. M.; Rompel, A.; Andrews, J. C.; Sauer, K.; Yachandra, V. K.; Klein, M. *Proc. Natl. Acad. Sci. U. S. A.* **1996**, *93*, 3335-3340.

(99) Stemmler, T. L.; Sossong, T. M., Jr.; Goldstein, J. I.; Ash, D. E.; Elgren, T. E.; Kurtz, D. M.; Penner-Hahn, J. E. *Biochemistry* **1997**, *36*, 9847-9858.

(100) Blackburn, N. J.; Rhames, F. C.; Ralle, M.; Jaron, S. *JBIC* **2000**, *5*, 341-353.

(101) Ono, T.-a.; Noguchi, T.; Inoue, Y.; Kusunoki, M.; Matsushita, T.; Oyanagi, H. *Science* **1992**, *258*, 1335-1337.

(102) Iuzzolino, L.; Dittmer, J.; Dörner, W.; Meyer-Klaucke, W.; Dau, H. *Biochemistry* **1998**, *37*, 17112-17119.

(103) Limburg, J.; Szalai, V. A.; Brudvig, G. W. *J. Chem. Soc., Dalton Trans.* **1999**, 1353-1362.

(104) Sanner, V. H. Ph. D. thesis, Uppsala University, 1941.

(105) Tsutsumi, K. *J. Phys. Soc. Jpn.* **1959**, *14*, 1696-1706.

(106) Urch, D. S.; Wood, P. R. *X-Ray Spectrom.* **1978**, *7*, 9-11.

(107) Peng, G.; de Groot, F. M. F.; Hämäläinen, K.; Moore, J. A.; Wang, X.; Grush, M. M.; Hastings, J. B.; Siddons, D. P.; Armstrong, W. H.; Mullins, O. C.; Cramer, S. P. *J. Am. Chem. Soc.* **1994**, *116*, 2914-2920.

(108) Bergmann, U.; Grush, M. M.; Horne, C. R.; DeMarois, P.; Penner-Hahn, J. E.; Yocum, C. F.; Wright, D. W.; Dubé, C. E.; Armstrong, W. H.; Christou, G.; Eppley, H. J.; Cramer, S. P. *J. Phys. Chem. B* **1998**, *102*, 8350-8352.

(109) Bergmann, U.; Cramer, S. P. In *SPIE Conference on Crystal and Multilayer Optics*; SPIE: San Diego, CA, 1998; Vol. 3448, pp 198-209.

(110) Berthold, D. A.; Babcock, G. T.; Yocum, C. F. *FEBS Lett.* **1981**, *134*, 231-234.

(111) Kuwabara, T.; Murata, N. *Plant Cell Physiol.* **1982**, *23*, 533-539.

(112) Porra, R. J.; Thompson, W. A.; Kriedemann, P. E. *Biochim. Biophys. Acta* **1989**, *975*, 384-394.

(113) Renger, G. *Biochim. Biophys. Acta* **1972**, *256*, 428-439.

(114) Jaklevic, J.; Kirby, J. A.; Klein, M. P.; Robertson, A. S.; Brown, G. S.; Eisenberger, P. *Solid State Commun.* **1977**, *23*, 679-682.

(115) Cramer, S. P.; Tench, O.; Yocum, M.; George, G. N. *Nucl. Instrum. Methods Phys. Res., Sect. A* **1988**, *A266*, 586-591.

(116) Goodin, D. B.; Falk, K.-E.; Wydrzynski, T.; Klein, M. P. "SSRL Activity Report," Stanford Synchotron Radiation Laboratory, 1979.

(117) Shinkarev, V. P.; Wraight, C. A. *Proc. Natl. Acad. Sci. U. S. A.* **1993**, *90*, 1834-1838.

(118) Forbush, B.; Kok, B.; McGloin, M. P. *Photochem. Photobiol.* **1971**, *14*, 307-321.

(119) Jursinic, P. *Biochim. Biophys. Acta* **1981**, *635*, 38-52.

(120) Styring, S.; Rutherford, A. W. *Biochemistry* **1987**, *26*, 2401-2405.

(121) Styring, S.; Rutherford, A. W. *Biochim. Biophys. Acta* **1988**, *933*, 378-387.

(122) Vermaas, W. F. J.; Renger, G.; Dohnt, G. *Biochim. Biophys. Acta* **1984**, *764*, 194-202.

(123) Chylla, R. A.; Garab, G.; Whitmarsh, J. *Biochim. Biophys. Acta* **1987**, *894*, 562-571.

(124) Chylla, R. A.; Whitmarsh, J. *Plant Physiol.* **1989**, *90*, 765-772.

(125) Visser, H.; Anxolabéhère-Mallart, E.; Bergmann, U.; Glatzel, P.; Robblee, J. H.; Cramer, S. P.; Girerd, J.-J.; Sauer, K.; Klein, M. P.; Yachandra, V. K., submitted for publication.

(126) Conradson, S. D.; Burgess, B. K.; Newton, W. E.; McDonald, J. W.; Rubinson, J. F.; Gheller, S. F.; Mortenson, L. E.; Adams, M. W. W.; Mascharak, P. K.; Armstrong, W. A.; Holm, R. H. *J. Am. Chem. Soc.* **1985**, *107*, 7935-7940.

(127) McDermott, A. E.; Yachandra, V. K.; Guiles, R. D.; Sauer, K.; Klein, M. P.; Parrett, K. G.; Golbeck, J. H. *Biochemistry* **1989**, *28*, 8056-8059.

(128) Ryan, D. E.; Grant, K. B.; Nakanishi, K.; Frank, P.; Hodgson, K. O. *Biochemistry* **1996**, *35*, 8651-8661.

(129) Musgrave, K. B.; Donahue, J. P.; Lorber, C.; Holm, R. H.; Hedman, B.; Hodgson, K. O. *J. Am. Chem. Soc.* **1999**, *121*, 10297-10307.

(130) Nivorozhkin, A. L.; Segal, B. M.; Musgrave, K. B.; Kates, S. A.; Hedman, B.; Hodgson, K. O.; Holm, R. H. *Inorg. Chem.* **2000**, *39*, 2306-2313.

(131) DeBeer, S.; Randall, D. W.; Nersissian, A. M.; Valentine, J. S.; Hedman, B.; Hodgson, K. O.; Solomon, E. I. *J. Phys. Chem. B* **2000**, *104*, 10814-10819.

(132) True, A. E.; Orville, A. M.; Pearce, L. L.; Lipscomb, J. D.; Que, L., Jr. *Biochemistry* **1990**, *29*, 10847-10854.

(133) True, A. E.; Scarrow, R. C.; Randall, C. R.; Holz, R. C.; Que, L., Jr. *J. Am. Chem. Soc.* **1993**, *115*, 4246-4255.

(134) Scarrow, R. C.; Trimitsis, M. G.; Buck, C. P.; Grove, G. N.; Cowling, R. A.; Nelson, M. J. *Biochemistry* **1994**, *33*, 15023-15035.

(135) Pavlosky, M. A.; Zhang, Y.; Westre, T. E.; Gan, Q.-F.; Pavel, E. G.; Campochiaro, C.; Hedman, B.; Hodgson, K. O.; Solomon, E. I. *J. Am. Chem. Soc.* **1995**, *117*, 4316-4327.

(136) Loeb, K. E.; Zaleski, J. M.; Westre, T. E.; Guajardo, R. J.; Mascharak, P. K.; Hedman, B.; Hodgson, K. O.; Solomon, E. I. *J. Am. Chem. Soc.* **1995**, *117*, 4545-4561.

(137) Westre, T. E.; Loeb, K. E.; Zaleski, J. M.; Hedman, B.; Hodgson, K. O.; Solomon, E. I. *J. Am. Chem. Soc.* **1995**, *117*, 1309-1313.

(138) Westre, T. E.; Kennepohl, P.; DeWitt, J. G.; Hedman, B.; Hodgson, K. O.; Solomon, E. I. *J. Am. Chem. Soc.* **1997**, *119*, 6297-6314.

(139) Tsutsumi, K.; Nakamori, H. *J. Phys. Soc. Jpn.* **1968**, *25*, 1419-1424.

(140) Tsutsumi, K.; Nakamori, H.; Ichikawa, K. *Phys. Rev. B: Condens. Matter* **1976**, *13*, 929-933.

(141) Taguchi, M.; Uozumi, T.; Kotani, A. *J. Phys. Soc. Jpn.* **1997**, *66*, 247-256.

(142) Zheng, M.; Dismukes, G. C. *Inorg. Chem.* **1996**, *35*, 3307-3319.

(143) Cheniae, G. M.; Martin, I. F. *Biochim. Biophys. Acta* **1971**, *253*, 167-181.

(144) Tamura, N.; Cheniae, G. *Biochim. Biophys. Acta* **1987**, *890*, 179-194.

(145) Zaltsman, L.; Ananyev, G. M.; Bruntrager, E.; Dismukes, G. C. *Biochemistry* **1997**, *36*, 8914-8922.

(146) Messinger, J.; Seaton, G.; Wydrzynski, T.; Wacker, U.; Renger, G. *Biochemistry* **1997**, *36*, 6862-6873.

(147) Kuzek, D.; Pace, R. J. *Biochim. Biophys. Acta* **2001**, *1503*, 123-137.

(148) Riggs, P. J.; Yocum, C. F.; Penner-Hahn, J. E.; Mei, R. *J. Am. Chem. Soc.* **1992**, *114*, 10650-10651.

(149) Whittaker, J. W. In *Metalloenzymes Involving Amino-acid Residue and Related Radicals*; Sigel, A., Sigel, H., Eds.; Marcel Dekker, Inc.: New York, 1994; Vol. 30, pp 315-360.

(150) Clark, K.; Penner-Hahn, J. E.; Whittaker, M. M.; Whittaker, J. W. *J. Am. Chem. Soc.* **1990**, *112*, 6433-6434.

(151) Wang, Y.; DuBois, J. L.; Hedman, B.; Hodgson, K. O.; Stack, T. D. P. *Science* **1998**, *279*, 537-540.

(152) Rothlisberger, U.; Carloni, P.; Doclo, K.; Parrinello, M. *JBIC* **2000**, *5*, 236-250.

(153) Boussac, A.; Rutherford, A. W.; Styring, S. *Biochemistry* **1990**, *29*, 24-32.

(154) Messinger, J.; Wacker, U.; Renger, G. *Biochemistry* **1991**, *30*, 7852-7862.

(155) Sauer, K.; Guiles, R. D.; McDermott, A. E.; Cole, J. L.; Yachandra, V. K.; Zimmermann, J.-L.; Klein, M. P.; Dexheimer, S. L.; Britt, R. D. *Chem. Scr.* **1988**, *28A*, 87-91.

(156) Huheey, J. E.; Keiter, E. A.; Keiter, R. L. *Inorganic Chemistry: Principles of Structure and Reactivity*; 4th ed.; HarperCollins Publishers: New York, 1993.

(157) Chu, H.-A.; Nguyen, A. P.; Debus, R. J. *Biochemistry* **1995**, *34*, 5839-5858.

(158) DeRose, V. J.; Yachandra, V. K.; McDermott, A. E.; Britt, R. D.; Sauer, K.; Klein, M. P. *Biochemistry* **1991**, *30*, 1335-1341.

(159) Tang, X.-S.; Diner, B. A.; Larsen, B. S.; Gilchrist, M. L., Jr.; Lorigan, G. A.; Britt, R. D. *Proc. Natl. Acad. Sci. U. S. A.* **1994**, *91*, 704-708.

(160) Debus, R. J.; Campbell, K. A.; Peloquin, J. M.; Pham, D. P.; Britt, R. D. *Biochemistry* **2000**, *39*, 470-478.

(161) Cinco, R. M.; Fernandez, C.; Messinger, J.; Robblee, J. H.; Visser, H.; McFarlane, K. L.; Bergmann, U.; Glatzel, P.; Cramer, S. P.; Sauer, K.; Klein, M. P.; Yachandra, V. K. In *Photosynthesis: Mechanisms and Effects*; Garab, G., Ed.; Kluwer Academic Publishers: Dordrecht, 1998; Vol. 2, pp 1273-1278.

(162) Heath, R. L.; Hind, G. *Biochim. Biophys. Acta* **1969**, *172*, 290-299.

(163) Izawa, S.; Heath, R. L.; Hind, G. *Biochim. Biophys. Acta* **1969**, *180*, 388-398.

(164) Preston, C.; Pace, R. J. *Biochim. Biophys. Acta* **1985**, *810*, 388-391.

(165) Wincencjusz, H.; van Gorkom, H. J.; Yocum, C. F. *Biochemistry* **1997**, *36*, 3663-3670.

(166) Fernandez, C.; Cinco, R. M.; Robblee, J. H.; Messinger, J.; Pizarro, S. A.; Sauer, K.; Klein, M. P.; Yachandra, V. K. In *Photosynthesis: Mechanisms and Effects*; Garab, G., Ed.; Kluwer Academic Publishers: Dordrecht, 1998; Vol. 2, pp 1399-1402.

(167) Pizarro, S. A., manuscript in preparation.

(168) Yachandra, V. K.; Guiles, R. D.; Sauer, K.; Klein, M. P. *Biochim. Biophys. Acta* **1986**, *850*, 333-342.

(169) Ono, T.-a.; Zimmermann, J.-L.; Inoue, Y.; Rutherford, A. W. *Biochim. Biophys. Acta* **1986**, *851*, 193-201.

(170) Beck, W. F.; Brudvig, G. W. *Chem. Scr.* **1988**, *28A*, 93-98.

(171) Lindberg, K.; Vänngård, T.; Andréasson, L.-E. *Photosynth. Res.* **1993**, *38*, 401-408.

(172) Lindberg, K.; Andréasson, L.-E. *Biochemistry* **1996**, *35*, 14259-14267.

(173) Larson, E. J.; Pecoraro, V. L. In *Manganese Redox Enzymes*; Pecoraro, V. L., Ed.; VCH Publishers: New York, 1992; pp 1-28.

(174) Baldwin, M. J.; Stemmler, T. L.; Riggs-Gelasco, P. J.; Kirk, M. L.; Penner-Hahn, J. E.; Pecoraro, V. L. *J. Am. Chem. Soc.* **1994**, *116*, 11349-11356.

(175) Messinger, J.; Renger, G. *FEBS Lett.* **1990**, *277*, 141-146.

(176) Vass, I.; Deák, Z.; Jegerschöld, C.; Styring, S. *Biochim. Biophys. Acta* **1990**, *1018*, 41-46.

(177) Messinger, J.; Schröder, W. P.; Renger, G. *Biochemistry* **1993**, *32*, 7658-7668.

(178) Klein, M. P.; Sauer, K.; Yachandra, V. K. *Photosynth. Res.* **1993**, *38*, 265-277.

(179) Lavergne, J.; Junge, W. *Photosynth. Res.* **1993**, *38*, 279-296.

(180) Witt, H. T. *Ber. Bunsen-Ges.* **1996**, *100*, 1923-1942.

(181) Renger, G.; Hanssum, B. *FEBS Lett.* **1992**, *299*, 28-32.

(182) Ioannidis, N.; Schansker, G.; Barynin, V. V.; Petrouleas, V. *JBIC* **2000**, *5*, 354-363.

(183) Messinger, J.; Badger, M.; Wydrzynski, T. *Proc. Natl. Acad. Sci. U. S. A.* **1995**, *92*, 3209-3213.

(184) Hillier, W.; Messinger, J.; Wydrzynski, T. *Biochemistry* **1998**, *37*, 16908-16914.

(185) Chu, H.-A.; Sackett, H.; Babcock, G. T. *Biochemistry* **2000**, *39*, 14371-14376.

(186) Noguchi, T.; Sugiura, M. *Biochemistry* **2000**, *39*, 10943-10949.

(187) Zimmermann, J.-L.; Rutherford, A. W. *Biochim. Biophys. Acta* **1986**, *851*, 416-423.

(188) Petrouleas, V.; Diner, B. A. *Biochim. Biophys. Acta* **1987**, *893*, 126-137.

(189) Brudvig, G. W.; Casey, J. L.; Sauer, K. *Biochim. Biophys. Acta* **1983**, *723*, 366-371.

(190) Lakshmi, K. V.; Eaton, S. S.; Eaton, G. R.; Brudvig, G. W. *Biochemistry* **1999**, *38*, 12758-12767.

(191) Åhrling, K. A.; Pace, R. J. *Biophys. J.* **1995**, *68*, 2081-2090.

(192) Åhrling, K. A.; Smith, P. J.; Pace, R. J. *J. Am. Chem. Soc.* **1998**, *120*, 13202-13214.

(193) Powers, L. *Biochim. Biophys. Acta* **1982**, *683*, 1-38.

(194) Scott, R. A. In *Structural and Resonance Techniques in Biological Research*; Rousseau, D. L., Ed.; Academic Press: Orlando, 1984; pp 295-362.

(195) Cramer, S. P. In *X-ray Absorption: Principles, Applications, Techniques of EXAFS, SEXAFS and XANES*; Koningsberger, D. C., Prins, R., Eds.; John Wiley & Sons: New York, 1988; Vol. 92, pp 327-320.

(196) Sayers, D. E.; Stern, E. A.; Lytle, F. *Phys. Rev. Lett.* **1971**, *27*, 1204-1207.

(197) Rehr, J. J.; Mustre de Leon, J.; Zabinsky, S. I.; Albers, R. C. *J. Am. Chem. Soc.* **1991**, *113*, 5135-5140.

(198) Mustre de Leon, J.; Rehr, J. J.; Zabinsky, S. I.; Albers, R. C. *Phys. Rev. B: Condens. Matter* **1991**, *44*, 4146-4156.

(199) Yachandra, V. K.; Guiles, R. D.; McDermott, A. E.; Cole, J. L.; Britt, R. D.; Dexheimer, S. L.; Sauer, K.; Klein, M. P. *Biochemistry* **1987**, *26*, 5974-5981.

(200) McDermott, A. E.; Yachandra, V. K.; Guiles, R. D.; Cole, J. L.; Dexheimer, S. L.; Britt, R. D.; Sauer, K.; Klein, M. P. *Biochemistry* **1988**, *27*, 4021-4031.

(201) MacLachlan, D. J.; Hallahan, B. J.; Ruffle, S. V.; Nugent, J. H. A.; Evans, M. C. W.; Strange, R. W.; Hasnain, S. S. *Biochem. J.* **1992**, *285*, 569-576.

(202) Mukerji, I.; Andrews, J. C.; DeRose, V. J.; Latimer, M. J.; Yachandra, V. K.; Sauer, K.; Klein, M. P. *Biochemistry* **1994**, *33*, 9712-9721.

(203) Riggs-Gelasco, P. J.; Mei, R.; Yocum, C. F.; Penner-Hahn, J. E. *J. Am. Chem. Soc.* **1996**, *118*, 2387-2399.

(204) Wieghardt, K. *Angew. Chem., Int. Ed. Engl.* **1989**, *28*, 1153-1172.

(205) George, G. N.; Prince, R. C.; Cramer, S. P. *Science* **1989**, *243*, 789-791.

(206) Cinco, R. M.; Robblee, J. H.; Rompel, A.; Fernandez, C.; Yachandra, V. K.; Sauer, K.; Klein, M. P. *J. Phys. Chem. B* **1998**, *102*, 8248-8256.

(207) Latimer, M. J.; DeRose, V. J.; Mukerji, I.; Yachandra, V. K.; Sauer, K.; Klein, M. P. *Biochemistry* **1995**, *34*, 10898-10909.

(208) Guiles, R. D.; Zimmermann, J.-L.; McDermott, A. E.; Yachandra, V. K.; Cole, J. L.; Dexheimer, S. L.; Britt, R. D.; Wieghardt, K.; Bossek, U.; Sauer, K.; Klein, M. P. *Biochemistry* **1990**, *29*, 471-485.

(209) Boussac, A.; Kuhl, H.; Ghibaudi, E.; Rögner, M.; Rutherford, A. W. *Biochemistry* **1999**, *38*, 11942-11948.

(210) Hanssum, B.; Dohnt, G.; Renger, G. *Biochim. Biophys. Acta* **1985**, *806*, 210-220.

(211) Babcock, G. T.; Sauer, K. *Biochim. Biophys. Acta* **1973**, *325*, 504-519.

(212) McMaster, W. H.; Del Grande, N. K.; Mallett, J. H.; Hubbell, J. H. "Compilation of x-ray cross sections," Lawrence Radiation Laboratory, 1969.

(213) Rehr, J. J.; Albers, R. C.; Zabinsky, S. I. *Phys. Rev. Lett.* **1992**, *69*, 3397-3400.

(214) Sayers, D. E.; Lytle, F. W.; Stern, E. A. *J. Non-Cryst. Solids* **1972**, *8-10*, 401-407.

(215) Lee, P. A.; Pendry, J. B. *Phys. Rev. B* **1975**, *11*, 2795-2811.

(216) Lee, P. A.; Citrin, P. H.; Eisenberger, P.; Kincaid, B. M. *Rev. Mod. Phys.* **1981**, *53*, 769-806.

(217) Teo, B. K. *EXAFS : basic principles and data analysis*; Springer-Verlag: Berlin, 1986.

(218) O'Day, P. A.; Rehr, J. J.; Zabinsky, S. I.; Brown, G. E., Jr. *J. Am. Chem. Soc.* **1994**, *116*, 2938-2949.

(219) Franzen, L.-G.; Styring, S.; Étienne, A.-L.; Hansson, Ö.; Vernotte, C. *Photobiochem. Photobiophys.* **1986**, *13*, 15-28.

(220) Yamada, Y.; Tang, X.-S.; Ito, S.; Sato, K. *Biochim. Biophys. Acta* **1987**, *891*, 129-137.

(221) Enami, I.; Kamino, K.; Shen, J.-R.; Satoh, K.; Katoh, S. *Biochim. Biophys. Acta* **1989**, *977*, 33-39.

(222) Noren, G. H.; Boerner, R. J.; Barry, B. A. *Biochemistry* **1991**, *30*, 3943-3950.

(223) Sandusky, P. O.; DeRoo, C. L. S.; Hicks, D. B.; Yocum, C. F.; Ghanotakis, D. F.; Babcock, G. T. In *The Oxygen Evolving Complex of Photosynthesis*; Inoue, Y., Crofts, A. R., Govindjee, Murata, N., Renger, G., Satoh, K., Eds.; Academic Press: Tokyo, 1983; pp 189-199.

(224) Ghanotakis, D. F.; Babcock, G. T.; Yocum, C. F. *Biochim. Biophys. Acta* **1984**, *765*, 388-398.

(225) Bowes, J. M.; Stewart, A. C.; Bendall, D. S. *Biochim. Biophys. Acta* **1983**, *725*, 210-219.

(226) Ohno, T.; Satoh, K.; Katoh, S. *Biochim. Biophys. Acta* **1986**, *852*, 1-8.

(227) Cheniae, G. M.; Martin, I. F. *Plant Physiol.* **1971**, *47*, 568-575.

(228) Yocum, C. F.; Yerkes, C. T.; Blankenship, R. E.; Sharp, R. R.; Babcock, G. T. *Proc. Natl. Acad. Sci. U. S. A.* **1981**, *78*, 7507-7511.

(229) Ke, B.; Inoué, H.; Babcock, G. T.; Fang, Z.-X.; Dolan, E. *Biochim. Biophys. Acta* **1982**, *682*, 297-306.

(230) Shen, J.-R.; Satoh, K.; Katoh, S. *Biochim. Biophys. Acta* **1988**, *936*, 386-394.

(231) Pauly, S.; Witt, H. T. *Biochim. Biophys. Acta* **1992**, *1099*, 211-218.

(232) Bunker, G. A.; Hasnain, S. S.; Sayers, D. E. In *X-ray absorption fine structure*; Hasnain, S. S., Ed.; E. Horwood: New York :, 1991; pp 751-770.

(233) Binsted, N.; Strange, R. W.; Hasnain, S. S. *Biochemistry* **1992**, *31*, 12117-12125.

(234) Bertagnolli, H.; Ertel, T. S. *Angew. Chem., Int. Ed. Engl.* **1994**, *33*, 45-66.

(235) Liang, W.; Latimer, M. J.; Dau, H.; Roelofs, T. A.; Yachandra, V. K.; Sauer, K.; Klein, M. P. *Biochemistry* **1994**, *33*, 4923-4932.

(236) Dau, H.; Andrews, J. C.; Roelofs, T. A.; Latimer, M. J.; Liang, W.; Yachandra, V. K.; Sauer, K.; Klein, M. P. *Biochemistry* **1995**, *34*, 5274-5287.

(237) DeRose, V. J.; Latimer, M. J.; Zimmermann, J.-L.; Mukerji, I.; Yachandra, V. K.; Sauer, K.; Klein, M. P. *Chem. Phys.* **1995**, *194*, 443-459.

(238) Kurreck, J.; Garbers, A.; Reifarth, F.; Andréasson, L.-E.; Parak, F.; Renger, G. *FEBS Lett.* **1996**, *381*, 53-57.

(239) Christou, G.; Vincent, J. B. In *Metal Clusters in Proteins*; Que, L., Jr., Ed.; American Chemical Society: Washington, D. C., 1988; Vol. 372, pp 238-255.

(240) Pence, L. E.; Caneschi, A.; Lippard, S. J. *Inorg. Chem.* **1996**, *35*, 3069-3072.

(241) Darovsky, A.; Kezerashvili, V.; Coppens, P.; Weyhermüller, T.; Hummel, H.; Wieghardt, K. *Inorg. Chem.* **1996**, *35*, 6916-6917.

(242) Pecoraro, V. L.; Hsieh, W.-Y. In *Manganese and Its Role in Biological Processes*; Sigel, A., Sigel, H., Eds.; Marcel Dekker Inc.: New York, 2000; Vol. 37, pp 429-504.

(243) Boussac, A.; Girerd, J.-J.; Rutherford, A. W. *Biochemistry* **1996**, *35*, 6984-6989.

(244) Boussac, A.; Kuhl, H.; Un, S.; Rögner, M.; Rutherford, A. W. *Biochemistry* **1998**, *37*, 8995-9000.

(245) Beck, W. F.; de Paula, J. C.; Brudvig, G. W. *J. Am. Chem. Soc.* **1986**, *108*, 4018-4022.

(246) Britt, R. D.; Zimmermann, J.-L.; Sauer, K.; Klein, M. P. *J. Am. Chem. Soc.* **1989**, *111*, 3522-3532.

(247) Frapart, Y.-M. Ph. D. thesis, Université de Paris-Sud, 1996.

(248) Sivaraja, M.; Tso, J.; Dismukes, G. C. *Biochemistry* **1989**, *28*, 9459-9464.

(249) Boussac, A.; Zimmermann, J.-L.; Rutherford, A. W. *Biochemistry* **1989**, *28*, 8984-8989.

(250) Latimer, M. J.; DeRose, V. J.; Yachandra, V. K.; Sauer, K.; Klein, M. P. *J. Phys. Chem. B* **1998**, *102*, 8257-8265.

(251) Gilchrist, M. L., Jr.; Ball, J. A.; Randall, D. W.; Britt, R. D. *Proc. Natl. Acad. Sci. U. S. A.* **1995**, *92*, 9545-9549.

(252) Tang, X.-S.; Randall, D. W.; Force, D. A.; Diner, B. A.; Britt, R. D. *J. Am. Chem. Soc.* **1996**, *118*, 7638-7639.

(253) Peloquin, J. M.; Campbell, K. A.; Britt, R. D. *J. Am. Chem. Soc.* **1998**, *120*, 6840-6841.

(254) Geijer, P.; Deák, Z.; Styring, S. *Biochemistry* **2000**, *39*, 6763-6772.

(255) Bashkin, J. S.; Schake, A. R.; Vincent, J. B.; Chang, H.-R.; Li, Q.; Huffman, J. C.; Christou, G.; Hendrickson, D. N. *J. Chem. Soc., Chem. Commun.* **1988**, 700-702.

(256) Hodgson, D. J.; Schwartz, B. J.; Sorrell, T. N. *Inorg. Chem.* **1989**, *28*, 2226-2228.

(257) Mabad, B.; Cassoux, P.; Tuchagues, J.-P.; Hendrickson, D. N. *Inorg. Chem.* **1986**, *25*, 1420-1431.

(258) Kessissoglou, D. P.; Butler, W. M.; Pecoraro, V. L. *Inorg. Chem.* **1987**, *26*, 495-503.

(259) Yu, S. B.; Wang, C. P.; Day, E. P.; Holm, R. H. *Inorg. Chem.* **1991**, *30*, 4067-4074.

(260) Kitajima, N.; Singh, U. P.; Amagai, H.; Osawa, M.; Morooka, Y. *J. Am. Chem. Soc.* **1991**, *113*, 7757-7758.

(261) Teo, B. K.; Antonio, M. R.; Averill, B. A. *J. Am. Chem. Soc.* **1983**, *105*, 3751-3762.

(262) Smith, P. J.; Pace, R. J. *Biochim. Biophys. Acta* **1996**, *1275*, 213-220.

(263) Smith, P. J.; Pace, R. J. *Appl. Magn. Reson.* **1996**, *11*, 443-460.

(264) Boussac, A.; Rutherford, A. W. *Biochim. Biophys. Acta* **2000**, *1457*, 145-156.

(265) Zouni, A.; Jordan, R.; Schlodder, E.; Fromme, P.; Witt, H. T. *Biochim. Biophys. Acta* **2000**, *1457*, 103-105.

(266) George, G. N.; Hilton, J.; Temple, C.; Prince, R. C.; Rajagopalan, K. V. *J. Am. Chem. Soc.* **1999**, *121*, 1256-1266.

(267) Hwang, J.; Krebs, C.; Huynh, B. H.; Edmondson, D. E.; Theil, E. C.; Penner-Hahn, J. E. *Science* **2000**, *287*, 122-125.

(268) Shulman, R. G.; Eisenberger, P.; Blumberg, W. E.; Stombaugh, N. A. *Proc. Natl. Acad. Sci. U. S. A.* **1975**, *72*, 4003-4007.

(269) Shulman, R. G.; Eisenberger, P.; Kincaid, B. M. *Annu. Rev. Biophys. Bioeng.* **1978**, *7*, 559-578.

(270) Teo, B.-K.; Shulman, R. G.; Brown, G. S.; Meixner, A. E. *J. Am. Chem. Soc.* **1979**, *101*, 5624-5631.

(271) Riggs-Gelasco, P. J.; Shu, L.; Chen, S.; Burdi, D.; Huynh, B. H.; Que, L., Jr.; Stubbe, J. *J. Am. Chem. Soc.* **1998**, *120*, 849-860.

(272) Jaron, S.; Blackburn, N. J. *Biochemistry* **1999**, *38*, 15086-15096.

(273) Pidcock, E.; DeBeer, S.; Obias, H. V.; Hedman, B.; Hodgson, K. O.; Karlin, K. D.; Solomon, E. I. *J. Am. Chem. Soc.* **1999**, *121*, 1870-1878.

(274) Goussias, C.; Ioannidis, N.; Petrouleas, V. *Biochemistry* **1997**, *36*, 9261-9266.

(275) Nugent, J. H. A.; Diner, B. A.; Evans, M. C. W. *FEBS Lett.* **1981**, *124*, 241-244.

(276) Randall, D. W.; Gelasco, A.; Caudle, M. T.; Pecoraro, V. L.; Britt, R. D. *J. Am. Chem. Soc.* **1997**, *119*, 4481-4491.

(277) Force, D. A.; Randall, D. W.; Lorigan, G. A.; Clemens, K. L.; Britt, R. D. *J. Am. Chem. Soc.* **1998**, *120*, 13321-13333.

(278) Cooper, S. R.; Dismukes, G. C.; Klein, M. P.; Calvin, M. *J. Am. Chem. Soc.* **1978**, *100*, 7248-7252.

(279) Dismukes, G. C.; Sheats, J. E.; Smegal, J. A. *J. Am. Chem. Soc.* **1987**, *109*, 7202-7203.

(280) Khangulov, S. V.; Barynin, V. V.; Voevodskaya, N. V.; Grebenko, A. I. *Biochim. Biophys. Acta* **1990**, *1020*, 305-310.

(281) Zheng, M.; Khangulov, S. V.; Dismukes, G. C.; Barynin, V. V. *Inorg. Chem.* **1994**, *33*, 382-387.

(282) Cox, A. D.; Beaumont, J. H. *Philos. Mag. B* **1980**, *42*, 115-126.

(283) Heald, S. M. In *X-ray Absorption: Principles, Applications, Techniques of EXAFS, SEXAFS and XANES*; Koningsberger, D. C., Prins, R., Eds.; John Wiley & Sons: New York, 1988; Vol. 92, pp 87-118.

(284) Penner-Hahn, J. E.; Benfatto, M.; Hedman, B.; Takahashi, T.; Doniach, S.; Groves, J. T.; Hodgson, K. O. *Inorg. Chem.* **1986**, *25*, 2255-2259.

(285) Kutzler, F. W.; Scott, R. A.; Berg, J. M.; Hodgson, K. O.; Doniach, S.; Cramer, S. P.; Chang, C. H. *J. Am. Chem. Soc.* **1981**, *103*, 6083-6088.

(286) Smith, T. A.; Penner-Hahn, J. E.; Berding, M. A.; Doniach, S.; Hodgson, K. O. *J. Am. Chem. Soc.* **1985**, *107*, 5945-5955.

(287) Templeton, D. H.; Templeton, L. K. *Acta Crystallogr., Sect. A: Found. Crystallogr.* **1980**, *A36*, 237-241.

(288) Templeton, D. H.; Templeton, L. K. *Acta Crystallogr., Sect. A: Found. Crystallogr.* **1982**, *A38*, 62-67.

(289) Scott, R. A.; Hahn, J. E.; Doniach, S.; Freeman, H. C.; Hodgson, K. O. *J. Am. Chem. Soc.* **1982**, *104*, 5364-5369.

(290) Guss, J. M.; Freeman, H. C. *J. Mol. Biol.* **1983**, *169*, 521-563.

(291) Heald, S. M.; Stern, E. A. *Phys. Rev. B* **1977**, *16*, 5549-5559.

(292) Heald, S. M.; Stern, E. A. *Phys. Rev. B* **1978**, *17*, 4069-4081.

(293) Tullius, T. D. Ph. D. thesis, Stanford University, 1979.

(294) Mahapatra, S.; Das, P.; Mukherjee, R. *J. Chem. Soc., Dalton Trans.* **1993**, 217-220.

(295) Mahapatra, S.; Lal, T. K.; Mukherjee, R. *Inorg. Chem.* **1994**, *33*, 1579-1580.

(296) Lal, T. K.; Mukherjee, R. *Inorg. Chem.* **1998**, *37*, 2373-2382.

(297) Bendix, J.; Deeth, R. J.; Weyhermüller, T.; Bill, E.; Wieghardt, K. *Inorg. Chem.* **2000**, *39*, 930-938.

(298) Workman, J. M.; Powell, R. D.; Procyk, A. D.; Collins, T. J.; Bocian, D. F. *Inorg. Chem.* **1992**, *31*, 1548-1550.

(299) Lytle, F. W.; Greegor, R. B.; Sandstrom, D. R.; Marques, E. C.; Wong, J.; Spiro, C. L.; Huffman, G. P.; Huggins, F. E. *Nucl. Instrum. Methods Phys. Res., Sect. A* **1984**, *226*, 542-548.

(300) Zabinsky, S. I.; Rehr, J. J.; Aukudinov, A.; Albers, R. C.; Eller, M. J. *Phys. Rev. B: Condens. Matter* **1995**, *52*, 2995-3009.

(301) Westre, T. E.; Di Cicco, A.; Filipponi, A.; Natoli, C. R.; Hedman, B.; Solomon, E. I.; Hodgson, K. O. *J. Am. Chem. Soc.* **1994**, *116*, 6757-6768.

(302) Laplaza, C. E.; Johnson, M. J. A.; Peters, J.; Odom, A. L.; Kim, E.; Cummins, C. C.; George, G. N.; Pickering, I. J. *J. Am. Chem. Soc.* **1996**, *118*, 8623-8638.

(303) Stebler, M.; Ludi, A.; Bürgi, H.-B. *Inorg. Chem.* **1986**, *25*, 4743-4750.

(304) Wieghardt, K.; Bossek, U.; Ventur, D.; Weiss, J. *J. Chem. Soc., Chem. Commun.* **1985**, 347-349.

(305) George, G. N.; Cramer, S. P.; Frey, T. G.; Prince, R. C. *Biochim. Biophys. Acta* **1993**, *1142*, 240-252.

(306) le Grand, J. B.; Mears, C. A.; Hiller, L. J.; Frank, M.; Labov, S. E.; Netel, H.; Chow, D.; Friedrich, S.; Lindeman, M. A.; Barfknecht, A. T. *Appl. Phys. Lett.* **1998**, *73*, 1295-1297.

(307) de Groot, F. M. F. *J. Electron Spectrosc. Relat. Phenom.* **1994**, *67*, 529-622.

(308) Wang, H.; Ge, P.; Riordan, C. G.; Brooker, S.; Woomer, C. G.; Collins, T.; Melendres, C. A.; Graudejus, O.; Bartlett, N.; Cramer, S. P. *J. Phys. Chem. B* **1998**, *102*, 8343-8346.

(309) George, S. J.; van Elp, J.; Chen, J.; Ma, Y.; Chen, C. T.; Park, J. B.; Adams, M. W. W.; Searle, B. G.; de Groot, F. M. F.; et al. *J. Am. Chem. Soc.* **1992**, *114*, 4426-4427.

(310) van Elp, J.; George, S. J.; Chen, J.; Peng, G.; Chen, C. T.; Tjeng, L. H.; Meigs, G.; Lin, H.-J.; Zhou, Z. H.; Adams, M. W. W.; Searle, B. G.; Cramer, S. P. *Proc. Natl. Acad. Sci. U. S. A.* **1993**, *90*, 9664-9667.

(311) Wang, H.; Peng, G.; Miller, L. M.; Scheuring, E. M.; George, S. J.; Chance, M. R.; Cramer, S. P. *J. Am. Chem. Soc.* **1997**, *119*, 4921-4928.

(312) George, S. J.; Lowery, M. D.; Solomon, E. I.; Cramer, S. P. *J. Am. Chem. Soc.* **1993**, *115*, 2968-2969.

(313) Christiansen, J.; Peng, G.; Young, A. T.; LaCroix, L. B.; Solomon, E. I.; Cramer, S. P. *Inorg. Chim. Acta* **1996**, *243*, 229-232.

(314) Wang, H.; Bryant, C.; Randall, D. W.; LaCroix, L. B.; Solomon, E. I.; LeGros, M.; Cramer, S. P. *J. Phys. Chem. B* **1998**, *102*, 8347-8349.

(315) van Elp, J.; Peng, G.; Zhou, Z. H.; Adams, M. W. W.; Baidya, N.; Mascharak, P. K.; Cramer, S. P. *Inorg. Chem.* **1995**, *34*, 2501-2504.

(316) Cramer, S. P.; Peng, G.; Christiansen, J.; Chen, J.; van Elp, J.; George, S. J.; Young, A. T. *J. Electron Spectrosc. Relat. Phenom.* **1996**, *78*, 225-229.

(317) Wang, H.; Ralston, C. Y.; Patil, D. S.; Jones, R. M.; Gu, W.; Verhagen, M.; Adams, M.; Ge, P.; Riordan, C.; Marganian, C. A.; Mascharak, P.; Kovacs, J.; Miller, C. G.; Collins, T. J.; Brooker, S.; Croucher, P. D.; Wang, K.; Steifel, E. I.; Cramer, S. P. *J. Am. Chem. Soc.* **2000**, *122*, 10544-10552.

(318) Ralston, C. Y.; Wang, H.; Ragsdale, S. W.; Kumar, M.; Spangler, N. J.; Ludden, P. W.; Gu, W.; Jones, R. M.; Patil, D. S.; Cramer, S. P. *J. Am. Chem. Soc.* **2000**, *122*, 10553-10560.

(319) Caliebe, W. A.; Kao, C.-C.; Hastings, J. B.; Taguchi, M.; Kotani, A.; Uozumi, T.; de Groot, F. M. F. *Phys. Rev. B: Condens. Matter Mater. Phys.* **1998**, *58*, 13452-13458.